UNIVERSITAT
POLITÈCNICA
DE VALÈNCIA

Departamento de Máquinas y Motores Térmicos

DOCTORAL THESIS:

“Numerical study of a radial turbine of variable geometry at off-design conditions reaching choked flow”

Presented by: D. JUAN DAVID ECHAVARRÍA OLAYA
Supervised by: DR. D. ANDRÉS OMAR TISEIRA IZAGUIRRE

in fulfillment of the requisites for the degree of

Doctor of Philosophy

Valencia, May 2023

PhD. Thesis

“Numerical study of a radial turbine of variable geometry at off-design conditions reaching choked flow”

AUTHORS

Presented by:	D. JUAN DAVID ECHAVARRÍA OLAYA
Supervised by:	DR. D. ANDRÉS OMAR TISEIRA IZAGUIRRE

DEFENSE COMMITTEE

Chairman:	DR. D. JOSÉ RAMÓN SERRANO CRUZ
Secretary:	DR. D. PABLO FAJARDO PEÑA
Member:	DR. D. AARON COSTALL

Valencia, May 2023

Numerical study of a radial turbine of variable geometry at off-design conditions reaching choked flow

Juan David Echavarría Olaya

Abstract

In turbochargers with variable geometry turbine (VGT), the stator vanes move to a closed position to drive high exhaust back pressure during the engine braking mode. Thus, shock waves are generated at the stator. Furthermore, depending on the operational conditions in the use of radial turbines in other applications like reverse Brayton cycle for refrigeration, Organic Rankine Cycles, and gas turbine auxiliary power unit (GTAPU), sonic flow and shock waves can appear.

The current work focuses on studying the flow behavior of a commercial turbocharger turbine of variable geometry at off-design conditions reaching choked flow. A detailed examination of the flow patterns within the turbine has been carried out using CFD simulations, identifying and quantifying the most important phenomena under different operational points. Reynolds Averaged Navier Stokes (RANS) and unsteady RANS simulations have been performed to obtain the flow structures in stator and rotor as well as the turbine map.

The CFD results show that the region of the computational domain where the sonic conditions appear depends on the stator vanes position and the pressure ratio. When the stator vanes are in the closed position (10% VGT) the flow through the stator accelerates and, depending on pressure ratio, the static pressure on the suction side decreases until a certain point where a sudden increase reveals the presence of a shock wave that expands through the vaneless space. The intensity of the shock wave at higher pressure ratio varies with the rotational speed.

To analyze the rotor-stator interaction, numerical simulations were carried out with the stator vanes at the closed position, 10% VGT, and at wider position, 30% VGT. The number of shocks a fluid particle experiences upstream of the rotor is correlated with the fluid shock losses. Close to the stator vanes, the pressure losses are high; toward the center of the vaneless space, they start to decrease, and close to the rotor they start to increase. The rotor-stator interaction creates shock waves, whose intensity depends on the position of the rotor leading edge and the blade speed. At higher rotational speed, load fluctuation occurs close to the leading edge, which may compromise the blade's integrity.

When the turbine has the stator vanes open (80% VGT) and operates at the selected higher pressure ratio, the choking condition appears in a plane at the rotor trailing edge. Furthermore, the development of the choked area depends on the rotational speed and tip leakage. Thus, the effect of the tip leakage flow on the main flow under sonic conditions was investigated decreasing and increasing the tip gap up to 50% of the original geometry given by the manufacturer. The flow through the gap accelerates and then mixes with the main flow, generating a vortex. The effects of the vortex on the flow at the rotor trailing edge plane when the tip gap varies are more significant at higher speed than at lower speed. The vortex stays closer to the tip suction side at higher speed, generating a subsonic region that increases with the tip gap height. At higher and lower rotational speeds, the tip leakage flow does not affect the main flow close to the hub.

Besides changing the rotor geometry to analyze the effects on the choked flow, the flat surface of the stator suction side has been modified to analyze the impact of two grooved surfaces configuration. The results reveal that the grooves especially affect the turbine efficiency at higher speed, where the increase is between 2 and 6 efficiency points. Furthermore, the grooves reduce the supersonic pocket developed on the suction side and diminish the shock wave intensity.

Finally, exergy analysis has been carried out to quantify the available energy in each region of the computational domain when the turbine operates with the vanes at closed and opened positions and at lower and higher speed and pressure ratios. The results help determine in which regions the losses must be diminished, finding that the bigger fraction of exergy budget corresponds to the rotor followed by the stator and vaneless space. A similar analysis has been conducted to compare the impact on the flow when the stator has a grooved surface instead of a flat surface. In the results highlight the cases at higher pressure ratio and higher speed, where the 5 and 11 grooves configuration present in the stator an increase of the energy quality of 8.2% and 15.9%, respectively. The exergy variation in the vaneless space presents a drop of 23.0% and 40.2% for 5 and 11 grooves, respectively. Thus, the normalized work of the rotor increases 8.7% and 7.7% because of the reduction of the shock wave intensity.

Resumen

En los turbocompresores con turbina de geometría variable (VGT por sus siglas en inglés) los vanos del estator se mueven a una posición cerrada para generar una contrapresión durante el modo de frenado del motor. De este modo, se generan ondas de choque en el estator. Además, en otras aplicaciones donde se utilizan turbinas radiales como en ciclos reversos de Brayton para refrigeración, ciclos orgánicos Rankine, y en las turbinas para la unidad de potencia auxiliar, dependiendo de las condiciones de operación, pueden aparecer condiciones sónicas y ondas de choque.

El presente trabajo se centra en el estudio del comportamiento del flujo a través de una turbina de geometría variable de un turbocompresor comercial en condiciones fuera de diseño alcanzando condiciones de choque. Se ha realizado un análisis detallado del patrón de flujo dentro de la turbine usando simulaciones CFD, identificando y cuantificando los fenómenos más importantes bajo diferentes condiciones de operación. Se han llevado a cabo simulaciones estacionarias usando Reynolds Averaged Navier Stokes (RANS) y no estacionarias (unsteady RANS) para obtener las características del flujo en el estator y en el rotor, además de obtener el mapa de la turbina.

Los resultados CFD muestran que la región del dominio computacional donde aparecen las condiciones sónicas depende de la posición de los vanos del estator y la relación de presiones. Cuando los vanos del estator están en una posición cerrada (10% VGT), el fluido se acelera y, dependiendo de la relación de presiones, la presión estática en el lado de succión disminuye hasta cierto punto donde un incremento repentino revela la presencia de una onda de choque, la cual se expande por el espacio sin vanos. La intensidad de la onda de choque bajo la relación de presiones más altas varia con la velocidad de giro.

Para analizar la interacción entre el rotor y el estator se llevaron a cabo simulaciones numéricas con los vanos del estator en una posición cerrada, 10% VGT, y en una posición más abierta, 30% VGT. El número de choques que una partícula del fluido experimenta aguas arriba del rotor está correlacionado con las pérdidas por choque del fluido. Cerca de los vanos del estator, las pérdidas de presión son altas, hacia el centro del espacio sin vanos las pérdidas disminuyen y cerca del rotor empiezan a incrementar. La interacción entre el rotor y el estator crea ondas de choque cuya intensidad depende de la posición del borde de ataque del rotor y de la velocidad de giro. A la velocidad de giro más alta, ocurren fluctuaciones en la carga cerca del borde de ataque, las cuales pueden comprometer la integridad de la pala.

Cuando la turbina tiene los vanos del estator abiertos (80% VGT) y opera a la relación de presión más alta seleccionada, las condiciones de choque aparecen en el plano del borde de fuga del rotor. Además, el desarrollo del área chocada depende de la velocidad de giro y de las fugas en la punta del álabe. Así, se investigó los efectos de las fugas en la punta del alabe sobre el flujo principal bajo condiciones sónicas disminuyendo e incrementando el intersticio entre la punta del álabe y la carcasa hasta un 50% en base a la geometría dada por el fabricante. El flujo a través de este espacio se acelera para posteriormente mezclarse con el flujo principal y generar un vórtice. Los efectos del vórtice sobre el flujo en el plano ubicado en el borde de fuga del rotor cuando el intersticio varía son más significativos a altas velocidades que a bajas velocidades. El vórtice permanece más cerca del lado de succión a altas velocidades generando una región subsónica que incrementa con la altura del intersticio. Las fugas en la punta del álabe no afectan al flujo principal cerca del cubo cuando la turbina opera a altas y bajas velocidades.

A parte de cambiar la geometría del rotor para analizar los efectos sobre las condiciones de choque, la superficie plana del lado de succión del vano del estator ha sido modifica para analizar el impacto de dos configuraciones usando ondulaciones sobre la superficie. Los resultados revelan que las ondulaciones afectan especialmente la eficiencia de la turbina a altas velocidades, generando un incremento entre 2 y 6 puntos de eficiencia. Además, las ondulaciones reducen la región supersónica sobre el lado de succión y disminuyen la intensidad de la onda de choque.

Finalmente se ha realizado un análisis exergético para cuantificar la energía disponible en cada región del dominio computacional cuando la turbina opera con los vanos en una posición cerrada y abierta a bajas y altas velocidades y relaciones de presiones. Los resultados ayudan a determinar en cual región se deben de disminuir las pérdidas, encontrando que la mayor fracción de exergía estimada corresponde al rotor seguido del estator y el espacio sin vanos. Un análisis similar se ha llevado a cabo para comparar el impacto sobre el flujo cuando el estator tiene una superficie ondulada en lugar de una superficie plana. En los resultados destacan los casos a alta relación de presión y alta velocidad, donde las configuraciones con 5 y 11 ondulaciones presentan en el estator un incremento en la calidad de la energía de 8.2% y 15.9%, respectivamente. El cambio en la exergía en el espacio sin vanos presenta una caída del 23.0% y 40.2% para los casos de 5 y 11 ondulaciones respectivamente. Así, el trabajo normalizado del rotor incrementa 8.7% y 7.7% como consecuencia de la disminución de la intensidad de la onda de choque en el espacio sin vanos.

Resum

En turbocompressors amb turbina de geometria variable (VGT per les seues sigles en anglès), les paletes de l'estàtor es mouen a una posició tancada per generar una contrapressió durant el mode de frenada del motor. D'aquesta forma, es generen unes ones de xoc en l'estàtor. A més, en altres aplicacions on s'utilitzen turbines radials com els cicles inversos de Brayton per a refrigeració, cicles orgànics de Rankine o en turbines per a la unitat de potencia auxiliar, depenent de les condicions d'operació poden aparéixer condicions sòniques i d'ones de xoc.

El present treball es centra en l'estudi del comportament del flux en una turbina radial de geometria variable d'un turbocompressor comercial en condicions fora de disseny, arribant a condicions de xoc. S'ha realitzat un anàlisi detallat del patró de flux dins d'aquestes turbines utilitzant simulacions CFD, identificant i quantificant els fenòmens més importants a diferents condicions d'operació. S'han realitzat simulacions estacionàries utilitzant Reynolds Averaged Navier Stokes (RANS) i no estacionàries (Unsteady-RANS) per a obtenir les característiques del flux en l'estàtor i en el rotor, a més d'obtenir el mapa de la turbina.

Els resultats CFD mostren que la regió del domini computacional on apareixen les condicions sòniques depenen de la posició de les paletes de l'estàtor i de la relació de pressions. Quan les paletes de l'estàtor estan en una posició tancada (10% VGT), el flux s'accelera i, depenent de la relació de pressions, la pressió estàtica en el costat de succió disminueix fins a cert punt on un increment brusc denota la presència d'una ona de xoc que s'expandix per l'espai sense paletes. L'intensitat de la ona de xoc a relacions de pressions elevades varia amb la velocitat de rotació.

Per analitzar l'interacció entre rotor i estàtor es van realitzar simulacions numèriques amb les paletes de l'estàtor en una posició tancada, 10% VGT, i en una posició més oberta, 30% VGT. El nombre de xocs que una partícula del fluid experimenta aigües amunt del rotor està correlacionat amb les pèrdues per xoc del fluid. Prop de les paletes de l'estàtor, les pèrdues de pressión són elevades, cap al centre de l'espai sense paletes les pèrdues disminueixen i prop del rotor comencen a incrementarse. L'interacción entre rotor i estàtor crea ones de xoc amb una intensitat que depèn de la posició de la vora d'atac del rotor i de la velocitat de rotació. A la velocitat de rotació més elevada, prop de de la vora d'atac ocorren fluctuacions en la càrrega que poden comprometre la integritat de la pala.

Quan la turbina té les paletes de l'estàtor obertes (80% VGT) i opera a la relació de pressió més elevada de les seleccionades, les condicions de xoc apareixen en el pla de la vora de fuga del rotor. A més, el desenvolupament de l'àrea xocada depèn de la velocitat de rotació i de les fugues en la punta de les paletes. Així, s'ha investigat els efectes de les fugues en la punta de les paletes sobre el flux principal sota condicions sòniques, disminuint i incrementant l'interstici entre la punta de la paleta i la carcasa fins un 50% en base a la geometria donada pel fabricant. El flux en aquest espai s'accelera per a posteriorment mesclar-se amb el flux principal i generar

un vòrtex. Els efectes del vòrtex sobre el flux en el pla ubicat a la vora de fuga del rotor quan l'interstici varia són més significatives a velocitats altes que a velocitats baixes. El vòrtex roman més prop del costat de succió a velocitats elevades generant una regió subsònica que incrementa amb l'altura de l'interstici. Les fugues en la punta de les paletes no afecten al flux principal prop del cub quan la turbina opera tant a altes com baixes velocitats.

A part de canviar la geometria del rotor per analitzar els efectes sobre les condicions de xoc, la superfície plana del costat de succió de les paletes de l'estàtor han sigut modificades per analitzar l'impacte de dos configuracions diferents utilitzant ondulacions sobre la superfície. Els resultats revelen que estes ondulacions afecten especialment a l'eficiència de la turbina a velocitats elevades, generant un increment entre 2 i 6 punts d'eficiència. A més, estes ondulacions redueixen la regió supersònica sobre el costat de succió i disminueixen l'intensitat de l'ona de xoc.

Finalment, s'ha realitzat un anàlisi exergètic per quantificar l'energia disponible en cada regió del domini computacional quan la turbina opera amb les paletes en posicions tancades i obertes a baixes i altes velocitats i relacions de pressions. Els resultats ajuden a determinar la regió en la que es deuen disminuir les pèrdues, trobant que la major fracció d'exergia estimada correspon al rotor, seguit per l'estàtor i l'espai sense paletes. Un anàlisi similar s'ha realitzat per comparar l'impacte sobre el flux quan l'estàtor té una superfície ondulada en lloc d'una plana. En aquests resultats, destaquen els casos d'alta relació de pressió i alta velocitat, on les configuracions amb 5 i 11 ondulacions presenten un increment de la qualitat de l'energía en l'estàtor del 8.2% i 15.9% respectivament. El canvi en l'exergía en l'espai sense paletes presenta una caiguda del 23% i 40.2% per als casos de 5 i 11 ondulcaions respectivament. Així, el treball normalitzat del rotor incrementa un 8.7% i un 7.7% a conseqüència de la disminució de l'intensitat de l'ina de xoc en l'espai sense paletes.

List of publications

The papers presented here are the basis of this thesis:

- “Numerical simulation of a radial turbine at off desing conditions in presence of choked flow”, in *ASME Turbo Expo 2020: Turbomachinery Technical Conference and Exposition* (2020) by Tiseira, García-Cuevas, Inhestern and Echavarría [1].
- “Development of Choked Flow in Variable Nozzle Radial Turbines”, in *International Journal of Engine Research* (2021) by Tiseira, García-Cuevas, Inhestern and Echavarría [2].
- “Choking dynamic of highly swirled flow in variable nozzle radial turbines”, in *Aerospace Science and Technology* (2022) by Tiseira, Dolz, Inhestern and Echavarría [3].
- “Numerical analysis of the effects of different rotor tip gaps in a radial turbine operating at high pressure ratios reaching choked flow”, in *Energies* (2022) by Galindo, Tiseira, Navarro, Inhestern and Echavarría [4].
- “Numerical analysis of the effects of grooved stator vanes in a radial turbine operating at high pressure ratios reaching choked flow”, in *Aerospace* (2023) by Galindo, Tiseira, Navarro, Inhestern and Echavarría [5].

Division of work between authors

The mentioned publications have been done in cooperation with other researchers from the CMT - Motores Térmicos. The author signatures of these publications are in order of seniority. The results discussions were done mainly in collaboration with his supervisor, Assist. Prof. Tiseira. The rest of co-authors also helped in the results discussions.

Funding acknowledgements

The respondent would like to acknowledge the financial support received through the "Subprograma de Formación de Profesorado Universitario (FPU)". Ministerio de Universidades. FPU18/02628 and by the "FPI Subprograma 2". Universitat Politècnica de València. PAID-10-18.

Acknowledgements

In the first place, I would like to express my sincere acknowledgement to Dr. Andrés Omar Tiseira and Dr. Lukas Benjamin Inhestern, Dr. Luis Miguel García-Cuevas for their guidance and support. I would also thank the CMT-Motores Térmicos and Universitat Politècnica de València for giving me the opportunity of completing this PhD thesis.

I would like to thank Antonio Gil and Pau Raga for their assistance in the CFD troubleshooting. Also, Adolfo Guzmán “Fito", Valentín Ucedo and Miguel Ángel Ortiz for their support during experimental measurements for different projects and Amparo Cutillas for her never-ending assistance with all the paperwork. I would also acknowledge Dr. José Galindo, Dr. Vicente Dolz, Dr. Roberto Navarro, and José Ramón Serrano for their advice and revision of my work during these years. Specially, I would like to thank my fellow PhD students Nico, Fabio, Pau, Alberto, Miguel Ángel, Alejandro, and Miguel for making my daily work more enjoyable and support me in the best and worst moments.

Finally, the people who deserve my gratitude more are my parents, sister, and family. Despite the distance, they have always given me the strength to finish this Ph.D. thesis.

“Denn Zeit ist Leben. Und das Leben wohnt im Herzen.”
Michael Ende, Momo

Contents

Contents xiii

List of Figures . . . xvi

List of Tables . . . xxi

Nomenclature xxiii

1 Introduction 1

1.1 Background . . . 2

1.2 Motivation . . . 4

1.3 Objectives . . . 5

1.4 Working plan . . . 6

1.5 Contents . . . 7

1.6 References . . . 8

2 Literature Review 11

2.1 Introduction . . . 12

2.2 CFD modeling . . . 13

2.3 Flow through the stator . . . 14

2.4 Rotor-Stator interaction . . . 15

2.5 Tip leakage . . . 17

2.6 Effects of the geometry variation . . . 18

2.7 Entropy and exergy analysis in radial turbine . . . 19

2.8 References . . . 22

3 CFD simulations setup 37

3.1 Introduction . . . 39

3.2 Geometry Description . . . 39

3.3 Numerical Setup . . . 42

3.4 Summary . . . 49

3.5 References . . . 50

4 Performance Characteristics 57

4.1 Introduction 59
4.2 Performance Characteristics 59
4.3 Summary 70
4.4 References 71

5 Stator Flow Characteristics 73
5.1 Introduction 74
5.2 Numerical Results 74
5.3 Summary 79
5.4 References 80

6 Flow characteristics through the vaneless space. 81
6.1 Introduction 83
6.2 Numerical Results 83
6.3 Unsteady Rotor-Stator Interaction 90
6.4 Summary 97
6.5 References 99

7 Rotor Flow Characteristics 101
7.1 Introduction 103
7.2 Numerical Results 103
7.3 Summary 112
7.4 References 113

8 Exergy Analysis 115
8.1 Introduction 116
8.2 Numerical Results 116
8.3 Summary 120
8.4 References 121

9 Effects of the variation of the rotor tip gap at high pressure ratios reaching choked flow. 123
9.1 Introduction 126
9.2 Geometry description 126
9.3 Performance characteristics 127
9.4 Characteristics of flow through the tip gap 131
9.5 Summary 152
9.6 References 155

10 Grooved Stator Vanes 159
10.1 Introduction 161
10.2 Geometry Description 161
10.3 Mesh analysis 162

10.4 Performance Characteristics 165
10.5 Analysis of the stator flow behavior 168
10.6 Summary 181
10.7 References 184

11 Conclusions and future works 187
11.1 Introduction 189
11.2 Stator flow features 189
11.3 Stator-Rotor interaction 189
11.4 Rotor flow features 190
11.5 Exergy analysis 191
11.6 Effects of the geometry change 192
11.7 Future works 194
11.8 References 203

References 205

List of Figures

1.1 Global expected turbocharger growth [6]. 3

3.1 Stator and rotor geometry. VT: Vane throat. VST: Vaneless space throat. 40
3.2 Computational domain. 41
3.3 Section view of the mesh. 43
3.4 Variation of mass flow and turbine power with different mesh configurations relative to the finest simulated mesh for opened and closed position. 45
3.5 Selected points to evaluate the Mach number. Point A (at R=24.41 mm) and Point B (at R=26.08 mm). 46

4.1 Considered planes for the performance characteristics analysis. . . . 59
4.2 Turbine map based on steady and unsteady results; experimental 3882 rpm/$\sqrt{\text{K}}$: black; experimental 5830 rpm/$\sqrt{\text{K}}$: dark gray; experimental up to 7456 rpm/$\sqrt{\text{K}}$: light gray; simulated: colored. 62
4.3 Reduced mass flow based on the mean total temperature and total pressure close to the rotor TE. 65
4.4 Relative Mach number with opened VGT position and operating point of choked passage flow at the rotor TE plane; red line: $Ma_{rel.} = 1$. . . . 66
4.5 Total pressure ratio and total temperature difference of the inlet properties and relative numbers at rotor TE plane. 68

5.1 Considered planes for the stator flow analysis. 74
5.2 Mach number of URANS simulations at a radial plane and at a plane parallel to the stator SS (see Figure 5.1(b)) with closed VGT position; red line: $Ma = 1$. 75
5.3 Mach number and stator vane pressure profile snapshots of URANS simulations at 50% span of the stator passage with closed VGT position; red line: $Ma = 1$. 76
5.4 Mach number and stator vane pressure profile snapshots for two operating points of URANS simulations with the same reduced mass flow, closed VGT position and at 50% span of the stator passage; left: lower speed; right: higher speed; red line: $Ma = 1$. 77

6.1 Turbine geometry with highlighted sections for following analysis. Dimensions in millimeters 83
6.2 Mach number and stator vane surface pressure profiles at 50% span of the stator passage and higher PR; red line: $Ma = 1$. 85

6.3 Mach number with 30% VGT position for higher PR and higher speed; red surface: $Ma = 1$. 86
6.4 Streamlines restricted to 50% span at higher PR, describing the flow path in the vaneless space with respect to the Mach number. 86
6.5 Mach number and total pressure along analyzed constrained streamlines for 10% VGT at 50% span and higher PR; upper: lower speed; lower: higher speed. 87
6.6 Mach number and total pressure along analyzed constrained streamlines for 30% VGT at 50% span and higher PR; upper: lower speed; lower: higher speed. 88
6.7 Total pressure evolution in the vaneless space for 10% VGT at higher PR. 89
6.8 Total pressure evolution in the vaneless space for 30% VGT at higher PR. 89
6.9 Relative Mach number for 10% VGT at higher PR; left: lower speed; right: higher speed; red line: $Ma_{rel.} = 1$. 90
6.10 Transient numerical schlieren for 10% VGT opening at 50% span of the stator passage with higher simulated PR; left side: lower speed; right side: higher speed. 92
6.11 Transient evolution of Mach number (left side) and total pressure (right side) for 10% VGT opening at different radial positions for higher PR and lower speed. 94
6.12 Transient evolution of Mach number (left side) and total pressure (right side) for 10% VGT opening at different radial positions for higher PR and higher speed. 95
6.13 Transient evolution of static pressure in the rotor for 10% VGT with higher PR at low speed (left side) and high speed (right side). 96

7.1 Iso-span planes and TE plane in the rotor 103
7.2 Relative Mach number snapshots of URANS simulations with closed VGT position higher PR close to the TE of the rotor; red line: $Ma_{rel.} = 1$. 104
7.3 Relative Mach number snapshots of URANS simulations with opened VGT position; red line: $Ma_{rel.} = 1$. 105
7.4 Numerical schlieren of URANS simulations at 50% rotor span with opened VGT position. 106
7.5 Relation between the reduced mass flow and the area ratio under supersonic conditions. 107
7.6 Relative Mach number and rotor pressure profile snapshots at 20% rotor span with opened VGT position for lower simulated PR at lower speed (left) and at higher speed (right); red line: $Ma_{rel.} = 1$. 108

7.7 Relative Mach number and rotor pressure profile snapshots at 50% rotor span with opened VGT position for lower simulated PR at lower speed (left) and at higher speed (right); red line: $Ma_{rel.} = 1$. 109
7.8 Relative Mach number and rotor pressure profile snapshots at 80% rotor span with opened VGT position for lower simulated PR at lower speed (left) and at higher speed (right); red line: $Ma_{rel.} = 1$. 110
7.9 Relative rotor inlet angle snapshots of URANS simulations with opened VGT position and lower simulated PR of two speeds at the rotor inlet plane. 111

8.1 Considerated planes as the inlet and outlet of the stator and rotor. . 117
8.2 Exergy analysis for the evaluated operational points; lower: 3882 rpm/$\sqrt{\text{K}}$; middle: 5830 rpm/$\sqrt{\text{K}}$; higher: 8421 rpm/$\sqrt{\text{K}}$. 118

9.1 Geometry of the different tip gaps for the following analysis. 127
9.2 Turbine map based on steady and usteady results; Steady: Dashed lines; Unsteady: Markers 129
9.3 Relation between the reduced mass flow and the area ratio under supersonic conditions. 130
9.4 Relative mass flow fraction passing through the tip gap along the SS. The first two vertical lines of points correspond to lower PR and the last two vertical lines of points correspond to higher PR. 131
9.5 Normal component of the relative velocity on the rotor tip PS and SS for the case of +0pTG at lower PR; Black lines enclose the regions with $Rel.Mach \geq 1$; URANS simulations; The value equal to 1.0 in the abscissa represents the position of the TE. 133
9.6 Normal component of the relative velocity on the rotor tip SS for the case +0pTG; Black lines enclose the regions with $Rel.Mach \geq 1$; URANS simulations; The value equal to 1.0 in the abscissa represents the position of the TE. 134
9.7 Mass flux on SS at lower PR and both rotational speeds; URANS simulations. 135
9.8 Mass flux on SS at higher PR for the case of +0pTG; URANS simulations. 136
9.9 Scraping ratio evaluated at different tip gaps; The value equal 1.0 in the abscissa represents the position of the TE. 136
9.10 Flow behaviors for the case of +0pTG along a meridional line at the middle of the SS tip gap of the -50pTG case (Figure 9.1); for the two analyzed PR and two rotational speeds; URANS simulations. 138
9.11 Relative Mach number, static pressure difference and relative total pressure difference evaluated along a meridional line at the middle of the tip gap of the -50pTG case (Figure 9.1); URANS simulations. . 139

9.12 Rotor pressure profile at 80% and 95% rotor span for lower simulated PR; URANS simulations. 140
9.13 Relative Mach number snapshots at 80% rotor span for lower simulated PR at lower speed (left) and at higher speed (right); red line: $Ma_{rel.} = 1$. 142
9.14 Relative velocity streamlines RANS simulations through the rotor Tip and rotor TE; gray streamlines: Main flow from rotor passage; streamlines in the inferno color scale: Flow from tip PS. 143
9.15 Relative velocity streamlines from the rotor TE going through two points: the first one closer to the shroud: blue streamline and the second one closer to the hub: orange streamline; RANS simulations . 145
9.16 Relative Mach number and static pressure evolution along streamlines close to the shroud and hub (Figure 9.15); The value equal to 1.0 in the abscissa represents the position of the TE; RANS simulation146
9.17 Tangential, radial and axial component of the relative velocity along streamlines close to the shroud and hub (Figure 9.15); The value equal to 1.0 in the abscissa represents the position of the TE; RANS simulation 148
9.18 Relative velocity streamlines going through two points: the first one closer to the inducer: blue streamline and the second one closer to the exducer: orange streamline; RANS simulations 149
9.19 Entropy generation rate normalized along streamlines close to the inducer and exducer (Figure 9.18); the value equals 1.0 in the abscissa represents the position of the TE; blue vertical dashed line: the position where the streamline enters the PS tip gap at the inducer; orange vertical dashed line: the position where the streamline enters the tip gap PS at the exducer; RANS simulation. 150
9.20 Entropy generation rate normalized along streamlines close to the hub (Figure 9.15); the value equals 1.0 in the abscissa represents the position of the TE; RANS simulation. 151

10.1 Stator geometry with different grooved surfaces. 161
10.2 View of mesh selected for the geometry with a grooved surface in the stator vanes. 162
10.3 Selected points to evaluate the Mach number. Point A (at the middle of the stator vaneless space) and Point B (at R6=26.08 mm, Figure 6.1).162
10.4 Mesh analysis Part A. The red dot corresponds to the mesh parameters used with the case without grooves. 163
10.5 Mesh analysis Part B. The red dot corresponds to the mesh parameters used with the case without grooves. 164

10.6 Turbine map based on steady results of the original stator geometry (0 grooves) and unsteady results with and without grooved surface; Steady: Dashed lines; Unsteady: Markers. 167
10.7 Mach number and stator vane pressure profile snapshots of URANS simulations at 50% span of the stator passage with closed VGT position at higher speed and higher PR; red line: $Ma = 1$. 170
10.8 Mach number and stator vane pressure profile snapshots of URANS simulations at 50% span of the stator passage with closed VGT position at lower speed and higher PR; red line: $Ma = 1$. 172
10.9 Transient numerical schlieren for closed VGT opening at 50% span of the stator passage with higher simulated PR and higher speed; left side: Original geometry; middle: Geometry with 5 grooves in the stator; right side: Geometry with 11 grooves in the stator. 175
10.10 Transient numerical schlieren for 10% VGT opening at 50% span of the stator passage with higher simulated PR and lower speed; left side: Original geometry; middle: Geometry with 5 grooves in the stator; right side: Geometry with 11 grooves in the stator. 176
10.11 Rotor blade loading at 50% span with closed VGT position. 177
10.12 Exergy analysis for the evaluated operational points; lower: 3882 rpm/$\sqrt{\mathrm{K}}$; higher: 8421 rpm/$\sqrt{\mathrm{K}}$. 180

11.1 Descriptions of the test bench. 194
11.2 Pressure taps for the measurement of the instant pressure. 196
11.3 Twin-entry turbine geometry [7]. 198
11.4 Twin-entry turbine computational domain [8]. 198
11.5 Relative Mach number snapshots of RANS simulations with opened VGT position; MFR=0.0; red line: $Ma_{rel.} = 1$. 199
11.6 Relative Mach number snapshots of RANS simulations with opened VGT position; MFR=0.53; red line: $Ma_{rel.} = 1$. 200
11.7 Relative Mach number snapshots of RANS simulations with opened VGT position; MFR=1.0; red line: $Ma_{rel.} = 1$. 201

List of Tables

3.1 Turbine geometry parameters. 40
3.2 Mesh independence study. 46
3.3 Differences in some parameters of the case at higher pressure ratio when using one degree and two degrees to define the time step. . . . 48
3.4 Summary of the evaluated operational points. 49

4.1 Evaluated pressure ratio URANS simulations. 60
4.2 Deviation experimental and RANS simulations. 63
4.3 Deviation RANS and URANS simulations. 63

9.1 Turbine geometry description. 126
9.2 Variation of the performance parameters with respect to the original geometry (+0pTG). 130

10.1 Mesh independence study. 165
10.2 Differences in some parameters of the case at higher pressure ratio when using one degree and two degrees to define the time step. . . . 165
10.3 Pressure ratio and performance of the turbine and stator for the evaluated cases with and without grooved surface; URANS simulations. 168

11.1 Main characteristics of the engine. 195
11.2 Main characteristics of the screw compressor. 195

Nomenclature

Abbreviations

BEV	Battery Electric Vehicle
BSR	Blade Speed Ratio
CFD	Computational Fluid Dynamics
ICE	Internal Combustion Engine
LE	Leading Edge
PR	Pressure Ratio
PS	Pressure Side
RANS	Reynolds Average Navier Stokes
SS	Suction Side
TE	Trailing Edge
URANS	Unsteady Reynolds Average Navier Stokes
VGT	Variable Geometry Turbine

Greek Symbols

α	Stator Blade Angle
β	Relative Rotor Inflow Angle
Δ	Difference
ϵ	Relative error between two grids
η	Isentropic Efficiency
γ	Ratio of Specific Heats
ω	Relative velocity
π	Corresponding Pressure Ratio
Ψ	Exergy
ρ	Density
θ	Tangential component

Notations

$\dot{m}$	Mass Flow
$\dot{m}_{red.}$	Reduced Mass Flow
$\dot{W}$	Power
$\vec{n}$	Unit Normal Vector
$\vec{u}$	Velocity Vector
A	Area
c_p	Specific Heat
D	Rotor Diameter
e	Specific Exergy

H	Height
h	Specific Enthalpy
Ma	Mach Number
N	Rotational Speed
p	Pressure or Order of Accuracy Method
R	Gas Constant
R	Radius or Scraping Ratio
r	Radial Coordinate or Refinement Factor Ratio
S	Surface Area
s	Specific Entropy
T	Temperature
t	Time
u	Velocity Magnitude
y^+	Non-dimensional Wall Distance
z	z-Coordiante (axial direction)

Subscripts and superscripts

$bl.$	Blade
f	Flow
in	Turbine Inlet Section
$isen$	Isentropic Value
o	The Dead State
$red.$	Reduced Numbers
$rel.$	Relative Value
$rot.$	Rotor
s	Static Conditions
$stat$	Stator Value
$surf.$	Stator Vane or Rotor Blade Surface
t	Total or Stagnation Conditions
t,s	Total-To-Static Value
t,t	Total-To-Total Value
$throat$	Throat of Choked Row
tip	Rotor blade tip
tot	Total or Stagnation Conditions
$turb.$	Overall Turbine Value

Symbols

$*$	Choked
$+$	Positive Direction
$-$	Negative Direction
$\bar{\ }$	Area Average
$\perp$	Perpendicular

CHAPTER 1

Introduction

Contents

1.1 Background 2
1.2 Motivation 4
1.3 Objectives 5
1.4 Working plan 6
1.5 Contents 7
1.6 References 8

1.1 Background

IN 1905 Swiss born engineer Dr. Alfred Büchi received the first patent on a turbocharger for a marine engine. Nevertheless, the first turbocharger were not used in marine or automotive engines, they were implemented in airplanes to increase the air density at elevated altitude. Despite of not being able to eliminate the power losses in altitude the performance was improved allowing reach higher altitudes. To give an example in 1918 a turbocharger is applied to a V12 liberty airplane. In the 1920s the turbochargers were implemented in transport systems as ships and trains due to their big dimensions. In 1938 the trucks were the first automotive to use turbochargers and the first passenger cars did not appear until the 60s but presenting failures in their performance. Then in the 70s, the oil crisis generated a new awareness of fuel reduction and the concept of downsizing using turbochargers without losing power became a great opportunity for cleaner engines. The Mercedes Benz 300DS, which debuted on the market in 1978, was the first successful application to a diesel passenger automobile. With its accomplishments of reduced emissions and improved efficiency, this became the first step in b reducing the engine impact in the environment. Other manufactures as BMW and Saab were the first to bring to the market cars equipped with gasoline engines and turbochargers.

The introduction of the variable geometry turbine (VGT) in turbochargers represented a great step forward for new systems. The first passenger car equipped with a VG turbo was the Honda Legend, which came on the market in 1988. Nevertheless, this type of technology start in 1936 with the work of Dr. Werner Theodor von der Nuell, head of the laboratory for aviation (DVL) in Berlin. Furthermore, after the end of World War II, a small group of former BMW employees began under the leadership of Dr. Müller in the Württembergische Metallwarenfabrik to build a VGT turbocharger. The first construction drawing dates from 01 September 1945.

In passenger cars at the time the VGT was still limited and it took some years before it would catch on. The VGT turbocharger had clear advantages in that it was able to act like both a small and large turbocharger due to the rotating vane system in the turbine inlet. Because of this, the VGT turbocharger could make a narrow throat area when taking off, thus reducing turbo lag and at the same time offering a high flow capacity at maximum power operation. MHI began developing VGT turbochargers in 1984 for truck applications and started mass production in 1994 [9]. In 1995, Garrett launched a VGT turbocharger matched to VW-Audi's 1.9 L direct-injection diesel engine [10]. BorgWarner presented its first VGT technology for diesel engines in 1997 and in 2006 introduced a VGT turbocharger for the Porsche 911 3.6 L engine [11]. While Mitsubishi's VGT turbochargers for passenger cars were launched in 2001, and this new technology quickly spread to the European market.

VGT turbochargers are an essential component for auto manufacturers as they work to improve the driveability, including increased transient response, improve torque, fuel efficiency, and emissions of vehicles. Turbocharger sales is expected to grow to 61 million units in 2030 as depicts Figure 1.1. The growth will mainly take place in Europe, North America and China due to increasingly stringent legislation in these regions [6].

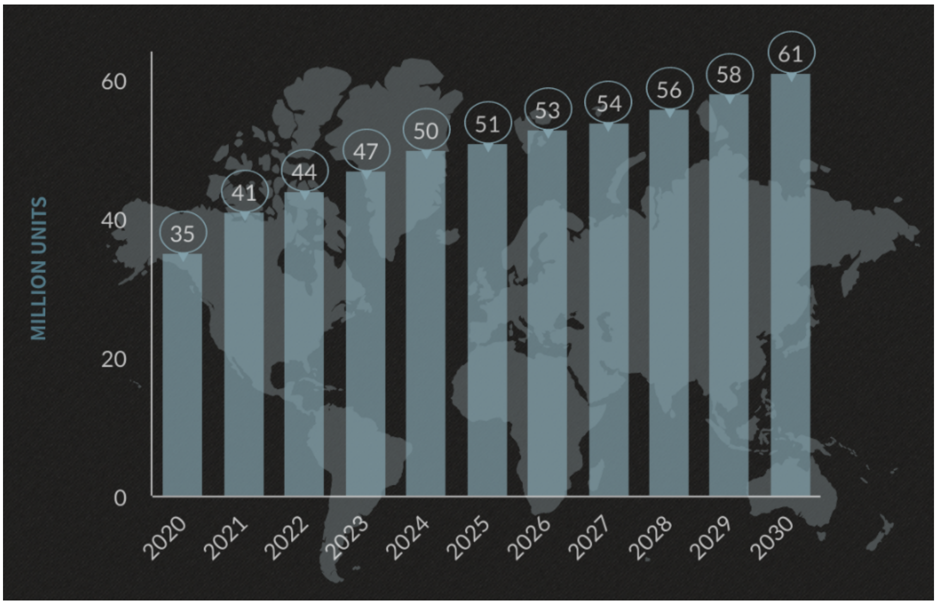

Figure 1.1: Global expected turbocharger growth [6].

New technologies such as battery electric vehicles (BEV) have become more popular as an alternative to internal combustion engines (ICE). Nevertheless, BEV have drawbacks such as low energy density compared with liquid fuels, limiting the driving distance. Another disadvantage is the battery, which life is limited and shorter than the life of the vehicle itself, and the human rights violations and high prices that face the supply of their raw materials. Furthermore, the electricity to recharge the batteries is produced in most cases from non-renewable energy sources. Thus, the use new turbocharger in ICE and hybrid configurations play and important role in the future of transport sector not only for the fuel consumption and pollutant emissions, but also about improving the engine response for safety and driving experience reasons.

Turbochargers can be evaluated experimentally or through simulations using computational fluid dynamics (CFD). Nonetheless, there is also an interest in creating trustworthy one-dimensional models to quickly anticipate the behavior of turbochargers. These models can then be used with complete engine simulation algorithms to forecast the engine's overall performance.

The research institute where the current thesis has been done, CMT-Motores Térmicos, has thoroughly investigated turbochargers and has developed increasingly accurate models. The first approach to this topic was carried out in the PhD thesis of F. Payri [12]. Turbocharger modelling in transient loads was further investigated by J.R. Serrano [13] and A. Rodríguez [14] in their PhD thesis. The one-dimensional modelling has been improved considering other physical phenomena in different PhD theses. M.A. Reyes included heat flows and improved the pulsating performance in the turbocharger modelling [15], M.A. López modelled the turbocharger rotor dynamics [16], and A. Dombrovsky synthesised the effect of the turbocharger modelling on the engine performance [17]. The modelling of the turbocharger compressor and turbine has also been improved separately, taking into account other effects. C. Cervelló modelled variable geometry turbines in her PhD thesis [18], P. Fajardo characterised radial turbines under pulsating flow [19], L.M. García-Cuevas modelled the mechanical losses and the turbine performance under unsteady pulsating flow [20], L.B. Inhestern modelled turbines at extreme off-design conditions [21], P. Soler worked on the turbine acoustics [22], V. Samala characterised the flow behaviour of twin-entry and dual-volute turbines [23], A. Gómez proposed a methodology to model spark ignition internal combustion engines using VGT turbochargers [24], and N. Medina carried out a flow capacity and efficiency modelling of twin-entry radial turbines under unequal admission conditions through CFD analysis and experiments [25].

1.2 Motivation

As crude oil and natural gas prices have risen dramatically in recent years, many European Union (EU) countries have been forced to adopt new strategies to meet energy demand. Furthermore, future limitations on greenhouse gases and other pollutants are expected to become more restrictive, even reaching the limit of "zero-emissions" in urban areas. Thus, automotive developers consider improving the ICE in fuel consumption and emissions and propose new hybrid vehicles.

The strategy of producing engines with smaller architectures requires higher boosting for the same performance. The boosting is achieved with a turbocharger driven by the energy recovery of the exhaust gases and contributes to reducing emissions. Current studies in turbocharging technologies deal with new models to determine the turbine behavior at off-design conditions or methodologies to obtain adiabatic turbine maps useful when matching with the engine. The different turbocharger technologies become potential solutions when improving fuel consumption and power demand nowadays. Double-entry, twin-entry, and variable geometry turbines are examples of turbocharger technologies applied to ICE.

The turbochargers are not only found in the automotive sector but also in the commercial aircraft industry, where they are used in the gas turbine auxiliary power unit (GTAPU) or in the environmental control system (ECS), as well as in the reverse Brayton cycle for refrigeration, reaching very low temperatures. In this system, the variable geometry turbine determines the optimum rack position for each operational condition and controls the refrigeration capacity. As the turbine inlet flow temperature is low, it is possible to reach sonic conditions, limiting the system's operation. In the case of an engine with a variable geometry turbine, as the stator vanes are in a closed position to drive high exhaust back pressure during the engine braking mode, shock waves are generated at the stator vanes exit.

Thus, developing sonic regions in radial turbines represents an essential field of study to improve the design of new systems to work in a wider operating range. In the current study, a variable geometry turbine (VGT) has been selected to analyze and understand the internal flow behavior when reaching choking conditions to precisely predict the performance at off-design conditions, which results helpful in developing 1D models. CFD simulations could help to study some internal phenomena that are difficult to assess with experimental measurements, such as shock waves and tip leakages.

1.3 Objectives

The aim of this thesis is to contribute to a better knowledge of the phenomenon that appears when a radial turbine of variable geometry operates at off-design conditions reaching choked flow. The understanding of the flow behavior allows improving on the one hand, the design of the turbine and, on the other hand, the one-dimensional models of radial turbines that take as input a narrow range of experimental data being able to evaluate the losses affecting the flow performance and extrapolate the turbine map at a low computational cost. The one-dimensional models are also implemented for matching with the engine.

CFD simulations will carry out to evaluate the turbine performance parameters when operating at different stator vanes positions, pressure ratios, and rotational speed that generates sonic conditions and the development of almost entirely choked flow. Furthermore, the thesis will be centered on the following aspects:

- Analyze the choking conditions at the stator, rotor, and stator-rotor interaction.

- Study the effects of changing the geometry of the stator and rotor. The stator suction surface will be modified to diminish the presence of shock waves. Regarding the rotor, the impact of the variation of the tip gap on the choking conditions will be evaluated. The influence on the performance parameters and the flow characteristics will be presented for both cases.
- Evaluate from a energetic point of view the exergy in the turbine when operates at different conditions including the development of choked flow.

1.4 Working plan

The methodology to achieve the objectives presented in the current Thesis is based on different aspects. First, previous studies carried out at CMT-Motores Térmicos, including experimental test and numerical simulations at low pressure ratios, have been used as starting point of the turbine performance to compare their trend with the operational conditions reaching choked flow modeled using CFD. An exhaustive literature review with the main topics that cover the current Thesis will be carried out. Thus, scientific articles about radial turbines at off-design conditions are selected, especially those where the turbine operates at high-pressure ratios and maximum mass flow, limiting the integrity of the turbine components. Based on these studies, it was chosen to extend the knowledge of the flow characteristics going through the stator, the flow behavior in the region between the stator exit and rotor inlet denoted as vaneless space, and the features along the rotor passage.

The theoretical work will be centered on using steady and unsteady Reynolds-averaged Navier-Stokes simulations (RANS and URANS, respectively). First, a mesh independence study is performed to ensure accurate results with the lowest computational cost possible. Furthermore, proper boundary conditions are selected. Then, the turbine map at high-pressure ratios, different rotational speeds, and stator vanes positions. The next step is to analyze the internal flow pattern at different spans and the pressure profiles of the stator vanes and rotor blades. Furthermore, exergy analysis is carried out to quantify the system performance under a specified reference environment. After understanding the flow behavior in the original geometry designed by the manufacturer, the effects of varying geometrical aspects will be analyzed to improve the performance of the turbine.

1.5 Contents

The current work has been structured as follows:

Chapter 2 presents a literature review on turbochargers evaluation using numerical and experimental test, focusing on variable geometry turbines under operational condition with the presence of sonic flow.

Chapter 3 presents the description of the geometry selected for the current Thesis and the CFD simulation setup. A mesh independence study has been carried out to obtain valid results under an proper computational cost. Furthermore, the boundary conditions are described.

Chapter 4 presents the performance parameters of the turbine obtained with CFD simulations and some experimental test data. Additionally, some parameters in the relative frame at the rotor trailing edge are also analyzed.

Chapter 5 presents the characteristics of the flow when the stator vanes are in a closed position, revealing the presence of supersonic region at the stator suction side depending of the operational point.

Chapter 6 presents the flow behavior in the vaneless space in order to analyze the effects of the rotor blade passing on this region and on the stator suction side, where the shock waves are developed.

Chapter 7 present the analysis of the flow when the stator vanes are at opened position to study the development of the choked flow in the rotor through the analysis of the blade pressure profile and the flow pattern at different spans and at the rotor trailing edge plane.

Chapter 8 presents the exergy in each region of the computational domain when the turbine flow presents sonic conditions. Furthermore, the shaft work concerning the maximum available energy at the turbine inlet under a specified reference environment is depicted.

Chapter 9 presents the effects of varying the gap between the rotor blade and the wall casing on the turbine performance and on the main flow going through the rotor when the turbine operates in points close to choked conditions. Furthermore, the flow profile along a meridional plane at the tip gap and different streamlines are analyzed.

Chapter 10 presents the impact of changing the flat surface of the stator suction side to a grooved surface on the flow passing through the stator, around the rotor leading edge, and on the performance parameters. Exergy analysis of the different geometries is also presented.

Chapter 11 summaries the main contributions of the current Thesis. Furthermore, the possible future works to extend and simplify the analysis of the choking conditions are also described.

1.6 References

[6] Mitsubishi Turbocharger and Engine Europe. *Turbo trends*. 2023. URL: https://www.turbocharger.mtee.eu/turbo-trends/ (cit. on p. 3).

[9] Mitsubishi Turbocharger and Engine Europe. *A history of turbocharging*. 2020. URL: https://www.turbocharger.mtee.eu/a-history-of-turbocharging/ (cit. on p. 2).

[10] Garrett Motion. *VNT Turbochargers*. 2023. URL: https://www.garrettmotion.com/es/turbocharger-technology/how-a-turbo-works/broadest-turbo-range/vnt-turbochargers/ (cit. on p. 2).

[11] BorgWarner. *BorgWarner Turbochargers with Variable Turbine Geometry (VTG)*. 2020. URL: https://www.borgwarner.com/newsroom/press-releases/2020/09/08/borgwarner-vtg-turbochargers-to-boost-large-number-of-global-oem-s-vehicles (cit. on p. 2).

[12] F. Payri. “Predicción de las actuaciones de los grupos de sobrealimentación para motores diesel de automoción”. PhD thesis. Universidad Politécnica de Madrid, 1973 (cit. on p. 4).

[13] J. R. Serrano Cruz. “Análisis y modelado de transitorios de carga en MEC turboalimentados”. PhD thesis. Universitat Politècnica de València, 1999 (cit. on p. 4).

[14] A. Rodríguez. “Analisis comparativo y sintesis de la respuesta transitoria en motores diesel de inyeccion directa turboalimentados”. PhD thesis. Universitat Politècnica de València, 2001 (cit. on p. 4).

[15] M. Á. Reyes-Belmonte. “Contribution to the experimental characterization and 1-D modelling of turbochargers for IC engines”. PhD thesis. Universitat Politècnica de València, 2013. DOI: 10.4995/Thesis/10251/34777 (cit. on p. 4).

[16] M. A. López Hidalgo. “Estudio teórico-experimental de la dinámica rotacional de un turbocompresor de MCIA. Aplicación al diagnóstico de fallos”. PhD thesis. Universitat Politècnica de València, 2014. DOI: 10.4995/Thesis/10251/37746 (cit. on p. 4).

[17] A. Dombrovsky. “Synthesis of the 1{D} modelling of turbochargers and its effects on engine performance prediction”. PhD thesis. Universitat Politècnica de València, 2017. DOI: 10.4995/Thesis/10251/82307 (cit. on p. 4).

[18] C. Cervelló. “Contribución a la caracterización experimental y al modelado de turbinas de geometría variable en grupos de sobrealimentación”. PhD thesis. Universitat Politècnica de València, 2005. DOI: 10.4995/Thesis/10251/1902 (cit. on p. 4).

[19] P. Fajardo Peña. “Methodology for the numerical characterization of a radial turbine under steady and pulsating flow”. PhD thesis. Universitat Politècnica de València, 2012. DOI: `10.4995/Thesis/10251/16878` (cit. on p. 4).

[20] L. M. García-Cuevas González. “Experiments and modelling of automotive turbochargers under unsteady conditions”. PhD thesis. Universitat Politècnica de València, 2014. DOI: `10.4995/Thesis/10251/48458` (cit. on p. 4).

[21] L. B. Inhestern. “Measurement, simulation, and 1D-modeling of turbocharger radial turbines at design and extreme off-design conditions”. PhD thesis. Universitat Politècnica de València, 2019. DOI: `10.4995/Thesis/10251/119989` (cit. on pp. 4, 47).

[22] P. Soler Blanco. “Simulation and modelling of the performance of radial turbochargers under unsteady flow”. PhD thesis. Universitat Politècnica de València, 2020. DOI: `10.4995/Thesis/10251/141609` (cit. on p. 4).

[23] V. Samala. “Experimental characterization and mean line modelling of twin-entry and dual-volute turbines working under different admission conditions with steady flow”. PhD thesis. Universitat Politècnica de València, 2020. DOI: `10.4995/Thesis/10251/153475` (cit. on p. 4).

[24] A. Gómez Vilanova. “Modelling and analysis methodology of SI IC engines turbocharged by VGT”. PhD thesis. Universitat Politècnica de València, 2021. DOI: `10.4995/Thesis/10251/181929` (cit. on p. 4).

[25] N. Medina Tomás. “Flow capacity and efficiency modelling of twin-entry radial turbines under unequal admission conditoins through CFD analysis and experiments”. PhD thesis. Universitat Politècnica de València, 2022. DOI: `10.4995/Thesis/10251/185820` (cit. on p. 4).

CHAPTER 2

Literature Review

Contents

2.1 Introduction 12
2.2 CFD modeling 13
2.3 Flow through the stator 14
2.4 Rotor-Stator interaction 15
2.5 Tip leakage 17
2.6 Effects of the geometry variation 18
2.7 Entropy and exergy analysis in radial turbine 19
2.8 References 22

2.1 Introduction

IN order to improve the air quality and protect it in a sustainable manner in the next years, the countries members of the European Union have set down regulations regarding to the emissions from various types of engines [26, 27]. For that reason, automotive manufacturers are working on different systems as downsized engines with turbochargers, to reduce the emissions of gaseous and particulate pollutants [28, 29]. To meet the engine power and torque targets, the downsized engine with the selected turbocharger represents an innovative concept capable of reducing a considerable percentage of the CO_2 emissions and improve the fuel economy [30, 31, 32, 33], as well as to be able of operate over a broader range of pressure ratios and large capacity over a wide operating range [34, 35].

There are different technologies to boost the engine [36], one of them, as was mentioned in Chapter 1 is the VGT turbocharger, which allows to improve the transient response as well as the torque deficiency at low-speed conditions [37, 38, 39]. Thus, the operation of this technology under certain conditions will be the object of the current thesis.

Besides of the use of turbochargers in the automotive sector, are commonly implemented for energy recovery in complex systems as in the commercial aircraft industry [40]. In a commercial airplane, the turbocharger can be found in new technologies that are an alternative to the traditional gas turbine auxiliary power units (GTAPUs) [41] or may be part of the environmental control system (ECS) [42] having different configurations, one of them is used to convert the energy of the cabin discharged air into mechanical energy and pre-supercharge the fresh air for reducing the electrical power required by the electrically driven ECS [43]. Transforming the traditional bleed engine style for the ECS to the electrically driven one, turbochargers can reduce the input power and increase the coefficient of performance (COP) [44]. Other applications include hydrogen hybrid engines [45, 46, 47], hybrid electrical turbines [48], fuel cells [49], biofuel propulsion [50, 51], and Organic Rankine Cycle [52, 53, 54]. Therefore, the improvement of the radial turbine in these systems still plays an important role in the current propulsion technologies.

Over the last few years, with the improvement of computational tools and experimental measuring techniques, different studies have been carried out to characterize the internal flow behavior of the radial turbine as the flow goes through its components such as the volute, stator, and rotor. However, since radial turbine geometry is quite compact and relatively small, especially in urban automotive engines, the installation of sensors in each of the aforementioned elements is quite limited [55] and in some cases it is necessary to scale the geometry [56, 57] to measure the pressure and velocity inside the stator [58]. Furthermore, the complex three-dimensional flow structure occurring in the stage turbine cannot be completely modeled by the one-dimensional approach available in the literature [59]. Thus, the use 3D computational fluid dynamics (CFD) stands as an important tool to analyze losses, improve turbine internal aerodynamic performance [60], and develop extrapolation models of the turbine map at high expansion ratio as the models presented by Serrano et al. [61], Romagnoli et al. [62] or Meroni et al. [63], due to the difficulty to obtain measurements under these off-design conditions. These kind of models can be connected directly to the one-dimensional whole engine models to achieve an optimum engine-turbocharger matching and engine performance [64, 65].

2.2 CFD modeling

The are different types of CFD simulations to analyze the internal flow in turbomachinery by solving or modeling the turbulence. In Direct Numerical Simulations (DNS) no turbulence model is used and the cell size of the meshed computational domain needs to be of the Kolmogorov length scale, where the turbulent vortexes dissipate. DNS has extremely high computational cost. Nevertheless, the computational cost can be reduced by modeling the turbulence on different levels. Large Eddy Simulations (LES) [66] are capable of solving the large turbulent scales, but they model the small turbulent scales. Furthermore, the entire turbulence spectrum can be modeled. This approach, called Reynolds Averaged Navier-Stokes simulations (RANS) inherently leads to a steady-state method. Turbulent variations from the averaged value are called Reynolds stresses. If the simulations are time-dependent, like time-varying boundary conditions, sliding or deforming mesh problem or transient heat transfer unsteady Reynolds Averaged Navier-Stokes simulations (URANS) are required instead of RANS. The turbulence closure is often achieved by two-equation models, which can widely be found in industry and investigation. The most important two-equation models can be named as $k-\epsilon$ model and the $k-\omega$ model. The $k-\epsilon$, model is known for having a good accuracy in free-stream and the $k-\omega$ model shows good results close to the wall regions. The Shear Stress Transport (SST) model proposed by Menter [67] combines the $k-\epsilon$ and the $k-\omega$ model between both regions. This model has become the most common model employed in radial turbomachinery [68]. The hybrid technique of Detached Eddy Simulations (DES) finds increasingly application to analyze the aerothermodynamics considering heat transfer under transient conditions or aeroacoustics [69]. In this approach URANS models are used in the boundary layer region and LES in the free stream zones. Different studies can be found in the literature using RANS and LES models. Bhide et al. [70, 71] characterized the flow field of rectangular supersonic jets. Results reveal a higher turbulence kinetic energy, and its production in the regions with the highest Reynolds stresses for the LES simulations, while the RANS are comparatively lower. Nevertheless, the radial velocity profiles at various streamwise locations using RANS and LES are in good agreement up to a few diameters downstream of the nozzle exit. Boatch et al. [72] analyzed a centrifugal compressor aeroacoustics using URANS and DES. URANS simulations present better agreement with experimental data than DES regarding compressor global variables. Furthermore, DES did not provide a better prediction of the pressure spectra than URANS. Nevertheless, DES is better for analyzing the detachment of the flow at the blades SS. In this thesis the RANS and URANS simulations are used to characterize the internal flow of a variable geometry turbine. The choose of these models besides of saving computational time is based on previous works of Serrano et al. [73] at high blade to jet speed ratios using the same geometry turbine and based on the good concordance between simulations and experimental data carry out by Galindo et al. [74] to the analyze the flow in a twin-entry turbine.

2.3 Flow through the stator

When an engine equiped with a VGT turbocharger operates at low speed, the moving stator vanes, reduce the area of the nozzle, increasing the velocity of the exhaust gas and the energy consumed by the turbine [75]. Nevertheless, this action results in a low volumetric efficiency [76] and high exhaust back pressure and can even lead to the development of shock waves in the stator.

In a turbine with the stator vanes closed and high inlet pressure, Zhao et al. [77] found that two shock waves appears, the first shock wave is generated near the throat of nozzle and it is followed by the second shock wave on the SS of the vane near the TE, existing a transonic region between them. Depending on the turbine geometry at closed vane position, the nozzle shock wave and nozzle clearance flow cause a high unsteady blade loading, according to Kawakubo et al. [34] the shock wave can penetrate deeply into the impeller LE and a strong positive pressure is exerted on the SS, then it diffracts on the PS. Furthermore, as stated by Sato et al. [78] at closed vane position, the effects of shock waves and nozzle clearance flows on excitation force are intensified with increasing pressure ratio and the Mach number.

At opened vane position, there is no presence of shock waves, but the blade loading is less, however the nozzle clearance contributes to the formation of a strong shock wave on the mid-chord of the impeller SS producing a highly disturbed flow field. Furthermore, the excitation force is independent of the pressure ratio, contrary to the case at closed vane position, but depends on the density at the rotor inlet and the choked flows occurred near the rotor TE.

A lot of studies including the aforementioned have been carried out with CFD, and validated with experimental test depending on the possibility of install the measuring instruments inside of the compact components of the turbocharger due to space limitations, being necessary in some cases scale the geometry [56, 57] to analyze the effects on the separation bubble and tip leakage flow, as well as the measurement of the pressure and velocity inside the stator using pitot tubes [58]. Furthermore, CFD is a useful and reliable tool to characterize the internal aerodynamic of the turbine at off-design operational points, where the mass flow can be extremely low and the turbine can work with negative efficiency [73].

Regarding to the nozzle leakage flow, Zhao et al. [79] identified that the increase in the endwall clearance lead to a significant rise in Mach number throughout the chord, due to the reduction of the boundary layer effects in this region. According to Qiu et al. [80] the nozzle clearance carries a portion of the flow that is not turned by the nozzle vanes and has a high radial velocity and a small swirl which influence the power output and the turbine efficiency; moreover, the choking limit of the nozzle is also increased because of the presence of the clearance.

2.4 Rotor-Stator interaction

As was mentioned before the operation principle of the VGT is based on the position change of the stator vanes to alter the nozzle geometry reducing or increasing the exhaust gas velocity upstream of the rotor [75]. When a VGT works with rather closed nozzle vanes, as is the case during sudden ICE accelerations, the turbine works with high-pressure ratios. Under these conditions, the turbine may choke, and shock waves generate important losses. The shock can be located between the stator vanes throat and TE area [81]. The interaction among shock, leakage flow, and nozzle wake affect the unsteady flow and blade loads. Therefore it is necessary to investigate this interaction to understand the underlying mechanism contributing to the change in the flow characteristics [82, 83] to design an optimal turbine that provides the maximal efficiency [84]. Liu et al. [85] found that the strong nozzle leakage flow weakens the shock strength at the nozzle trailing edge and affects the inlet flow angle distribution of the rotor blade, and increases the rotor blade aerodynamic losses. Chen [86] highlights that the exhaust gases of diesel engines at low speed can lead to a shock impinging on downstream rotor blades affecting the integrity of the turbine; moreover, the nozzle clearance leakage flow increases flow unsteadiness inside the passage of the turbine wheel and leads to a significant increase of turbine vibration stress [87, 88]. Similar results were obtained by the investigation of Shi et al. [89] about the effects of the nozzle vanes clearance leakages, wake and shock wave on the rotor blade pressure fluctuations, showing that the shock wave and nozzle vanes clearance leakages are the main reason for the fluctuations; moreover, the pressure response on the SS of the blade near LE is mainly influenced by the shock wave.

Rubechini et al. [90] highlighted that the strength of the unsteady interaction is related with the pattern of the shock wave at the region between the nozzle and the rotor, such pattern depend on the nozzle geometry. The shock impinging the rotor LE result in a strong pressure fluctuations and generating a high entropy rate within the rotor. The vibrations generated by the pressure fluctuations can be measured by the tip-timing method in which the deflection causes the blade to pass a series of laser probes earlier or later than a predicted time, hence the difference of this times can be used to calculate the deflection from the initial position for each individual blade [91, 92]. According to Sauret [93] even if the turbine was created for subsonic flow, when operates at high pressure ratios the choked flow can appear in the nozzle together with a small separation region near the rotor LE.

To improve the energy extraction from the exhaust gas is important to study the flow field in the vaneless space, the interaction of the nozzle leakage flow with the main flow, the flow losses, and conditions of the incoming flow to the rotor. This is the reason why several investigations have been focused on this region. Sato et al. [78] conducted unsteady CFD and experimental analyses to investigate the effects of rotor-stator interaction on the rotor excitation forces, concluding that at stator vanes closed position, the effect of shock waves on the excitation force is intensified when increasing the pressure ratio and Mach number. These results suggest that excitation force can be calculated using the dynamic pressure and Mach number at the rotor inlet in a one-dimensional model.

Yang et al. [94] perform numerical simulations to study the generation and weakening mechanism of the shock wave in VGTs. The shock waves at the vane TE vary in intensity and shape when the distance between the vanes and rotor blade changes; moreover, the shrinkage degree between the stator vane TE and the rotor blade can weaken the TE shock wave and thus, reduce the pressure fluctuations on the rotor blade leading to high cycle fatigue. According to Liu et al. [95] the pressure fluctuation level is three times the subsonic condition at transonic conditions.

The stator vanes thickness, solidity, and number are other important aspects related to the shock and rotor load. Yang et al. [81] found that thickness and number of stator vanes affect the intensity of the shock in the vaneless space. When increasing the vane number and the solidity, the intensity of the shock decreases around 75%, moreover at 50% span, the shock changes in shape and strength due to the impact of the relative position between rotor and stator. Regarding the load, the spikes appear at the rotor TE, and its magnitude and the fluctuation amplitude decrease when the blade number increases. Similar results were obtained by Hayami et al. [96]. Simpson et al. [97] found that increasing the values of both the solidity and the distance between vane TE and rotor LE lead to a reduction in the amplitudes of the measured and predicted static pressure variations at the rotor inlet, besides being more aerodynamically efficient to achieve a circumferential uniform flow state around the rotor periphery.

Paniagua et al. [98] analyzed the stator-rotor interaction in highly loaded high-pressure turbines finding that the vane shock impingement on the rotor generates a separation bubble on the rotor that is responsible for the generation of high losses. The increase of static pressure and heat flux fluctuations results from the more intensive vane TE direct shock and reflected shock impacting the rotor.

The unsteady, pulsating flow is responsible for a complex flow field in the radial turbine [99, 100, 101]. According to Qi et al. [102] the inlet pulsating flow influences the clearance leakage flow and the shock wave position, shifting the shock wave downstream to the nozzle TE. In addition to that, the inlet pulsating flow influences the separation caused by the incidence angle at the rotor inlet, thus decreasing the turbine efficiency. Furthermore, based on the results of Xue et al. [103] the secondary flow is the main source of flow loss in the nozzle under pulsating flow conditions, but this loss is lower under quasi-steady conditions.

There are relatively few studies about the swirled flow in the vaneless space of radial turbines. One of them is the experimental study carried out by Fontaneto et al. [104] using Particle Image Velocimetry (PIV) and micro cylindrical pressure probes to describe the strongly swirling flow field whose tangential velocity increases downstream. The swirl flow is mainly highlighted on the one hand at the inlet of the nozzle due to the strong nature of the flow discharging from the engines affecting the power output [105, 106, 107]. On the other hand, the minimum adverse flow-swirl at the turbine outlet is evaluated to obtain an optimum blade outlet angle during the development of loss models [108] or analyzed through experimental LDV (Laser Doppler Velocimeter) to validate CFD results [109].

2.5 Tip leakage

One of the main fluid-flow losses in a turbine corresponds to the leakage flow, i.e., secondary flows going through the narrow clearance between either the impeller or the stator vanes and the turbine housing. Using CFD, Tamaki et al. [55] found that the leakage flow in the stator increases as the nozzle opening decreases; besides, the existence of the nozzle clearance is a factor that decreases the turbocharger performance during the period of the engine acceleration. Regarding rotor leakage flow, the study of He et al. [110] disclosed that among tip clearance, backface clearance, and backface cavity (all three in the rotor), the tip clearance flow (also known as tip leakage) has the most significant impact on the aerodynamic parameters at the rotor outlet, and the maximum efficiency penalty is about 7.7%.

With the intention to propose one-dimensional loss models and design procedures in radial turbine, several numerical studies have been focused on the impact of blade loading on rotor tip leakage, as often a higher blade loading causes greater tip leakage, which in turn decreases turbine efficiency [111, 112]. However, Zhang et al. [113] show that, in a high pressure turbine, the local flow through the tip gap may choke, therefore limiting the effect of blade loading over tip leakage mass flow rate. In a similar study using CFD, Wheeler et al. [114] showed that, as the blade exit Mach number is increased, the tip leakage flow becomes choked and invariant to changes in the flow through the blade, thus reducing the tip losses.

Other studies have presented experimental and numerical investigations not only of the aerodynamic conditions but also of aerothermal performance [115] of an uncooled winglet tip, under transonic conditions, as by O'Dowds et al. [116]. The results reveal that the local heat transfer distribution on the rotor blade tip is affected by the relative casing motion and leads to a smaller supersonic region over the tip. However, a significant portion of the tip leakage flow remains transonic with identifiable choked regions and shock wave structures. It is worth mentioning that most studies related to turbine tip leakage corresponds to axial configurations rather than radial turbines as well as when comparing the leakages losses in axial and radial turbines [117, 118]. For the analysis of radial turbine leakage flow, we highlight the experimental work of Dambach et al. [119] and the CFD and loss model of Serrano et al. [120].

2.6 Effects of the geometry variation

The stator shock waves can be weakened by small changes in the stator geometry. Chen et al. [121] modeled the SS of the vane flatter with the aim to reduce the shock loss and shockwaves in the vaneless space of turbochargers turbines with VGT. In the work of Sonoda et al. [122] a locally high concave curvature and a small groove on the vane PS near the TE led to a double shock structure and reduce the TE loss and shock loss.

The unsteadiness of the flow through the rotor generated by the interaction between the blades and the second shock wave can be mitigated with the use of grooves on the SS of the vanes that generates an oblique shock and a reducing the pressure fluctuations, similar effect is caused by the in the air ramp intake of military aircrafts. Thus, Lei et al. [123] study numerically and experimentally the behavior of the sock wave on a linear turbine nozzle with and without a grooved surface on the SS, founding that with the grooved vane, the normal shock wave near the TE on the SS of the geometry without grooves change to an oblique shock wave followed by a normal shock wave of low intensity. The first shock wave decreases the flow speed upstream and the pressure distortion downstream of the vane. Furthermore, at high PR, the shock wave can be effectively mitigated.

For their part, Zhao et al. [124] showed that the presence of grooves raise the pressure and cause pre-compression of the main flow before the shock wave. Compared with smooth surfaces, the use of grooves on nozzle vane surface can increase local flow loss. Nevertheless, some flow loss is offset by the weakening of the shock wave. Continuing with this study Zhao et al. [125] carried out CFD and experimental tests to analyze the shock wave structure alterations using different grooves configurations in a turbine nozzle, where the groove depth, width, and number vary. The results show that the single strong shock became a multiple shock wave structure with a weaker intensity, diminishing shock wave loss and reducing the aerodynamic excitation . Varying the groove width and depth causes minor changes in the shock wave intensity and wake loss.

2.7 Entropy and exergy analysis in radial turbine

The entropy generation due to irreversible processes gives a quantitative accounting of loss production in the flow field. This information is useful for the turbomachinery designer to show where the calculated losses arise and assess the potential for improvement [126].

Ziaja et al. [127] performed an entropy generated analysis to estimate in each region of the computational domain the contribution of the losses related with boundary layer, tip clearance gap, wake flow, and secondary flow losses in the core flow. The major loss is generated in the rotor, occurring in the clearance gap and boundary layer region. In the stator region, the entropy generation rate is mainly due to friction losses at the stator sidewalls, while in the diffuser, losses within core flow and due to friction dominate. From this findings, the tip clearance gap and diffuser core flow losses exhibit potential for improvement.

Zhang et al. [128] also quantify the entropy generation as the indicator to analyze the loss mechanisms in a radial turbine for the heavy-duty diesel engine but applied to a ORC using air and R245fa under similar conditoins , and modeled using CFD. The losses responsible of decreasing the turbine efficiency are: flow separation on the stator vane SS near the LE, shock wave in the throat formed by the vanes, vortex loss after the vane TE, local incidence loss near the rotor hub, boundary layer separation vortex loss on the rotor blase SS, and tip leakages in the rotor. When using R245fa as a working fluid, the vane shock wave losses decrease, but rotor SS separation vortex losses increase and lead to isentropic efficiency lower than the efficiency with air as a working fluid when the turbine operates at a velocity ratio from 0.5 to 0.9.

For a moving fluid, the theoretical maximum shaft work that can be extracted is the value the exergy. Thus, exergy is important to evaluate the turbine performance and to quantify the thermo-fluid related losses. With the aim to study the effects of upstream exhaust manifold on the turbine performance, including the effects on heat transfer related losses Lim et al. [129] used the exergy based method to quantify the losses predicted by two methods, one considering the exhaust manifold and other without the exhaust manifold. It was found that the presence of exhaust manifold is most important in the estimation of heat transfer and internal irreversibilities in the scroll. The downstream turbine parts, like the rotor and the diffuser, are little affected by the exhaust manifold. Nevertheless, integration of the exhaust manifold into the computational model is necessary to the study of the flow's entire exergy budget in order to have a better understanding of losses. The distortion of the flow field in the scroll caused by the exhaust manifold has no impact on predicted turbine power or total internal irreversibilities in the rotor. Since total internal irreversibilities depend on the flow field gradients, the result indicates that mixing due to the rotation is high enough such that the flow disturbances due to the incoming pulse is smeared out in the rotor. The mixing process govern strongly the heat transfer process and the internal irreversibilities mechanisms downstream of the rotor.

In other study Lim et al. [130] use Detached Eddy Simulation (DES) to carry out an exergy analysis in order to identify and to quantify the related aerothermodynamic losses, as well as to investigate the effectiveness of exhaust energy utilization in the turbine system. Different cases with constant wall temperature were imposed besides of an adiabatic case. The analysis showed that the most sensitive mechanisms related with heat loss is the exergy lost by heat transfer and thermal irreversibilities, and turbine power drop due to heat loss is relatively insignificant as compared to the exergy lost. Moreover, exergy analysis using ambient as the dead state revealed that even under idealized isentropic gas expansion, a single-stage turbine is not effective to extract all the available exhaust energy in the system.

In an extension of the aforementioned study but using RANS simulations under adiabatic and diabatic conditions and validated with experimental data Lim et al. [131] conclude that despite that the simulations provide valid results in the prediction of turbine aerothermodynamics a more sophisticated methodology like Conjugate Heat Transfer (CHT) is necessary to accurately predict the predict the heat loss and the temperature field in a diabatic turbocharger turbine at low speed lines. Nevertheless, at high speed lines the CFD RANS simulations predict good results without CHT. Thus, at high speed, the exergy analysis ratify that the heat transfer increases flow exergy lost through heat loss and internal irreversibilities. The exergy budget in the scroll presents the higher heat loss (at diabatic conditions) while in rotor the 5% exergy budget represents the internal irreversibilities and 40% the turbine power. The low effectiveness of the turbine in extracting the available energy as useful mechanical work indicates the possibility of install a heat recovery system downstream of the rotor to take advantage of the wasted energy.

2.8 References

[26] European Union. *UN Regulation No 49 – Uniform provisions concerning the measures to be taken against the emission of gaseous and particulate pollutants from compression-ignition engines and positive ignition engines for use in vehicles*. Brussels, 2023. URL: https://eur-lex.europa.eu/legal-content/EN/TXT/?uri=CELEX%7B%5C%%7D3A42023X0064%7B%5C&%7Dqid=1678886878531 (cit. on p. 12).

[27] European Commission. *Commission proposes new Euro 7 standards to reduce pollutant emissions from vehicles and improve air quality*. Brussels, 2022. URL: https://ec.europa.eu/commission/presscorner/detail/en/ip%7B%5C_%7D22%7B%5C_%7D6495 (cit. on p. 12).

[28] L. Cheng, P. Dimitriou, W. Wang, J. Peng, and A. Aitouche. "A novel fuzzy logic variable geometry turbocharger and exhaust gas recirculation control scheme for optimizing the performance and emissions of a diesel engine". In: *International Journal of Engine Research* 21.8 (2020), pp. 1298–1313. DOI: 10.1177/1468087418809261. URL: https://doi.org/10.1177/1468087418809261 (cit. on p. 12).

[29] K. Song, D. Upadhyay, and H. Xie. "An assessment of the impacts of low-pressure exhaust gas recirculation on the air path of a diesel engine equipped with electrically assisted turbochargers". In: *International Journal of Engine Research* 22.1 (2021), pp. 3–21. DOI: 10.1177/1468087419854294. URL: https://doi.org/10.1177/1468087419854294 (cit. on p. 12).

[30] C. Carey et al. "Extreme engine downsizing". In: *Innovations in Fuel Economy and Sustainable Road Transport*. Woodhead Publishing, 2011, pp. 135–147. ISBN: 9780857092137. DOI: 10.1533/9780857095879. URL: http://www.sciencedirect.com/science/article/pii/B9780857092137500127 (cit. on p. 12).

[31] J. W. Turner, A. Popplewell, S. Richardson, A. G. Lewis, S. Akehurst, C. J. Brace, and S. W. Bredda. "Ultra boost for economy: Realizing a 60% downsized engine concept". In: *Internal Combustion Engines: Performance, Fuel Economy and Emissions*. London, UK: Woodhead Publishing, 2013, pp. 3–17. ISBN: 9781782421849. DOI: 10.1533/9781782421849.1.3. URL: http://www.sciencedirect.com/science/article/pii/B9781782421832500019 (cit. on p. 12).

[32] A. J. Feneley, A. Pesiridis, and A. M. Andwari. "Variable Geometry Turbocharger Technologies for Exhaust Energy Recovery and Boosting-A Review". In: *Renewable and Sustainable Energy Reviews* 71 (2017), pp. 959–975. ISSN: 1364-0321. DOI: 10.1016/j.rser.2016.12.125.

URL: http://www.sciencedirect.com/science/article/pii/S1364032116311807 (cit. on p. 12).

[33] D. Dong, Y. Moriyoshi, and J. Zhu. “To improve the performance of a variable geometry turbocharged SI engine by porous material application”. In: *Applied Thermal Engineering* 197 (Oct. 2021), p. 117373. ISSN: 1359-4311. DOI: 10.1016/J.APPLTHERMALENG.2021.117373 (cit. on p. 12).

[34] T. Kawakubo. “Unsteady Rotor-Stator Interaction of a Radial-Inflow Turbine With Variable Nozzle Vanes”. In: *Proceedings of ASME Turbo Expo 2010: Power for Land, Sea and Air*. Glasgow, UK, 2010, pp. 2075–2084. DOI: 10.1115/GT2010-23677. URL: https://doi.org/10.1115/GT2010-23677 (cit. on pp. 12, 14, 103).

[35] J. G. Hawley, F. J. Wallace, A. R. J. Cox, R. W. Horrocks, and G. L. Bird. “Reduction of Steady State NOx Levels from an Automotive Diesel Engine Using Optimised VGT/EGR Schedules”. In: *SAE Technical Paper* 108 (1999), pp. 1172–1184. DOI: 10.4271/1999-01-0835. URL: https://doi.org/10.4271/1999-01-0835 (cit. on pp. 12, 41, 83).

[36] A. Romagnoli et al. “Assessment of supercharging boosting component for heavily downsized gasoline engines”. In: *11th International Conference on Turbochargers and Turbocharging*. Oxford: Woodhead Publishing, 2014, pp. 13–26. ISBN: 9780081000335. DOI: 10.1533/978081000342.13. URL: http://www.sciencedirect.com/science/article/pii/B9780081000335500020 (cit. on p. 12).

[37] B. Hu, C. Brace, S. Akehurst, C. Copeland, and J. W. Turner. “The effect of divided exhaust period for improved performance in a highly downsized turbocharged gasoline engine”. In: *11th International Conference on Turbochargers and Turbocharging*. Ed. by I. o. M. Engineers. Oxford: Woodhead Publishing, 2014, pp. 27–39. ISBN: 9780081000335. DOI: 10.1533/978081000342.27. URL: http://www.sciencedirect.com/science/article/pii/B9780081000335500032 (cit. on p. 12).

[38] V. de Bellis, F. Bozza, S. Marelli, and M. Capobianco. “Experimental Investigation and 1D Simulation of a Turbocharger Compressor Close to Surge Operation”. In: *SAE International Journal of Engines* 8.4 (2015). ISSN: 19463944. DOI: 10.4271/2015-01-1720. URL: https://doi.org/10.4271/2015-01-1720 (cit. on p. 12).

[39] D. Mirza-Hekmati, W. P. Heath, J. M. Apsley, and J. R. Forbes. “Downspeeding diesel engines with two-stage turbochargers: Analysis and control considerations”. In: *International Journal of Engine Research* (2020), pp. 1–12. DOI: 10.1177/1468087420976482. URL: https://doi.org/10.1177/1468087420976482 (cit. on p. 12).

[40] W. Bruensicke and R. Cholvin. "The turbocharger function in the light aircraft field". In: *General Aviation Aircraft Design and Operations Meeting*. Wichata, Kansas, 1964, pp. 1–9. DOI: https://doi.org/10.2514/6.1964-191. URL: https://arc.aiaa.org/doi/abs/10.2514/6.1964-191 (cit. on p. 12).

[41] F. J. Jiménez-Espadafor Aguilar and J. A. Vélez Godiño. "Innovative power train configurations for aircraft auxiliary power units focused on reducing carbon footprint". In: *Aerospace Science and Technology* 106.1270-9638 (2020), p. 106109. ISSN: 12709638. DOI: 10.1016/j.ast.2020.106109. URL: http://www.sciencedirect.com/science/article/pii/S1270963820307914 (cit. on p. 12).

[42] I. Jennions, F. Ali, M. E. Miguez, and I. C. Escobar. "Simulation of an aircraft environmental control system". In: *Applied Thermal Engineering* 172 (2020), p. 114925. ISSN: 1359-4311. DOI: 10.1016/j.applthermaleng.2020.114925. URL: https://doi.org/10.1016/j.applthermaleng.2020.114925 (cit. on p. 12).

[43] H. Yang, X. Zhang, C. Wang, and C. Yang. "Design Analysis of Power Recovery Systems for Cabin Exhaust Air". In: *Procedia Engineering* 121.1877-7058 (2015), pp. 248–255. DOI: 10.1016/j.proeng.2015.08.1065. URL: http://www.sciencedirect.com/science/article/pii/S1877705815027939 (cit. on p. 12).

[44] H. Yang, X. Zhang, C. Wang, and C. Yang. "Experimental and theoretical study on a novel energy-saving ECS for commercial airliners". In: *Applied Thermal Engineering* 127 (2017), pp. 1372–1381. ISSN: 1359-4311. DOI: https://doi.org/10.1016/j.applthermaleng.2017.08.043. URL: http://www.sciencedirect.com/science/article/pii/S1359431117324596 (cit. on pp. 12, 47).

[45] J. Ribau, C. Silva, F. P. Brito, and J. Martins. "Analysis of four-stroke, Wankel, and microturbine based range extenders for electric vehicles". In: *Energy Conversion and Management* 58 (2012), pp. 120–133. ISSN: 0196-8904. DOI: https://doi.org/10.1016/j.enconman.2012.01.011. URL: https://www.sciencedirect.com/science/article/pii/S0196890412000271 (cit. on p. 12).

[46] A. García, J. Monsalve-Serrano, S. Martínez-Boggio, and K. Wittek. "Potential of hybrid powertrains in a variable compression ratio downsized turbocharged VVA Spark Ignition engine". In: *Energy* 195 (2020), p. 117039. ISSN: 0360-5442. DOI: https://doi.org/10.1016/j.energy.2020.117039. URL: https://www.sciencedirect.com/science/article/pii/S0360544220301468 (cit. on p. 12).

[47] L. Estrada, E. Moreno, A. Gonzalez-Quiroga, A. Bula, and J. Duarte-Forero. “Experimental assessment of performance and emissions for hydrogen-diesel dual fuel operation in a low displacement compression ignition engine”. In: *Heliyon* 8.4 (2022), e09285. ISSN: 2405-8440. DOI: `https://doi.org/10.1016/j.heliyon.2022.e09285`. URL: `https://www.sciencedirect.com/science/article/pii/S2405844022005734` (cit. on p. 12).

[48] S. Chiesa, M. Fioriti, and R. Fusaro. “Possible hybrid propulsion configuration for transport jet aircraft”. In: *Aviation* 20 (2016), pp. 145–154. DOI: `10.3846/16487788.2016.1200849`. URL: `https://doi.org/10.3846/16487788.2016.1200849` (cit. on p. 12).

[49] T. Wittmann, S. Lück, C. Bode, and J. Friedrichs. “Modelling the Condensation Phenomena within the Radial Turbine of a Fuel Cell Turbocharger”. In: *International Journal of Turbomachinery, Propulsion and Power* 6.3 (2021). ISSN: 2504-186X. DOI: `10.3390/ijtpp6030023`. URL: `https://www.mdpi.com/2504-186X/6/3/23` (cit. on p. 12).

[50] Y. S. M. Altarazi, A. R. Abu Talib, J. Yu, E. Gires, M. F. Abdul Ghafir, J. Lucas, and T. Yusaf. “Effects of biofuel on engines performance and emission characteristics: A review”. In: *Energy* 238 (2022), p. 121910. ISSN: 0360-5442. DOI: `https://doi.org/10.1016/j.energy.2021.121910`. URL: `https://www.sciencedirect.com/science/article/pii/S0360544221021587` (cit. on p. 12).

[51] T. Jeyaseelan, N. Chacko, P. N, S. M. K. O, J. Alexander, and E. Porpatham. “Partial hydrogenation and hydrogen induction: A comparative study with B20 operation in a turbocharged CRDI diesel engine”. In: *International Journal of Hydrogen Energy* 46.43 (2021), pp. 22659–22669. ISSN: 0360-3199. DOI: `https://doi.org/10.1016/j.ijhydene.2021.04.068`. URL: `https://www.sciencedirect.com/science/article/pii/S0360319921013987` (cit. on p. 12).

[52] F. Alshammari. “Radial Turbine Expander Design, Modelling and Testing for Automotive Organic Rankine Cycle Waste Heat Recovery”. Thesis. Brunel University London, 2018, pp. 1–275. URL: `http://bura.brunel.ac.uk/handle/2438/16007` (cit. on p. 12).

[53] D. I. Permana, D. Rusirawan, and I. Farkas. “A bibliometric analysis of the application of solar energy to the organic Rankine cycle”. In: *Heliyon* 8.4 (2022), e09220. ISSN: 2405-8440. DOI: `https://doi.org/10.1016/j.heliyon.2022.e09220`. URL: `https://www.sciencedirect.com/science/article/pii/S2405844022005084` (cit. on p. 12).

[54] G. Polanco Piñerez, G. Valencia Ochoa, and J. Duarte-Forero. “Energy, exergy, and environmental assessment of a small-scale solar organic Rankine cycle using different organic fluids”. In: *Heliyon* 7.9 (2021), e07947. ISSN: 2405-8440. DOI: `https://doi.org/10.1016/j.heliyon.2021.e07947`. URL: `https://www.sciencedirect.com/science/article/pii/S2405844021020508` (cit. on p. 12).

[55] *The Effect of Clearance Flow of Variable Area Nozzles on Radial Turbine Performance*. Vol. 6. Turbo Expo: Power for Land, Sea, and Air. Berlin, Germany: ASME, 2008, pp. 1519–1529. DOI: `10.1115/GT2008-50461`. URL: `https://doi.org/10.1115/GT2008-50461` (cit. on pp. 12, 17, 39).

[56] A. O. T. Izaguirre, R. N. García, L. B. Inhestern, and N. H. Gómez. “Design and numerical analysis of flow characteristics in a scaled volute and vaned nozzle of radial turbocharger turbines”. In: *Energies* 13.11 (2020), p. 19. ISSN: 19961073. DOI: `10.3390/en13112930`. URL: `https://doi.org/10.3390/en13112930` (cit. on pp. 12, 15).

[57] G. Dufour, X. Carbonneau, J.-b. Cazalbou, and P. Chassaing. “Practical Use of Similarity and Scaling Laws for Centrifugal Compressor Design”. In: *Turbo Expo: Power for Land, Sea, and Air*. Vol. 6. Barcelona, Spain: ASME, 2006, pp. 1131–1140. DOI: `10.1115/GT2006-91227`. URL: `https://doi.org/10.1115/GT2006-91227` (cit. on pp. 12, 15).

[58] J. Galindo, A. O. Tiseira Izaguirre, L. M. García-Cuevas, and N. Hervás Gómez. “Experimental approach for the analysis of the flow behaviour in the stator of a real centripetal turbine”. In: *International Journal of Engine Research* 22.6 (2020), pp. 1–11. ISSN: 20413149. DOI: `10.1177/1468087420916281`. URL: `https://doi.org/10.1177/1468087420916281` (cit. on pp. 12, 15, 196).

[59] N. Binder, S. Le Guyader, and X. Carbonneau. “Analysis of the Variable Geometry Effect in Radial Turbines”. In: *Journal of Turbomachinery* 134.4 (July 2011). ISSN: 0889-504X. DOI: `10.1115/1.4003713`. URL: `https://doi.org/10.1115/1.4003713` (cit. on p. 13).

[60] A. Marsan and S. Moreau. “Analysis of the flow structure in a radial turbine”. In: *11th European Conference on Turbomachinery Fluid Dynamics and Thermodynamics, ETC 2015*. Madrid: EUROTURBO, 2015, pp. 1–13. DOI: `ETC2015-207`. URL: `euroturbo.eu/publications/proceedings-papers/etc2015-207/` (cit. on pp. 13, 39).

[61] J. R. Serrano, F. J. Arnau, L. M. García-Cuevas, and A. Dombrovsky. “Development and validation of a radial turbine efficiency and mass flow model at design and off-design conditions”. In: *Energy Conversion and Management* 128 (2016), pp. 281–293. DOI: `10.1016/j.enconman.2016`

.09.032. URL: https://doi.org/10.1016/j.enconman.2016.09.032 (cit. on pp. 13, 61).

[62] A. Romagnoli and R. Martinez-Botas. "Performance prediction of a nozzled and nozzleless mixed-flow turbine in steady conditions". In: *International Journal of Mechanical Sciences* 53.8 (2011), pp. 557–574. ISSN: 00207403. DOI: 10.1016/j.ijmecsci.2011.05.003. URL: http://www.sciencedirect.com/science/article/pii/S0020740311000920 (cit. on p. 13).

[63] A. Meroni, M. Robertson, R. Martinez-Botas, and F. Haglind. "A methodology for the preliminary design and performance prediction of high-pressure ratio radial-inflow turbines". In: *Energy* 164 (2018), pp. 1062–1078. ISSN: 03605442. DOI: 10.1016/j.energy.2018.09.045. URL: https://doi.org/10.1016/j.energy.2018.09.045 (cit. on pp. 13, 202).

[64] M. Tancrez, J. Galindo, C. Guardiola, P. Fajardo, and O. Varnier. "Turbine adapted maps for turbocharger engine matching". In: *Experimental Thermal and Fluid Science* 35.1 (2011), pp. 146–153. ISSN: 08941777. DOI: 10.1016/j.expthermflusci.2010.07.018. URL: http://dx.doi.org/10.1016/j.expthermflusci.2010.07.018 (cit. on pp. 13, 62).

[65] G. Zamboni, S. Moggia, and M. Capobianco. "Effects of a dual-loop exhaust gas recirculation system and variable nozzle turbine control on the operating parameters of an automotive diesel engine". In: *Energies* 10.1 (2017), p. 47. ISSN: 19961073. DOI: 10.3390/en10010047. URL: https://doi.org/10.3390/en10010047 (cit. on p. 13).

[66] V. R. Petha Sethuraman and H. D. Kim. "Characteristics of Shock Train Flow in Divergent Channels". In: *Recent Asian Research on Thermal and Fluid Sciences*. Ed. by A. Suryan, D. H. Doh, M. Yaga, and G. Zhang. Singapore: Springer Singapore, 2020, pp. 353–364. ISBN: 978-981-15-1892-8. DOI: DOIhttps://doi.org/10.1007/978-981-15-1892-8_28. URL: https://link.springer.com/chapter/10.1007%7B%5C%%7D2F978-981-15-1892-8%7B%5C_%7D28 (cit. on p. 13).

[67] Siemens. *STAR-CCM + 2019.1 Release version 14.02.010-R8*. 2019. URL: https://www.plm.automation.siemens.com/global/es/products/simcenter/STAR-CCM.html (cit. on pp. 13, 42).

[68] F. R. Menter, R. Langtry, and T. Hansen. "CFD simulation of turbomachinery flows - Verfication, validation and modelling". In: *ECCOMAS 2004 - European Congress on Computational Methods in Applied Sciences and Engineering*. July. Jyvaskyla, 2004, pp. 1–14. URL: http://www.mit.jyu.fi/eccomas2004/proceedings/pdf/954.pdf (cit. on pp. 13, 42).

[69] J. Galindo, A. Tiseira, R. Navarro, and M. A. López. "Influence of tip clearance on flow behavior and noise generation of centrifugal compressors in near-surge conditions". In: *International Journal of Heat and Fluid Flow* 52 (2015), pp. 129–139. ISSN: 0142-727X. DOI: `https://doi.org/10.1016/j.ijheatfluidflow.2014.12.004`. URL: `https://www.sciencedirect.com/science/article/pii/S0142727X14001751` (cit. on pp. 13, 127).

[70] K. Bhide, K. Siddappaji, S. Abdallah, and K. Roberts. "Improved Supersonic Turbulent Flow Characteristics Using Non-Linear Eddy Viscosity Relation in RANS and HPC-Enabled LES". In: *Aerospace* 8.11 (2021). ISSN: 2226-4310. DOI: `10.3390/aerospace8110352`. URL: `https://www.mdpi.com/2226-4310/8/11/352` (cit. on p. 13).

[71] K. Bhide and S. Abdallah. "Turbulence statistics of supersonic rectangular jets using Reynolds Stress Model in RANS and WALE LES". In: *AIAA AVIATION 2022 Forum*. Chicago, 2022. DOI: `10.2514/6.2022-3344`. URL: `https://arc.aiaa.org/doi/abs/10.2514/6.2022-3344` (cit. on p. 13).

[72] A. Broatch, J. Galindo, R. Navarro, and J. García-Tíscar. "Numerical and experimental analysis of automotive turbocharger compressor aeroacoustics at different operating conditions". In: *International Journal of Heat and Fluid Flow* 61 (2016), pp. 245–255. ISSN: 0142-727X. DOI: `https://doi.org/10.1016/j.ijheatfluidflow.2016.04.003`. URL: `https://www.sciencedirect.com/science/article/pii/S0142727X16301163` (cit. on p. 14).

[73] J. R. Serrano, A. Gil, R. Navarro, and L. B. Inhestern. "Extremely low mass flow at high blade to jet speed ratio in variable geometry radial turbines and its influence on the flow pattern a CFD analysis". In: *ASME Turbo Expo 2017: Turbomachinery Technical Conference and Exposition*. Charlotte, NC, USA: ASME, 2017, pp. 1–13. DOI: `10.1115/GT2017-63368`. URL: `https://asmedigitalcollection.asme.org/GT/proceedings-abstract/GT2017/50954/V008T26A005/243279` (cit. on pp. 14, 15, 39, 41, 44, 47, 48).

[74] J. Galindo, J. R. Serrano, L. M. García-Cuevas, and N. Medina. "Using a CFD analysis of the flow capacity in a twin-entry turbine to develop a simplified physics-based model". In: *Aerospace Science and Technology* 112 (2021), p. 106623. ISSN: 1270-9638. DOI: `https://doi.org/10.1016/j.ast.2021.106623`. URL: `https://www.sciencedirect.com/science/article/pii/S1270963821001334` (cit. on pp. 14, 48, 202).

[75] T. Huayin. "Application of Variable Geometry Turbine on Gasoline Engines and the Optimisation of Transient Behaviours". PhD thesis. University of Bath, 2016, p. 232. URL: https://purehost.bath.ac.uk/ws/portalfiles/portal/187959568/Huayin%7B%5C_%7DThesis.pdf (cit. on pp. 14, 15).

[76] H. Tang, S. Akehurst, C. J. Brace, S. Garrett, and L. Smith. "Optimisation of transient response of a gasoline engine with variable geometry turbine turbocharger". In: *11th International Conference on Turbochargers and Turbocharging*. Ed. by I. o. M. Engineers. Oxford: Woodhead Publishing, 2014, pp. 163–175. ISBN: 9780081000335. DOI: 10.1533/978081000342.163. URL: http://www.sciencedirect.com/science/article/pii/B9780081000335500147 (cit. on p. 14).

[77] B. Zhao, H. Sun, X. Shi, M. Qi, and S. Guo. "Investigation of using multi-shockwave system instead of single normal shock for improving radial inflow turbine reliability". In: *International Journal of Heat and Fluid Flow* 71.March (2018), pp. 170–178. ISSN: 0142727X. DOI: 10.1016/j.ijheatfluidflow.2018.03.018. URL: http://www.sciencedirect.com/science/article/pii/S0142727X17305507 (cit. on p. 14).

[78] W. Sato, A. Yamagata, and H. Hattori. "A Study of Aerodynamic Excitation Forces on a Radial Turbine Blade Due to Rotor-Stator Interaction". In: *Institution of Mechanical Engineers - 11th International Conference on Turbochargers and Turbocharging*. Ed. by I. o. M. Engineers. Oxford: Woodhead Publishing, 2014, pp. 389–398. ISBN: 9780081000335. URL: http://www.sciencedirect.com/science/article/pii/B9780081000335500317 (cit. on pp. 14, 16).

[79] B. Zhao, C. Yang, L. Hu, H. Sun, J. Yi, C. Eric, X. Shi, and A. Engeda. "Understanding of the Interaction between Clearance Leakage Flow and Main Passage Flow in a VGT Turbine". In: *Advances in Mechanical Engineering* 7.2 (2015), p. 652769. DOI: 10.1155/2014/652769. URL: https://doi.org/10.1155/2014/652769 (cit. on p. 15).

[80] X. Qiu, M. R. Anderson, and N. C. Baines. "Meanline Modeling of Radial Inflow Turbine With Variable Area Nozzle". In: *ASME Turbo Expo 2009: Power for Land, Sea and Air*. Florida: ASME, 2009, pp. 1–7. DOI: 10.1115/GT2009-59170. URL: https://doi.org/10.1115/GT2009-59170 (cit. on p. 15).

[81] D. Yang, L. Cao, C. Yang, D. Lao, and H. Sun. "Investigations on the effect of guide vane thickness and solidity on shock and unsteady flow characteristic of VNT". In: *Journal of Mechanical Science and Technology* 34.6 (2020), pp. 2423–2433. ISSN: 19763824. DOI: 10.1007/s12206-020-

0518-4. URL: https://link.springer.com/article/10.1007/s12206-020-0518-4 (cit. on pp. 15, 16).

[82] B. Zhao, M. Qi, H. Zhang, and X. Shi. "Investigation on effects of shock wave on vortical wake flow in a turbine nozzle cascade". In: *Aerospace Science and Technology* 98 (2020), pp. 1–9. ISSN: 1270-9638. DOI: https://doi.org/10.1016/j.ast.2020.105690. URL: https://www.sciencedirect.com/science/article/pii/S1270963819327348 (cit. on pp. 15, 171).

[83] B. Zhao, M. Qi, H. Sun, X. Shi, and C. Ma. "A comprehensive analysis on the structure of groove-induced shock waves in a linear turbine". In: *Aerospace Science and Technology* 87.1270-9638 (2019), pp. 331–339. ISSN: 12709638. DOI: 10.1016/j.ast.2019.02.036. URL: http://www.sciencedirect.com/science/article/pii/S1270963818320388 (cit. on pp. 15, 42).

[84] S. Mehrnia, K. Miyagawa, J. Kusaka, and Y. Nakamura. "Radial turbine optimization under unsteady flow using nature-inspired algorithms". In: *Aerospace Science and Technology* 103.1270-9638 (2020), p. 105903. ISSN: 12709638. DOI: 10.1016/j.ast.2020.105903. URL: http://www.sciencedirect.com/science/article/pii/S127096382030585X (cit. on p. 15).

[85] Y. Liu, D. Lao, Y. Liu, C. Yang, and M. Qi. "Investigation on the effects of nozzle openings for a radial turbine with variable nozzle". In: *SAE 2014 World Congress & Exhibition*. Vol. 01. Detroit, United Staes: SAE International, 2014, pp. 1–8. ISBN: 2014011648. DOI: 10.4271/2014-01-1648. URL: https://doi.org/10.4271/2014-01-1648 (cit. on p. 15).

[86] H. Chen. "Turbine wheel design for Garrett advanced variable geometry turbines for commercial vehicle applications". In: *8th International Conference on Turbochargers and Turbocharging*. Ed. by B. T. .-. 8. I. C. o. T. Institution of Mechanical Engineers Combustion Engines & Fuels Group and Turbocharging. Woodhead Publishing, 2006, pp. 317–327. ISBN: 1845691741. DOI: 10.1533/9781845697099.6.317. URL: http://www.sciencedirect.com/science/article/pii/B9781845691745500270 (cit. on pp. 15, 177).

[87] L. Hu, H. Sun, J. Yi, E. Curtis, A. Morelli, J. Zhang, B. Zhao, C. Yang, X. Shi, and S. Liu. "Investigation of nozzle clearance effects on a radial turbine: Aerodynamic performance and forced response". In: *SAE 2013 World Congress & Exhibition*. Vol. 1. Detroit, United States: SAE International, 2013, pp. 1–11. DOI: 10.4271/2013-01-0918. URL: https://doi.org/10.4271/2013-01-0918 (cit. on p. 15).

[88] T. Heuer, M. Gugau, A. Klein, and P. Anschel. “An analytical approach to support high cycle fatigue validation for turbocharger turbine stages”. In: *Turbo Expo: Power for Land, Sea, and Air*. Vol. 1. Berlin, Germany: ASME, 2008, pp. 723–732. ISBN: 9780791843116. DOI: 10.1115/GT2008-50764. URL: https://doi.org/10.1115/GT2008-50764 (cit. on p. 15).

[89] X. Shi, C. Yang, Y. Liu, S. T. Liu, and B. Zhao. “Numerical investigation on the high-cycle pressure fluctuation mechanism of VNT rotor”. In: *11th International Conference on Turbochargers and Turbocharging*. Ed. by I. o. M. Engineers. Oxford: Woodhead Publishing, 2014, pp. 411–418. DOI: 10.1533/978081000342.411. URL: https://doi.org/10.1533/978081000342.411 (cit. on p. 15).

[90] F. Rubechini, M. Marconcini, A. Arnone, A. S. Del Greco, and R. Biagi. “Special Challenges in the CFD Modeling of Transonic Turbo-Expanders”. In: *ASME Turbo Expo 2013: Turbine Technical Conference and Exposition*. San Antonio, Texas, USA: ASME, 2013, pp. 1–10. DOI: 10.1115/GT2013-95554. URL: https://doi.org/10.1115/GT2013-95554 (cit. on pp. 16, 103).

[91] J. M. Allport, M. L. Jupp, A. Pezouvanis, G. W. Janicki, A. I. Pierończyk, A. J. Day, P. Olley, B. Mason, and M. K. Ebrahimi. “Turbocharger blade vibration: Measurement and validation through laser tip-timing”. In: *10th International Conference on Turbochargers and Turbocharging*. Ed. by IMechE. 2. Woodhead Publishing, 2012, pp. 173–181. ISBN: 9780857092090. DOI: 10.1533/9780857096135.3b.173. URL: http://www.sciencedirect.com/science/article/pii/B9780857092090500145 (cit. on p. 16).

[92] N. Bachschmid, E. Pesatori, S. Bistolfi, and S. Chatterton. “Blade Vibration Measurements and Excitation Force Evaluation”. In: *Proceedings of the 9th IFToMM International Conference on Rotor Dynamics*. Ed. by P. Pennacchi. Cham: Springer International Publishing, 2015, pp. 65–78. ISBN: 978-3-319-06590-8. URL: https://link.springer.com/chapter/10.1007/978-3-319-06590-8%7B%5C_%7D6 (cit. on p. 16).

[93] E. Sauret. “Open Design of High Pressure Ratio Radial-Inflow Turbine for Academic Validation”. In: *Proceedings of the ASME 2012 International Mechanical Engineering Congress and Exposition*. Ed. by ASME. Vol. 7. Houston, USA, 2012, pp. 3183–3197. DOI: 10.1115/IMECE2012-88315. URL: https://doi.org/10.1115/IMECE2012-88315 (cit. on p. 16).

[94] D. Yang, D. Lao, C. Yang, L. Hu, and H. Sun. “Investigations on the Generation and Weakening of Shock Wave in a Radial Turbine With Variable Guide Vanes”. In: *ASME Turbo Expo 2016: Turbomachinery

Technical Conference and Exposition 2D: Turbom (June 2016), pp. 1–9. DOI: 10.1115/GT2016-57047. URL: https://doi.org/10.1115/GT2016-57047 (cit. on p. 16).

[95] J. Liu, W. Y. Qiao, and W. H. Duan. “Investigation of Unsteady Aerodynamic Excitation on Rotor Blade of Variable Geometry Turbine”. In: *International Journal of Rotating Machinery* 2019 (2019), pp. 1–13. ISSN: 15423034. DOI: 10.1155/2019/4396546. URL: https://www.hindawi.com/journals/ijrm/2019/4396546/ (cit. on p. 16).

[96] H. Hayami, Y. Senoo, Y. I. Hyun, and M. Yamaguchi. “Effects of tip clearance of nozzle vanes on performance of radial turbine rotor”. In: *Journal of Turbomachinery* 112.1 (1990), pp. 58–63. DOI: 10.1115/1.2927421. URL: https://doi.org/10.1115/1.2927421 (cit. on p. 16).

[97] A. T. Simpson, S. W. Spence, and J. K. Watterson. “Numerical and experimental study of the performance effects of varying vaneless space and vane solidity in radial turbine stators”. In: *Journal of Turbomachinery* 135.3 (2013), pp. 1–12. ISSN: 0889504X. DOI: 10.1115/1.4007525. URL: https://doi.org/10.1115/1.4007525 (cit. on p. 17).

[98] G. Paniagua, T. Yasa, A. De La Loma, L. Castillon, and T. Coton. “Unsteady strong shock interactions in a transonic turbine: Experimental and numerical analysis”. In: *Journal of Propulsion and Power* 24.4 (2008), pp. 722–731. ISSN: 07484658. DOI: 10.2514/1.34774. URL: https://doi.org/10.2514/1.34774 (cit. on pp. 17, 42).

[99] H. Kosuge, N. Yamanaka, I. Ariga, and I. Watanabe. “Performance of Radial Flow Turbines Under Pulsating Flow Conditions”. In: *Journal of Engineering for Power* 98.1 (1976), pp. 53–59. ISSN: 0022-0825. DOI: 10.1115/1.3446110. URL: https://doi.org/10.1115/1.3446110 (cit. on p. 17).

[100] D. Palfreyman and R. F. Martinez-Botas. “The Pulsating Flow Field in a Mixed Flow Turbocharger Turbine: An Experimental and Computational Study”. In: *Journal of Turbomachinery* 127.1 (2005), pp. 144–155. ISSN: 0889-504X. DOI: 10.1115/1.1812322. URL: https://doi.org/10.1115/1.1812322 (cit. on p. 17).

[101] A. Costall, R. F. Martinez-botas, and D. Palfreyman. “Detailed Study of Pulsating Flow Performance in a Mixed Flow Turbocharger Turbine”. In: *ASME Turbo Expo 2005: Power for Land, Sea, and Air*. Reno Hilton, Reno Tahoe, Nevada: ASME, 2005, pp. 1415–1433. DOI: 10.1115/GT2005-68828. URL: https://doi.org/10.1115/GT2005-68828 (cit. on p. 17).

[102] M. Qi, X. Lei, Z. Wang, and C. Ma. “Investigation on the flow characteristics of a VNT turbine under pulsating flow conditions”. In: *Proceedings of the Institution of Mechanical Engineers, Part D: Journal of Automobile Engineering* 233.2 (2019), pp. 396–412. DOI: 10.1177/0954407017744922. URL: https://doi.org/10.1177/0954407017744922 (cit. on p. 17).

[103] Y. Xue, M. Yang, R. F. Martinez-Botas, B. Yang, and K. Deng. “Unsteady performance of a mixed-flow turbine with nozzled twin-entry volute confronted by pulsating incoming flow”. In: *Aerospace Science and Technology* 95.1270-9638 (2019), p. 105485. ISSN: 12709638. DOI: 10.1016/j.ast.2019.105485. URL: http://www.sciencedirect.com/science/article/pii/S1270963819323430 (cit. on p. 17).

[104] F. Fontaneto, T. Arts, M. Simon, and P. Picot. “Aerodynamic Performance of an Ultra-Low Aspect Ratio Centripetal Turbine Stator”. In: *International Journal of Turbomachinery, Propulsion and Power* (2016), pp. 1–13. ISSN: 2504-186X. DOI: 10.3390/ijtpp1010003. URL: https://www.mdpi.com/2504-186X/1/1/3 (cit. on p. 17).

[105] A. C. Jones. “Design and Test of a Small, High Pressure Ratio Radial Turbine”. In: *Journal of Turbomachinery* 118.2 (1996), pp. 362–370. ISSN: 0889-504X. DOI: 10.1115/1.2836651. URL: https://doi.org/10.1115/1.2836651 (cit. on p. 17).

[106] *Effects of Inlet Conditions on the Turbine Performance of a Radial Turbine*. Vol. 6. Turbo Expo: Power for Land, Sea, and Air. Berlin, Germany: ASME, 2008, pp. 1985–2001. DOI: 10.1115/GT2008-51088. URL: https://doi.org/10.1115/GT2008-51088 (cit. on p. 17).

[107] M. Cerdoun and A. Ghenaiet. “Unsteady behaviour of a twin entry radial turbine under engine like inlet flow conditions”. In: *Applied Thermal Engineering* 130 (2018), pp. 93–111. ISSN: 1359-4311. DOI: https://doi.org/10.1016/j.applthermaleng.2017.11.001. URL: https://www.sciencedirect.com/science/article/pii/S1359431117308712 (cit. on p. 17).

[108] *Validation and Development of Loss Models for Small Size Radial Turbines*. Vol. 7. Turbo Expo: Power for Land, Sea, and Air. Glasgow, UK: ASME, 2010, pp. 1937–1949. DOI: 10.1115/GT2010-22666. URL: https://doi.org/10.1115/GT2010-22666 (cit. on p. 17).

[109] H. Tamaki, S. Ouchida, and M. Unno. “Experimental Fluid Dynamics Applications in Radial Turbomachines: Inlet Recirculation in Centrifugal Compressor, Rotating Stall and Flow in Vaneless Diffuser, and Improvement in Accuracy of CFD for Predicting Flow Fields in a Radial Turbine Rotor”. In: *Journal of Physics: Conference Series* 1909 (2021). DOI: 10.10

88/1742-6596/1909/1/012089. URL: https://10.0.4.64/1742-6596/1909/1/012089 (cit. on p. 17).

[110] P. He, Z. Sun, H. Zhang, H. Chen, and C. Tan. "Investigation of clearance flows in deeply scalloped radial turbines". In: *Proceedings of the Institution of Mechanical Engineers, Part A: Journal of Power and Energy* 226.8 (2012), pp. 951–962. DOI: 10.1177/0957650912460361. URL: https://doi.org/10.1177/0957650912460361 (cit. on pp. 17, 144).

[111] J. Kammeyer, C. Natkaniec, and J. R. Seume. "Tip leakage in small radial turbines: Optimum tip-gap and efficiency loss correlations". In: *Turbo Expo: Power for Land, Sea, and Air*. Glasgow, UK: ASME, 2010, pp. 1–11. DOI: 10.1115/GT2010-22680. URL: https://doi.org/10.1115/GT2010-22680 (cit. on p. 18).

[112] J. R. Serrano, R. Navarro, L. M. García-Cuevas, and L. B. Inhestern. "Contribution to tip leakage loss modeling in radial turbines based on 3D flow analysis and 1D characterization". In: *International Journal of Heat and Fluid Flow* 78 (2019), pp. 1–7. ISSN: 0955-5986. DOI: 10.1016/j.ijheatfluidflow.2019.108423. URL: http://www.sciencedirect.com/science/article/pii/S095559861530042X (cit. on pp. 18, 39, 69, 111, 132, 136).

[113] Q. Zhang and L. He. "Over-tip choking and its implications on turbine blade-tip aerodynamic performance". In: *Journal of Propulsion and Power* 27.5 (2011), pp. 1008–1014. ISSN: 07484658. DOI: 10.2514/1.B34112 (cit. on p. 18).

[114] A. P. S. Wheeler, T. Korakianitis, and S. Banneheke. "Tip-Leakage Losses in Subsonic and Transonic Blade Rows". In: *Journal of Turbomachinery* 135.1 (2012). ISSN: 0889-504X. DOI: 10.1115/1.4006424. URL: https://doi.org/10.1115/1.4006424 (cit. on pp. 18, 144).

[115] A. Pashayev, D. Askerov, and R. Sadiqov. "Numerical modeling of gas turbine cooled blades". In: *Aviation* 9 (2005), pp. 9–18. DOI: 10.3846/16487788.2005.9635905. URL: https://doi.org/10.3846/16487788.2005.9635905 (cit. on p. 18).

[116] D. O. O'Dowd, Q. Zhang, L. He, M. L. G. Oldfield, P. M. Ligrani, B. C. Y. Cheong, and I. Tibbott. "Aero-Thermal Performance of a Winglet at Engine Representative Mach and Reynolds Numbers". In: *ASME Turbo Expo 2010: Power for Land, Sea, and Air*. Glasgow, UK: ASME, June 2010, pp. 357–367. ISBN: 978-0-7918-4399-4. DOI: 10.1115/GT2010-22794. URL: https://doi.org/10.1115/GT2010-22794 (cit. on p. 18).

[117] A. M. Daabo, S. Mahmoud, R. K. Al-Dadah, A. M. Al Jubori, and A. Bhar Ennil. “Numerical analysis of small scale axial and radial turbines for solar powered Brayton cycle application”. In: *Applied Thermal Engineering* 120 (2017), pp. 672–693. ISSN: 1359-4311. DOI: https://doi.org/10.1016/j.applthermaleng.2017.03.125. URL: https://www.sciencedirect.com/science/article/pii/S1359431117320549 (cit. on p. 18).

[118] R. Dambach and H. P. Hodson. “Tip leakage flow: A comparison between small axial and radial turbines”. In: *IMechE Symposium*. London, UK, 2000, pp. 1–9. URL: http://www-g.eng.cam.ac.uk/whittle/publications/hph/2000-IMechE-RadialTips.pdf (cit. on pp. 18, 144).

[119] *An Experimental Study of Tip Clearance Flow in a Radial Inflow Turbine*. Vol. Volume 1. Turbo Expo: Power for Land, Sea, and Air. Stockholm: ASME, 1998, p. 12. DOI: 10.1115/98-GT-467. URL: https://doi.org/10.1115/98-GT-467 (cit. on pp. 18, 128).

[120] J. R. Serrano, R. Navarro, L. M. García-Cuevas, and L. B. Inhestern. “Turbocharger turbine rotor tip leakage loss and mass flow model valid up to extreme off-design conditions with high blade to jet speed ratio”. In: *Energy* 147 (2018), pp. 1299–1310. ISSN: 0360-5442. DOI: https://doi.org/10.1016/j.energy.2018.01.083. URL: https://www.sciencedirect.com/science/article/pii/S0360544218301014 (cit. on pp. 18, 39, 69, 104, 128, 131, 132).

[121] *Variable Geometry Turbine Nozzle Design for High Expansion Ratios*. Vol. 2B. Turbo Expo: Power for Land, Sea, and Air. Oslo, Norway: ASME, 2018, pp. 1–12. DOI: 10.1115/GT2018-75013. URL: https://doi.org/10.1115/GT2018-75013 (cit. on p. 18).

[122] T. Sonoda, T. Arima, M. Olhofer, B. Sendhoff, F. Kost, and P.-A. Giess. “A Study of Advanced High-Loaded Transonic Turbine Airfoils”. In: *Journal of Turbomachinery* 128.4 (2004), pp. 650–657. ISSN: 0889-504X. DOI: 10.1115/1.2221325. URL: https://doi.org/10.1115/1.2221325 (cit. on p. 18).

[123] X. Lei, M. Qi, H. Sun, and L. Hu. “Investigation on the Shock Control Using Grooved Surface in a Linear Turbine Nozzle”. In: *Journal of Turbomachinery* 139.12 (2017). ISSN: 0889-504X. DOI: 10.1115/1.4037860. URL: https://doi.org/10.1115/1.4037860 (cit. on pp. 18, 173).

[124] *Numerical Investigation of a Novel Approach for Mitigation of Forced Response of a Variable Geometry Turbine During Exhaust Braking Mode*. Vol. Volume 8: Turbo Expo: Power for Land, Sea, and Air. 2016. DOI: 10.1115/GT2016-56342. URL: https://doi.org/10.1115/GT2016-56342 (cit. on pp. 19, 171, 177).

[125] B. Zhao, M. Qi, H. Sun, X. Shi, and C. Ma. “Experimental and Numerical Investigation on the Shock Wave Structure Alterations and Available Energy Loss Variations With a Grooved Nozzle Vane”. In: *Journal of Turbomachinery* 141.5 (2019). ISSN: 0889-504X. DOI: 10.1115/1.4041819. URL: https://doi.org/10.1115/1.4041819 (cit. on pp. 19, 169).

[126] J. Moore and J. G. Moore. *Entropy Production Rates From Viscous Flow Calculations: Part I — A Turbulent Boundary Layer Flow*. Mar. 1983. DOI: 10.1115/83-GT-70. URL: https://doi.org/10.1115/83-GT-70 (cit. on pp. 19, 149).

[127] K. Ziaja, P. Post, A. Schramm, O. Willers, J. R. Seume, and F. di Mare. “Numerical Investigation of Loss Mechanisms in a Partially Loaded Supersonic ORC Axial Turbine Stage”. In: Rotterdam, Netherlands, June 2022. DOI: 10.1115/GT2022-82852. URL: https://doi.org/10.1115/GT2022-82852 (cit. on pp. 19, 149).

[128] L. Zhang, W. Zhuge, Y. Zhang, and T. Chen. “Similarity Theory Based Radial Turbine Performance and Loss Mechanism Comparison between R245fa and Air for Heavy-Duty Diesel Engine Organic Rankine Cycles”. In: *Entropy* 19.1 (2017), pp. 1–20. ISSN: 1099-4300. DOI: 10.3390/e19010025. URL: https://www.mdpi.com/1099-4300/19/1/25 (cit. on pp. 19, 149).

[129] S. M. Lim, A. Dahlkild, and M. Mihaescu. “Influence of Upstream Geometry on Pulsatile Turbocharger Turbine Performance”. In: *ASME Turbo Expo 2018: Turbomachinery Technical Conference and Exposition*. Oslo, Norway, June 2018, pp. 1–10. DOI: 10.1115/GT2018-76706. URL: https://doi.org/10.1115/GT2018-76706 (cit. on p. 20).

[130] S. M. Lim, A. Dahlkild, and M. Mihaescu. “Aerothermodynamics and Exergy Analysis in Radial Turbine With Heat Transfer”. In: *Journal of Turbomachinery* 140.9 (Aug. 2018), pp. 1–14. ISSN: 0889-504X. DOI: 10.1115/1.4040852. URL: https://doi.org/10.1115/1.4040852 (cit. on p. 20).

[131] S. M. Lim, S. Kazemi Bakhshmand, C. Biet, and M. Mihaescu. “Experimental and Numerical Investigation of a Turbocharger Turbine Using Exergy Analysis at Non-Adiabatic Conditions”. In: *SAE Powertrains, Fuels & Lubricants Meeting*. SAE International, 2020, pp. 1–9. DOI: 10.4271/2020-01-2225. URL: https://www.sae.org/publications/technical-papers/content/2020-01-2225/ (cit. on p. 20).

CHAPTER 3

CFD simulations setup

Contents

3.1 Introduction 39
3.2 Geometry Description 39
3.3 Numerical Setup 42
3.4 Summary 49
3.5 References 50

Figures

3.1 Stator and rotor geometry. VT: Vane throat. VST: Vaneless space throat. 40
3.2 Computational domain. 41
3.3 Section view of the mesh. 43
3.4 Variation of mass flow and turbine power with different mesh configurations relative to the finest simulated mesh for opened and closed position. 45
3.5 Selected points to evaluate the Mach number. Point A (at R=24.41 mm) and Point B (at R=26.08 mm). 46

Tables

3.1 Turbine geometry parameters. 40
3.2 Mesh independence study. 46

3.3 Differences in some parameters of the case at higher pressure ratio when using one degree and two degrees to define the time step. . . . 48
3.4 Summary of the evaluated operational points. 49

3.1 Introduction

OVER the last years, with the improvement of computational tools, different studies have been carried out to characterize the internal flow behavior of the radial turbine through the volute, stator, and rotor using computational fluid dynamics (CFD). Since the radial turbine geometry selected for this study is quite compact and relatively small, the installation of sensors in its interior is quite limited [55] to analyze the complexity of flow through experimental tests. Thus, CFD simulation is an important tool for analyzing the flow profile and improving the internal aerodynamic performance of the turbine [60]. Nevertheless, the limitations that can have the CFD simulations are the time and the computational cost to obtain adequate results depending on the type of simulations. Well-known numerical techniques to study the turbulent flow are Direct Numerical Simulation (DNS), Large Eddy Simulation (LES) [132], steady and unsteady Reynolds-averaged Navier-Stokes simulations (RANS and URANS respectively) DNS provides the most reliable results with a fine mesh but is extremely time-consuming, especially for high Reynolds numbers. LES simulations are used as an alternative to DNS at much higher Reynolds numbers, but the time needed for calculation is still considerable. Steady and unsteady RANS simulations model all scales of turbulence and need less time, and computational cost since the mesh can be coarser. The results quality depends on the setup of the simulations, but they can reach enough quality results. Thus, RANS simulations are used for the current work.

This chapter presents the variable geometry turbine CFD simulations setup. The geometry characteristics are described, the models to properly simulate the turbine are selected, and a mesh independence study is performed to select the mesh that allows a balance between the accuracy of the results and computational costs. The simulations are characterized by being carried out under adiabatic conditions, low inlet temperatures, and high-pressure ratios.

3.2 Geometry Description

A commercial turbocharger fitted with a variable geometry turbine (VGT), found in a four cylinder, 2L diesel engines of sport utility vehicles (SUV), has been used for this study. The turbine was previously experimental and numerical studied at different conditions up to low mass flows, and even negative turbine power output by Serrano et al. [73, 120, 112]. The stator consists of eleven vanes, while the rotor has nine blades, as shown in Figure 3.1(a). The dimensions and features of the stator and rotor passage are presented in Table 3.1. The inlet and outlet ducts, the volute, stator and rotor made part of the computational fluid domain as illustrated in Figure 3.2. The length of the inlet and outlet ducts

Table 3.1: Turbine geometry parameters.

Stator				
Stator vane number	11			
Tip clearance	0.2 mm			
Nozzle vane height	8 mm			
Chord length	18.95 mm			
Vane angle α	78.34 °	72.94 °	53.45 °	43.02 °
(VGT opening)	(10%)	(30%)	(80%)	(100%)
Vane throat (VT) area	11.88 mm^2	21.74 mm^2	59.77 mm^2	68.20 mm^2
Vaneless space throat (VST) area	60.48 mm^2	57.02 mm^2	34.79 mm^2	23.39 mm^2
Rotor				
Inlet diameter	41 mm			
Outlet diameter	38 mm			
Blade number	9			
Outlet blade angle	59°			
Tip clearance	0.36 mm to 0.4 mm			

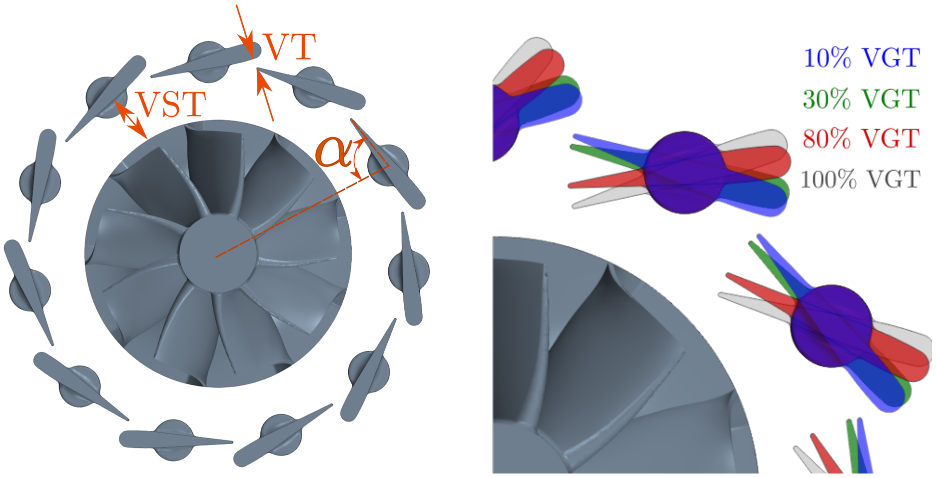

(a) Top view.

(b) Different VGT openings

Figure 3.1: Stator and rotor geometry. VT: Vane throat. VST: Vaneless space throat.

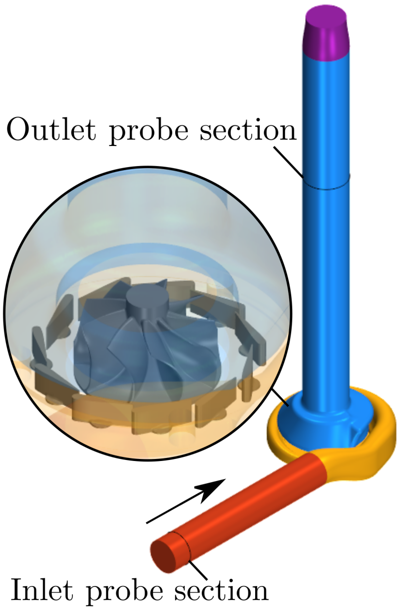

Figure 3.2: Computational domain.

are six and nine diameters, respectively, which results in a distance equal to 200 mm and 400 mm, respectively, being long enough to include the experimental measurement section in the domain. The probe section are placed at the same location of experimental measurement probes, which are located according to turbocharger gas stand test code [133]. Furthermore, downstream of the outlet probe section a convergent duct with an exit diameter equal to the wheel outlet diameter is part of the computational domain. This allows to set a similar static pressure in the outlet of the domain as it would expect in the outlet of the rotor. This is more suitable for the study of the choked flow in the rotor outlet as similar downstream pressures can be obtained. Three stator vanes positions are considered in this study to analyze the choking phenomena in the stator and rotor, as well as the rotor-stator interaction. The positions of the stator vanes will be denoted as VGT position. The first is a VGT opening of 10% representing a closed position, the second is a 30% opening, and the third is 80% representing a widely opened position as shown by Figure 3.1(b). These VGT positions can be set by the control system of the engine at full load or load acceptance transient (sudden tip-in) test [35, 134, 135, 136, 137, 138]. The maximum aperture of the vanes allowed by the mechanism that controls their position is presented in Table 3.1 and depicted in Figure 3.1(b) as 100% VGT to put in context the selected vanes positions. In the simulations conducted by Serrano et al. [73] the VGT positions were stepwise varied with the highest pressure ratio until the reduced mass flow was matched with the selected points of the experimental test [139]. Those particular VGT positions were experimentally assessed in previous work up to low flow conditions and high blade speed ratios. They will be maintained in this investigation to allow consistent map information. From this point forward, 10% and 80% VGT opening will be also referred as closed and open position respectively.

3.3 Numerical Setup

To examine the internal flow field of the turbine under varying conditions the CFD software Star-CCM+ 2019.1 (Build 14.02.010-R8) was employed in the current work. The working fluid is air and was considered as an ideal and compressible gas. Since the flow at high-pressure ratios reaching choking conditions with occurring shock waves is the focus of this research, the density-based coupled solver has been chosen [67]. For the couple flow model the implicit integration is selected and the second-order upwind discretization scheme is used for evaluating face values for convection and diffusion fluxed. Furthermore, for the couple flow model, the Weiss-Smith preconditioned Roe's Flux Difference Splitting (ROE FDS) scheme is selected for evaluating inviscid fluxes. First, steady Reynolds averaged Navier Stokes (RANS) simulations, and second, unsteady RANS (URANS) simulations were run. In RANS simulations, a multiple reference frame simulates the rotor movement. The convergent solution is then used as an initial condition for the URANS simulations with a sling mesh of the rotor region for simulating the rotor movement. This procedure makes the URANS simulations converge faster. To obtain turbulence closure, the $k-\omega$ SST model [140] with a Durbin scale limiter for realizability and compressibility corrections has been selected, as detailed by Fajardo [141] and as it is widely recommended and well-validated for radial turbomachinery in the literature [68, 142, 143, 144] even under transonic and supersonic conditions [83, 145, 98]. Furthermore, with a finer grid and improved resolution in the near wall region the model generates results that agree well with the experimental data [146, 147]. Comparing with different turbulent models the $k-\omega$ SST model predictions are closer to the experimental value in terms of wall pressure distribution [148]. Under supersonic conditions the flow field structure, surface pressure, velocity profiles and the overall features of these complex flow fields can be predicted [149, 148]. However, the SST model needs improvement on the wake flow [150]. The entire fluid domain, which consists of the inner volume of the volute, stator and rotor has been discretized through an unstructured polyhedral mesh, whereas for the inlet and outlet duct, a generalized cylinder mesher has been used to generate an extruded mesh along the duct's length as can be seen in the Figure 3.3 (a). In the boundary layer region prism layers

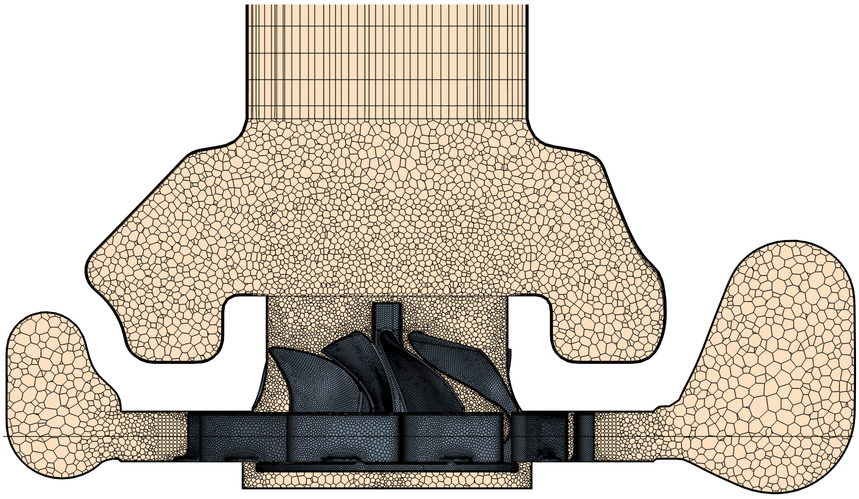

(a) Front view.

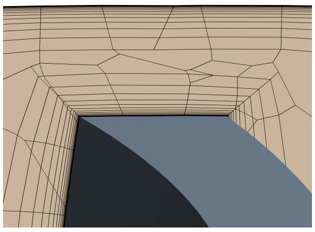

(c) Rotor tip.

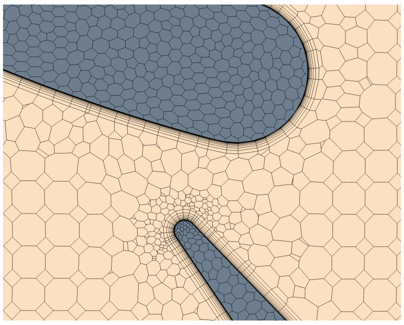

(b) Stator vane.

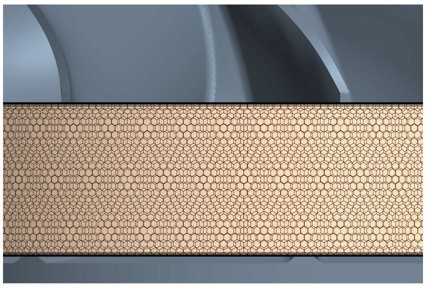

(d) Stator-Rotor interface.

Figure 3.3: Section view of the mesh.

have been generated, allowing to capture of viscous gradients close to the wall, a mesh with similar characteristics was used by Serrano et. al [73] aiming a low Reynolds criteria, nevertheless higher mass flow with elevated Reynolds number are analyzed in the presented work.

3.3.1 Mesh independence

To obtain a suitable number of cells, an extensive mesh sensitivity analysis study has been carried out to achieve a grid-independent numerical solution. In this manner, an operation point with an inlet pressure of 5.5 bar that allows what will be considered a higher pressure ratio and a rotational speed of 3882 rpm/$\sqrt{\mathrm{K}}$, which will be denoted as the lower speed, for the closed and the opened VGT positions, have been selected to find a grid size that has a good enough resolution to cover all simulated operating conditions and gives reliable results [151, 152]. For the volute, stator, and rotor, the core and boundary layers have been changed independently using five different core mesh densities from coarser to finer and three boundary layer meshes. A core of medium density and fifteen prism layers in the boundary layer has been used for the inlet and outlet duct having a y^+ of 0.46 and 0.34, respectively, for the closed position. In contrast, for the opened position, the y^+ is 1.12 and 0.84, respectively. Thus, fifteen types of meshes for the closed VGT position and another fifteen for the opened VGT position have been generated. Figure 3.4 depicts the mesh analysis that evaluated the relative variation of the mass flow and power regarding the finest mesh, which has the highest core mesh density and 20 prism layers in the boundary layer. All generated meshes have a medium y^+-value close to one to fulfill the low Reynolds criteria. The change in the number of prism layers in the boundary layers does not significantly affect the mass flow in both VGT positions as it does with the power for the closed position. At opened VGT position, the mass flow and power do not experience changes of high order using the three different boundary meshes. Furthermore, the power at the closed position fluctuates more than at the opened position when the number of prism in the boundary layer varies. The most significant difference occurs with the coarser and the coarse cores, while the variations with the medium and fine cores are quite similar. Nevertheless, the computational time of the fine core is higher than the medium core.

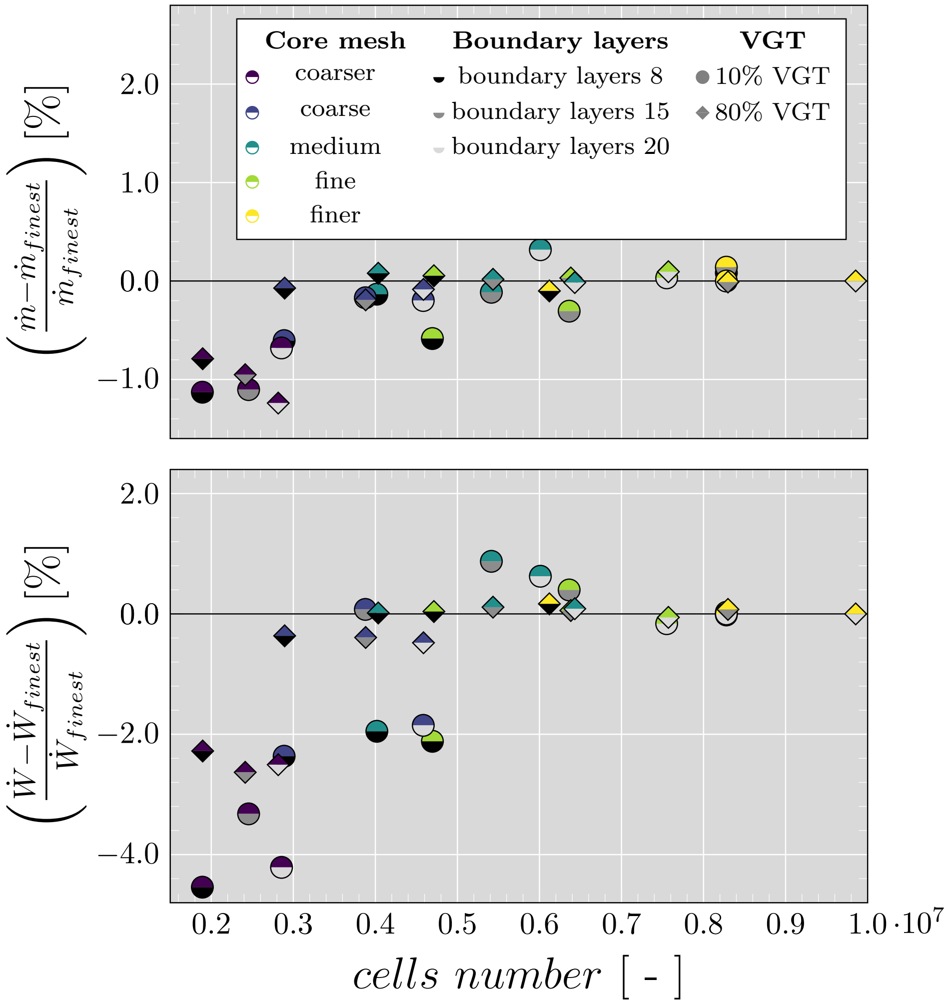

Figure 3.4: Variation of mass flow and turbine power with different mesh configurations relative to the finest simulated mesh for opened and closed position.

$$GCI = \frac{3 \cdot |\epsilon|}{r^p - 1} \tag{3.1}$$

Table 3.2: Mesh independence study.

VGT [%]	Core mesh	Boundary layer	Cells number [$\cdot 10^6$]	$\dot{m}$ [kg/s]	$\dot{W}$ [kW]	Ma_{pointA} [-]	Ma_{pointB} [-]	$\nabla\rho_{at\,SS}$ [kg/m^3]
10	medium	15	5.41	0.1714	1.4604	1.0450	1.3126	217.6083
	finest	20	8.28	0.1716	1.4477	1.0250	1.3388	211.8260
80	medium	15	5.43	0.4628	3.4579	0.6139	0.7175	222.7534
	finest	20	9.85	0.4627	3.4540	0.6141	0.7125	244.4962
GCI (10% VGT medium core and 15 boundary layer)[%]				0.26	1.96	4.37	4.39	6.12
GCI (80% VGT medium core and 15 boundary layer)[%]				0.02	0.15	0.05	0.91	11.66

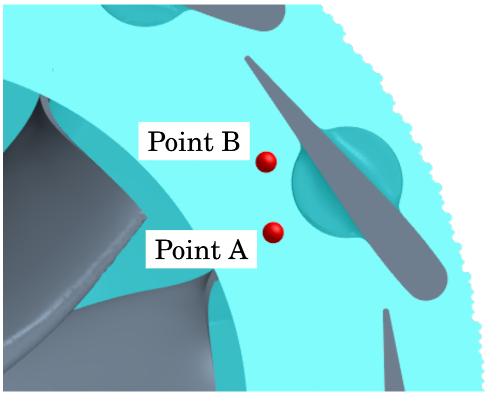

Figure 3.5: Selected points to evaluate the Mach number. Point A (at R=24.41 mm) and Point B (at R=26.08 mm).

Besides the analysis presented in Figure 3.4, where the medium core mesh represents a good option, the grid convergence index (GCI) [153] is calculated using the medium and finest mesh to quantify the numerical uncertainty, as shown in Table 3.2, of the mass flow, the power, the Mach number and the density gradient at the SS of the vane. For the Mach number two points in the vaneless space were selected, one at the middle of the vaneless space at R=24.41 mm, Point A, and the other at R=26.08 mm, Point B, as depicts Figure 3.5. The GCI is defined in Equation 3.1, where ϵ, r, and p represent the relative error between two grids, the refinement factor ratio, and the order of accuracy method, respectively. The mesh denoted as a medium core mesh with 15 cells in the boundary layer presents a lower GCI, implying a lower error in the mass flow rate and turbine power, which ensures the accuracy of the simulation and a grid-independent solution. Consequently, the mesh with a medium core and 15 cells to resolve the boundary layer has been chosen for the calculation of the different operation points that will be presented in the following sections. This mesh owns 5.4 million cells with an expansion ratio in the prism layer mesh of 1.3. For the closed VGT position, a mean y^+ of 0.7 has been achieved for the turbocharger geometry (volute, rotor, stator and outlet volume), while the opened VGT position presents a mean y^+ of 1.3.

3.3.2 Boundary Conditions

In a previous PhD thesis by L. B. Inhestern [21] six different reduced rotational speeds were measured: 1710, 2830, 3890, 4890, 5830 and 6715 rpm/$\sqrt{\text{K}}$. For the first four reduced speeds extremely high blade speed ratios were measured. These reduced speeds are equivalent to a physical speed range from 45 to 130 krpm when operating at a common turbine inlet temperature of around 700 K, and from 56 to 160 krpm at around 1100 K. This is a common range for the diesel engine exhaust gas temperature upstream of the turbine. Furthermore, based on previous experimental data [21] of a four cylinder 2L turbocharged diesel engine with the same analyzed turbine, at full load the measurements reveals that the turbine can reach reduced speeds of 5194 rpm/$\sqrt{\text{K}}$, at 70% VGT and producing an engine power of 38 kW, and 8748 rpm/$\sqrt{\text{K}}$ at 26% VGT and producing an engine power of 116 kW. Thus, simulations were conducted with the three stator vane positions mentioned in the previous section (closed, 30% VGT and opened position) and with two different reduced turbine speeds, one at 3882 rpm/$\sqrt{\text{K}}$ and the other at 8421 rpm/$\sqrt{\text{K}}$, which can be referred to as lower and higher speed, respectively. Nevertheless, for the opened VGT position, a rotational speed of 5830 rpm/$\sqrt{\text{K}}$ called medium speed was additionally simulated. The reduced speed is calculated using Equation 3.2.

$$N_{red} = \frac{N}{\sqrt{T_{tot,in}}} \tag{3.2}$$

For the steady and unsteady cases, the turbine total inlet temperature is set as a boundary condition with a value of 340.55 K. Such a low temperature has been chosen, because previous experimental measurements were executed in quasi-adiabatic conditions and thus it is possible to maintain similar conditions of the Mach number. Future measurements will be done in choked condition as an extension of the same map under the same measurement principle. For the same reason adiabatic walls can be applied in these simulations [73]. Furthermore, turbines operating with low inlet temperature can be found in Organic Rankine cycle [154, 155], air cycle heat pump [156, 157] and in the environmental control system (ECS) of commercial aircraft [158, 44]. The outlet static pressure was kept constant at 1.0 bar. The inlet total pressure was varied from moderate up to high total pressures to achieve iso-speed lines with developing choke conditions for the steady cases.

Based on the steady results, the operational points with a total pressure of 3.0 bar and 5.5 bar imposed at the inlet duct have been simulated using an unsteady solver (URANS simulations), to consider the rotor movement and analyze its effect on the development and reach of choked flow while maintaining the boundary condition values in the inlet and outlet ducts. These inlet total pressures allow what will be considered lower and higher pressure ratios. The time step size has been selected as the time that the turbine wheel takes to rotate two degrees depending on the rotational speed [73, 151]. Some authors as Galindo et al. [74] use one degree to define the time step, but as the differences are less than 1% as shown in Table 3.3 and to reduce the computational cost the two degrees rotation was selected to define the time step. This size corresponds to 180 time steps per rotor revolution. Furthermore, 20 inner iteration steps were necessary to bring each time step to convergence by looking at the residuals of inner iterations and applying a low CFL number of 2. The convergence has been reached after around three rotor rotations for the cases of low speed and after approximately eight revolutions at high speed independent of the VGT position.

Table 3.3: Differences in some parameters of the case at higher pressure ratio when using one degree and two degrees to define the time step.

VGT [%]	$N_{red.}$ $[\frac{rpm}{\sqrt{K}}]$	Dev. $\dot{m}$ [%]	Dev. $\pi_{turb.}$ [%]
10	3882	-0.05	0.006
	8421	-0.56	0.35

3.4 Summary

This chapter presents the configuration of the turbine employed in the CFD simulations carried out for the current study. The selected radial turbine is used in automotive turbocharges and is equipped with variable geometry vanes. The turbine has eleven stator vanes and nine rotor blades. The stator vanes positions analyzed correspond to 10% VGT (closed position), 30% VGT and 80% VGT (opened position). The CFD software Star-CCM+ 2019.1 (Build 14.02.010-R8) has been employed for the study of the internal flow of the computational domain formed by the inlet and outlet duct, volute, stator and rotor. RANS and URANS simulations with $k-\omega$ SST turbulence model are conducted using air as working fluid and considered as ideal and compressible gas.

After performing a mesh independence study, a mesh of 5.4 million cells and 15 prism layers in the boundary layer has been chosen. The simulations were carried out with three rotational speeds, while the inlet total pressure was variated from moderate up to high values for the RANS simulations. For URANS simulations, two operational points of each speed line are solved to consider the rotor movement's effects as shown in Table 3.4. The walls are considered adiabatic similar to previous experimental tests. Furthermore, the time step size has been selected as the time that the rotor takes to rotate two degrees depending on the rotational speed. The simulations take 20 inner iterations each time step to ensure the convergence of the results.

Table 3.4: Summary of the evaluated operational points.

VGT [%]	$N_{red.}$ (label) $\left[\frac{\text{rpm}}{\sqrt{\text{K}}}\right]$	$p_{tot,in}$ [bar]	$\pi_{turb.}$ [-]	$T_{tot,in}$ [K]	$p_{stat,out}$ [bar]
10	3882 (lower)	3.0	lower	340.55	1.0
		5.5	higher		
	8421 (higher)	3.0	lower		
		5.5	higher		
30	3882 (lower)	3.0	lower	340.55	1.0
		5.5	higher		
	8421 (higher)	3.0	lower		
		5.5	higher		
80	3882 (lower)	3.0	lower	340.55	1.0
		5.5	higher		
	5830 (middle)	3.0	lower		
		5.5	higher		
	8421 (higher)	3.0	lower		
		5.5	higher		

3.5 References

[21] L. B. Inhestern. “Measurement, simulation, and 1D-modeling of turbocharger radial turbines at design and extreme off-design conditions”. PhD thesis. Universitat Politècnica de València, 2019. DOI: 10.4995/Thesis/10251/119989 (cit. on pp. 4, 47).

[35] J. G. Hawley, F. J. Wallace, A. R. J. Cox, R. W. Horrocks, and G. L. Bird. “Reduction of Steady State NOx Levels from an Automotive Diesel Engine Using Optimised VGT/EGR Schedules”. In: *SAE Technical Paper* 108 (1999), pp. 1172–1184. DOI: 10.4271/1999-01-0835. URL: https://doi.org/10.4271/1999-01-0835 (cit. on pp. 12, 41, 83).

[44] H. Yang, X. Zhang, C. Wang, and C. Yang. “Experimental and theoretical study on a novel energy-saving ECS for commercial airliners”. In: *Applied Thermal Engineering* 127 (2017), pp. 1372–1381. ISSN: 1359-4311. DOI: https://doi.org/10.1016/j.applthermaleng.2017.08.043. URL: http://www.sciencedirect.com/science/article/pii/S1359431117324596 (cit. on pp. 12, 47).

[55] *The Effect of Clearance Flow of Variable Area Nozzles on Radial Turbine Performance*. Vol. 6. Turbo Expo: Power for Land, Sea, and Air. Berlin, Germany: ASME, 2008, pp. 1519–1529. DOI: 10.1115/GT2008-50461. URL: https://doi.org/10.1115/GT2008-50461 (cit. on pp. 12, 17, 39).

[60] A. Marsan and S. Moreau. “Analysis of the flow structure in a radial turbine”. In: *11th European Conference on Turbomachinery Fluid Dynamics and Thermodynamics, ETC 2015*. Madrid: EUROTURBO, 2015, pp. 1–13. DOI: ETC2015-207. URL: euroturbo.eu/publications/proceedings-papers/etc2015-207/ (cit. on pp. 13, 39).

[67] Siemens. *STAR-CCM + 2019.1 Release version 14.02.010-R8*. 2019. URL: https://www.plm.automation.siemens.com/global/es/products/simcenter/STAR-CCM.html (cit. on pp. 13, 42).

[68] F. R. Menter, R. Langtry, and T. Hansen. “CFD simulation of turbomachinery flows - Verfication, validation and modelling”. In: *ECCOMAS 2004 - European Congress on Computational Methods in Applied Sciences and Engineering*. July. Jyvaskyla, 2004, pp. 1–14. URL: http://www.mit.jyu.fi/eccomas2004/proceedings/pdf/954.pdf (cit. on pp. 13, 42).

[73] J. R. Serrano, A. Gil, R. Navarro, and L. B. Inhestern. “Extremely low mass flow at high blade to jet speed ratio in variable geometry radial turbines and its influence on the flow pattern a CFD analysis”. In: *ASME Turbo Expo 2017: Turbomachinery Technical Conference and Exposition*. Charlotte, NC, USA: ASME, 2017, pp. 1–13. DOI: 10.1115/GT2017-63

368. URL: https://asmedigitalcollection.asme.org/GT/proceedings-abstract/GT2017/50954/V008T26A005/243279 (cit. on pp. 14, 15, 39, 41, 44, 47, 48).

[74] J. Galindo, J. R. Serrano, L. M. García-Cuevas, and N. Medina. “Using a CFD analysis of the flow capacity in a twin-entry turbine to develop a simplified physics-based model”. In: *Aerospace Science and Technology* 112 (2021), p. 106623. ISSN: 1270-9638. DOI: https://doi.org/10.1016/j.ast.2021.106623. URL: https://www.sciencedirect.com/science/article/pii/S1270963821001334 (cit. on pp. 14, 48, 202).

[83] B. Zhao, M. Qi, H. Sun, X. Shi, and C. Ma. “A comprehensive analysis on the structure of groove-induced shock waves in a linear turbine”. In: *Aerospace Science and Technology* 87.1270-9638 (2019), pp. 331–339. ISSN: 12709638. DOI: 10.1016/j.ast.2019.02.036. URL: http://www.sciencedirect.com/science/article/pii/S1270963818320388 (cit. on pp. 15, 42).

[98] G. Paniagua, T. Yasa, A. De La Loma, L. Castillon, and T. Coton. “Unsteady strong shock interactions in a transonic turbine: Experimental and numerical analysis”. In: *Journal of Propulsion and Power* 24.4 (2008), pp. 722–731. ISSN: 07484658. DOI: 10.2514/1.34774. URL: https://doi.org/10.2514/1.34774 (cit. on pp. 17, 42).

[112] J. R. Serrano, R. Navarro, L. M. García-Cuevas, and L. B. Inhestern. “Contribution to tip leakage loss modeling in radial turbines based on 3D flow analysis and 1D characterization”. In: *International Journal of Heat and Fluid Flow* 78 (2019), pp. 1–7. ISSN: 0955-5986. DOI: 10.1016/j.ijheatfluidflow.2019.108423. URL: http://www.sciencedirect.com/science/article/pii/S095559861530042X (cit. on pp. 18, 39, 69, 111, 132, 136).

[120] J. R. Serrano, R. Navarro, L. M. García-Cuevas, and L. B. Inhestern. “Turbocharger turbine rotor tip leakage loss and mass flow model valid up to extreme off-design conditions with high blade to jet speed ratio”. In: *Energy* 147 (2018), pp. 1299–1310. ISSN: 0360-5442. DOI: https://doi.org/10.1016/j.energy.2018.01.083. URL: https://www.sciencedirect.com/science/article/pii/S0360544218301014 (cit. on pp. 18, 39, 69, 104, 128, 131, 132).

[132] E. M. Smirnov, A. G. Abramov, N. G. Ivanov, P. E. Smirnov, and S. A. Yakubov. “- DNS and RANS/LES-computations of complex geometry flows using a parallel multiblock finite-volume code”. In: *Parallel Computational Fluid Dynamics 2003*. Ed. by A. Ecer, N. Satofuka, J. Periaux, and P. Fox. Amsterdam: Elsevier, 2004, pp. 219–226. ISBN: 978-0-444-51612-1. DOI: https://doi.org/10.1016/B978-044451612-1/50028-

7. URL: https://www.sciencedirect.com/science/article/pii/B9780444516121500287 (cit. on p. 39).

[133] SAE Engine Power Test Code Committee. *Turbocharger Gas Stand Test Code*. 1995. DOI: 10.4271/J1826_199503. URL: https://doi.org/10.4271/J1826%7B%5C_%7D199503 (cit. on p. 41).

[134] M. Ammann, N. P. Fekete, L. Guzzella, and A. H. Glattfelder. "Model-based control of the VGT and EGR in a turbocharged common-rail diesel engine: Theory and passenger car implementation". In: *SAE Technical Papers* 112 (2003), pp. 527–538. ISSN: 26883627. DOI: 10.4271/2003-01-0357. URL: https://doi.org/10.4271/2003-01-0357. (cit. on pp. 41, 83).

[135] J. Chauvin, A. Albrecht, G. Corde, and N. Petit. "Modeling and control of a Diesel HCCI engine". In: *Proceedings of the Fifth IFAC Symposium on Advances in Automotive Control* (2007), pp. 1–8. DOI: 10.3182/20070820-3-US-2918.00064 (cit. on pp. 41, 83).

[136] O. Flärdh and J. Mårtensson. "Exhaust pressure modeling and control on an si engine with vgt". In: *Control Engineering Practice* 25 (2014), pp. 26–35. ISSN: 0967-0661. DOI: https://doi.org/10.1016/j.conengprac.2013.11.021. URL: https://www.sciencedirect.com/science/article/pii/S0967066113002359 (cit. on p. 41).

[137] P. Dickinson, K. Glover, N. Collings, Y. Yamashita, Y. Yashiro, and T. Hoshi. "Real-time control of a two-stage serial VGT Diesel engine using MPC". In: *IFAC-PapersOnLine* 48.15 (2015), pp. 117–123. ISSN: 2405-8963. DOI: https://doi.org/10.1016/j.ifacol.2015.10.017. URL: https://www.sciencedirect.com/science/article/pii/S2405896315018935 (cit. on p. 41).

[138] J. Galindo, V. Dolz, J. Monsalve-Serrano, M. A. Bernal, and L. Odillard. "Impacts of the exhaust gas recirculation (EGR) combined with the regeneration mode in a compression ignition diesel engine operating at cold conditions". In: *International Journal of Engine Research* 22.12 (2021), pp. 3548–3557. DOI: 10.1177/14680874211013986. URL: https://doi.org/10.1177/14680874211013986 (cit. on pp. 41, 83).

[139] J. R. Serrano, A. Tiseira, L. M. García-Cuevas, L. B. Inhestern, and H. Tartoussi. "Radial turbine performance measurement under extreme off-design conditions". In: *Energy* 125 (2017), pp. 72–84. ISSN: 03605442. DOI: 10.1016/j.energy.2017.02.118. URL: http://www.sciencedirect.com/science/article/pii/S0360544217303018 (cit. on pp. 42, 59, 61).

[140] F. R. Menter. “Two-equation eddy-viscosity turbulence models for engineering applications”. In: *AIAA Journal* 32.8 (1994), pp. 1598–1605. ISSN: 00011452. DOI: `10.2514/3.12149`. URL: `https://doi.org/10.2514/3.12149` (cit. on p. 42).

[141] P. Fajardo. “Methodology for the Numerical Characterization of a Radial Turbine under Steady and Pulsating Flow”. PhD thesis. Universitat Politècnica de València, 2012, p. 222. URL: `riunet.upv.es/bitstream/handle/10251/16878/tesisUPV3883.pdf` (cit. on p. 42).

[142] A. T. Simpson, S. W. T. Spence, and J. K. Watterson. “A Comparison of the Flow Structures and Losses Within Vaned and Vaneless Stators for Radial Turbines”. In: *Journal of Turbomachinery* 131.3 (2009), pp. 1–15. ISSN: 0889-504X. DOI: `10.1115/1.2988493`. URL: `https://doi.org/10.1115/1.2988493` (cit. on p. 42).

[143] J. Galindo, P. Fajardo, R. Navarro, and L. M. García-Cuevas. “Characterization of a radial turbocharger turbine in pulsating flow by means of CFD and its application to engine modeling”. In: *Applied Energy* 103 (2013), pp. 116–127. ISSN: 03062619. DOI: `10.1016/j.apenergy.2012.09.013`. URL: `http://dx.doi.org/10.1016/j.apenergy.2012.09.013` (cit. on p. 42).

[144] Y. Xue, M. Yang, L. Pan, K. Deng, X. Wu, and C. Wang. “Gasdynamic behaviours of a radial turbine with pulsating incoming flow”. In: *Energy* 218 (2021), p. 119523. ISSN: 03605442. DOI: `10.1016/j.energy.2020.119523`. URL: `http://www.sciencedirect.com/science/article/pii/S036054422032630X` (cit. on p. 42).

[145] K. Ananthakrishnan and M. Govardhan. “Influence of fillet shapes on secondary flow field in a transonic axial flow turbine stage”. In: *Aerospace Science and Technology* 82-83 (2018), pp. 425–437. ISSN: 1270-9638. DOI: `https://doi.org/10.1016/j.ast.2018.08.040`. URL: `https://www.sciencedirect.com/science/article/pii/S1270963818307533` (cit. on p. 42).

[146] R. Balasubramanian, S. Barrows, and J. P. Chen. *Investigation of shear-stress transport turbulence model for turbomachinery applications*. January. Reno, Nevada, United States: Amercian Institute of Aeronautics and Astronautics, 2008, pp. 1–18. ISBN: 9781563479373. DOI: `10.2514/6.2008-566`. URL: `https://arc.aiaa.org/doi/abs/10.2514/6.2008-566` (cit. on p. 42).

[147] F. R. Menter. “Review of the shear-stress transport turbulence model experience from an industrial perspective”. In: *International Journal of Computational Fluid Dynamics* 23.4 (2009), pp. 305–316. ISSN: 10618562.

DOI: 10.1080/10618560902773387. URL: https://doi.org/10.1080/10618560902773387 (cit. on p. 42).

[148] P. Ram, T. Kim, and H. D. Kim. "Numerical Study on Shock Train Characteristics in Divergent Channels". In: *Journal of Applied Fluid Mechanics* 13 (2020), pp. 1081–1092. DOI: 10.36884/jafm.13.04.30837. URL: https://doi.org/10.36884/jafm.13.04.30837 (cit. on p. 42).

[149] A. Zheltovodov. "Shock waves/turbulent boundary-layer interactions - Fundamental studies and applications". In: *Fluid Dynamics Conference*. New Orleans, United States: AIAA, 1996, pp. 1–28. DOI: 10.2514/6.1996-1977. URL: https://arc.aiaa.org/doi/abs/10.2514/6.1996-1977 (cit. on p. 42).

[150] J. E. Bardina, P. G. Huang, and T. J. Coakley. *Turbulence modeling validation*. Snowmass Village, Colorado, United States: National Aeronautics and Space Administration, 1997, pp. 1–16. DOI: 10.2514/6.1997-2121. URL: https://arc.aiaa.org/doi/abs/10.2514/6.1997-2121 (cit. on p. 42).

[151] J. Galindo, S. Hoyas, P. Fajardo, and R. Navarro. "Set-Up Analysis and Optimization of CFD Simulations for Radial Turbines". In: *Engineering Applications of Computational Fluid Mechanics* 7.4 (2013), pp. 441–460. DOI: 10.1080/19942060.2013.11015484. URL: https://doi.org/10.1080/19942060.2013.11015484 (cit. on pp. 44, 48).

[152] K. Hazizi, A. Ramezanpour, A. Costall, and M. Asadi. "Numerical analysis of a turbocharger compressor". In: *XII International Conference on Computational Heat, Mass and Momentum Transfer (ICCHMT 2019)*. Vol. 128. E3S Web of Conferences, 2019, pp. 1–8. DOI: 10.1051/e3sconf/201912806012. URL: https://doi.org/10.1051/e3sconf/201912806012 (cit. on p. 44).

[153] P. J. Roache. "Perspective: A Method for Uniform Reporting of Grid Refinement Studies". In: *Journal of Fluids Engineering* 116.3 (1994), pp. 405–413. ISSN: 0098-2202. DOI: 10.1115/1.2910291. URL: https://doi.org/10.1115/1.2910291 (cit. on pp. 46, 164).

[154] J. Harinck, T. Turunen-Saaresti, P. Colonna, S. Rebay, and J. van Buijtenen. "Computational Study of a High-Expansion Ratio Radial Organic Rankine Cycle Turbine Stator". In: *Journal of Engineering for Gas Turbines and Power* 132.5 (2010), pp. 1–6. ISSN: 0742-4795. DOI: 10.1115/1.3204505. URL: https://doi.org/10.1115/1.3204505 (cit. on p. 47).

[155] E. Sauret and Y. Gu. “Three-dimensional off-design numerical analysis of an organic Rankine cycle radial-inflow turbine”. In: *Applied Energy* 135 (2014), pp. 202–211. ISSN: 03062619. DOI: `10.1016/j.apenergy.2014.08.076`. URL: `https://www.sciencedirect.com/science/article/pii/S0306261914008873` (cit. on p. 47).

[156] S. Li, S. Wang, Z. Ma, and T. Zhang. “An air cycle heat pump heating system using a turbocharger for full electric vehicle”. In: *Procedia Engineering* 205 (2017), pp. 1405–1411. ISSN: 1877-7058. DOI: `https://doi.org/10.1016/j.proeng.2017.10.316`. URL: `https://www.sciencedirect.com/science/article/pii/S1877705817349810` (cit. on p. 47).

[157] S. Li, S. Wang, Z. Ma, S. Jiang, and T. Zhang. “Using an air cycle heat pump system with a turbocharger to supply heating for full electric vehicles”. In: *International Journal of Refrigeration* 77 (2017), pp. 11–19. ISSN: 0140-7007. DOI: `https://doi.org/10.1016/j.ijrefrig.2017.03.004`. URL: `https://www.sciencedirect.com/science/article/pii/S0140700717300993` (cit. on p. 47).

[158] I. Pérez-Grande and T. J. Leo. “Optimization of a commercial aircraft environmental control system”. In: *Applied Thermal Engineering* 22.17 (2002), pp. 1885–1904. ISSN: 1359-4311. DOI: `https://doi.org/10.1016/S1359-4311(02)00130-8`. URL: `https://www.sciencedirect.com/science/article/pii/S1359431102001308` (cit. on p. 47).

CHAPTER 4

Performance Characteristics

Contents

4.1 Introduction 59
4.2 Performance Characteristics 59
4.3 Summary 70
4.4 References 71

Figures

4.1 Considered planes for the performance characteristics analysis. . . . 59
4.2 Turbine map based on steady and unsteady results; experimental 3882 rpm/$\sqrt{\mathrm{K}}$: black; experimental 5830 rpm/$\sqrt{\mathrm{K}}$: dark gray; experimental up to 7456 rpm/$\sqrt{\mathrm{K}}$: light gray; simulated: colored. 62
4.3 Reduced mass flow based on the mean total temperature and total pressure close to the rotor TE. 65
4.4 Relative Mach number with opened VGT position and operating point of choked passage flow at the rotor TE plane; red line: $Ma_{rel.} = 1$. . . . 66
4.5 Total pressure ratio and total temperature difference of the inlet properties and relative numbers at rotor TE plane. 68

Tables

4.1 Evaluated pressure ratio URANS simulations. 60
4.2 Deviation experimental and RANS simulations. 63
4.3 Deviation RANS and URANS simulations. 63

4.1 Introduction

This chapter presents the characteristics of the turbine map before analyzing the internal flow field. The performance characteristics was evaluated using RANS simulations and some specific points using URANS to assess the importance of the rotor movement. The reduced mass flow, the total-to-static efficiency of the turbine and the stator efficiency are evaluated for different pressure ratios and at three rotational speeds. Furthermore, the differences between RANS and URANS simulations are presented and the trend of the results are validated using previous experimental test by Serrano et al. [139].

4.2 Performance Characteristics

To deepen the understanding of the choked flow first the trend and characteristics of the turbine map are analyzed. The turbine map was obtained from the steady flow results, moreover, based on these results two operating points of each speed line were chosen to demonstrate the flow pattern just during the development of passage choking and with fully choked characteristics. These points were simulated in URANS simulations. Thus, global performance parameter were evaluated with both steady and unsteady state simulations to assess the importance of unsteady effects caused by blade row interaction on the performance characteristics. Here, the transient simulation results have been time-averaged over one rotor rotation. The plane in the rotor trailing edge (TE) depicted in Figure 4.1(a) has been used to process particular fluid numbers for this analysis. The reduced mass flow and the isentropic efficiency total to static considered for this study are defined in Equation 4.1 and Equation 4.2, respectively, where the term $\pi_{turb.}$ is the total to static pressure ratio (PR) between the inlet probe section and the outlet probe section depicted in Figure 3.2. In these sections, the pressure was evaluated by using mass flow averaging.

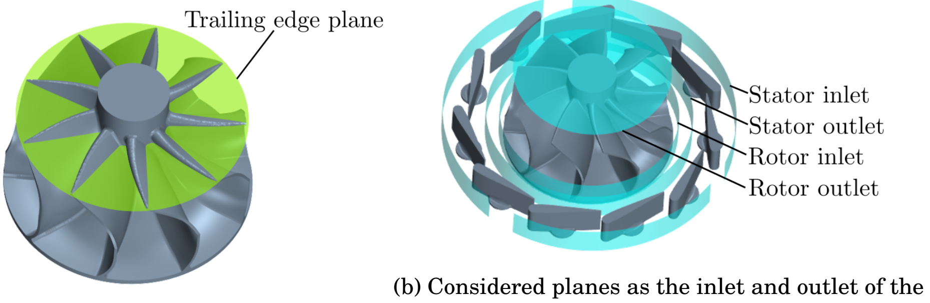

(a) Considered plane at rotor TE.

(b) Considered planes as the inlet and outlet of the stator and rotor.

Figure 4.1: Considered planes for the performance characteristics analysis.

$$\dot{m}_{red.,in} = \frac{\dot{m} \cdot \sqrt{T_{tot,in}}}{p_{tot,in}} \tag{4.1}$$

$$\eta_{tot,stat} = \frac{T_{tot,in} - T_{tot,out}}{T_{tot,in} \cdot \left[1 - \left(\frac{1}{\pi_{turb.}}\right)^{\frac{\gamma-1}{\gamma}}\right]} \tag{4.2}$$

The results of the total to static PR ($\pi_{turb.}$) for the unsteady simulations are listed in the Table 4.1 together with the designation as lower or higher, that from here will be considered. Furthermore, in the same table, the total to total PR in the stator ($\pi_{stator\,tot,tot}$) calculated between the inlet probe section and the stator outlet plane (see Figure 4.1(b)) is presented, as well as the stator efficiency defined according to the Equation 4.3 and Equation 4.4, where $\pi_{stator\,tot,stat}$ is the total to static PR in the stator. As can be seen, the PR in the stator does not change significantly when the pressure at the inlet of the turbine or the rotational speed increases, due to the fact that the function of the vanes is to direct the flow toward the rotor where the main expansion take place as well as increase the velocity of the flow when the vanes are closed.

Table 4.1: Evaluated pressure ratio URANS simulations.

VGT [%]	$N_{red.}$ $\left[\frac{\text{rpm}}{\sqrt{\text{K}}}\right]$	$\pi_{turb.}$ [-]		$\pi_{stator\,tot,tot}$ [-]	η_{stator} [-]
10	3882	lower	2.95	1.21	0.69
		higher	5.16	1.34	0.83
	8421	lower	2.64	1.12	0.73
		higher	4.48	1.22	0.71
30	3882	lower	2.91	1.10	0.82
		higher	4.70	1.12	0.82
	8421	lower	2.57	1.06	0.82
		higher	4.93	1.10	0.82
80	3882	lower	2.55	1.06	0.87
		higher	3.53	1.05	0.88
	5830	lower	2.69	1.05	0.87
		higher	3.82	1.05	0.89
	8421	lower	2.75	1.05	0.86
		higher	4.17	1.05	0.86

$$\eta_{stator} = \left(\frac{u_{stator\,out}}{u_{stator\,isen,out}}\right)^2 \tag{4.3}$$

$$u_{stator\,isen,out} = \begin{cases} \text{If } \frac{1}{\pi_{stator\,tot,stat}} > \left(\frac{2}{\gamma+1}\right)^{\frac{\gamma}{\gamma-1}} \\ \sqrt{2 \cdot c_p \cdot T_{stator\,tot,in} \cdot \left[1 - \left(\frac{1}{\pi_{stator\,tot,stat}}\right)^{\frac{\gamma-1}{\gamma}}\right]} \\ \text{If } \frac{1}{\pi_{stator\,tot,stat}} \leq \left(\frac{2}{\gamma+1}\right)^{\frac{\gamma}{\gamma-1}} \\ \sqrt{2 \cdot c_p \cdot T_{stator\,tot,in} \cdot \left(\frac{\gamma-1}{\gamma+1}\right)} \end{cases} \tag{4.4}$$

$$BSR = \frac{N_{red} \cdot \pi \cdot D_{in}}{60 \cdot \sqrt{2 \cdot c_{p,turb.} \cdot \left[1 - \left(\frac{1}{\pi_{turb.}}\right)^{\frac{\gamma-1}{\gamma}}\right]}} \tag{4.5}$$

In Figure 4.2, the reduced mass flow and the total-to-static efficiency of all simulated operating points in steady and unsteady simulations are depicted. Here, also the experimental results of previously performed standardized experiments of the same turbocharger turbine at various rotor speeds are shown [139]. These data were obtained in the typical measurement range of automotive turbocharger turbines, which does not cover such high PRs as they were observed in this study. However, the results can be used to obtain a qualitative validation of the simulation results. While the experimental results of 3882 rpm/$\sqrt{\text{K}}$ and 5830 rpm/$\sqrt{\text{K}}$ can directly be compared, the results of higher speeds up to 7456 rpm/$\sqrt{\text{K}}$ are shown to allow an estimation of trends towards higher speeds. The trends and magnitudes of simulated reduced mass flows and efficiencies at lower PR can be confirmed by those data for the selected VGT positions. Additionally, simulated and experimental efficiencies are comparable with the demonstration against the blade speed ratio (BSR) defined in Equation 4.5. Here, it can be seen that the simulated efficiencies match well the experimental measurement trends. This way, e.g. the higher simulated speed at opened VGT position matches well the experimental data at higher BSRs.

According to the observations made by Serrano et al. [159] an overlapping of speed lines in the BSR plots can be expected towards higher BSR when the stator vanes are opened, while at closed VGTs the speed lines of isentropic efficiency total to static are wider spread. Serrano et al. [61] noted this last trend in a previous study. Future measurement results will extend the map to supply further experimental validation at high PR. Meanwhile, as depicted in Table 4.2, some closer experimental data to the RANS simulations have been selected to validate the simulations, showing a difference of less than 2%. The URANS simulations for turbomachinery better describe the flow behavior according to Galindo et al. [8]. In line with the common literature, the reduced mass flow starts to stagnate as soon as full choking is achieved in the turbine, as it can be found in different publications showing measurements at opened and closed VGT positions [64, 160, 161].

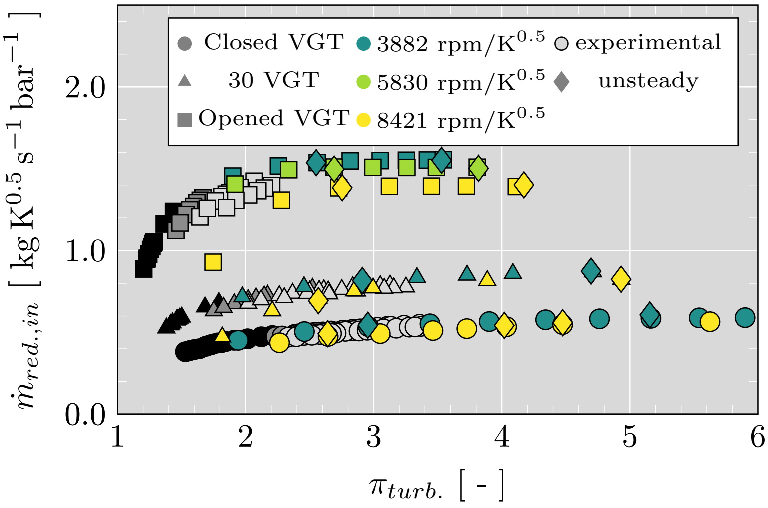

(a) Reduced mass flow map.

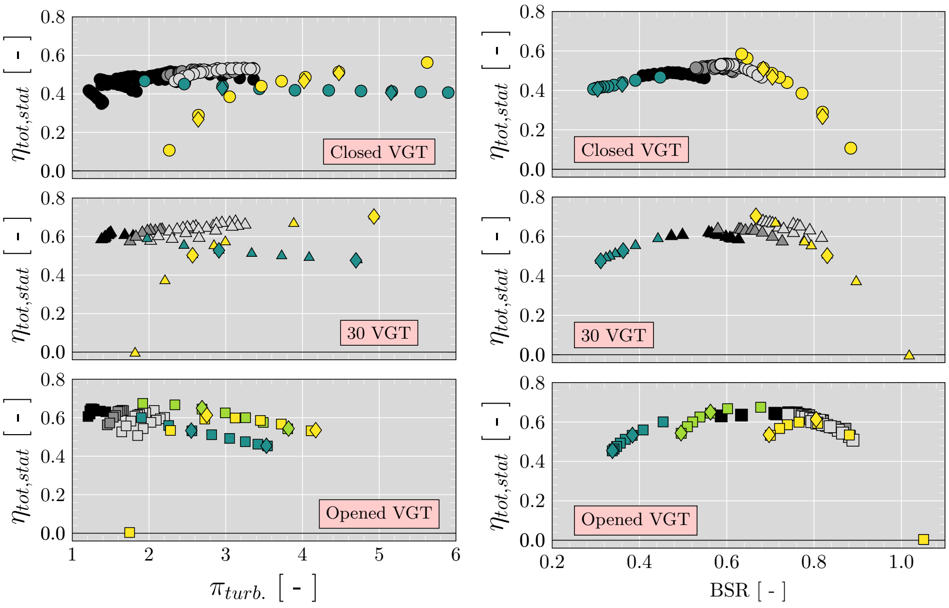

(b) Efficiency vs. pressure ratio map.   (c) Efficiency vs. blade-speed-ratio (BSR) map.

Figure 4.2: Turbine map based on steady and unsteady results; experimental 3882 rpm/$\sqrt{\text{K}}$: black; experimental 5830 rpm/$\sqrt{\text{K}}$: dark gray; experimental up to 7456 rpm/$\sqrt{\text{K}}$: light gray; simulated: colored.

Table 4.2: Deviation experimental and RANS simulations.

VGT [%]		Experimental	RANS	Dev. $\left[\frac{\text{Exper.}-\text{RANS}}{\text{Exper.}}\%\right]$
10	$N_{red.}$ $\left[\frac{\text{rpm}}{\sqrt{\text{K}}}\right]$	3862	3882	-0.51
	$\pi_{turb.}$ [-]	1.91	1.94	-1.71
	$\dot{m}_{red.}$ $\left[\frac{\text{kg}}{\text{s}}\frac{\sqrt{\text{K}}}{\text{bar}}\right]$	0.451	0.452	0.06
	BSR [-]	0.450	0.447	0.66
30	$N_{red.}$ $\left[\frac{\text{rpm}}{\sqrt{\text{K}}}\right]$	8411	8421	-0.13
	$\pi_{turb.}$ [-]	2.87	2.84	0.77
	$\dot{m}_{red.}$ $\left[\frac{\text{kg}}{\text{s}}\frac{\sqrt{\text{K}}}{\text{bar}}\right]$	0.752	0.753	-0.11
	BSR [-]	0.790	0.793	-0.44
80	$N_{red.}$ $\left[\frac{\text{rpm}}{\sqrt{\text{K}}}\right]$	5783	5830	-0.81
	$\pi_{turb.}$ [-]	1.91	1.92	-0.34
	$\dot{m}_{red.}$ $\left[\frac{\text{kg}}{\text{s}}\frac{\sqrt{\text{K}}}{\text{bar}}\right]$	1.425	1.405	1.39
	BSR [-]	0.673	0.677	-0.57

Table 4.3: Deviation RANS and URANS simulations.

VGT	$N_{red.}$ (label)	$\pi_{turb.}$	Dev. $\dot{m}_{red.}$	$\Delta\eta_{tot,stat}$
[%]	$\left[\frac{\text{rpm}}{\sqrt{\text{K}}}\right]$	[-]	$\left[\frac{\text{RANS}-\text{URANS}}{\text{RANS}}\%\right]$	[% points]
10	3882 (lower)	lower	-1.63	0.91
		higher	-3.52	0.63
	8421 (higher)	lower	-3.42	2.21
		higher	-2.02	0.52
30	3882 (lower)	lower	-0.08	0.08
		higher	-0.54	0.28
	8421 (higher)	lower	2.26	0.31
		higher	-0.10	0.29
80	3882 (lower)	lower	0.06	-0.11
		higher	0.24	-0.10
	5830 (middle)	lower	0.85	-0.51
		higher	0.47	-0.13
	8421 (higher)	lower	-0.01	-2.00
		higher	-0.71	-0.31

As it can be seen in Table 4.3, the differences in the reduced mass flow between the steady and unsteady conditions are small, being less than 1% for each reduced speed at opened vane position. At 30% VGT a similar trend occurs except for the case at higher speed and lower PR. At closed vane position the differences are higher and the maximum difference is presented in the operating point at lower speed and higher PR with a value of -3.52%. With regards to the efficiency as shows Figure 4.2-(b), the maximum change take place at higher speed and lower PR, with -2.00% points at opened vane position and 2.21% points at closed position. For the rest of the unsteady points of each vanes position the deviations from the steady cases are less than 1% points. Thus, the reproduced trends and overall rather low deviations permit evaluating the trends of the turbine map through steady simulations with a rotating reference frame to simulate rotor movement. For a further evaluation, the rotor has been rotated by 20 deg, which corresponds to the highest possible deviation of the rotor geometry with 9 blades. Results show less than 0.01% points of deviation in the efficiency and around 0.1% deviation in the simulated mass flow. Both values can be considered as negligible variations, which demonstrate low impact of the simulated rotor position in RANS simulations.

The mass flow map with closed vane position shown in Figure 4.2-(a) indicates that the flow under the conditions of the higher iso-speed reaches the choking condition at higher PR than the lower speed. At a PR of 5.6 the operating point joins the speed line of the lower speed, which shows stagnated reduced mass flow after reaching a PR of around 5. At 30% VGT the iso-speeds are very close when reaching choking conditions but with a slight separation. On the other hand, the speed lines of the opened VGT presents separately choked lines, as it typically can be found for opened VGT positions. However, the middle speed is located very close to the lower simulated speed when the flow is choked. Regarding to the effects on the efficiency, the development of the choked flow is mainly related with the PR. Thus, when the PR is increased at closed VGT and lower rotational speed the efficiency starts to decrease until certain point after which remains constant as is depicted in Figure 4.2-(b). On the contrary at higher speed the efficiency increases as the PR increases. Nevertheless, in both cases the reduced mass flow stagnates at a PR less than the PR at which the efficiency starts to keep constant. At 30% VGT the efficiency presents a similar behavior as the closed position when the PR variate at a constant rotational speed. At opened VGT the efficiency reaches a maximum peak for each rotational speed, then as the PR continues increasing, the efficiency drops.

In one-dimensional modeling the rotor is typically modeled as a nozzle, where the throat is located directly in the rotor outlet. In this case, choking is reached when a relative Mach number of one is obtained in the rotor outlet. Consequently, the reduced mass flow, based on the numbers obtained in the corresponding rotor TE plane, is maintained at the same value for all reduced speeds. Taking advantage of following presented results, it can be said that for the opened VGT position only the rotor passage becomes choked. To analyze the phenomenon in more detail, the reduced mass flow in Equation 4.6 based on total numbers extracted close to the rotor TE is depicted in Figure 4.3. Here, the flow did not experience high shock losses in the main passage yet.

$$\dot{m}_{red.,TE} = \frac{\dot{m} \cdot \sqrt{T_{tot,TE}}}{p_{tot,TE}} \tag{4.6}$$

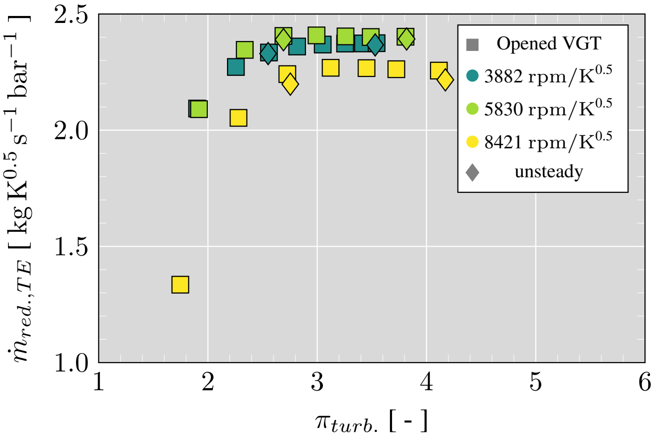

Figure 4.3: Reduced mass flow based on the mean total temperature and total pressure close to the rotor TE.

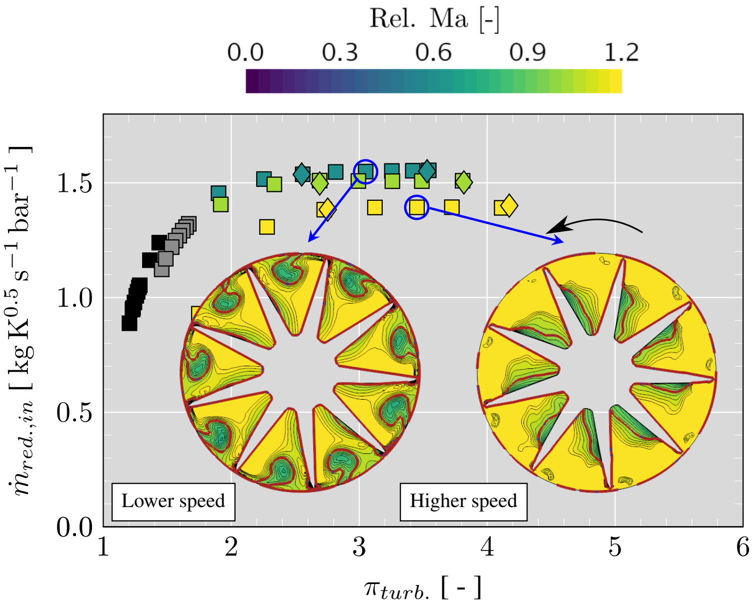

Figure 4.4: Relative Mach number with opened VGT position and operating point of choked passage flow at the rotor TE plane; red line: $Ma_{rel.} = 1$.

Here, $\dot{m}_{red.,TE}$ appears not to stagnate in the same order as in the previously analyzed map of the overall reduced mass flow. The middle speed converges to a higher value than the others, although it is close to the value of the lower speed. According to traditional one-dimensional modeling, a choking at the same reduced mass flow in the relative frame would be expected close to the rotor outlet. However, the radial turbine owns a highly three dimensional "non-ideal" geometry with tip leakage flow, as it can be seen in Figure 4.4 for the TE plane, which has been depicted in Figure 4.1(a). The shown operating points are the first points after stagnation in the $\dot{m}_{red.,TE}$ map. It is visible that the majority of the passage is choked. However, the tip leakage vortex causes locally subsonic flow, which avoids complete rotor choking close to the rotor TE. Over the choked area a relative Mach number above one can be identified, since the flow becomes further accelerated after the non-idealized turbine rotor throat. At higher speed, the sub-sonic regions at the hub close to the PS result from the location of the TE plane. At these low spans the rotor trailing edge is further downstream of the demonstrated plane. However, the flow further accelerates along the PS and becomes fully choked although it is not visible in this representation. This will be further illustrated in analysis of the three-dimensional flow in Chapter 7. The average relative Mach number in the TE plane achieves with 1.13 a 7% lower value for the lower speed than the one at higher speed with a relative Mach number of 1.22.

According to Equation 4.7 the reduced mass flow decreases for increasing Mach numbers above 1.

$$\dot{m}_{red.} = A \cdot \sqrt{\frac{\gamma}{R}} \cdot Ma \cdot \left(1 + \frac{\gamma - 1}{2} \cdot Ma^2\right)^{-\frac{\gamma+1}{2(\gamma-1)}} \tag{4.7}$$

Hence, the reduced mass flow extracted close to the TE is higher when the passage flow is choked but the tip leakage flow generates zones of lower Mach numbers, reducing the mass flow averaged Mach number in this section. To estimate the impact on the overall reduced mass flow, as defined in Equation 4.1, some simplifications can be made. Assuming that the main part of the work is extracted until the TE plane, the turbine inlet total temperature can be reformulated in dependence of the total temperature in the plane at the TE, the efficiency and the turbine PR:

$$T_{tot,in} = \frac{T_{tot,TE}}{1 - \eta_{tot,stat} \cdot \left[1 - \left(\frac{1}{\pi_{turb.}}\right)^{\frac{\gamma-1}{\gamma}}\right]}. \tag{4.8}$$

To achieve a dependency of the total temperature in the relative reference frame, the Equation 4.8 can be reformulated to:

$$T_{tot,in} = \frac{T_{tot,rel.,TE} \cdot \frac{1+\frac{\gamma-1}{2} \cdot Ma_{TE}^2}{1+\frac{\gamma-1}{2} \cdot Ma_{rel.,TE}^2}}{1 - \eta_{tot,stat} \cdot \left[1 - \left(\frac{1}{\pi_{turb.}}\right)^{\frac{\gamma-1}{\gamma}}\right]}. \tag{4.9}$$

The relation between total pressure just before the development of shocks and total inlet pressure can be drawn:

$$p_{tot,in} = p_{tot,rel.,TE} \cdot \pi_{tot,rel.,TE}. \tag{4.10}$$

Indeed, when the pressure is measured further downstream this PR will additionally depend on the area ratio and swirl, related to the rotational speed of the turbine and shock losses. Substituting Equation 4.9 and Equation 4.10 in the turbine map value of the reduced mass flow according to Equation 4.1, the following relation is derived:

$$\dot{m}_{red.,in} = \frac{\frac{\dot{m} \cdot \sqrt{T_{tot,rel,TE}}}{p_{tot,rel.,TE}} \cdot \sqrt{\frac{1+\frac{\gamma-1}{2} \cdot Ma_{TE}^2}{1+\frac{\gamma-1}{2} \cdot Ma_{rel.,TE}^2}}}{\pi_{tot,rel.,TE} \cdot \sqrt{1 - \eta_{tot,stat} \cdot \left[1 - \left(\frac{1}{\pi_{turb.}}\right)^{\frac{\gamma-1}{\gamma}}\right]}}. \tag{4.11}$$

The first factor in the numerator can be recognized as the reduced mass flow calculated based on the conditions at the rotor TE. This highlights, the direct impact on the distribution of speed lines in the global reduced mass flow map. The second factor in the numerator takes the relative Mach number into account. This way the effect of the tip leakage flow strengthens the relative distance between the speed lines, when they are translated to the traditional map value. In the denominator $\pi_{tot,rel.,TE}$ can be found.

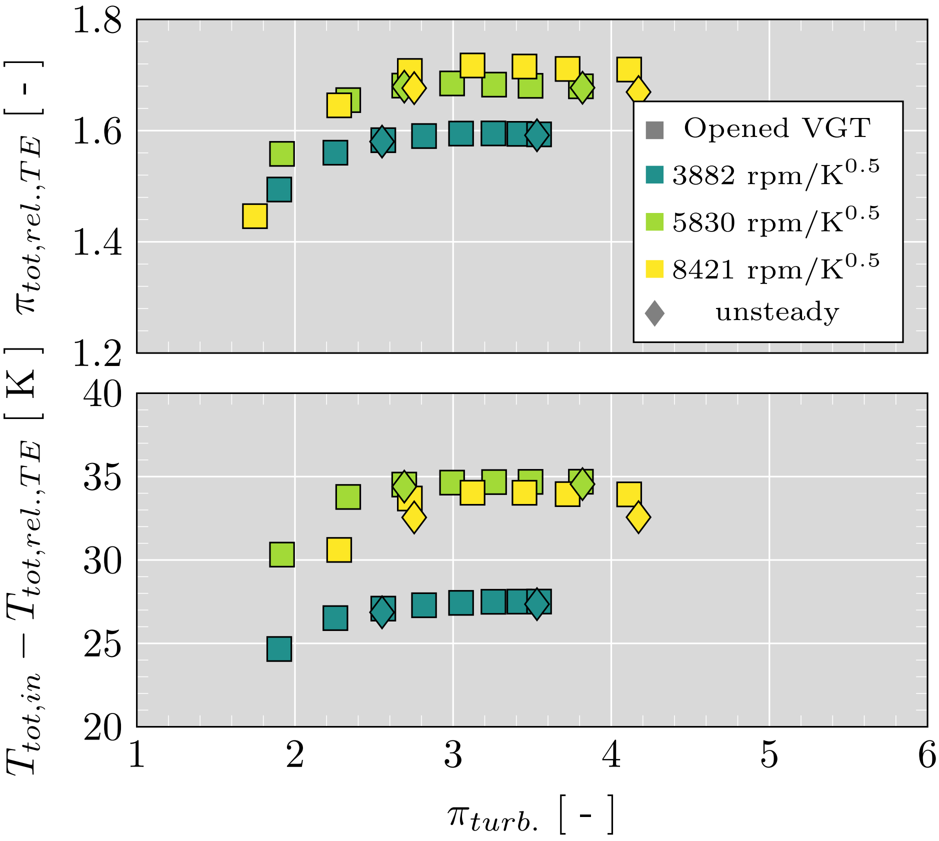

Figure 4.5: Total pressure ratio and total temperature difference of the inlet properties and relative numbers at rotor TE plane.

In Figure 4.5 it can be seen how the total PR $\pi_{tot,rel.,TE}$ starts to stagnate and to maintain its value at a turbine PR $\pi_{turb.}$ around 3. Here, the PR of the higher speed archives bigger values. This might cause a natural spreading of the speed lines even when no significant change of the tip leakage flow pattern can be identified. The final map value then further depends on the turbine PR and the turbine efficiency. At lower speed, the total temperature delta $T_{tot,in} - T_{tot,rel.,TE}$ stagnates at a slightly lower turbine PR, than the reduced mass flow at the rotor TE in the rotational frame. This could confirm the observation of a mostly choked passage flow. The possible variation of tip leakage flow towards higher pressure ratios has rather small impact on the extraction of specific enthalpy in the rotor passage [162, 120, 112], although it significantly contributes to pressure losses and thus, efficiency penalties. Further, it is worth highlighting that the total temperature difference $T_{tot,in} - T_{tot,rel.,TE}$ is the highest when the reduced speed is intermediate. It can be concluded that the tip leakage vortex omits the complete choking of the rotor passage outlet, which results in the increase of local and overall reduced mass flow at lower speeds, where a stronger tip leakage vortex can be observed. Biggest parts of the passage are aerodynamically choked, so that the relative values of the PR and total temperature delta up to the rotor TE remain constant. Further, when heat transfer is considered, the adiabatic efficiency in Equation 4.11 can be substituted with the non-adiabatic efficiency, highlighting the impact of heat transfer on the choking limitation. This dependency may be further analyzed in the future experimental campaign with a comparison of quasi-adiabatic and hot measurements.

4.3 Summary

The performance parameters have been obtained with the CFD simulations to analyze the development of the choked flow in the radial turbine. The rotational speeds of 3882 rpm/$\sqrt{\mathrm{K}}$, 5830 rpm/$\sqrt{\mathrm{K}}$ and 8421 rpm/$\sqrt{\mathrm{K}}$ under different PR until reaching a stagnated reduced mass flow trends have been evaluated using RANS simulations. The simulated operational points' trend has been validated with previous experimental measurements under a typical automotive turbocharger operational range. Based on the steady results, two operational points of each iso-speed have been chosen to analyze the flow during the development and the reach of the choking conditions and simulated using URANS. These points are considered as lower and higher PR.

Comparing the results of RANS and URANS simulations, the variation in the reduced mass flow at opened and 30% VGT are small in most of the cases. However, at closed VGT the differences can reach up to around 3%. Regarding efficiency, the deviation is less than 1% points except for the operational points at higher speed, and lower PR for both opened and closed positions. Thus, the turbine map can be evaluated by means of RANS simulations.

The turbine map depicts that flow at lower speed reaches the choking conditions at lower PR than at higher speed. At closed position, the iso-speed lines join in the same reduced mass flow after reaching choking conditions. Nevertheless, as the opening of the vanes increases, the iso-speed lines present separately choked lines. Furthermore, the reduced mass flow stagnates at a PR less than the PR at which the efficiency keeps constant.

In one-dimensional models, the rotor is typically modeled as a nozzle, and the choking is expected to be close to the rotor outlet. Nevertheless, the radial turbine has a complex three-dimensional geometry with tip leakages and other flow structures that limit the complete rotor choking close to the TE. A relation was derived from correlating the TE's flow conditions with the overall reduced mass flow. The terms in this expression take into account the direct impact on the speed lines distribution, which means the relative distance between them, the relative Mach number, the turbine PR, and turbine efficiency. One factor limiting the complete development of choked flow in the rotor outlet is the tip leakage vortex, which increases the local and overall reduced mass flow at lower speeds. As the major part of the passage is choked, the relative values of the PR and the total temperature delta up to the rotor TE remain constant.

4.4 References

[8] J. Galindo, J. R. Serrano, L. M. García-Cuevas, and N. Medina. "Twin-entry turbine losses: An analysis using CFD data". In: *International Journal of Engine Research* (2021), pp. 1–21. DOI: `10.1177/14680874211007647`. URL: `https://doi.org/10.1177/14680874211007647` (cit. on pp. 61, 197, 198).

[61] J. R. Serrano, F. J. Arnau, L. M. García-Cuevas, and A. Dombrovsky. "Development and validation of a radial turbine efficiency and mass flow model at design and off-design conditions". In: *Energy Conversion and Management* 128 (2016), pp. 281–293. DOI: `10.1016/j.enconman.2016.09.032`. URL: `https://doi.org/10.1016/j.enconman.2016.09.032` (cit. on pp. 13, 61).

[64] M. Tancrez, J. Galindo, C. Guardiola, P. Fajardo, and O. Varnier. "Turbine adapted maps for turbocharger engine matching". In: *Experimental Thermal and Fluid Science* 35.1 (2011), pp. 146–153. ISSN: 08941777. DOI: `10.1016/j.expthermflusci.2010.07.018`. URL: `http://dx.doi.org/10.1016/j.expthermflusci.2010.07.018` (cit. on pp. 13, 62).

[112] J. R. Serrano, R. Navarro, L. M. García-Cuevas, and L. B. Inhestern. "Contribution to tip leakage loss modeling in radial turbines based on 3D flow analysis and 1D characterization". In: *International Journal of Heat and Fluid Flow* 78 (2019), pp. 1–7. ISSN: 0955-5986. DOI: `10.1016/j.ijheatfluidflow.2019.108423`. URL: `http://www.sciencedirect.com/science/article/pii/S095559861530042X` (cit. on pp. 18, 39, 69, 111, 132, 136).

[120] J. R. Serrano, R. Navarro, L. M. García-Cuevas, and L. B. Inhestern. "Turbocharger turbine rotor tip leakage loss and mass flow model valid up to extreme off-design conditions with high blade to jet speed ratio". In: *Energy* 147 (2018), pp. 1299–1310. ISSN: 0360-5442. DOI: `https://doi.org/10.1016/j.energy.2018.01.083`. URL: `https://www.sciencedirect.com/science/article/pii/S0360544218301014` (cit. on pp. 18, 39, 69, 104, 128, 131, 132).

[139] J. R. Serrano, A. Tiseira, L. M. García-Cuevas, L. B. Inhestern, and H. Tartoussi. "Radial turbine performance measurement under extreme off-design conditions". In: *Energy* 125 (2017), pp. 72–84. ISSN: 03605442. DOI: `10.1016/j.energy.2017.02.118`. URL: `http://www.sciencedirect.com/science/article/pii/S0360544217303018` (cit. on pp. 42, 59, 61).

[159] J. R. Serrano, F. J. Arnau, L. M. García-Cuevas, and L. B. Inhestern. "An innovative losses model for efficiency map fitting of vaneless and variable vaned radial turbines extrapolating towards extreme off-design conditions". In: *Energy* 180 (2019), pp. 626–639. ISSN: 03605442. DOI: `10.1016/j.energy.2019.05.062`. URL: `http://www.sciencedirect.com/science/article/pii/S0360544219309314` (cit. on pp. 61, 202).

[160] Z. Filipi, Y. Wang, and D. Assanis. "Effect of variable geometry turbine (VGT) on diesel engine and vehicle system transient response". In: *SAE 2001 World Congress*. 724. Detroit, Michigan, United States: SAE International, 2001, pp. 1–21. DOI: `10.4271/2001-01-1247`. URL: `https://doi.org/10.4271/2001-01-1247` (cit. on p. 62).

[161] C. Rogo, T. Hájek, and A. G. Chen. *Variable stator radial turbine*. Cleveland, Ohio, United States: NASA United States, 1984, pp. 1–312. DOI: `9840014500`. URL: `https://ntrs.nasa.gov/search.jsp?R=19840014500` (cit. on p. 62).

[162] M. I. Yaras and S. A. Sjolander. "Prediction of Tip-Leakage Losses in Axial Turbines". In: *Journal of Turbomachinery* 114.1 (1992), pp. 204–210. ISSN: 0889-504X. DOI: `10.1115/1.2927987`. URL: `https://doi.org/10.1115/1.2927987` (cit. on p. 69).

CHAPTER 5

Stator Flow Characteristics

Contents

5.1 Introduction 74
5.2 Numerical Results 74
5.3 Summary 79
5.4 References 80

Figures

5.1 Considered planes for the stator flow analysis. 74
5.2 Mach number of URANS simulations at a radial plane and at a plane parallel to the stator SS (see Figure 5.1(b)) with closed VGT position; red line: $Ma = 1$. 75
5.3 Mach number and stator vane pressure profile snapshots of URANS simulations at 50% span of the stator passage with closed VGT position; red line: $Ma = 1$. 76
5.4 Mach number and stator vane pressure profile snapshots for two operating points of URANS simulations with the same reduced mass flow, closed VGT position and at 50% span of the stator passage; left: lower speed; right: higher speed; red line: $Ma = 1$. 77

5.1 Introduction

The region of the turbine where the choked flow takes place relies on the position of the stator vanes. Thus, this chapter presents the analysis of the development of the choked flow in the stator when the vanes are closed. The Mach number profile is evaluated along different planes and the pressure profile on the vanes when the turbine operates at lower and higher speeds with lower and higher PR.

5.2 Numerical Results

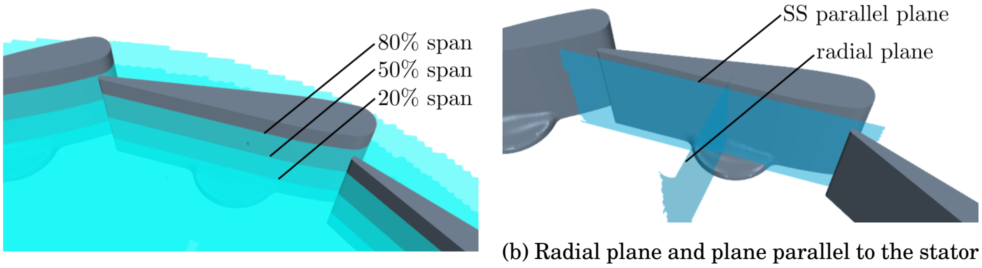

(a) Iso-span planes in the stator.

(b) Radial plane and plane parallel to the stator SS.

Figure 5.1: Considered planes for the stator flow analysis.

Depending on the stator vane position the choking occurs in the region of the stator or rotor. For the closed VGT position, the shock only appears in the stator according to the results of each one of the evaluated planes at 20, 50, and 80% span, along with a radial and parallel plane to the stator as depicted Figure 5.1. It was found that the area of the supersonic regions in these planes change slightly for each span despite of having a straight blade, the main reason for this result is the interaction of the primary flow with the stator blade tip leakages and the geometry of the stator's penny (also referred to as "button", it is the cylindrical platform feature of each variable stator vane) as can be seen in the Figure 5.2 with the velocity vectors in these regions. The presence of the penny generates vortexes, increasing the losses [163, 164]. However, it should be taking into account that the secondary losses appear to decrease with increasing Mach numbers [165]. Nevertheless, the more relevant changes that are the aim of this study only occur when the PR or the rotational speed varies. Hence, snapshots of the unsteady results are shown only at 50% span. Figure 5.3 depicts how the flow in the vaneless space (the region between the stator SS and the rotor inlet) becomes choked with increasing PR for the two selected speed lines. At a higher reduced speed of 8421 rpm/$\sqrt{\mathrm{K}}$ with higher

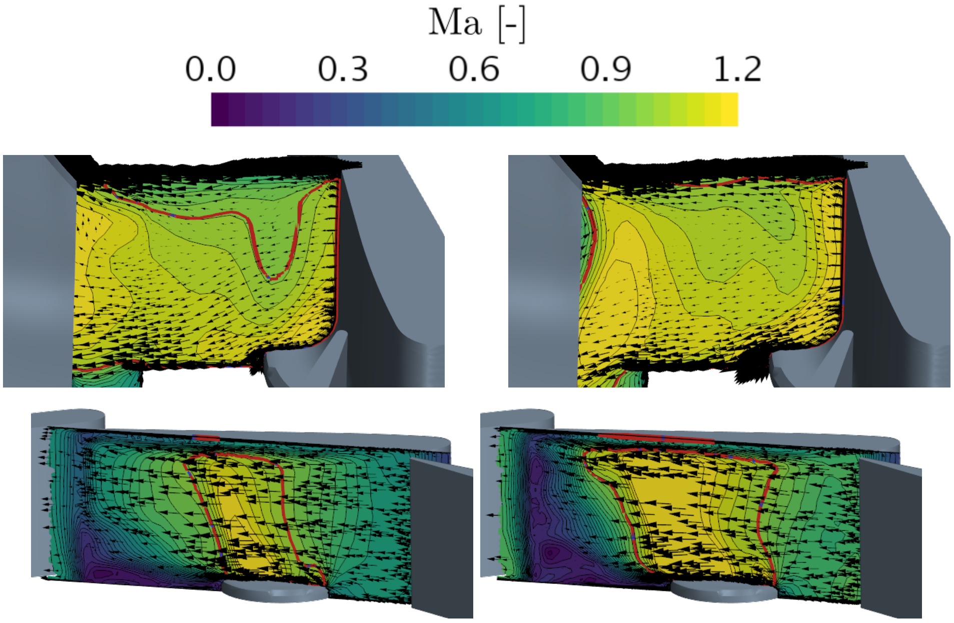

(a) Higher speed at higher PR.

(b) Lower speed at higher PR.

Figure 5.2: Mach number of URANS simulations at a radial plane and at a plane parallel to the stator SS (see Figure 5.1(b)) with closed VGT position; red line: $Ma = 1$.

PR, a supersonic pocket is developed at around 0.62 normalized chord length on the SS of the stator blade. The supersonic pocket expands up to close to the rotor inlet. There, another supersonic acceleration takes place, which connects the pockets of two neighboring stator blades. At this closed VGT position, the distance from blade curvature on the SS to the rotor inlet first shrinks and then augments again. This generates a throat were supersonic flow develops. From this throat the flow decelerates more due to the increase of positive radial velocity. In the pressure profiles, a sudden rise identifies a shock generating a sudden flow deceleration, as well as entropy and loss generation [166]. In comparison, the completely unchoked solution at lower PR owns a rather smooth pressure profile. The simulated operating points at lower reduced speed of 3882 rpm/$\sqrt{\mathrm{K}}$ represent points which are closer to choke and fully choked. Here, the appearance of the supersonic pocket can be observed at the results of lower PR. The supersonic area flow does not expand up to the rotor inlet yet and seems to be discontinuous on one stator vane, while the neighboring pocket is already reaching the rotor inlet and seems to interact with the rotor blade.

To analyze the unbiased impact of the rotational speed, two simulations

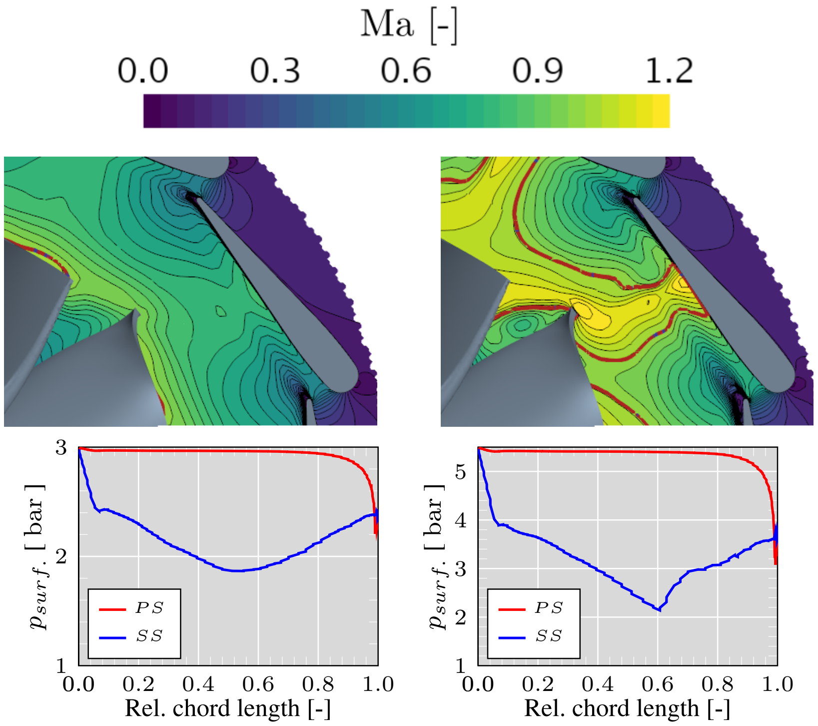

(a) Higher speed at lower PR.

(b) Higher speed at higher PR.

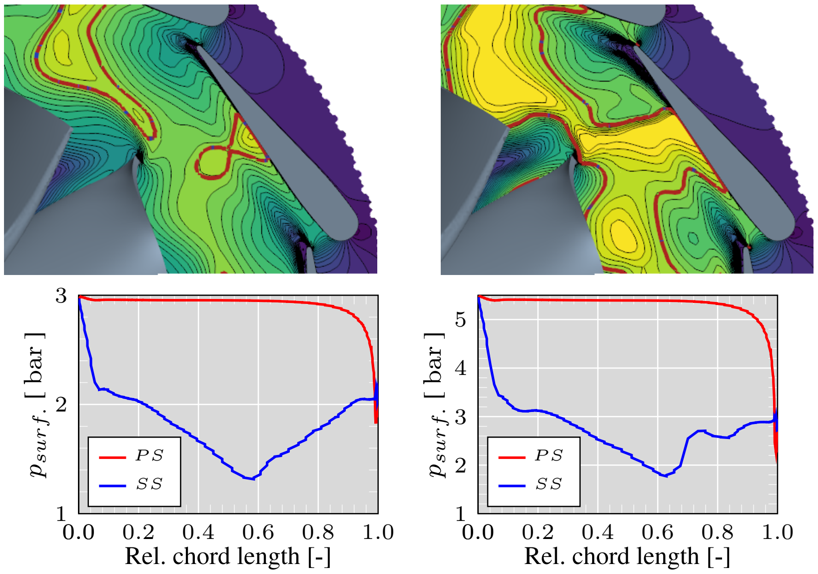

(c) Lower speed at lower PR.

(d) Lower speed at higher PR.

Figure 5.3: Mach number and stator vane pressure profile snapshots of URANS simulations at 50% span of the stator passage with closed VGT position; red line: $Ma = 1$.

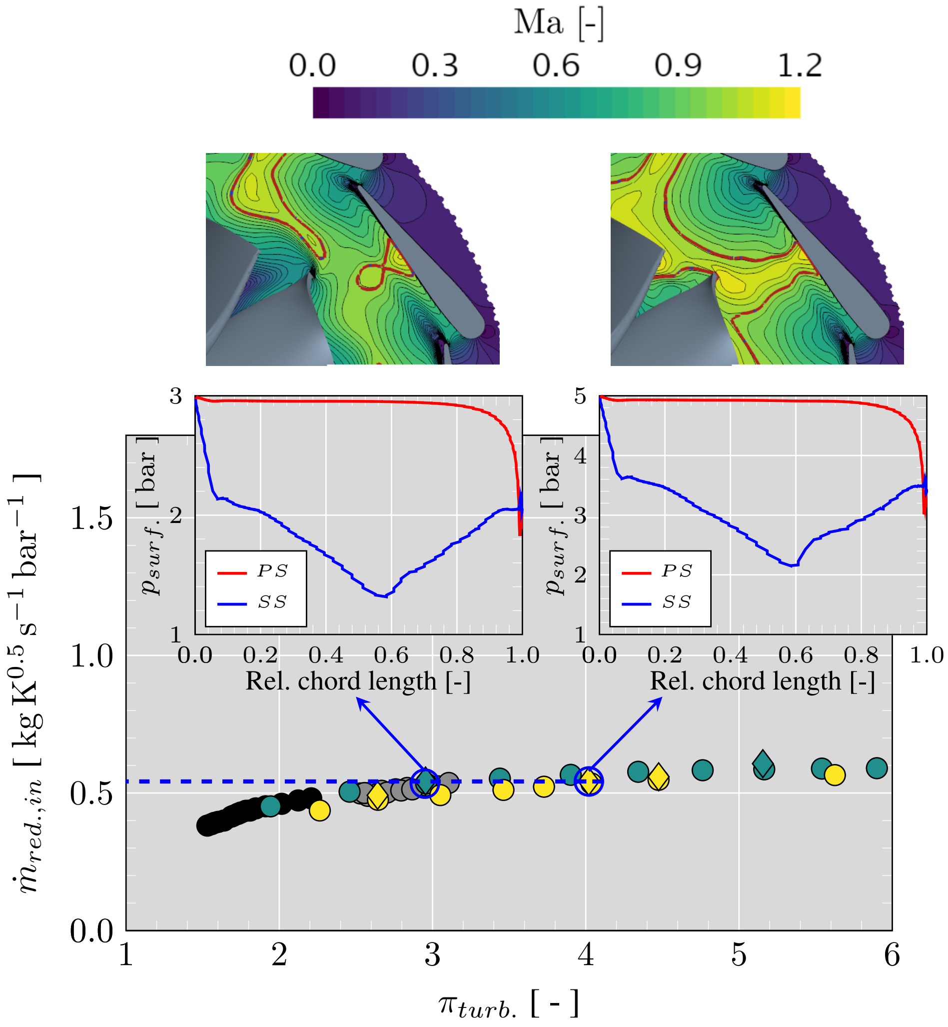

Figure 5.4: Mach number and stator vane pressure profile snapshots for two operating points of URANS simulations with the same reduced mass flow, closed VGT position and at 50% span of the stator passage; left: lower speed; right: higher speed; red line: $Ma = 1$.

where the reduced mass flow has been maintained at low and at high speed, as Figure 5.4 depicts, were analyzed. The pressure profiles look very similar in their qualitative shape, which confirms the aerodynamic similarity of both operating points around the stator vane. In the Mach number distribution the supersonic pocket at the vane SS is located at the same position. However, the overall Mach number distribution has a significantly different pattern for both speeds. At higher speed, the supersonic region reaches the rotor inlet on the SS and hits the LE joining with the contiguous supersonic region. At lower speed, the flow has much less flow with velocities above the sonic limit close to the rotor and the shock wave on the vane SS propagates less towards the rotor inlet.

In order to consider the effects of the rotor rotation, one blade passing at closed VGT position and higher PR was analyzed. The intensity of the supersonic pocket close to the vane SS does not present any variation at higher speed, whereas at lower speed the extension of the choked region varies. For both speeds the connection between the two neighboring pockets disappear after the blade passes the entire vane. It is worth highlighting that at no operating point the choked flow and shock waves appear in the perpendicular cross section between the stator TE and the neighboring vane. To reach choking conditions in the stator passage, the vanes need to be closed much further up to 0% VGT opening, which does not occur in real operational conditions.

5.3 Summary

The internal flow of the turbine when operating with the stator vanes at a closed position at lower and higher speeds and at lower and higher PR has been analyzed using the unsteady results. The Mach number contour at 50% span has been selected for this analysis due to the slight change presented in planes at 20% and 80% span. For the selected rotational speeds, the flow reaches sonic conditions in the vaneless space with increasing the PR.

At higher speed and higher PR, a supersonic pocket is developed on the SS of the stator blade and expands up to close to the rotor inlet. It is relevant to highlight that at closed VGT position, the distance from the vane SS to the rotor inlet generates a throat where the flow accelerates reaching sonic conditions. Furthermore, based on the pressure profile, a sudden rise on the SS reveals the presence of a shock wave compared with the subsonic flow at the same rotational speed but at a lower PR. At lower speed, the selected points at lower and higher PR present sonic conditions. At lower PR, a supersonic pocket appears on the SS without reaching the rotor inlet, while at the higher PR, the passage is fully choked.

The effect of the rotational speed when the reduced mass flow keeps constant was analyzed by taking the value at lower speed and lower PR. Results show different Mach number distributions. At higher speed, the supersonic region extends up to the rotor and hits the LE connecting with the neighboring region. At lower speed, as was mentioned above, the supersonic region on the SS does not expand up to the rotor inlet, but the adjacent pocket approaches the rotor inlet.

The effects of the blade passing on the supersonic pocket at higher PR was analyzed for the two rotational speed. At higher speed, the intensity of the supersonic region close to the SS does not present any variation, whereas at lower speed the extension of the region varies.

It is pertinent to highlight that in no operating point, the choking conditions and shock waves appear in the perpendicular cross-section between the stator TE and the adjacent vane.

5.4 References

[163] D. Pohl, J. Janssen, P. Jeschke, A. Halcoussis, and H. Wolf. “Variable Stator Vane Penny Gap Aerodynamic Measurements and Numerical Analysis in an Annular Cascade Wind Tunnel”. In: *International Journal of Gas Turbine, Propulsion and Power Systems* 11.2 (2020), pp. 44–55. DOI: `https://doi.org/10.38036/jgpp.11.2_44`. URL: `http://www.gtsj.org/english/index.html` (cit. on p. 74).

[164] S. Stummann, D. Pohl, P. Jeschke, H. Wolf, A. Halcoussis, and M. Franke. “Secondary Flow in Variable Stator Vanes With Penny-Cavities”. In: *ASME Turbo Expo 2017: Turbomachinery Technical Conference and Exposition*. Vol. Volume 2A: Charlotte, North Carolina, USA: ASME, 2017, pp. 1–12. ISBN: 978-0-7918-5078-7. DOI: `10.1115/GT201763771`. URL: `https://doi.org/10.1115/GT2017-63771` (cit. on p. 74).

[165] D. Japikse and N. Baines. *Introduction to Turbomachinery*. Concepts ETI, Inc, 1994 (cit. on p. 74).

[166] J. D. Denton. “Loss mechanisms in turbomachines.” In: *Journal of Turbomachinery* 115.(Cambridge, U.K.: Sep. 1-3, 1987), Bury St. Edmunds, U.K., Mech. Engng. Publications Ltd., 1987, Pap (1993), pp. 621–656. DOI: `10.1115/1.2929299`. URL: `https://doi.org/10.1115/1.2929299` (cit. on pp. 75, 144).

CHAPTER 6

Flow characteristics through the vaneless space.

Contents

6.1 Introduction 83
6.2 Numerical Results 83
6.3 Unsteady Rotor-Stator Interaction 90
6.4 Summary 97
6.5 References 99

Figures

6.1 Turbine geometry with highlighted sections for following analysis. Dimensions in millimeters 83
6.2 Mach number and stator vane surface pressure profiles at 50% span of the stator passage and higher PR; red line: $Ma = 1$. 85
6.3 Mach number with 30% VGT position for higher PR and higher speed; red surface: $Ma = 1$. 86
6.4 Streamlines restricted to 50% span at higher PR, describing the flow path in the vaneless space with respect to the Mach number. 86
6.5 Mach number and total pressure along analyzed constrained streamlines for 10% VGT at 50% span and higher PR; upper: lower speed; lower: higher speed. 87
6.6 Mach number and total pressure along analyzed constrained streamlines for 30% VGT at 50% span and higher PR; upper: lower speed; lower: higher speed. 88

6.7 Total pressure evolution in the vaneless space for 10% VGT at higher PR. 89
6.8 Total pressure evolution in the vaneless space for 30% VGT at higher PR. 89
6.9 Relative Mach number for 10% VGT at higher PR; left: lower speed; right: higher speed; red line: $Ma_{rel.} = 1$. 90
6.10 Transient numerical schlieren for 10% VGT opening at 50% span of the stator passage with higher simulated PR; left side: lower speed; right side: higher speed. 92
6.11 Transient evolution of Mach number (left side) and total pressure (right side) for 10% VGT opening at different radial positions for higher PR and lower speed. 94
6.12 Transient evolution of Mach number (left side) and total pressure (right side) for 10% VGT opening at different radial positions for higher PR and higher speed. 95
6.13 Transient evolution of static pressure in the rotor for 10% VGT with higher PR at low speed (left side) and high speed (right side). 96

6.1 Introduction

AFTER analyzing the sonic condition in the stator in the previous chapter, this section presents the flow characteristics in the vaneless space and the interaction between stator and rotor. Thus, the closed position and another slightly more open have been considered for this study under operations conditions of lower and higher speed at lower and higher PR. The Mach number and pressure profile at 50% span besides different cylinder sections and along streamlines have been evaluated.

6.2 Numerical Results

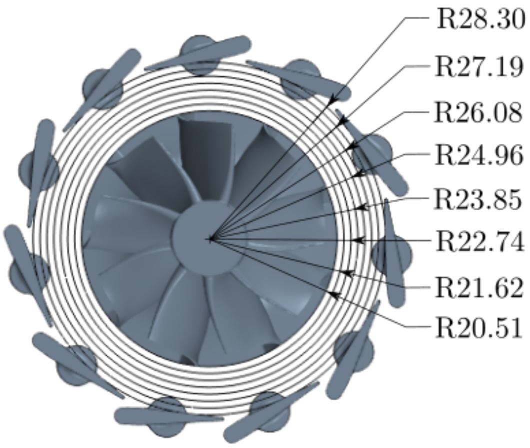

Figure 6.1: Turbine geometry with highlighted sections for following analysis. Dimensions in millimeters

To understand the choking mechanism in the stator and the vaneless space in more detail, the three-dimensional flow has been analyzed for 10% (closed position) and 30% VGT. The first position was selected based on the results presented in Chapter 5 where the supersonic regions extend up to the rotor inlet depending of the operational point. The 30% VGT opening was selected as the control system of the engine can set at full load or load acceptance transient (sudden tip-in) test [35, 135, 134, 138]. Eight equidistant radii from 20.51 mm to 28.30 mm, as depicts Figure 6.1 at stator span of 20%, 50%, and 80%, along with the complete passage height have been selected to study the flow in the vaneless space beside the plane at 50% span depicted in Figure 5.1(a).
In Figure 6.2 the Mach number distribution for higher and lower speed at higher

PR with 10% and 30% VGT opening in fully choked condition and at 50% of the span is shown. The choking area in all cases spans from the SS of the stator vane to the rotor entry. The depicted pressure profiles show an augmentation of the static pressure on the SS due to the development of a shock wave, after which the flow decelerates, becoming subsonic. The location of the shock wave seems to be unchanged, standing at around 0.6 Rel. chord length at higher speed and 0.68 Rel. chord length at lower speed, since the vane angle differs just 5.4° between both presented positions. Furthermore, the difference in the minimum pressure on the SS of 10% VGT and 30% VGT opening is only 0.5 bar for a given rotational speed. However, the small change in the vane angle has a considerable influence on the final choking reduced mass flow, as shown in Figure 4.2(a). Although the area between two stator vanes grows by a factor of around 1.83 (from 11.88 mm^2 to 21.74 mm^2, see Table 3.1), no flow with sonic speed has been identified in the throat of the stator vanes. The vaneless space throat area also changes rather less and even decreases when the stator vanes are more opened, with a factor of around 0.94 (see Table 3.1). While in all presented cases, a standing shock wave can be observed periodically with each stator vane in the vaneless space, at 30% VGT position and higher rotational speed, the standing shock exists only on a few stator vanes when the maximum reduced mass flow is reached. Figure 6.3 shows the isosurface of the absolute Mach number equal to one. For the represented case of more opened vanes with higher rotational speed, the reduced mass flow is slightly lower, which might cause the absence of standing shock waves and the effective choking in the vaneless space. Here, it is worth highlighting that the flow is choked in the absolute frame of reference in the inlet of the rotor. Further, the overall velocity, not the radial velocity component, is responsible for the flow choking as assumed in many one-dimensional models for choked flow in the rotor inlet. It seems that every flow particle which enters the rotor passes at least once through the isosurface. Similar to the observations made before regarding the standing shock wave on the stator vane, the flow seems to be fully choked when the flow passes only a few times through the closed surface representing the sonic limit before entering the rotor. Using streamlines restricted to a constant stator span as depicted in Figure 6.4, the theoretical flow path along a constant passage height can be analyzed. Here, a restricted streamline has been chosen to reduce the impact of the starting point, which would otherwise result in the random selection of a 3D streamline. Since processed streamlines at one time step of unsteady flow results are also not representative for the flow path of a particle, results of steady RANS simulations have been used for this analysis. These results indeed lose their validity when the streamline is close to the rotor blade as the number of blade passings does not reflect the real world with a moving rotor. However, this kind of analysis can give valuable insights into the physics of the choking procedure. At a span of 50%, the least flow

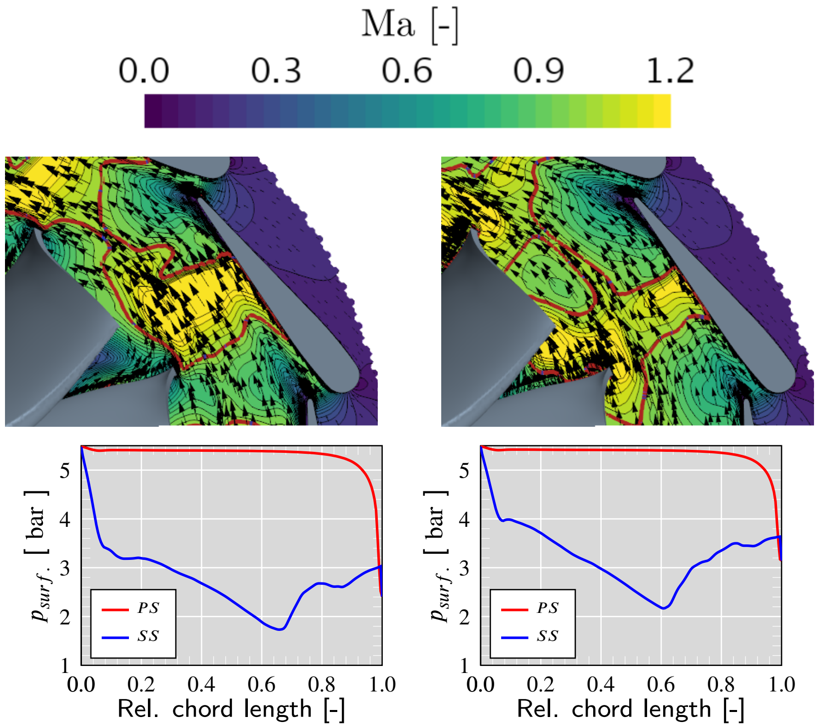

(a) Lower speed at 10% VGT opening. (b) Higher speed at 10% VGT opening.

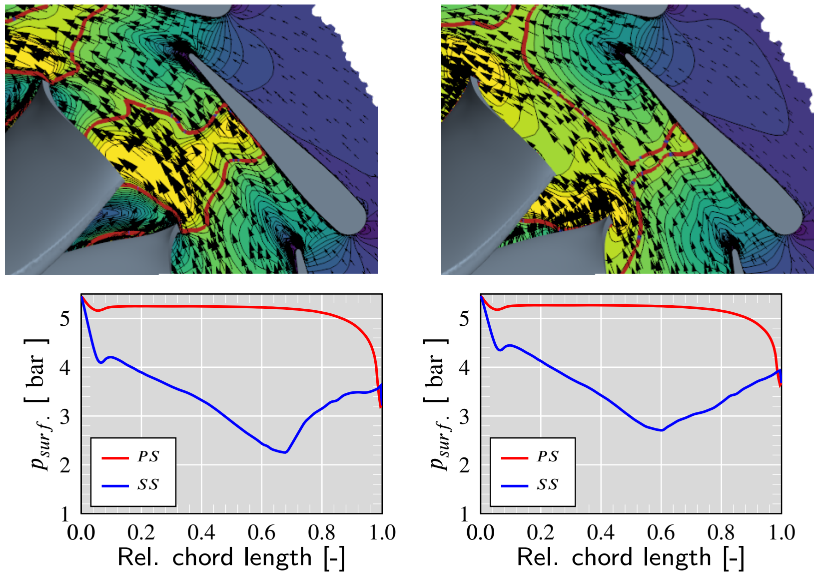

(c) Lower speed at 30% VGT opening. (d) Higher speed at 30% VGT opening.

Figure 6.2: Mach number and stator vane surface pressure profiles at 50% span of the stator passage and higher PR; red line: $Ma = 1$.

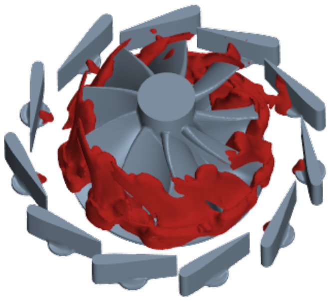

Figure 6.3: Mach number with 30% VGT position for higher PR and higher speed; red surface: $Ma = 1$.

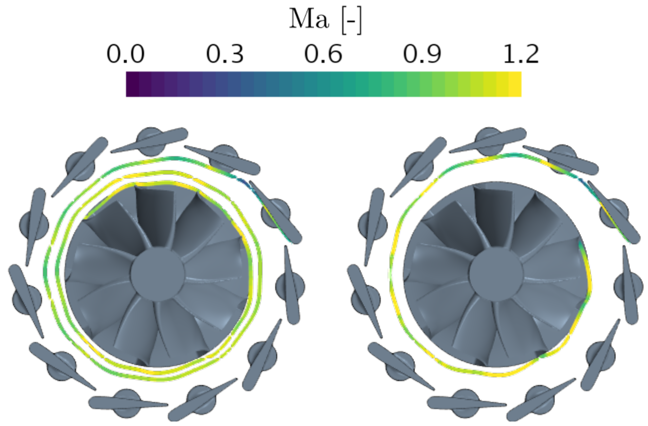

(a) Higher speed at 10% VGT (b) Lower speed at 10% VGT

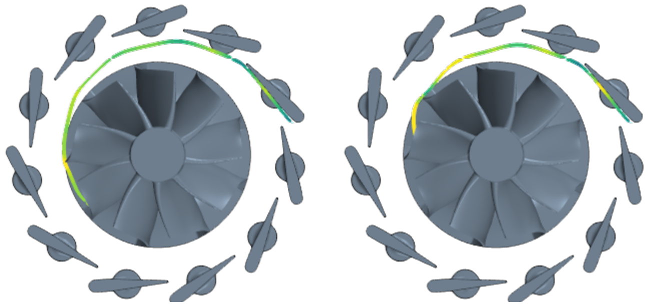

(c) Higher speed at 30% VGT (d) Lower speed at 30% VGT

Figure 6.4: Streamlines restricted to 50% span at higher PR, describing the flow path in the vaneless space with respect to the Mach number.

distortion by secondary flow phenomena was expected [167], which allows the least biased analysis of the choking mechanism. Hence, this span was selected for this analysis. Comparing the streamlines at the choked condition at 10% and 30% VGT, Figure 6.4(a) and Figure 6.4(c) respectively, the opening significantly influences the flow path length, even though the stator vane angle changes only 5.4 deg between both configurations. The flow length determines the number of stator vanes the streamline has to pass and therewith the passing of throat areas in the vaneless space. Furthermore, choking is caused as the flow passes several times through the throat between the rotor and stator vane, increasing the effective mass flow in the same throat. Hence, the area gets choked with a lower overall mass flow. This explains why the choking reduced mass flow at 30% VGT opening is around 1.5 times higher than for 10% VGT opening, although the vaneless throat area is even slightly smaller as it is shown in Table 3.1. The restricted streamlines trajectory changes when the rotational speed is lower and choking condition is reached at higher PR, as shown in Figure 6.4(b) and Figure 6.4(d). Close to the rotor, the flow turns towards the rotor, which shortens the length of the streamline. Results presented further in this chapter will indicate that local shocks in the relative reference frame of the rotor are responsible for the change in direction. Considering that the choking reduced mass flow is similar to the higher speed, this might indicate that not the entire throat area between rotor inlet and stator acts as the effective choking area (from the stator vane SS towards an effective radius upstream the rotor). In Figure 6.5 the evolution of the Mach number and total pressure along the previously presented streamlines shows the impact of both stator vane and rotor blade. Along the streamline, which passes several throats of the vaneless space, the flow experiences several accelerations above sonic speed and follows abrupt

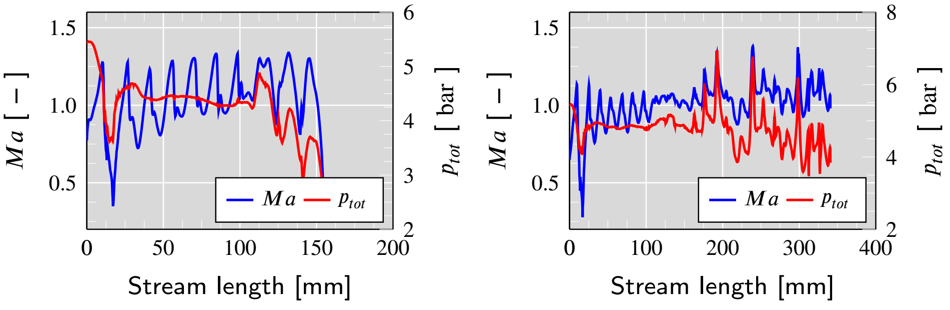

(a) Lower speed.

(b) Higher speed.

Figure 6.5: Mach number and total pressure along analyzed constrained streamlines for 10% VGT at 50% span and higher PR; upper: lower speed; lower: higher speed.

decelerations caused by shocks. Only with the first two decelerations, the total pressure shows a sudden reduction, which indicates a rather strong shock close to the SS of the stator vane. The newly increase of the total pressure may be explained by being fed by the static pressure of the flow at higher radius newly entering the vaneless space. This way, the flow becomes newly pressurized from upstream flow in the radial direction. Furthermore, increasing total pressure might additionally be caused by the analysis of a restricted streamline at 50% span. For a VGT opening of 10%, the evolution of the total pressure and the Mach number at lower and higher speed look similar until a length of 100 mm. Before, the flow experiences seven supersonic accelerations related to passing seven throats generated by stator vanes and the rotor inlet. From that point on, the flow turning changes towards the rotor at a lower speed, while the flow turning seems to be even reduced at a higher speed. However, in both cases, the flow appears to experience accelerations above the sonic speed now caused by the closeness of the rotor blades. While the total pressure just slightly decreases at higher speed, the total pressure is highly influenced by the rotor blades at lower speed and reduces significantly. This indicates the aforementioned shock losses caused by the rotor interaction. For the VGT opening of 30%, the same tendency can be observed, as is depicted in Figure 6.6. The flow experiences similar accelerations and decelerations for higher and lower speed up to a flow length of 40 mm. Then the same effect occurs as observed at 10% VGT position, and the flow is turned inwards by shocks experienced in the relative reference frame close to the rotor.

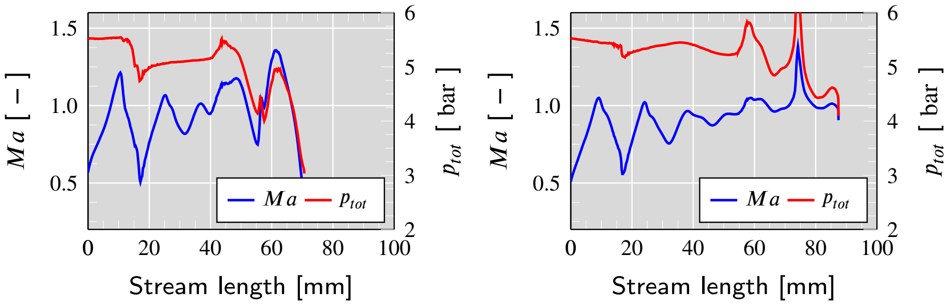

(a) Lower speed.

(b) Higher speed.

Figure 6.6: Mach number and total pressure along analyzed constrained streamlines for 30% VGT at 50% span and higher PR; upper: lower speed; lower: higher speed.

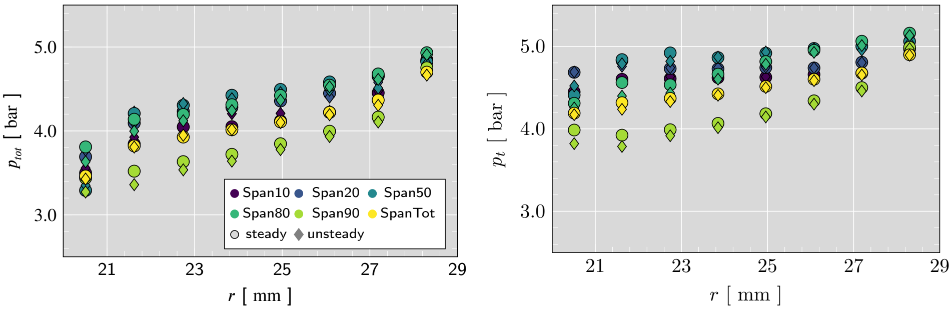

(a) Lower speed.

(b) Higher speed.

Figure 6.7: Total pressure evolution in the vaneless space for 10% VGT at higher PR.

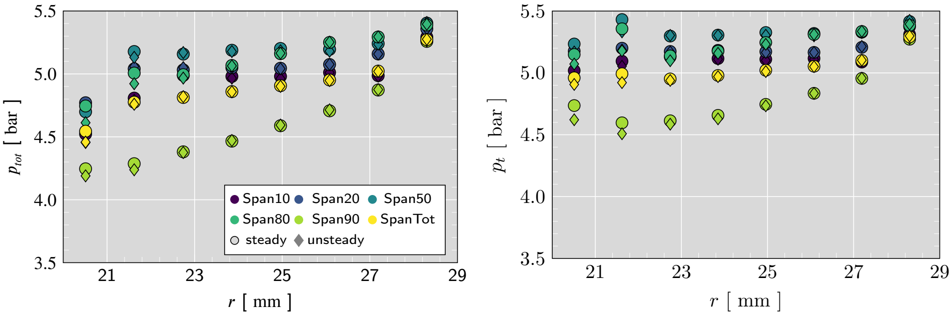

(a) Lower speed.

(b) Higher speed.

Figure 6.8: Total pressure evolution in the vaneless space for 30% VGT at higher PR.

To support the analysis of the restricted streamlines, the mass flow averaged total pressure at presented radii in Figure 6.1 are depicted in Figure 6.7 and Figure 6.8 for selected spans and for the entire passage height of the vaneless space obtained by RANS and time-averaged URANS simulation results. For all spans and considering the entire passage height, the evolutions of the averaged total pressure look qualitatively similar. A significant reduction in total pressure can be observed at a higher radius, close to the stator vane. This pressure loss is caused due to the shock losses, as the streamline analysis indicated. Then the total pressure evolution towards smaller radius around the center of the vaneless space shows relatively low-pressure losses. Finally, more considerable pressure losses can be observed close to the rotor inlet at a low radius. This may be caused due to the interaction with the rotor, as the previous analysis with restricted streamlines showed. Additional pressure losses may be caused by a sudden expansion of the flow passage just before the rotor inlet. Also, the cases with lower rotational speed represent higher pressure losses close to the rotor, as the flow experiences shock losses in the relative frame of reference before entering the rotor. The growing deviation of total pressure along the spans can be explained by secondary flow phenomena as horseshoe vortexes [167] and tip leakage vortexes at the shroud. As previously assumed, less impact of secondary flow phenomena causes low-pressure losses at 50% span. This confirms that the choking phenomena could be mainly analyzed in the streamlines mentioned above. Further, time-averaged URANS results are very similar to the ones of steady RANS simulations for the most radial positions and spans. This shows that the previous analysis of a restricted streamline allows representative conclusions for the entire passage of the vaneless space, which are also valid when the rotor is moving. The representation of the total pressure along the vaneless space also confirms strong losses at higher radius close to the stator vane, followed by lower losses due to rather weak shocks and viscous flow phenomena at intermediate radii and significant losses close to the rotor entry.

6.3 Unsteady Rotor-Stator Interaction

Based on the previous analysis of RANS results, it can be stated that rotor inlet and stator vanes build throats throughout the vaneless space. To assess the dynamic impact of the rotor motion on the effectively choked area and the generation of transient losses, URANS results are studied in the current section. Figure 6.9 shows the relative Mach number distribution in the vaneless space.

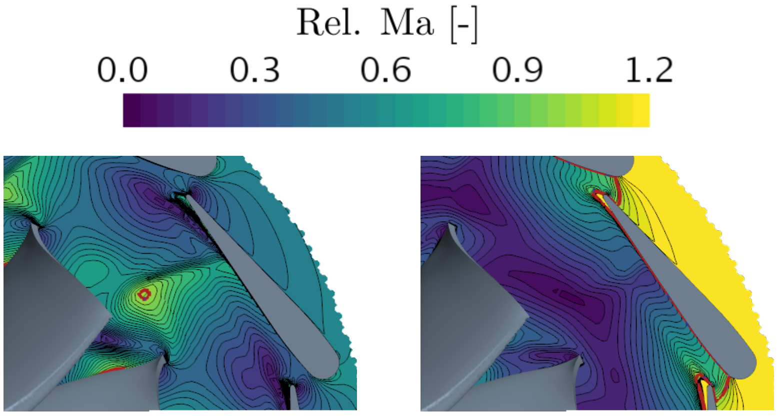

Figure 6.9: Relative Mach number for 10% VGT at higher PR; left: lower speed; right: higher speed; red line: $Ma_{rel.} = 1$.

While the relative Mach number at higher speed remains clearly subsonic, the lower rotational speed allows the evolution of sonic flow close to the turbine wheel inlet. This can cause strong shocks close to the rotor LE when the rotor passes this region. Due to the strong shock, the flow is turned inwards, and higher losses were observed close to the rotor when the rotational speed is low. This also seems to be the origin for very low efficiencies at low speeds when the turbine is choked with very closed stator vanes. For a deeper analysis of the rotor-stator interaction, numerical Schlieren is depicted in Figure 6.10 for one blade passing with both analyzed reduced speeds and both at the fully choked condition with 10% VGT opening.

The results obtained with a higher speed show negligible variations close to the stator vane, as it is shown in Figure 6.10-right side. The shock at the vane SS does not change its intensity over the entire blade passing. Although the orthogonal shock is diminishing in its intensity towards the rotor domain, the shock is extended when the rotor passes exactly the coordinates of the stator vane shock. For a short time, the rotor supports the formation of a throat, causing the extension of the shock in the absolute reference frame.

At lower speed, the stator vane shock is leaned backward and shows higher intensity in Figure 6.10-left side in comparison to the previously described operating point. The higher intensity may result from operation at slightly higher reduced mass flow. In contrast to the results at higher speeds, the shock wave seems to vary its angle depending on the rotor blade position. However, independent from the rotor blade position, the shock on the stator vane has a longer extension towards the rotor. As previously concluded, the moving rotor blade encounters locally supersonic speed, resulting in the formation of shock waves in the relative frame. Those shock waves cause distortions in the pressure field downstream of the standing shock, which explains the variation in the angle of the shock wave propagating from the stator SS. At the same time, it is to be expected that the passing rotor blade acts in the absolute frame like in the case of the higher speeds and assists in the formation of a throat. This interaction with the rotor explains the slight deviations of turbine efficiency between steady and unsteady RANS simulations. To allow more insight into the lost generation, which is needed for the development of one-dimensional loss models, the contribution of the losses of the flow just before entering into the rotor (losses at lower radius in Figure 6.7) has been studied. Therefore, the Mach number and the total pressure have been extracted at several radial positions along one entire circumference and at every time step.

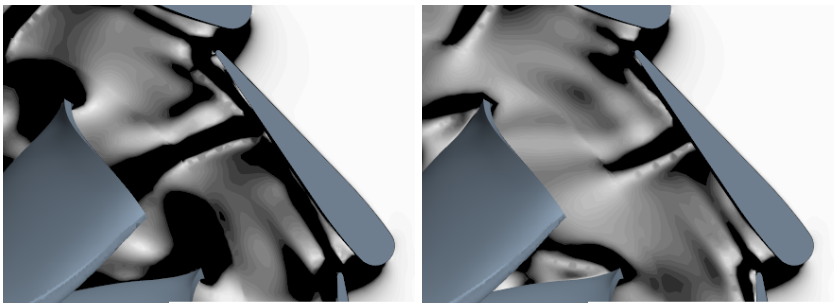

(a) $t = 25\%$ rotor blade passing.

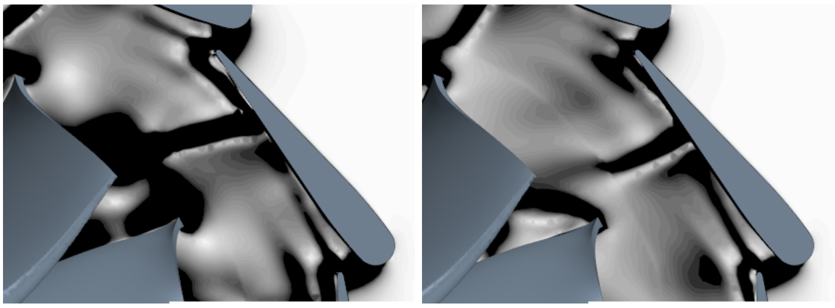

(b) $t = 50\%$ rotor blade passing.

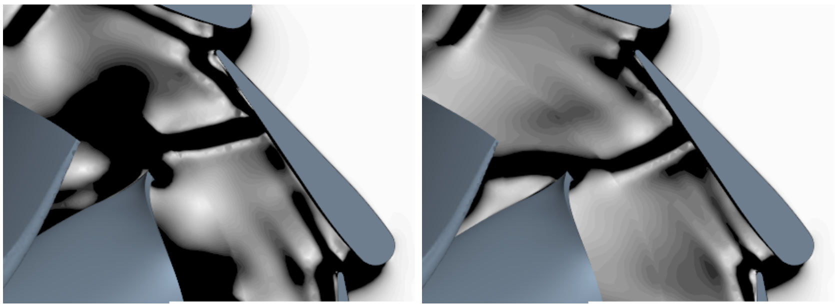

(c) $t = 75\%$ rotor blade passing.

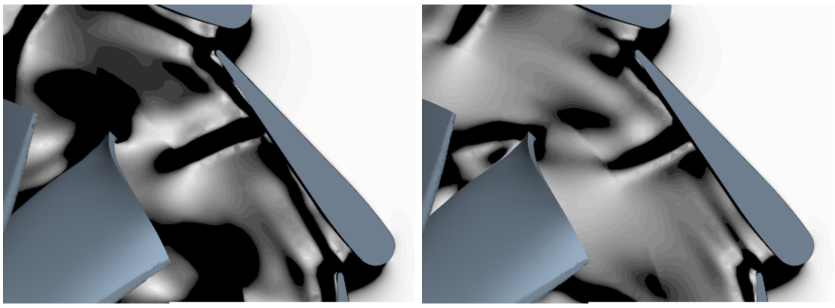

(d) $t = 100\%$ rotor blade passing.

Figure 6.10: Transient numerical schlieren for 10% VGT opening at 50% span of the stator passage with higher simulated PR; left side: lower speed; right side: higher speed.

The results for the lower speed are presented in Figure 6.11. At higher radius (Figure 6.11 (a) and (b)) the Mach number distribution seems to be independent of time. Here, eleven minima and maxima represent the interaction with the stator vanes. However, diagonal patterns with time dependency occur closer to the rotor. Those patterns are related to the movement of the rotor blades. The slope depends on the rotational speed of the rotor. Directly in front of the rotor inlet (Figure 6.11 (c) & (d)), the influence of the rotor is clearly visible, and nine minima and maxima, which equals the rotor blade number, can be identified.

These strong fluctuations are caused by the local acceleration in front of the rotor leading edge, as can be observed in the Mach number contour in Figure 6.2 for all operating points. Weak shock waves may generate the loss patterns which are visible in Figure 6.11 (d) - right. These shock waves seem to be continuously generated at any position of the rotor wheel. However, the intensity depends on the relative orientation to the stator vanes. Although the impact of the stator vane shock diminishes towards the rotor inlet, an explicit dependency on the shock waves close to the rotor leading edge can be identified. Islands of local maxima mark the presence of the stator vane shock. When the rotor passes this throat, the rotor blade supports the restriction of the effective throat area, causing a local acceleration in the absolute frame of reference. Due to the locally increased Mach number in the throat, the shock appears to be stronger. Additionally, the local sonic speed in the relative frame shown in Figure 6.9 contributes significantly to this loss. The variation of total pressure losses shown in Figure 6.11 (d) - right is related to this shock dynamic.

The comparison with the results at the higher speed emphasizes the importance of the strength of the shock caused in the relative frame. In Figure 6.12 maxima and minima in the Mach number are less distinguished, and total pressure losses are considerably lower. However, the diagonal pattern related to the rotor movement represents the dominant pattern and is less dependent on the stator position (due to the missing impact of shocks in the relative frame). Hence, the losses generated by the rotor in choking conditions depend on the number of rotor blades passed by a fluid particle, the flow angle, flow velocity, and rotor velocity. These parameters must then be considered in one-dimensional modeling of stator choking to estimate the generated losses adequately.

Concluding, the losses close to the stator blade depend on how many times a flow particle passes the stator vane (and its choked throat with the rotor). The number of rotor blades passed by a fluid particle influences the losses close to the rotor. This accounts for low speeds where an additional shock in the relative frame generates significant losses, as well as for the higher speed where the flow has a subsonic relative Mach number.

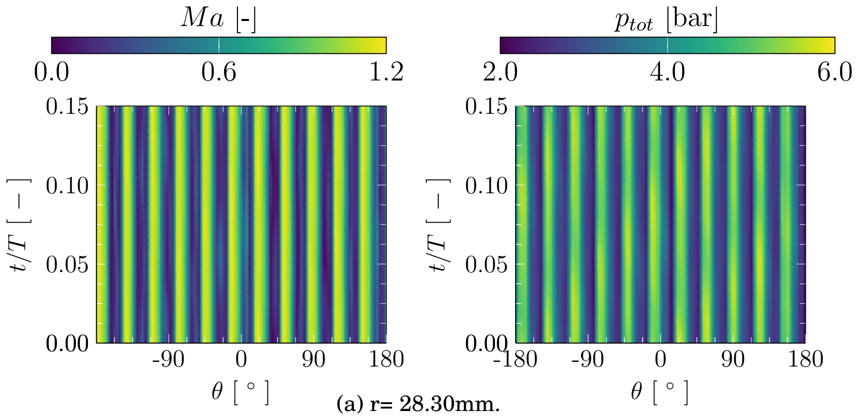

(a) r= 28.30mm.

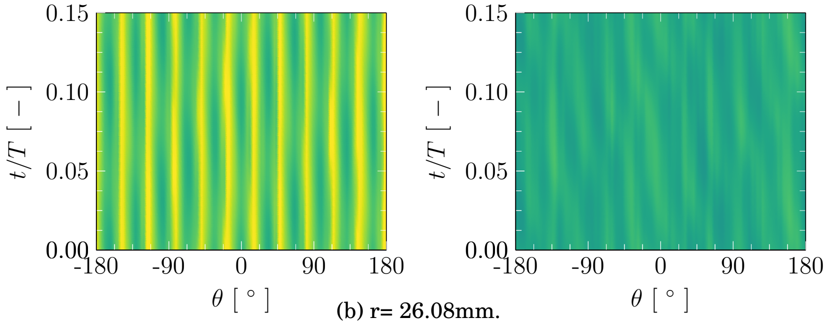

(b) r= 26.08mm.

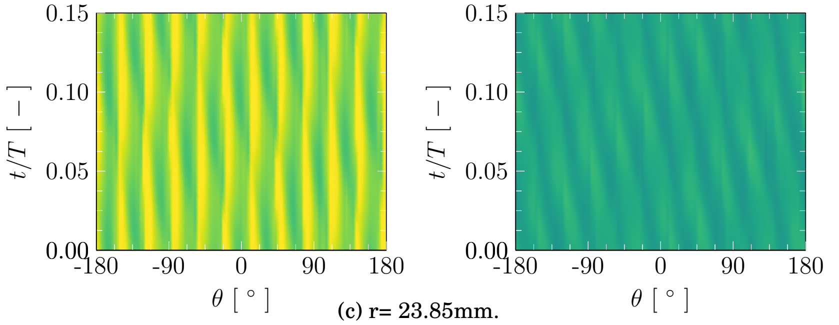

(c) r= 23.85mm.

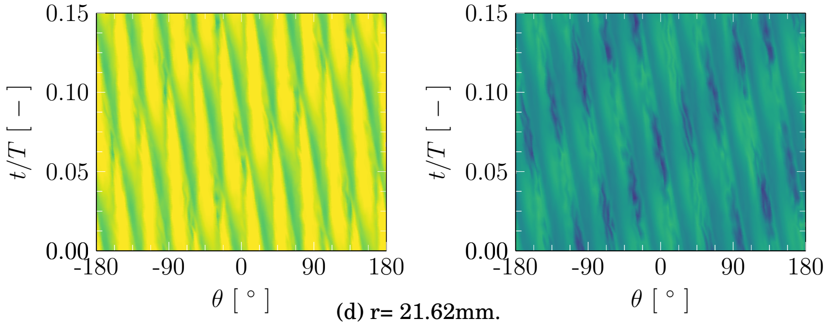

(d) r= 21.62mm.

Figure 6.11: Transient evolution of Mach number (left side) and total pressure (right side) for 10% VGT opening at different radial positions for higher PR and lower speed.

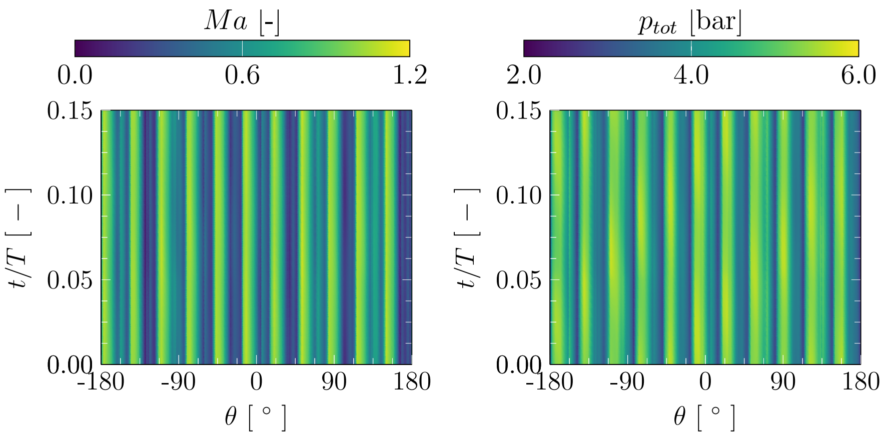

(a) r=28.30mm.

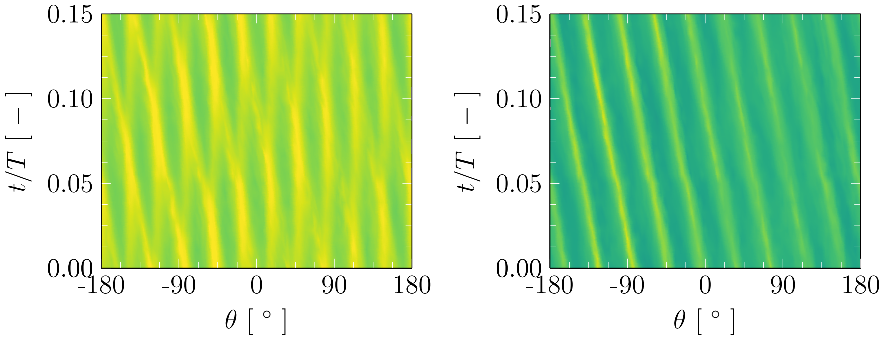

(b) r=21.62mm.

Figure 6.12: Transient evolution of Mach number (left side) and total pressure (right side) for 10% VGT opening at different radial positions for higher PR and higher speed.

To analyze the impact of the shock waves in the vaneless space on the rotor inlet, the transient surface pressure evolution and blade loading has been presented over time in Figure 6.13. The pressure profiles seem to be less affected by the interaction with the shock front propagating from the stator SS. This might indicate that the turbine pressure profile is mostly influenced by the shock in the relative frame. At higher speed, the standing shock causes important fluctuations on both SS and PS depending on where the shock stands (SS: Figure 6.10 (b); PS: Figure 6.10 (d)). The fluctuations result in oscillating blade loading in the rotor inlet. The blade loading oscillates from negative to positive values every time a stator blade is passed. This might result in structural problems and material damage after longer operation in this running condition.

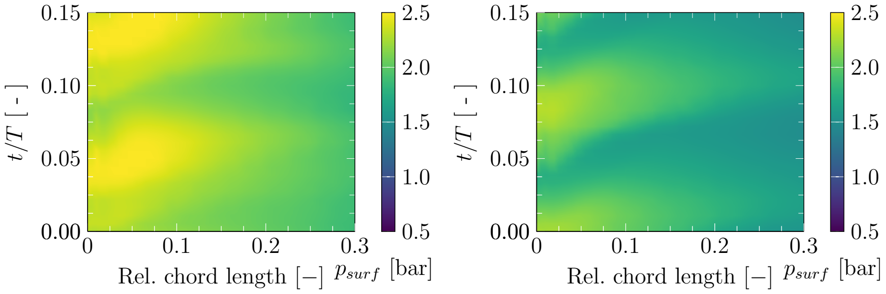

(a) Rotor blade surface pressure at 50 % span of the PS.

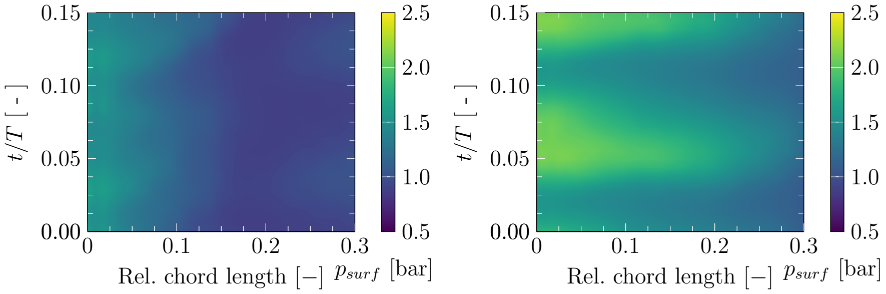

(b) Rotor blade surface pressure at 50 % span of the SS.

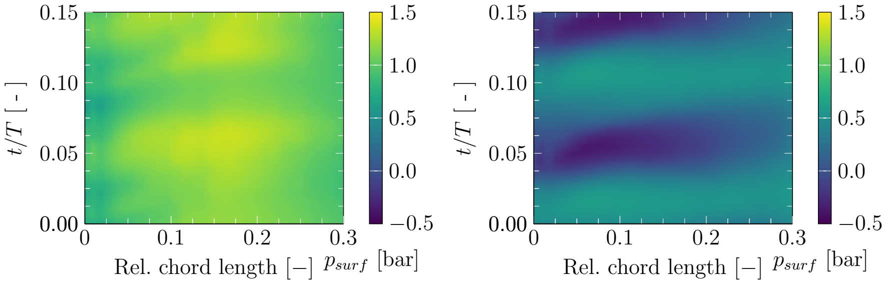

(c) Blade loading.

Figure 6.13: Transient evolution of static pressure in the rotor for 10% VGT with higher PR at low speed (left side) and high speed (right side).

6.4 Summary

This chapter presents the study of the flow at the vaneless space and the effects of the rotor movement on this region considering two vanes opening 10% and 30% VGT. For both positions the Mach number profile at higher PR operating at lower and higher speed the supersonic region extends from the vane SS to the rotor inlet. The pressure profile on the SS reveals the presence of a shock wave due to the rise of the static pressure, the location of the shock wave is the same for both VGT positions since the vane angle differs just slightly. Nevertheless, the small increase in the opening of the vanes represents a significant variation on the choking reduced mass flow. In the vaneless space can be observed periodically a standing shock wave on each stator vane, but at 30% VGT and higher rotational speed, the sonic regions exist only on few stator vanes as the reduced mass flow is slightly lower compared with the case at lower speed causing the absence of shock waves on each vane. Nevertheless, the flow reaches sonic conditions when passing only a few times just before entering the rotor.

To go deeper in this analysis, the flow path has been study using streamlines restricted at 50% stator span, the results reveals the influence of the vane opening on the flow path length, despite of the variation of just 5.4 deg when the position change from 10% to 30% VGT. Compared with the 30% opening the streamline at 10% VGT has to pass several time through the throats in the vaneless space increasing the effective mass flow. Thus, the area gets choked with a lower overall mass flow explaing why the choking reduced mass flow at 10% VGT is lower than at 30% VGT opening. Furthermore, at 10% VGT the flow experiences several accelerations above sonic speed followed by sudden decelerations caused by shock waves as the streamline passes several throats of the vaneless space. For both vanes opening, the flow appears to experience additional accelerations above the sonic speed as the flow approach very close to the rotor inlet. At lower speed the total pressure is more influenced by the rotor speed than at higher speed presenting a significant reduction in the value. Besides the streamlines analysis, different cylinder sections at different spans were considered to evaluate the total pressure. At higher radius, close to the stator vane, occurs an important reduction in the total pressure due to the shock losses as was indicated by the streamlines analysis. Around the center of the vaneless space the pressure losses are low but a significant loss occurs close to the rotor inlet at a lower radii.

For the analysis of the rotor-stator interaction at choking conditions a numerical Schlieren has been carried at lower and higher speed. At higher speed the variation of the shock wave on the stator SS is negligible over the entire blade passing. Nevertheless, close to the rotor inlet the shock is extended when the rotor passes just the stator vane shock supporting the formation of a throat. At lower speed the shock on the SS is leaned backward and shows a higher intensity compered with the case at higher speed. Furthermore, the blade passing affects the shock angle and supports the formation of shock waves in the relative frame. The interaction with the rotor explains the slight deviations of turbine efficiency between RANS and URANS simulations.

In addition to the aforementioned analysis the Mach number and the total pressure have been evaluated at several radial positions along one entire circumference and at every time step for the cases at higher PR. At lower speed and at a radius close to the stator vane, the Mach number pattern is independent of time, and the quantity of minima and maxima agrees with the stator vanes number. On the contrary, the pattern presents time dependency close to the rotor inlet, and the number of minima and maxima agrees with the rotor blade number. A similar behavior is found in the total pressure evolution, where significant pressure losses can be identified when the rotor blade passes the stator vane due to the local acceleration in the absolute and relative frame as the blade supports the formation of an effective throat. Similarly, the results at higher speed present the trend mentioned above, but the pressure losses are lower due to the absence of the shock in the relative frame.

On the rotor blade, the transient pressure evolution and blade loading over time has been evaluated to analyze the impact of the shock waves. The results show the lower effect of the shock wave on the stator vane over the blade pressure profile. Nevertheless at higher speed the blade loading in the rotor inlet oscillates from negative to positive values.

6.5 References

[35] J. G. Hawley, F. J. Wallace, A. R. J. Cox, R. W. Horrocks, and G. L. Bird. “Reduction of Steady State NOx Levels from an Automotive Diesel Engine Using Optimised VGT/EGR Schedules”. In: *SAE Technical Paper* 108 (1999), pp. 1172–1184. DOI: `10.4271/1999-01-0835`. URL: `https://doi.org/10.4271/1999-01-0835` (cit. on pp. 12, 41, 83).

[134] M. Ammann, N. P. Fekete, L. Guzzella, and A. H. Glattfelder. “Model-based control of the VGT and EGR in a turbocharged common-rail diesel engine: Theory and passenger car implementation”. In: *SAE Technical Papers* 112 (2003), pp. 527–538. ISSN: 26883627. DOI: `10.4271/2003-01-0357`. URL: `https://doi.org/10.4271/2003-01-0357.` (cit. on pp. 41, 83).

[135] J. Chauvin, A. Albrecht, G. Corde, and N. Petit. “Modeling and control of a Diesel HCCI engine”. In: *Proceedings of the Fifth IFAC Symposium on Advances in Automotive Control* (2007), pp. 1–8. DOI: `10.3182/20070820-3-US-2918.00064` (cit. on pp. 41, 83).

[138] J. Galindo, V. Dolz, J. Monsalve-Serrano, M. A. Bernal, and L. Odillard. “Impacts of the exhaust gas recirculation (EGR) combined with the regeneration mode in a compression ignition diesel engine operating at cold conditions”. In: *International Journal of Engine Research* 22.12 (2021), pp. 3548–3557. DOI: `10.1177/14680874211013986`. URL: `https://doi.org/10.1177/14680874211013986` (cit. on pp. 41, 83).

[167] M. Alexin Putra and F. Joos. “Investigation of Secondary Flow Behavior in a Radial Turbine Nozzle”. In: *Journal of Turbomachinery* 135.6 (2013). ISSN: 0889-504X. DOI: `10.1115/1.4024627`. URL: `https://doi.org/10.1115/1.4024627` (cit. on pp. 87, 90).

CHAPTER 7

Rotor Flow Characteristics

Contents

7.1 Introduction 103
7.2 Numerical Results 103
7.3 Summary 112
7.4 References 113

Figures

7.1 Iso-span planes and TE plane in the rotor 103
7.2 Relative Mach number snapshots of URANS simulations with closed VGT position higher PR close to the TE of the rotor; red line: $Ma_{rel.} = 1$.104
7.3 Relative Mach number snapshots of URANS simulations with opened VGT position; red line: $Ma_{rel.} = 1$. 105
7.4 Numerical schlieren of URANS simulations at 50% rotor span with opened VGT position. 106
7.5 Relation between the reduced mass flow and the area ratio under supersonic conditions. 107
7.6 Relative Mach number and rotor pressure profile snapshots at 20% rotor span with opened VGT position for lower simulated PR at lower speed (left) and at higher speed (right); red line: $Ma_{rel.} = 1$. 108
7.7 Relative Mach number and rotor pressure profile snapshots at 50% rotor span with opened VGT position for lower simulated PR at lower speed (left) and at higher speed (right); red line: $Ma_{rel.} = 1$. 109

7.8 Relative Mach number and rotor pressure profile snapshots at 80% rotor span with opened VGT position for lower simulated PR at lower speed (left) and at higher speed (right); red line: $Ma_{rel.} = 1$. 110
7.9 Relative rotor inlet angle snapshots of URANS simulations with opened VGT position and lower simulated PR of two speeds at the rotor inlet plane. 111

7.1 Introduction

THIS chapter presents the evaluation of the flow through the rotor when the turbine operates at lower and higher PR rotating at lower and higher speed. By using a plane at the rotor TE and three rotor span planes different flow patters have been revealed. Furthermore, besides of the PR the effects of the rotational speed, the tip leakages and the relative rotor inlet angle on development of sonic conditions will be analyzed.

7.2 Numerical Results

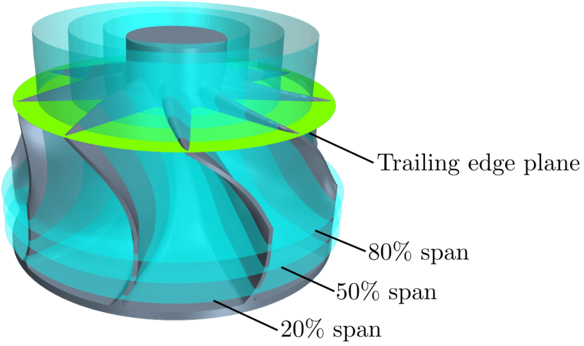

Figure 7.1: Iso-span planes and TE plane in the rotor

After studying the sonic conditions in the stator and vaneless space, where the shock wave on the vane SS extends to the rotor LE, as was also reported by Kawakubo et al. [34] and Rubechini et al. [90], who also highlighted that this shock generates pressure fluctuations on the rotor blade as was shown in Chapter 6, and high entropy rate, this chapter focuses on the rotor region. The closed and opened VGT positions are considered under the PR and rotational speed of lower and higher values to analyze the flow characteristics in the rotor, especially on a plane at rotor TE and 20%, 50%, and 80% rotor span as depicted in Figure 7.1. With closed VGT position, no supersonic flow is presented close to the rotor TE plane under operation conditions of lower inlet pressure and lower rotational speed. When the inlet pressure increases, supersonic flow can develop in the rotor, as can be seen in Figure 7.2 for both simulated speeds. However, the flow is not choked in the rotor. While areas of supersonic flow appear at the TE close to the hub at lower speed, first supersonic flow develops at the shroud at higher speeds. This observation is confirmed by the results of simulations with opened VGT positions, which are depicted in Figure 7.3. In the selected running conditions, the choking is much more developed at

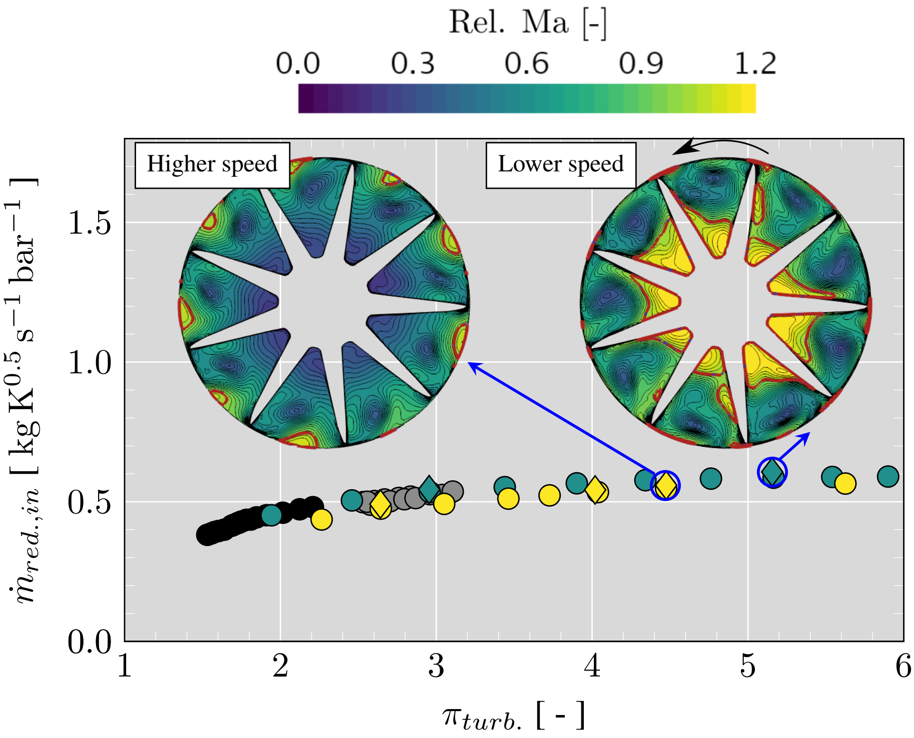

Figure 7.2: Relative Mach number snapshots of URANS simulations with closed VGT position higher PR close to the TE of the rotor; red line: $Ma_{rel.} = 1$.

elevated turbine PR of all three simulated reduced speeds. At lower speed, a damping influence of the tip leakage vortex is clearly visible close to the shroud [120]. Sonic tip leakage flow passes the tip gap and then experiences a rough deceleration being retarded to subsonic flow with a corresponding Mach number way below the Mach number of the surrounding passage. From there on the flow is not able to reach the sonic limit again. Increasing the PR, the rotor outlet becomes almost entirely choked, and strong TE shock waves are pronounced in the numerical Schlieren in Figure 7.4-(b). At a 50% span, these shocks cause a deceleration from supersonic to subsonic flow. Whereas at lower PR at 50% span no shock waves are reported as depicted in Figure 7.4-(a). Contrary to the case of lower speed, with the higher simulated speed at lower turbine PR, results show mostly supersonic Mach numbers close to the shroud, while the flow near the hub remains subsonic as shows Figure 7.3-(e) and without the presence of shock waves along the plane at 50% rotor span depicted in Figure 7.4-(e). With increased turbine PR, the passage becomes fully choked. Nevertheless, a subsonic regime is visible in Figure 7.3-(f) close to the PS of each blade. This

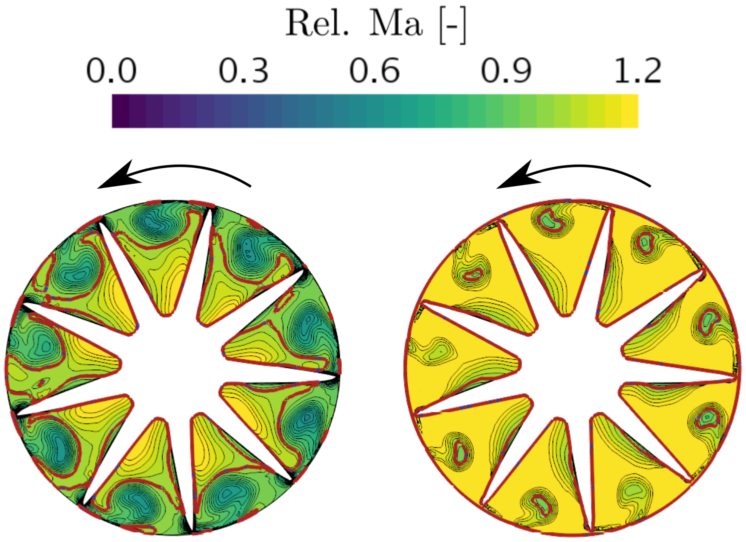

(a) Lower speed at lower PR.

(b) Lower speed at higher PR.

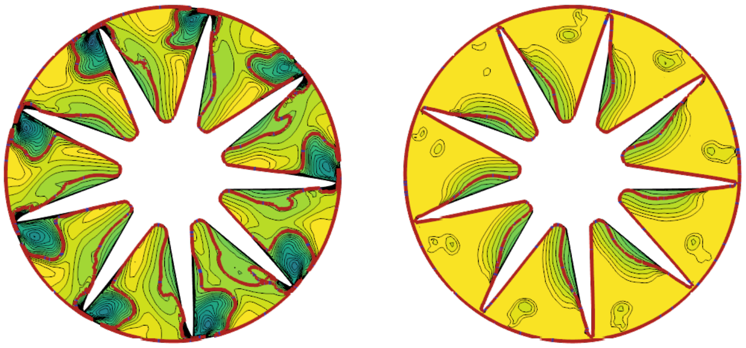

(c) Middle speed at lower PR.

(d) Middle speed at higher PR.

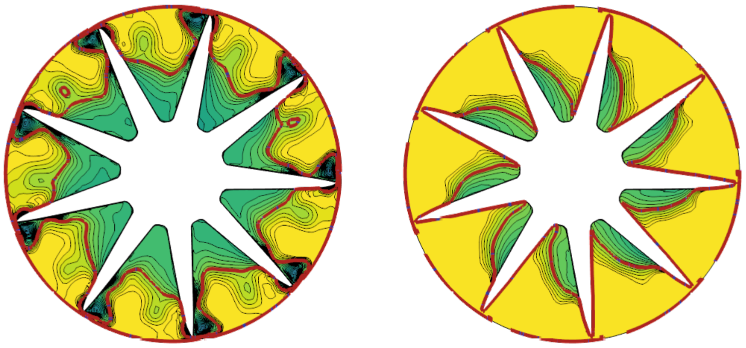

(e) Higher speed at lower PR.

(f) Higher speed at higher PR.

Figure 7.3: Relative Mach number snapshots of URANS simulations with opened VGT position; red line: $Ma_{rel.} = 1$.

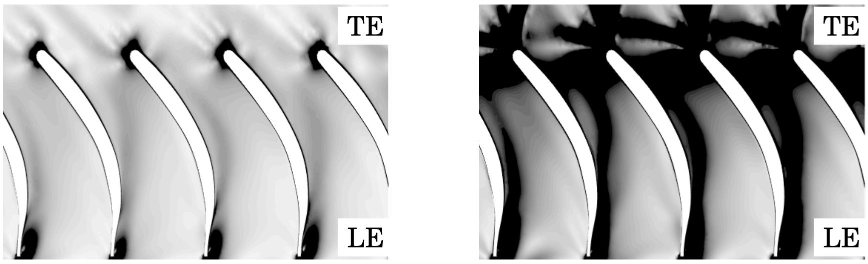

(a) Lower speed at lower PR. (b) Lower speed at higher PR.

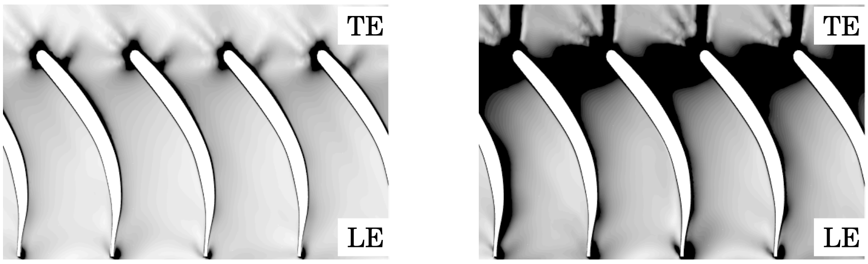

(c) Middle speed at lower PR. (d) Middle speed at higher PR.

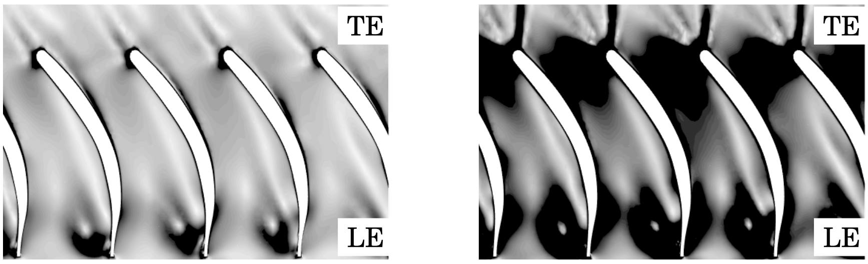

(e) Higher speed at lower PR. (f) Higher speed at higher PR.

Figure 7.4: Numerical schlieren of URANS simulations at 50% rotor span with opened VGT position.

subsonic flow originates from a upstream shock, which develops close to the TE shock, as it can be seen in the numerical Schlieren, Figure 7.4-(f). At middle speed and lower PR, Figure 7.3-(c), the mass flow rate through the tip gap is less than in the case of lower speed due to the shear force at the tip wall and mostly due to the reduction in the pressure difference driving the flow through the gap [168, 169]. As a consequence, the effects of the leakage flow starts to decrease and a considerable region of the main flow at the shroud accelerates becoming supersonic. When the PR jumps to a higher value, as visible in Figure 7.3-(d), the flow in the passage is practically choked. However, a subsonic flow on the PS persists. Overall, the evolution of the choked area of the middle speed represents a superposition of both dynamics, which were seen at the lower and higher speed, with a weaker expression. Hence, a smooth transition from the effects seen at low speed towards the effects seen at high speed seem to happen and no further dynamics need to be considered to fully characterize the choking process in the rotor. Figure 7.5 shows for the steady and unsteady simulation the relation of the ratio between the chocked area and the total area of the rotor TE plane with the reduced mass flow at opened VGT position. It is possible to observe that at lower speed the reduced mass flow stagnates first, which is consistent with the results of the turbine map in Figure 4.2-(a). Furthermore, it can be notice that as the PR reach the higher evaluated value in each iso-speed the variation in the area ratio is smaller. The difference in the area ratio between steady and unsteady simulations is due to the effect of the interaction of the flow with the moving blades of the rotor, which is greater at higher speed. Thus, even when the steady simulations can give good results for global parameters, to analyze variables related with the aerodynamic behavior of the flow, as the choked area, unsteady simulations should be carry out.

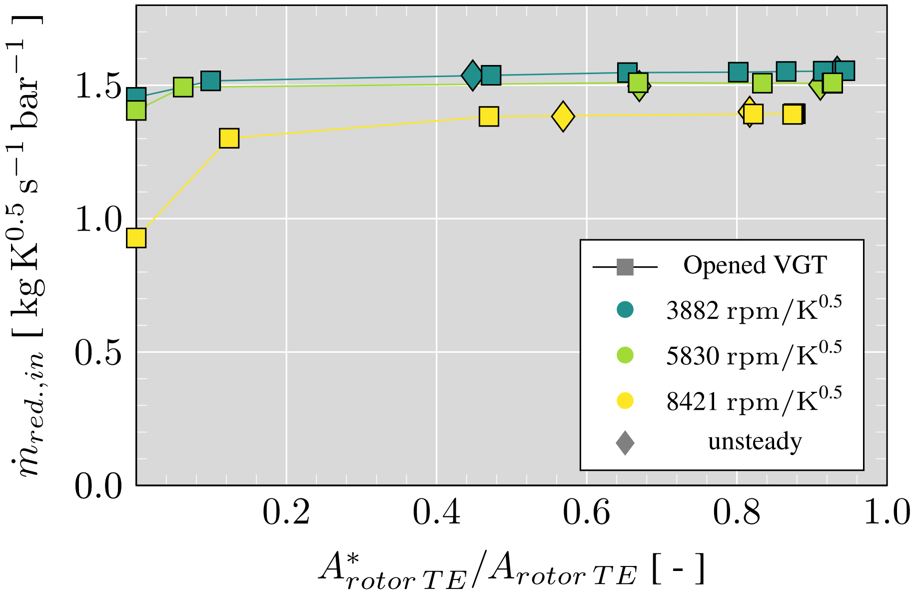

Figure 7.5: Relation between the reduced mass flow and the area ratio under supersonic conditions.

In order to extend the analysis of the choked flow at the rotor, blade-to-blade views with corresponding blade surface pressure profiles are shown for the lower and higher simulated speeds at lower PR in Figure 7.6 to Figure 7.8 for 20%, 50%, and 80% span. At lower speed, the flow through the passage seems to be choked at 20% and 50% span, Figure 7.6 and Figure 7.7 respectively, nevertheless at higher speed no choking appears at 20% span, while a much lower intensity of passage choking take place at 50% span. Regarding the corresponding pressure profile, these spans are exposed to high negative incidence. This reduces the acceleration on the SS and avoids choking at these spans . Nevertheless, at lower speed and 20% span, the pressure profile exhibited a sudden rise at 0.84 relative chord length, evidencing with the Mach number profile the presence of a shock wave. At 80% span, the supersonic region decreases, remaining a small region on the blade SS, while at higher speed, the passage is choked as depicted in Figure 7.8.

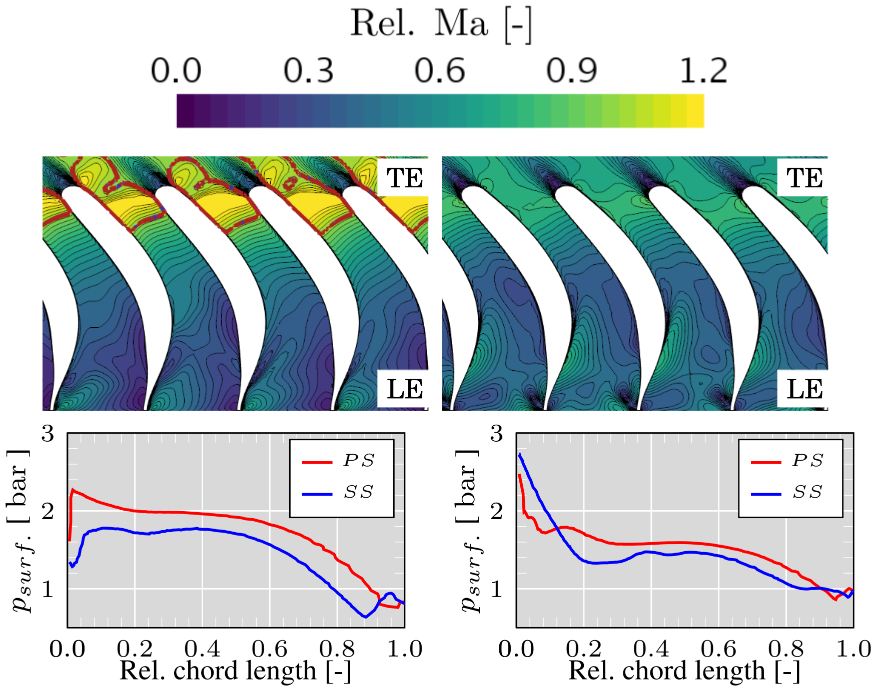

(a) Lower speed at 20% span.

(b) Higher speed at 20% span.

Figure 7.6: Relative Mach number and rotor pressure profile snapshots at 20% rotor span with opened VGT position for lower simulated PR at lower speed (left) and at higher speed (right); red line: $Ma_{rel.} = 1$.

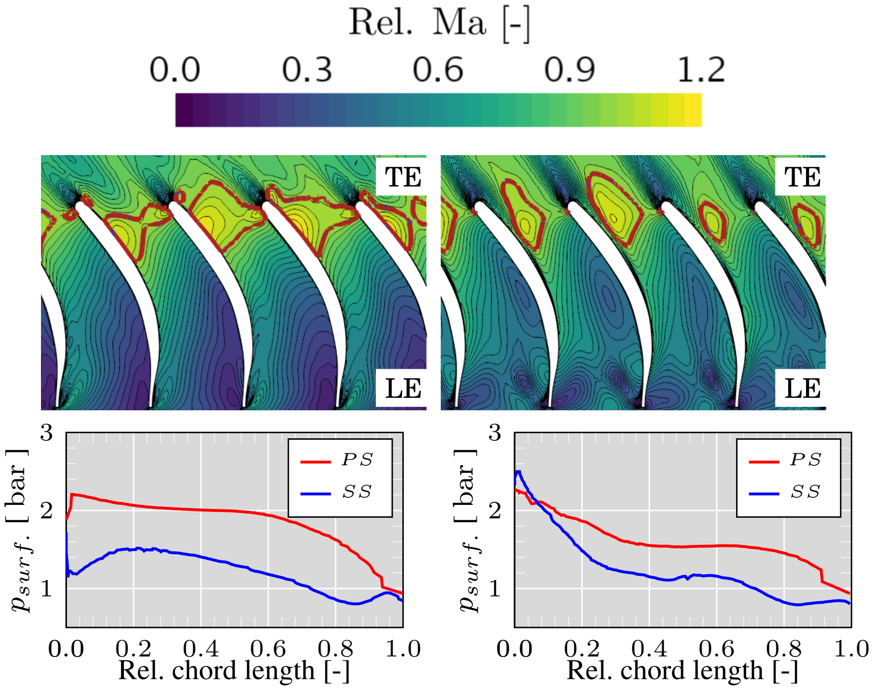

(a) Lower speed at 50% span.

(b) Higher speed at 50% span.

Figure 7.7: Relative Mach number and rotor pressure profile snapshots at 50% rotor span with opened VGT position for lower simulated PR at lower speed (left) and at higher speed (right); red line: $Ma_{rel.} = 1$.

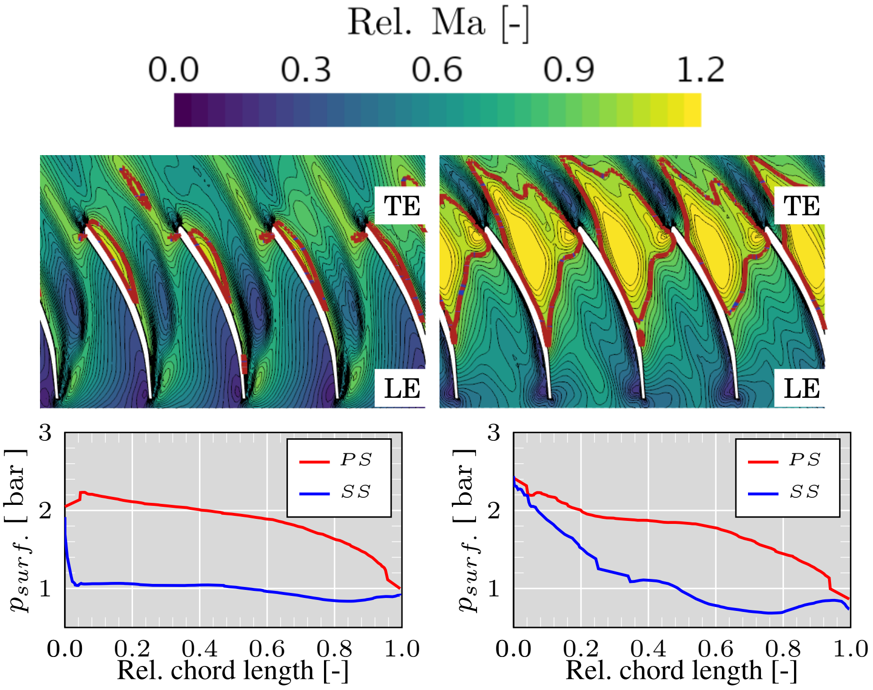

(a) Lower speed at 80% span.

(b) Higher speed at 80% span.

Figure 7.8: Relative Mach number and rotor pressure profile snapshots at 80% rotor span with opened VGT position for lower simulated PR at lower speed (left) and at higher speed (right); red line: $Ma_{rel.} = 1$.

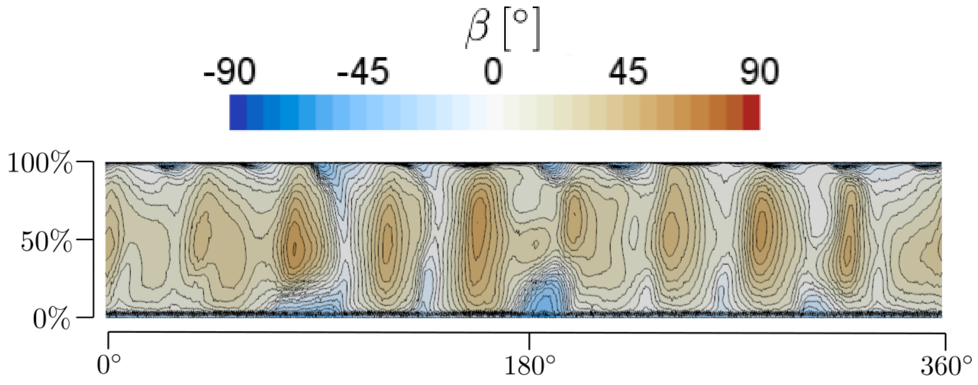

(a) Lower speed at lower PR.

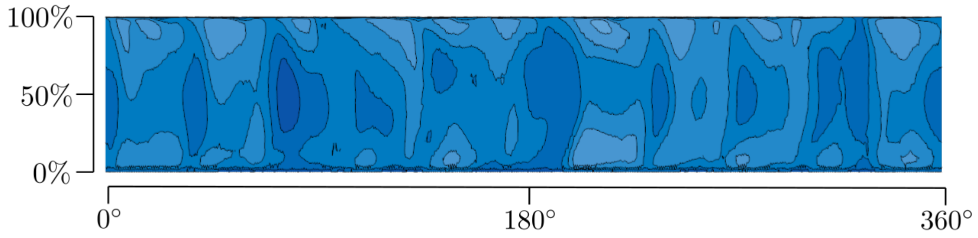

(b) Higher speed at lower PR.

Figure 7.9: Relative rotor inlet angle snapshots of URANS simulations with opened VGT position and lower simulated PR of two speeds at the rotor inlet plane.

The presence of high incidence can be confirmed by the relative inlet flow angle β, presented in Figure 7.9. At lower speed, the relative inlet flow angle is close to its optimum value. At higher speed, the high negative incidence is present over the entire circumference and passage height. Nevertheless, the intensity of the negative incidence becomes slightly less towards the hub and shroud due to the secondary flow structures as tip leakage flow in the stator row. The strong impact of secondary flow, as the stator tip leakage vortexes, causes lower β-angle at the shroud. This might damp the flow acceleration at 80% span less than at lower spans. Additionally, the curvature at higher spans is naturally higher in radial turbines which provokes generally stronger flow acceleration along the same spans. Furthermore, it must be considered that the tip leakage flow [112] and thus, the local avoidance of choking close to the shroud is reduced at higher speeds although the blade loading behaves similar at higher chord lengths. All three effects combined switch the trend that has been observed for lower speed and lead to the observed transition.

7.3 Summary

Analyzing the flow characteristics in the rotor with closed and opened VGT positions, it was found that at closed VGT, the flow at the rotor TE remains subsonic at lower PR and lower speed. In contrast, at higher PR, supersonic regions appear at lower and higher speeds but without generating in the rotor a choked condition. At opened VGT position and lower PR, the flow at the rotor TE is supersonic close to the hub or shroud, depending on the rotational speed. Even the choked flow can be observed to be more developed at elevated PR. At lower speed, tip leakages are related to the subsonic region close to the shroud due to the velocity reduction of the flow when it leaves the tip gap and mixes with the flow going through the main passage. Increasing the PR, the section at the rotor TE becomes almost wholly choked. Furthermore, along a 50% rotor span, strong shock waves appear at TE. On the contrary, at higher speed and lower PR, supersonic flow develops close to the shroud, and the flow near the hubs remains subsonic. When the pressure increases, the flow in the section reaches supersonic conditions except on a region close to the blades PS due to the flow deceleration after passing shock upstream along a 50% rotor span. At middle speed and lower PR, the tip leakage flow is reduced compared with the case of lower speed due to the relative movement of the shroud wall, and the reduction in the pressure difference between tip PS and SS. Thus, a considerable region at the shroud becomes supersonic. When the turbine operates at the higher PR the passage is practically choked remaining a small subsonic region on the PS. Hence, at middle speed the flow experiences a smooth transition from the effects at low speed to the effects at high speed.

The Mach number was evaluated at 20%, 50%, and 80% rotor span and operating at lower PR to extend the above mentioned analysis. At lower speed, the flow becomes supersonic at 20% and 50% span. At higher speed, small supersonic pockets appear at 50% rotor span, while at 80% span, the supersonic region extends blade to blade. Furthermore, the relative inlet angle evaluation shows a profile close to its optimum value at the lower speed. At the higher speed, the rotor inlet presents a high negative incidence, reducing the flow acceleration.

7.4 References

[34] T. Kawakubo. “Unsteady Rotor-Stator Interaction of a Radial-Inflow Turbine With Variable Nozzle Vanes”. In: *Proceedings of ASME Turbo Expo 2010: Power for Land, Sea and Air*. Glasgow, UK, 2010, pp. 2075–2084. DOI: 10.1115/GT2010-23677. URL: https://doi.org/10.1115/GT2010-23677 (cit. on pp. 12, 14, 103).

[90] F. Rubechini, M. Marconcini, A. Arnone, A. S. Del Greco, and R. Biagi. “Special Challenges in the CFD Modeling of Transonic Turbo-Expanders”. In: *ASME Turbo Expo 2013: Turbine Technical Conference and Exposition*. San Antonio, Texas, USA: ASME, 2013, pp. 1–10. DOI: 10.1115/GT2013-95554. URL: https://doi.org/10.1115/GT2013-95554 (cit. on pp. 16, 103).

[112] J. R. Serrano, R. Navarro, L. M. García-Cuevas, and L. B. Inhestern. “Contribution to tip leakage loss modeling in radial turbines based on 3D flow analysis and 1D characterization”. In: *International Journal of Heat and Fluid Flow* 78 (2019), pp. 1–7. ISSN: 0955-5986. DOI: 10.1016/j.ijheatfluidflow.2019.108423. URL: http://www.sciencedirect.com/science/article/pii/S095559861530042X (cit. on pp. 18, 39, 69, 111, 132, 136).

[120] J. R. Serrano, R. Navarro, L. M. García-Cuevas, and L. B. Inhestern. “Turbocharger turbine rotor tip leakage loss and mass flow model valid up to extreme off-design conditions with high blade to jet speed ratio”. In: *Energy* 147 (2018), pp. 1299–1310. ISSN: 0360-5442. DOI: https://doi.org/10.1016/j.energy.2018.01.083. URL: https://www.sciencedirect.com/science/article/pii/S0360544218301014 (cit. on pp. 18, 39, 69, 104, 128, 131, 132).

[168] M. I. Yaras and S. A. Sjolander. “Effects of simulated rotation on tip leakage in a planar cascade of turbine blades: Part I: Tip gap flow”. In: *Journal of Turbomachinery* 114.3 (1992), pp. 652–659. DOI: 10.1115/1.2929189. URL: https://doi.org/10.1115/1.2929189 (cit. on p. 106).

[169] M. I. Yaras and S. A. Sjolander. “Effects of Simulated Rotation on Tip Leakage in a Planar Cascade of Turbine Blades: Part II—Downstream Flow Field and Blade Loading”. In: *Journal of Turbomachinery* 114.3 (1992), pp. 660–667. DOI: 10.1115/1.2929190. URL: https://doi.org/10.1115/1.2929190 (cit. on p. 106).

CHAPTER 8

Exergy Analysis

Contents

8.1 Introduction . . . 116
8.2 Numerical Results . . . 116
8.3 Summary . . . 120
8.4 References . . . 121

Figures

8.1 Considerated planes as the inlet and outlet of the stator and rotor. . 117
8.2 Exergy analysis for the evaluated operational points; lower: 3882 rpm/$\sqrt{\mathrm{K}}$; middle: 5830 rpm/$\sqrt{\mathrm{K}}$; higher: 8421 rpm/$\sqrt{\mathrm{K}}$. . . 118

8.1 Introduction

ACCORDING to the literature, exergy analysis is a method that uses the conservation of mass and conservation of energy principles together with the second law of thermodynamics, for the evaluation, design, and improvement of system and process to make efficient use of the energy. The term exergy comes from the Greek words *ex* and *ergon*, meaning from and work, thus the exergy of a system represents the maximum shaft work that can be extracted from the system at a specified reference environment [170]. The exergy is also a correct parameter to quantify the system performance and indicates how much the system deviates from the ideal performance [171]. This chapter estimates the exergy in each region of the computational domain when the turbine operates with closed and opened stator vanes position at the lower and higher PR and the three rotational speeds considered for this study mentioned in previous chapters.

8.2 Numerical Results

For the turbocharger turbine analysis, the first law of thermodynamics is essential to guarantee the accuracy of energy balance and obtain the turbine performance map. Nevertheless, the first law of thermodynamics alone is insufficient in assisting us in identifying and quantifying the losses and potential improvements in a turbocharger turbine, which is the objective of this chapter. Thus, exergy evaluation is a valuable tool in engineering and is used in this study to deepen the understanding of the losses in turbine aerodynamics. The following parameters are evaluated to carry out the exergy analysis in the turbine domain. The specific exergy flow of a perfect gas is defined by the Equation 8.1,

$$e_f = h_t(T_t) - h_o - T_o\left[s(T_t, p_t) - s_o\right] \tag{8.1}$$

$$\Psi = \oiint_{S^*(t)} \left[\rho e_f (\vec{u} \cdot \vec{n})\right] dS \tag{8.2}$$

where h is the specific enthalpy (subscript t denotes the total quantity), s is the specific entropy and T_o is the dead state temperature, Here, the ambient conditions are used as dead state with T_o = 298.15 K and p_o = 101325 Pa. In order to obtain the net exergy passing through a control surface $S^*(t)$ the Equation 8.2 has been used, where ρ is the density of the fluid, $\vec{u}$ is the velocity vector of the fluid and $\vec{n}$ is the unit normal vector of $S^*(t)$. The exergy in the inlet duct is evaluated between the inlet probe section (see Figure 3.2) and the plane at the outlet of the inlet duct. For the volute, the plane at the outlet of the inlet duct and the stator inlet surface are selected, while for the stator and rotor the corresponding inlet and outlet planes in Figure 8.1 are selected. The vaneless

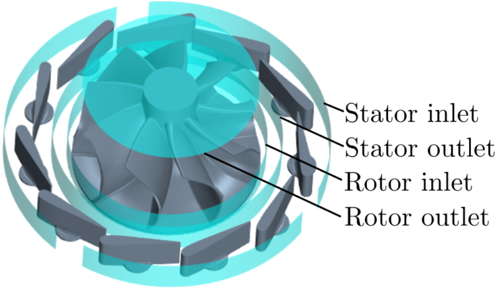

Figure 8.1: Considerated planes as the inlet and outlet of the stator and rotor.

space has been bounded by the stator outlet and the rotor inlet. Finally, the exergy in the outlet was estimated between the rotor outlet surface and the outlet probe section. The Figure 8.2(a) shows the results of the exergy normalized by the exergy at the inlet probe section in each region of the computational domain. The total height of the bar represents the normalized net exergy change within the domain bounded by the inlet probe plane and the outlet probe plane, being a value equal one the maximum reversible work available. The change in the exergy through the inlet duct is negligible and the variation in the volute only represent 1% for the opened VGT position. The fraction corresponding to the stator for the closed VGT is greater than at opened VGT position as it is expected due to the acceleration that suffer the fluid due to the position of the vanes. Furthermore, in this region of the computational domain, with the vanes closed the fraction of the exergy increases 3% points when the PR is increased at both rotational speed (lower and higher). The maximum change corresponds to the case of lower speed and higher PR, which is consistent due the presence of a stronger shock as is depicted in Figure 5.3(d). Regarding to the exergy in the vaneless space, this one is significant at closed VGT position due to the interaction between the rotor and stator which increase the irreversibilities. The bigger fraction of the exergy budget corresponds to the rotor. The remaining fraction corresponds to the outlet representing the entropy generated be the swirl of the flow just at the rotor outlet. It is worth mentioned that the flow exergy loss due to internal irreversibilities can be may due to the entropy generation of viscous friction and the heat transfer across finite temperature difference. Thus, as the presented study is under adiabatic conditions and low inlet temperature the viscous irreversibilities are more significant than the thermal irreversibilities. The ratio of the turbine power over the exergy flow at the inlet probe section was calculated for each operation point and is presented in Figure 8.2(b). For the closed VGT position, it is possible to observe that at lower speed, the ratio of the extracted turbine power over the maximum energy

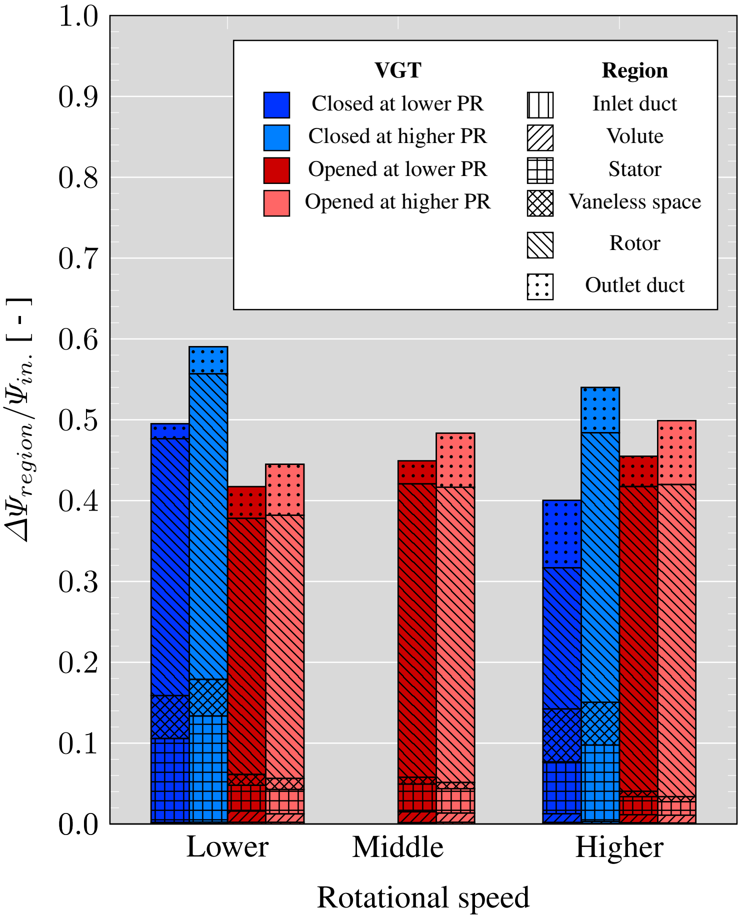

(a) Distribution of the normalized overall exergy in the turbine domain.

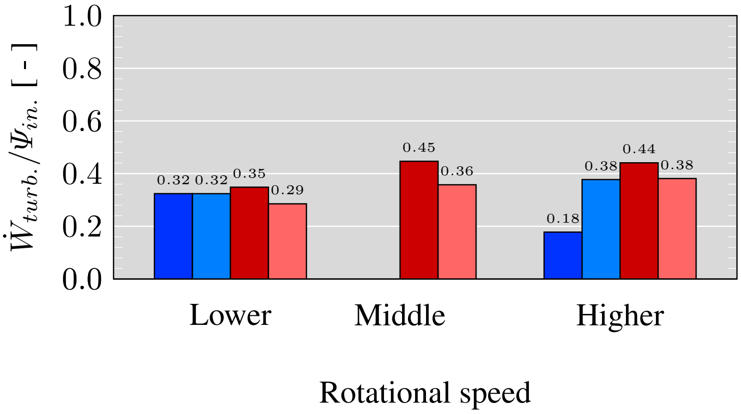

(b) Comparison of the turbine power with respect to the exergy at the inlet probe plane.

Figure 8.2: Exergy analysis for the evaluated operational points; lower: 3882 rpm/$\sqrt{\text{K}}$; middle: 5830 rpm/$\sqrt{\text{K}}$; higher: 8421 rpm/$\sqrt{\text{K}}$.

available at the inlet does not change significantly with increasing the PR, which is in concordance with the small change in the efficiency depicted in Figure 4.2(b). The most significant extraction of the maximum energy corresponds to the case of opened VGT at lower PR and middle speed.

8.3 Summary

An exergy analysis was carried in each region of the computational domain to evaluate the useful work potential of the system operating in an environment with a temperature of 298.15 K and a pressure of 101325 Pa. Starting with the inlet duct and volute, the normalized change in the exergy is negligible in all operational points. In the stator region, the available energy is greater with the vanes at a closed position than when the vanes are opened due to the flow acceleration. Moreover, the maximum variation occurs at lower speed and higher PR due to strong shock waves. Continuing the analysis in the vaneless space and similar to the stator, the corresponding fraction is relevant at closed VGT due to the interaction with the rotor and the extension of the shock waves, while at opened VGT represents a small portion of the net exergy change. The more significant fraction of the exergy budget corresponds to the rotor, which determines the useful shaft work potential. The final fraction corresponds to the outlet representing the energy that is discarded but can be the subject of future studies to take advantage of this budget and improve the turbine performance through changes in its geometry. Focusing on an expression that involves the shaft work, it was found that at closed VGT position and lower speed, the ratio of the turbine power and the available energy at the inlet does not change significantly with increasing the PR. Furthermore, the best use of the maximum energy corresponds to the case of opened VGT at lower PR and middle speed.

8.4 References

[170] I. Dincer and M. A. Rosen. *Exergy*. Ed. by I. D. Rosen and M. A. Ontario, Canada: Elsevier Science, 2013, p. 547. ISBN: 9780080970899. DOI: `https://doi.org/10.1016/C2010-0-68369-6`. URL: `https://www.sciencedirect.com/book/9780080970899/exergy` (cit. on p. 116).

[171] I. Dincer. “Exergy”. In: *Comprehensive Energy Systems*. Vol. 1-5. 2018. Chap. 1.6 Exergy, pp. 212–264. ISBN: 9780128095973. DOI: `10.1016/B978-0-12-809597-3.00106-1`. URL: `https://www.sciencedirect.com/referencework/9780128149256/comprehensive-energy-systems` (cit. on p. 116).

CHAPTER 9

Effects of the variation of the rotor tip gap at high pressure ratios reaching choked flow.

Contents

9.1 Introduction 126
9.2 Geometry description 126
9.3 Performance characteristics 127
9.4 Characteristics of flow through the tip gap 131
9.5 Summary 152
9.6 References 155

Figures

9.1 Geometry of the different tip gaps for the following analysis. 127
9.2 Turbine map based on steady and usteady results; Steady: Dashed lines; Unsteady: Markers 129
9.3 Relation between the reduced mass flow and the area ratio under supersonic conditions. 130
9.4 Relative mass flow fraction passing through the tip gap along the SS. The first two vertical lines of points correspond to lower PR and the last two vertical lines of points correspond to higher PR. 131

9.5 Normal component of the relative velocity on the rotor tip PS and SS for the case of +0pTG at lower PR; Black lines enclose the regions with $Rel.Mach \geq 1$; URANS simulations; The value equal to 1.0 in the abscissa represents the position of the TE. 133
9.6 Normal component of the relative velocity on the rotor tip SS for the case +0pTG; Black lines enclose the regions with $Rel.Mach \geq 1$; URANS simulations; The value equal to 1.0 in the abscissa represents the position of the TE. 134
9.7 Mass flux on SS at lower PR and both rotational speeds; URANS simulations. 135
9.8 Mass flux on SS at higher PR for the case of +0pTG; URANS simulations. 136
9.9 Scraping ratio evaluated at different tip gaps; The value equal 1.0 in the abscissa represents the position of the TE. 136
9.10 Flow behaviors for the case of +0pTG along a meridional line at the middle of the SS tip gap of the -50pTG case (Figure 9.1); for the two analyzed PR and two rotational speeds; URANS simulations. 138
9.11 Relative Mach number, static pressure difference and relative total pressure difference evaluated along a meridional line at the middle of the tip gap of the -50pTG case (Figure 9.1); URANS simulations. . 139
9.12 Rotor pressure profile at 80% and 95% rotor span for lower simulated PR; URANS simulations. 140
9.13 Relative Mach number snapshots at 80% rotor span for lower simulated PR at lower speed (left) and at higher speed (right); red line: $Ma_{rel.} = 1$. 142
9.14 Relative velocity streamlines RANS simulations through the rotor Tip and rotor TE; gray streamlines: Main flow from rotor passage; streamlines in the inferno color scale: Flow from tip PS. 143
9.15 Relative velocity streamlines from the rotor TE going through two points: the first one closer to the shroud: blue streamline and the second one closer to the hub: orange streamline; RANS simulations . 145
9.16 Relative Mach number and static pressure evolution along streamlines close to the shroud and hub (Figure 9.15); The value equal to 1.0 in the abscissa represents the position of the TE; RANS simulation146
9.17 Tangential, radial and axial component of the relative velocity along streamlines close to the shroud and hub (Figure 9.15); The value equal to 1.0 in the abscissa represents the position of the TE; RANS simulation 148
9.18 Relative velocity streamlines going through two points: the first one closer to the inducer: blue streamline and the second one closer to the exducer: orange streamline; RANS simulations 149

9.19 Entropy generation rate normalized along streamlines close to the inducer and exducer (Figure 9.18); the value equals 1.0 in the abscissa represents the position of the TE; blue vertical dashed line: the position where the streamline enters the PS tip gap at the inducer; orange vertical dashed line: the position where the streamline enters the tip gap PS at the exducer; RANS simulation. 150
9.20 Entropy generation rate normalized along streamlines close to the hub (Figure 9.15); the value equals 1.0 in the abscissa represents the position of the TE; RANS simulation. 151

Tables

9.1 Turbine geometry description. 126
9.2 Variation of the performance parameters with respect to the original geometry (+0pTG). 130

9.1 Introduction

In Chapter 7 was analyzed the flow through the rotor when reaching choked condition. The results revealed how the supersonic region distribution changes depending on the rotational speed and the effect of the rotor tip leakage, which is driven by the pressure difference between the PS and SS. The tip gap between the rotor blade and the wall casing is required for the turbine correct operation. Nevertheless, the flow passing through the tip is largely unturned, representing a decrease in the shaft work. Thus, this chapter analyzes the effects of the variation on the tip gap height on the main rotor flow and the flow characteristics through the tip gap when the turbine operates reaching choked conditions. For the analysis, a meridional plane along the tip gap, a plane at the rotor TE and at 80% rotor span has been considered, as well as the pressure profiles at 80% and 95% rotor span and different streamlines to deepen in the analysis.

9.2 Geometry description

Table 9.1: Turbine geometry description.

	Rotor			
Blade number	9			
Inlet diameter	41 mm			
Outlet diameter	38 mm			
Outlet blade angle	59°			
Case	+0pTG	-50pTG	-25pTG	+50pTG
Tip gap	0.36-0.40 mm	0.18-0.20 mm	0.27-0.30 mm	0.54-0.60 mm

The variable geometry turbine selected for this study has been modified considering three variations in the geometry of the rotor tip gap. The first two configurations correspond to a decrease in the gap of the 25% and 50% with respect to the original geometry and which will be denoted as -25pTG and -50pTG, respectively. The third case corresponds to an increase in the gap of 50% and will be donated as +50pTG. The tip gap of the original geometry given by the manufacturer will be denoted as +0pTG. The stator blade angle α is set equal to 53.45° that represents 80% VGT opening (Figure 3.1) to obtain chocked flow at the rotor outlet as depicts Chapter 7. Table 9.1 presents the dimensions and features of the rotor passage, and a scheme of the tip gap variation is shown in Figure 9.1. Furthermore, it is essential to remark that modification of the tip profile as a consequence of the thermal and rotational deformation of the rotor blade [69] is not considered in the study.

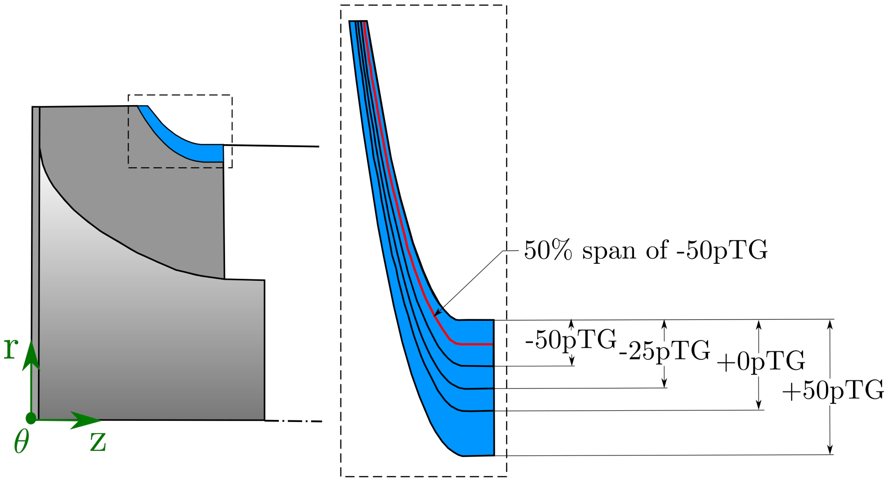

Figure 9.1: Geometry of the different tip gaps for the following analysis.

9.3 Performance characteristics

Using the boundary conditions described in Chapter 3, the reduced mass flow (Equation 4.1) and the isentropic efficiency total-to-static (Equation 4.2) at opened VGT position of all simulated operating points in URANS simulations are depicted in Figure 9.2. These data correspond to the lower and higher rotational speed, which have a value of 3882 and 8421 rpm/$\sqrt{\mathrm{K}}$, respectively. Furthermore, the RANS results obtained with the original geometry of +0pTG evaluated at low and high PR are included in the figure to remark the trend of the operational points at a constant rotational speed. Figure 9.2(a) shows that the reduced mass flow increases for the rising tip gap as the pressure losses decrease. At lower speed, the higher the tip gap is, the higher the PR obtained due to a reduction in the static pressure at the probe section. In addition, at lower speed, with rising tip gap a higher turbine enthalpy drop is needed to drive the rotor at a constant speed. While at higher speed, the increase in the tip gap generates a decrease in the PR as the static pressure close to the rotor TE increases. At higher speed the flow behavior through the tip gap is quite different compared with the case at lower speed and will be analyzed in more detail in the following section. Regarding the isentropic efficiency, it decreases when enlarging the tip gap as shown in Figure 9.2(b) against the blade speed ratio (BSR), defined in Equation 4.5. The reduction in the efficiency is due to the generation of entropy as the flow through the tip gap mixes with the main flow. Table 9.2 presents the deviation of the PR, the reduced mass flow and the efficiency with respect to the original geometry of +0pTG. An improvement of around 1.5% points can be achieved with a reduction in the tip gap of 50% at lower speed, while at higher speed, the increase in the efficiency is almost 3% points. Furthermore, a rise of 50% in the gap penalizes the efficiency up to 3% when the turbine operates at lower PR and higher speed.

The enlargement of the area of the plane at the rotor TE as a consequence of the increase in the tip gap contributes to the increase of the reduced mass flow and affects the sonic conditions at this plane. Figure 9.3 depicts the relation between the reduced mass flow and the area ratio under supersonic conditions. On the one hand, at lower speed, a lack of explicit trend is observed, implying that there is no substantial impact on the chocked area as the tip gap increases. On the other hand, at higher speed, the growth of the tip gap reduces the chocked area. To go deeper in this phenomenon, first the behavior of the flow through the tip gap is analyzed, where different regions can be distinguished. These regions correspond to the positive and negative tip leakage streams, where the negative flow (scraping flow) is caused by the relative case motion and goes from the SS to the PS [119]. In contrast, the positive flow is driven by the pressure difference between PS and SS. The negative and positive tip leakage mass flows can be evaluated according to Equation 9.1 and Equation 9.2 and are summed in Equation 9.3 [120] to analyze the impact as the tip gap variates. Figure 9.4 shows how the ratio of the tip leakage on the SS of the gap and the turbine inlet mass flow rises with the enlargement of the tip gap at constant rotational speed. The maximum ratio is 1.05%, which occurs in the case of +50pTG at lower speed and higher PR. That means that 1.05% of the stage mass flow rate does not contribute to driving the rotor of the radial inflow turbine. Concerning the original geometry of +0pTG, the relative mass flow that passes the gap decreases around 50% and increases around 60% for the cases with -50pTG and +50pTG respectively. Furthermore, as the rotational speed goes from the lower to the higher value, in the operational conditions of lower PR as well as for higher PR, the value of the relative mass flow slightly drops, being 6% the highest fall for the case of -25pTG at lower PR and reaching the higher speed, while for the case of +50pTG at higher PR the ratio remains constant. From the point of view of increasing the PR at a constant speed, growth in the relative mass flow can also be observed; however, some operational conditions generate a different behavior. The following points stand out: -50pTG at higher speed with growth of 8%, the case of +0pTG at lower and higher speed without any change and with a decrease of 4%, respectively. This supports the complexity and importance of the tip leakage flow and the impact on the performance parameters at off-design conditions.

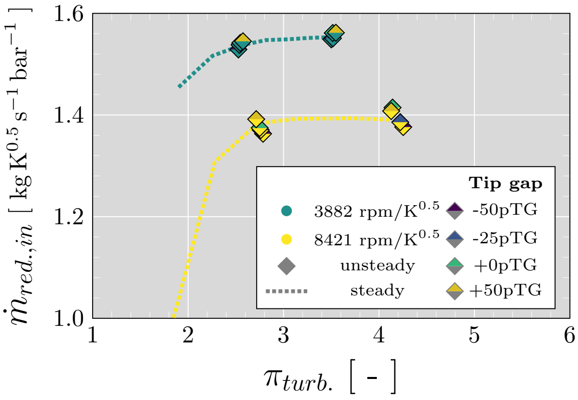

(a) Reduced mass flow map.

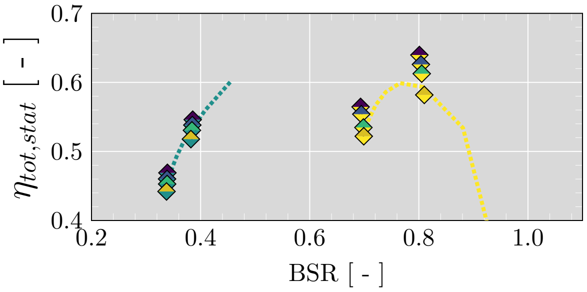

(b) Efficiency VS. BSR map.

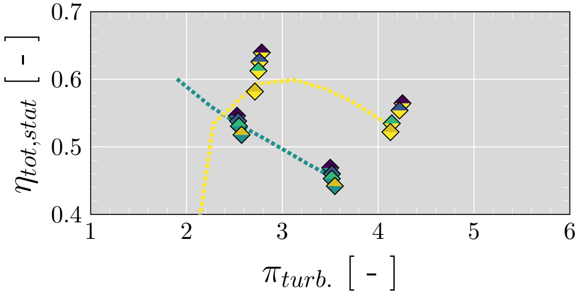

(c) Efficiency VS. PR map.

Figure 9.2: Turbine map based on steady and usteady results; Steady: Dashed lines; Unsteady: Markers

Table 9.2: Variation of the performance parameters with respect to the original geometry (+0pTG).

$N_{red.}$ $\left[\frac{\text{rpm}}{\sqrt{\text{K}}}\right]$	Ref. PR	Tip gap	Dev. $\pi_{turb.}$ [%]	Dev. $\dot{m}_{red.}$ [%]	$\Delta\eta_{t,s}$ [% points]
3882	lower	-50pTG	-0.79	-0.84	1.55
		-25pTG	-0.35	-0.25	0.76
		+0pTG	0	0	0
		+50pTG	1.08	0.21	-1.27
	higher	-50pTG	-0.44	-0.79	1.62
		-25pTG	0.05	-0.67	0.73
		+0pTG	0	0	0
		+50pTG	0.92	0.03	-1.08
8421	lower	-50pTG	1.28	-0.83	2.70
		-25pTG	0.41	-0.31	1.34
		+0pTG	0	0	0
		+50pTG	-1.34	1.25	-3.07
	higher	-50pTG	2.70	-2.70	2.99
		-25pTG	1.95	-2.03	1.93
		+0pTG	0	0	0
		+50pTG	-0.35	-0.48	-1.27

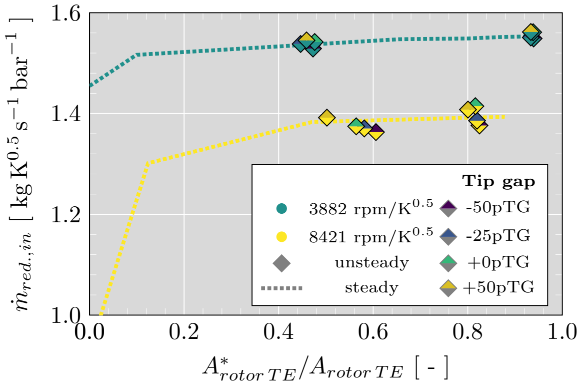

Figure 9.3: Relation between the reduced mass flow and the area ratio under supersonic conditions.

$$\frac{\dot{m}_{tip,-}}{\dot{m}_{turb.}} = \frac{|\int \rho \cdot \omega_{\perp,tip.-} \cdot dA_- |}{\dot{m}_{turb.}} \tag{9.1}$$

$$\frac{\dot{m}_{tip,+}}{\dot{m}_{turb.}} = \frac{\int \rho \cdot \omega_{\perp,tip.+} \cdot dA_+}{\dot{m}_{turb.}} \tag{9.2}$$

$$\frac{\dot{m}_{tip}}{\dot{m}_{turb.}} = \frac{\dot{m}_{tip,-}}{\dot{m}_{turb.}} + \frac{\dot{m}_{tip,+}}{\dot{m}_{turb.}} \tag{9.3}$$

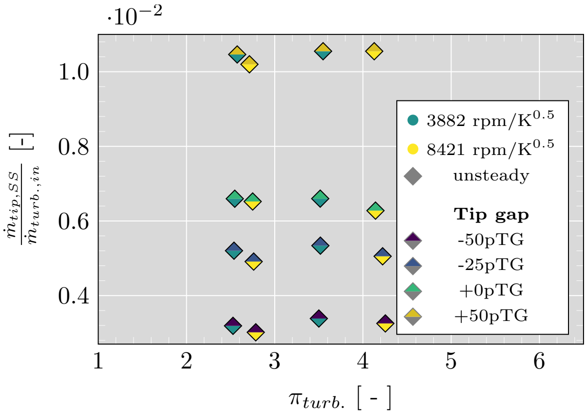

Figure 9.4: Relative mass flow fraction passing through the tip gap along the SS. The first two vertical lines of points correspond to lower PR and the last two vertical lines of points correspond to higher PR.

9.4 Characteristics of flow through the tip gap

After presenting the effects in the performance parameters and before analyzing the interaction with the main flow, the flow behavior in a meridional plane along the tip gap is used to analyze the tip leakage flow. First, the results from the case of +0pTG at lower PR and both rotational speeds will be analyzed. Considering Figure 9.5, it can be seen that the flow accelerates when going from the PS to the SS. At lower speed, Figure 9.5(a) and 9.5(c), the positive flow covers most of the tip gap area. While at higher speeds, Figure 9.5(b) and 9.5(d), a considerable region of negative flow induced by the shroud friction appears on the tip gap with the normal component of the relative velocity diminishing as the flow goes from the SS to the PS. The decrease of the positive tip leakage in the rotor inlet region might also be caused by a relative rotor inlet angle with higher negative incidence [120]. Regarding to the development of sonic conditions, at both rotational speeds, the flow entering through the PS close to the TE already present a relative Mach number above one and accelerates further as the flow reach the SS, especially in the region between 0.75 and 1.0 axial relative length close to the shroud. Focusing on the region of the tip gap along the SS, a more significant change occurs when the rotational speed increases rather than with an increase in the PR as Figure 9.6 shows. When the PR rises at both rotational speeds, and thus the blade loading, an increase in the positive leakage flow is visible over the tip gap. Furthermore, the case of higher rotational speed presents a reduction in the extension of the negative flow along the axial direction. Thus, the ratio between the negative tip leakage mass flow rate and inlet mass flow rate at higher speed decreases around 23% when the turbine operates at higher PR with a corresponding increase in the positive tip leakage. At higher speed, the entire region between 0.75 and 1.0 axial relative length becomes supersonic and the extension changes rather less when the PR rises. When the tip gap varies a similar behavior can be observed. To analyze the mass flux in the normal direction through the gap and the effects of the variation the tip gap Figure 9.7 is presented for the cases at lower PR and both rotational speeds. Based on the left side of Figure 9.7 is possible to observe that at lower speed the negative flow does not change significantly despite the growth in the tip gap, due to the relative motion of the flow close to the shroud wall remaining constant. The location of the maximum positive flux remains in the region around 0.95 relative radial length and 0.85 relative axial length, but its magnitude is increased as the tip gap grows. Furthermore, close to the TE ($z/H_{rot.bl.} = 1$) the mass flux gets higher with increasing tip gap. The right side of the Figure 9.7, which corresponds to the higher speed, shows that the negative mass flux fills more than half of the tip gap in the region between the LE and 0.65 relative length in the axial direction. Thus, less positive tip leakage mass flux passes through the tip gap in this region and diminishes even more as the tip gap decreases. This is particularly clear for the case of -50pTG (Figure 9.7(b)), with almost the entire gap occupied with scraping flow in the inducer region. Hence, during the manufacturing process is more important to keep small clearances in the exducer than in the inducer in order to affect less the efficiency. Comparing the left and right sides of Figure 9.7, on the one hand, losses generated by positive tip flow can be reduced at higher speed. On the other hand, new losses must be taken into account by the entropy generated due to the negative tip flow [112]. At higher PR similar trend as described above can be observed as Figure 9.8 shows for the case of +0pTG. Comparing the results in Figure 9.7(e) and 9.7(f) with the results presented in Figure 9.8 is possible to state that increasing PR leads to higher positive mass flux through the tip gap as described by Deng et al. [172] and Serrano et al. [120]. One can state that the negative mass flow is associated to the rotor speed, while the positive mass flow is rather correlated with the PR.

The scraping ratio can be used to explain and quantify the impact of the different

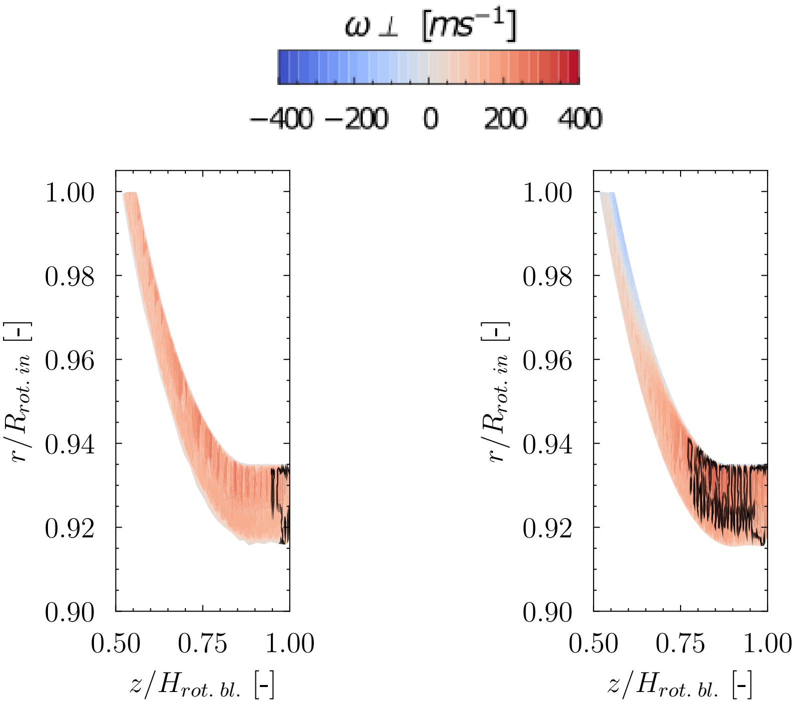

(a) Lower speed PS.

(b) Higher speed PS.

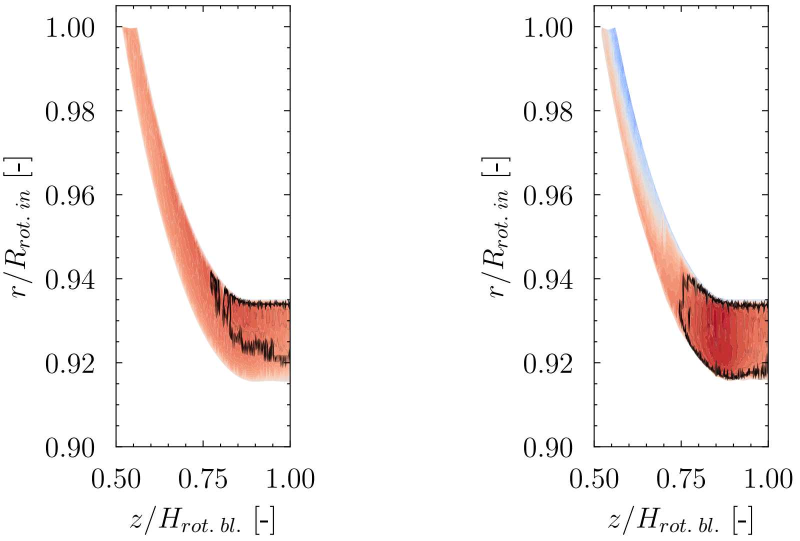

(c) Lower speed SS.

(d) Higher speed SS.

Figure 9.5: Normal component of the relative velocity on the rotor tip PS and SS for the case of +0pTG at lower PR; Black lines enclose the regions with $Rel.\,Mach \geq 1$; URANS simulations; The value equal to 1.0 in the abscissa represents the position of the TE.

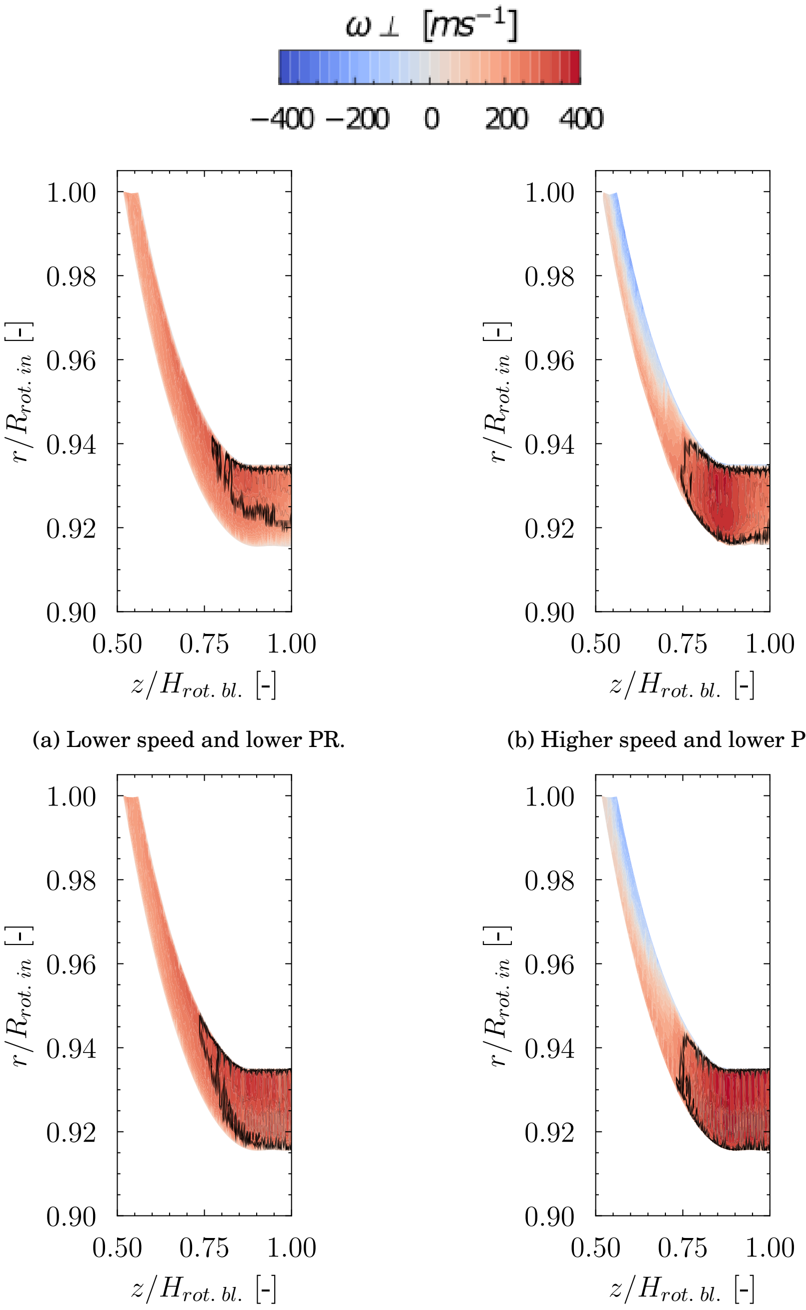

(a) Lower speed and lower PR.

(b) Higher speed and lower PR.

(c) Lower speed and higher PR.

(d) Higher speed and higher PR.

Figure 9.6: Normal component of the relative velocity on the rotor tip SS for the case +0pTG; Black lines enclose the regions with $Rel.Mach \geq 1$; URANS simulations; The value equal to 1.0 in the abscissa represents the position of the TE.

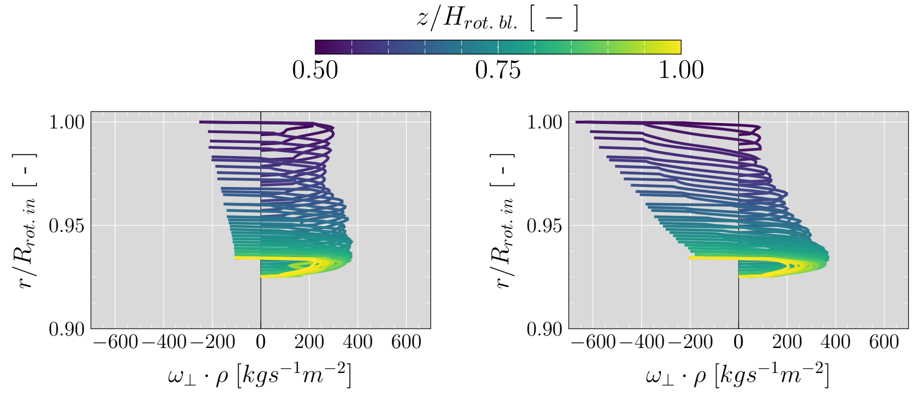

(a) Lower speed -50pTG.

(b) Higher speed -50pTG.

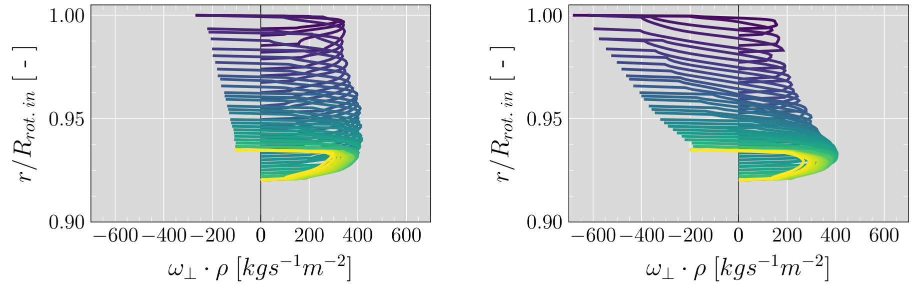

(c) Lower speed -25pTG.

(d) Higher speed -25pTG.

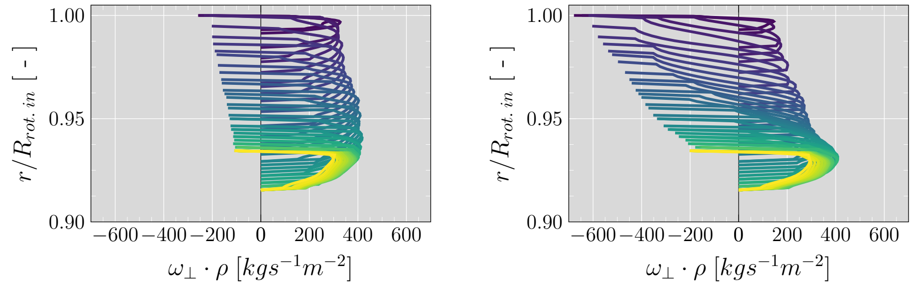

(e) Lower speed +0pTG.

(f) Higher speed +0pTG.

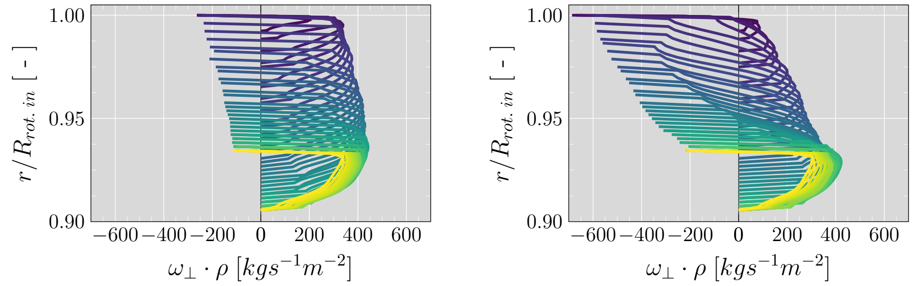

(g) Lower speed +50pTG.

(h) Higher speed +50pTG.

Figure 9.7: Mass flux on SS at lower PR and both rotational speeds; URANS simulations.

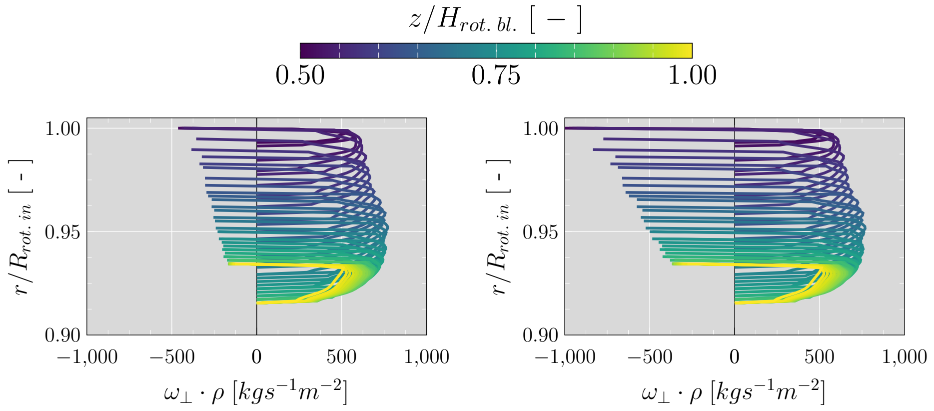

(a) Lower speed.

(b) Higher speed.

Figure 9.8: Mass flux on SS at higher PR for the case of +0pTG; URANS simulations.

physic mechanisms that drive tip leakage flow. This parameter is the momentum ratio of the positive tip leakages and the negative tip leakages defined in Equation 9.4 [112] and represented in Figure 9.9.

$$R = \frac{\rho_{+} \cdot \bar{\omega}^{2}_{tip,\perp,+}}{\rho_{-} \cdot \bar{\omega}^{2}_{tip,\perp,-}} \tag{9.4}$$

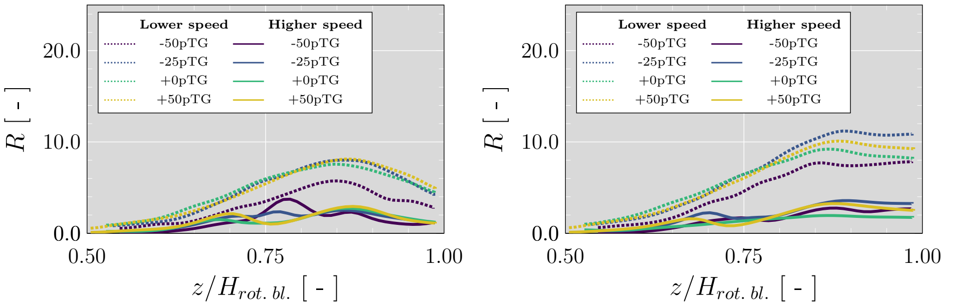

(a) Lower PR.

(b) Higher PR.

Figure 9.9: Scraping ratio evaluated at different tip gaps; The value equal 1.0 in the abscissa represents the position of the TE.

At lower PR and lower speed, Figure 9.9(a), a scraping ratio greater than one is presented in the major part of the relative axial length, indicating a small influence of the negative tip leakages flow and with a maximum peak around

0.85 relative axial length (also visible in Figure 9.6(a)) and which decreases together with the gap. At same PR and higher speed a scraping ratio minor than one between the LE and 0.65 indicates a dominant role of the dragged fluid in this region and which is depicted in Figure 9.6(b). Furthermore, for reductions in the tip gap until 25%, the leakage flow pattern did not change significantly in the exducer region, which agrees with the experimental study carried out by Dambach et al. [173]. When the PR reaches the higher analyzed value, Figure 9.9(b), the strong effect of the positive tip leakages at lower speed is notorious from 0.75 relative axial length as the flow became supersonic and reaches higher values than at lower PR and tending to be constant as the flow approach to the LE. This last constant behavior of the scraping ratio is also presented at higher speed close to the TE. The constant trend is due to the fact that under higher PR and lower speed as well as at higher speed almost the entire section of a plane at the rotor TE is chocked as was mentioned in Chapter 7.

To analyze the sonic conditions along the tip gap at the SS, the meridional red line indicated in Figure 9.1 was selected to evaluate different parameters. For the aforementioned line and the geometry of +0pTG, Figure 9.10(a) shows the evolution of the relative Mach number. At higher PR and both rotational speeds, the sonic condition is reached at 0.75 relative axial length, while at lower PR shifts downstream. Analyzing the normal component of the relative velocity shown in Figure 9.10(b) at higher speed is possible to identify three regions. The first one is near the LE at 0.55 relative axial length, where the relative motion of the casing (perpendicular to the blade) is high, and thus, dragged flow through the gap creates negative tip leakage. The second region appears as the flow moves downstream. Here, shroud relative motion has been decreased due to the reduced radius, whereas the local blade angle at the tip has increased. Thus, negative tip leakage perpendicular to the blade is decreased, and the positive tip leakage becomes more important as the blade loading over the tip increases, as will be shown further [173]. The third region is a drop-off in the relative velocity normal to the tip gap in the exducer area, where the scraping action relative to the pressure difference between both sides of the rotor blade has been already reduced [174]. However, at higher PR the dip in the relative velocity normal to the tip gap is less and trend to became constant as the rotor outlet is almost chocked. The sonic conditions mentioned above can also be noted with the drop in the static pressure that Figure 9.10(c) shows, as well as the slight increase in the pressure at the exducer region as a consequence of the reduction in the relative velocity normal to the tip gap. Figure 9.10(d) depicts how the relative total pressure remains without a significant change as flow goes through the gap without turning into shaft work. However, the relative total pressure decreases close to the exducer region at higher speed and both PR.

To analyze the impact of the variation in the tip gap on the sonic conditions, the meridional line depicted in Figure 9.1 is again considered. Figure 9.11(a)

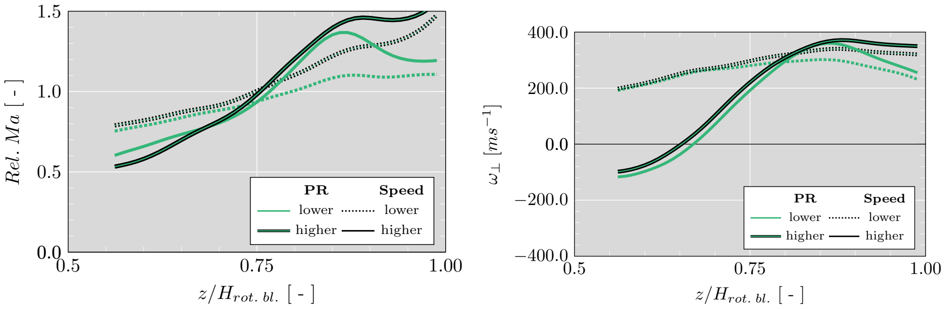

(a) Relative Mach number.

(b) Normal component of the relative velocity.

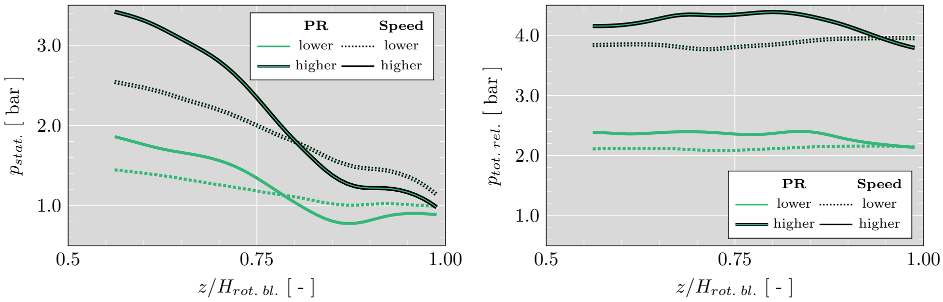

(c) Static pressure.

(d) Relative total pressure.

Figure 9.10: Flow behaviors for the case of +0pTG along a meridional line at the middle of the SS tip gap of the -50pTG case (Figure 9.1); for the two analyzed PR and two rotational speeds; URANS simulations.

and 9.11(b) confirms how the flow accelerates when passing from the PS to the SS, especially after 0.75 relative axial length where the blocking effect of the negative tip leakage diminishes and the flow reaches supersonic conditions on the SS. The relative Mach number decreases together with the tip gap, especially for -50pTG and even more at higher speeds, where the scraping flow is higher than at the rest of the analyzed tip gaps. Considering Figure 9.11(c) and 9.11(d), it is possible to observe that the average difference between the static pressure on the PS and SS (load) along the selected meridional line is slightly greater at lower speed than at higher speed, representing a stronger driving potential for the tip leakage. Furthermore, the difference in the static pressure decreases as the tip gap increases from around 0.75 relative axial length. The lines collapse together as the flow approaches the TE, confirming that the tip leakage flow pattern does not change significantly with varying the tip gap in the exducer region since the flow here is supersonic. Upstream of the point of 0.75 relative axial length, the driving pressure difference is affected by the negative tip leakage, especially at higher speed. At higher speed, the pressure

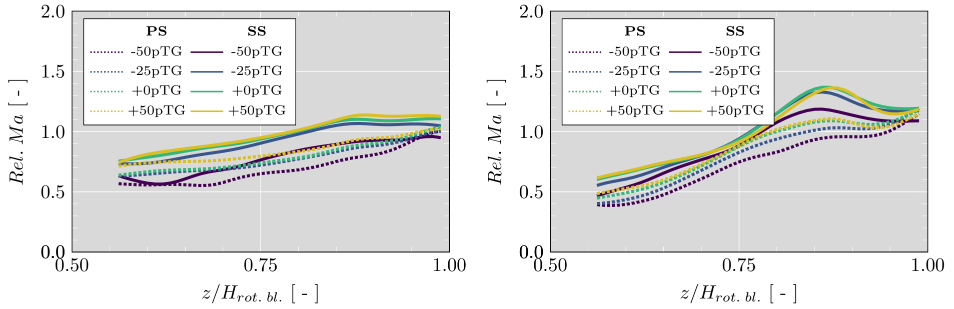

(a) Rel. Ma lower speed at lower PR.
(b) Rel. Ma higher speed at lower PR.

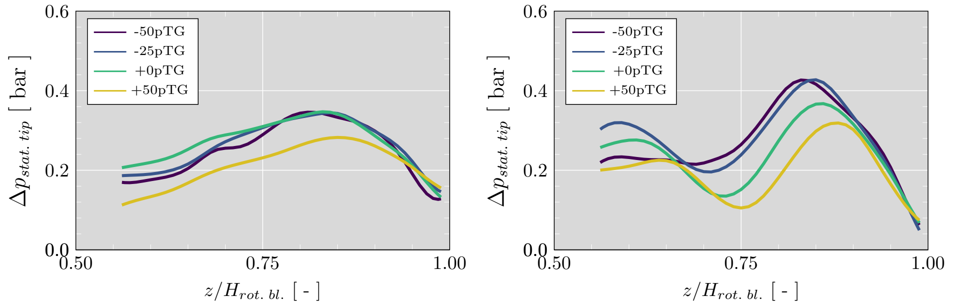

(c) Static pressure difference between tip PS and SS, lower speed at lower PR.
(d) Static pressure difference between tip PS and SS, higher speed at lower PR.

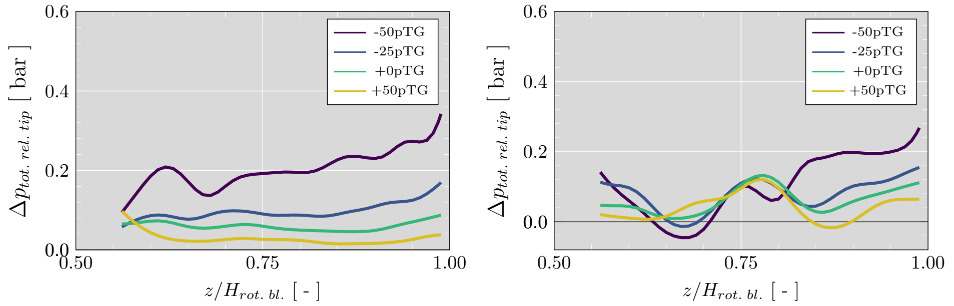

(e) Rel. total pressure difference between tip PS and SS, lower speed at lower PR.
(f) Rel. total pressure difference between tip PS and SS, higher speed at lower PR.

Figure 9.11: Relative Mach number, static pressure difference and relative total pressure difference evaluated along a meridional line at the middle of the tip gap of the -50pTG case (Figure 9.1); URANS simulations.

loading from the inducer drops for all cases except for -50pTG until a relative length between 0.70 and 0.75; then, the pressure difference starts to increase as the flow continues accelerating through the tip gap, reaching a higher Mach number. These results reflect the challenge and importance of modeling the effect of negative tip leakage in the inducer and mid-section by means numerical 1D models, since a successful prediction of the leakage mass flow rate will have a significant impact on turbine losses. The difference in the relative total pressure between PS and SS at lower speed depicted at Figure 9.11(e) shows an almost constant trend for all cases except -50pTG, as the flow through the tip is not used to drive the rotor. However, at higher speed Figure 9.11(f), the difference presents several fluctuations due to the interactions between the negative and positive tip leakages.

9.4.1 Effects of tip leakage on rotor blade

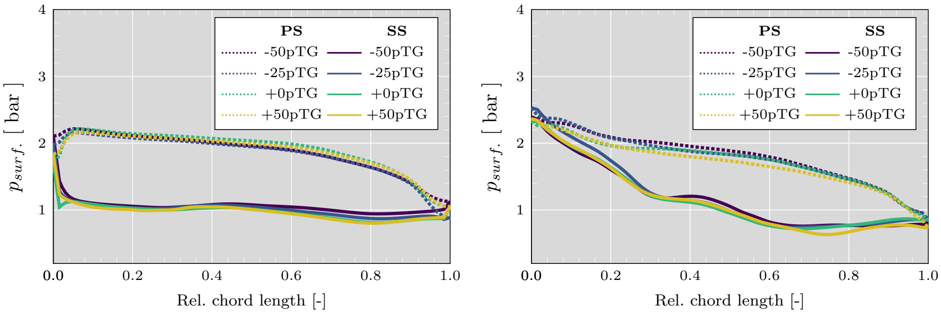

(a) Lower speed and lower PR at 80% span. (b) Higher speed and lower PR at 80% span.

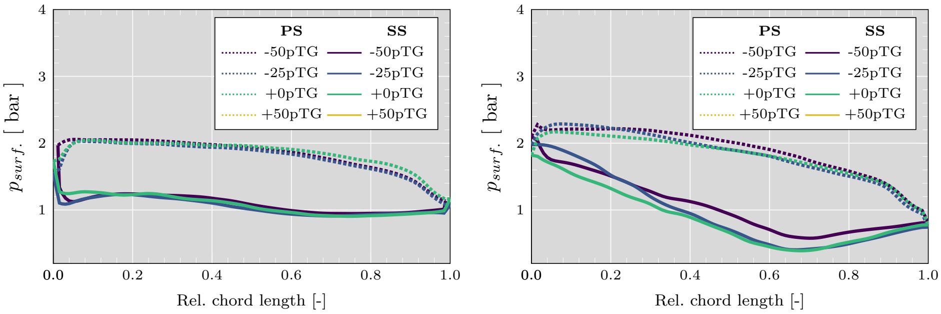

(c) Lower speed and lower PR at 95% span. (d) Higher speed and lower PR at 95% span.

Figure 9.12: Rotor pressure profile at 80% and 95% rotor span for lower simulated PR; URANS simulations.

The PS and SS pressure profiles at 80% and 95% span for different tip gaps both at lower and higher speed for the case of lower PR are displayed in Figure 9.12, to analyze the impact of the tip leakage on the blade loading. The pressure profile of +50pTG is not considered at 95% span because it does not cover the whole length of the blade. The Figure 9.12(a) depicts that the pressure difference between the PS and SS of the blade increases from the LE to the TE, with a maximum located between 0.1 and 0.3 relative chord length for the case of lower speed. The pressure at the inducer region increases with rotational speed, Figure 9.12(b). However, the load decreases and the maximum peak occurs around 0.6 relative chord length. Furthermore, the effects on blade loading depends on the span location. As the thickness of blade decreases from the hub to the shroud, the load increases in the same direction at higher speed as shown in Figure 9.12(b) and Figure 9.12(d), while at lower speed the load decreases from 80% to 95% rotor span as shown in Figure 9.12(a) and Figure 9.12(c). Figure 9.12 also depicts that a reduction in the tip gap height at lower speed and 80% span does not affect significantly the pressure profile on the PS although it generates a slight increase of the pressure on the SS from 0.6 to 1.0 relative chord length, while at 95% span the pressure decrease slightly on the PS from 0.6 to 1.0 relative chord length. At higher speed, a reduction in the tip gap height leads to increased pressure on the PS and on the SS, especially at 95% span. As the surface between two pressure curves is an indicator for the specific aerodynamic work of the blade, the changes mentioned above on the PS and SS generate a reduction in the area formed by the PS and SS pressure line, indicating a lower need for blade loading for the same turbine power. Thus, the turbine efficiency rises, decreasing tip gap heights, as depicted by Figure 9.2. This impact is more significant at higher speed, as displayed in Table 9.2. Moreover, at lower speed, the PS relative velocity increases steadily as the static pressure decreases on the PS from the LE to the TE. Along the SS, the static pressure decreases as the relative velocity increases toward the passage throat until reaching sonic conditions (around 0.6 relative chord length, see Figure 9.12(a)) and generates a small supersonic pocket on the SS, as depicts in Figure 9.13 left side. At higher speed, the static pressure has a steeper drop than at lower speed. The rise in the static pressure on the SS due to the supersonic conditions shifts upstream (around 0.4 relative chord length, see Figure 9.12(b)) compared with the case at lower speed. The supersonic pocket extends until the rotor passage outlet and reaches the PS of the neighboring blade at the TE, as shown in Figure 9.13 right side. Furthermore, the variation of the tip gap height affects the supersonic conditions.

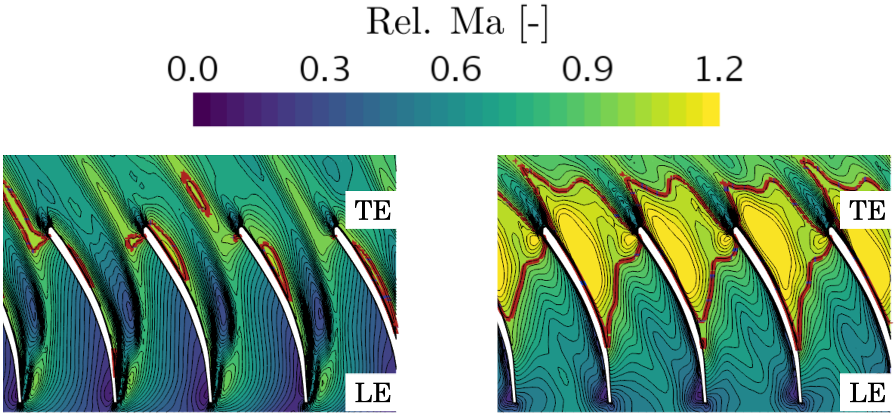

(a) Lower speed at lower PR -50pTG. (b) Higher speed at lower PR -50pTG.

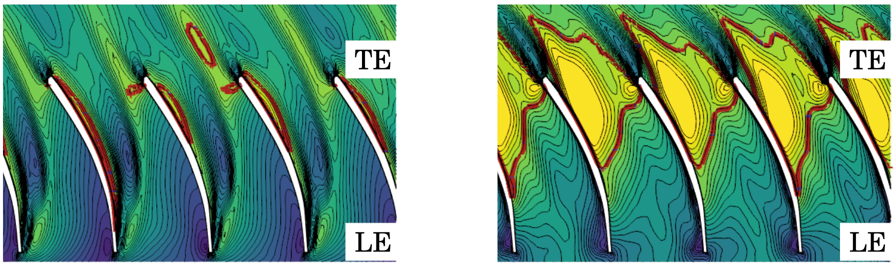

(c) Lower speed at lower PR -25pTG. (d) Higher speed at lower PR -25pTG.

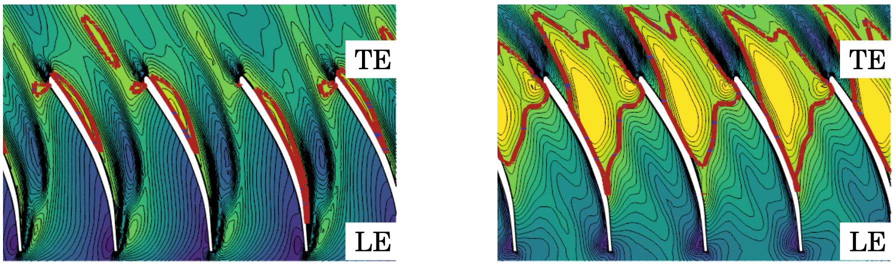

(e) Lower speed at lower PR +0pTG. (f) Higher speed at lower PR +0pTG.

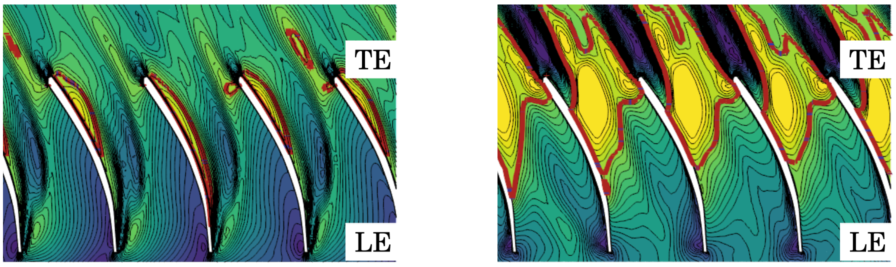

(g) Lower speed at lower PR +50pTG. (h) Higher speed at lower PR +50pTG.

Figure 9.13: Relative Mach number snapshots at 80% rotor span for lower simulated PR at lower speed (left) and at higher speed (right); red line: $Ma_{rel.} = 1$.

The subsonic region close to the TE on the SS extends upstream and slightly in the direction of the neighboring blade as the tip gap increases due to the expansion of secondary flow vortex, explaining the rise in the static pressure at around 0.70 relative chord length presented in Figure 9.12(b).
At lower speed, the leakage flow from the gap in the exducer region blends with the passage main flow and forms a passage vortex [174, 175], generating a subsonic region at rotor TE depicts in Figure 9.14 left side. However, the increase in the tip gap height does not affect the choked area at the TE significantly, as discussed in Figure 9.3.

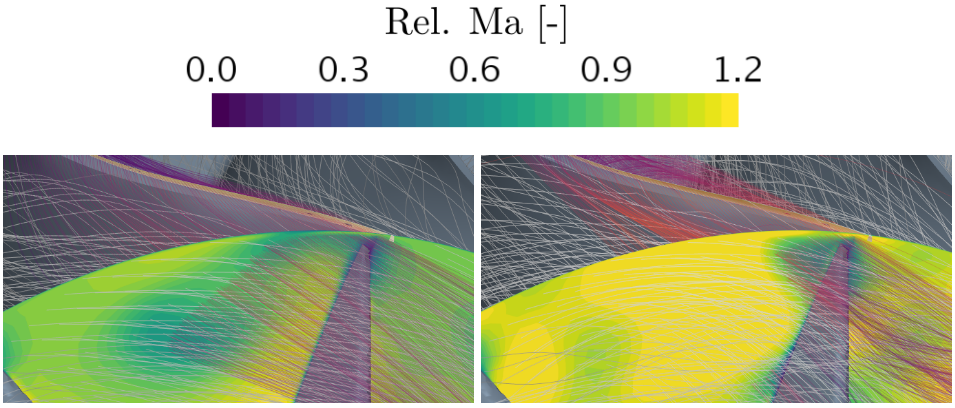

(a) Lower speed at lower PR -50pTG.

(b) Higher speed at lower PR -50pTG.

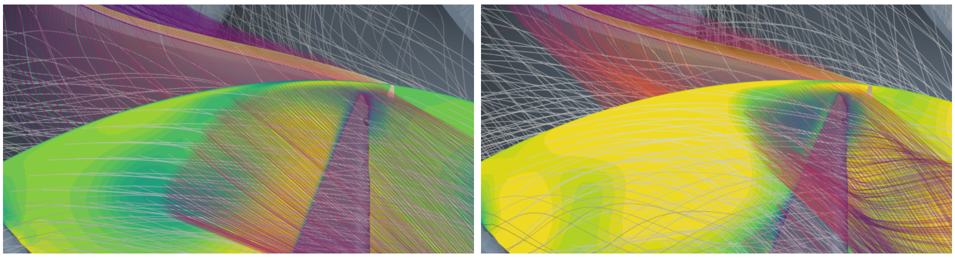

(c) Lower speed at lower PR +0pTG.

(d) Higher speed at lower PR +0pTG.

Figure 9.14: Relative velocity streamlines RANS simulations through the rotor Tip and rotor TE; gray streamlines: Main flow from rotor passage; streamlines in the inferno color scale: Flow from tip PS.

At higher speed, in the mid-section and exducer regions, the leakage velocity in the tip gap is less sensitive than that of the inducer region to relative casing motion that generates negative tip leakage. Furthermore, the vortex created by the interaction between the tip leakage and the main flow through the channel is pushed towards the blade SS generating a small subsonic region, so that the forming and developing of the leakage vortex are restrained owing to the high relative motion of the shroud, i.e., influenced by the centrifugal force [110, 176]. Thus, the rise in the tip gap impacts the choking conditions at the rotor TE as the subsonic region close to tip SS increases, as Figure 9.14 right side and Figure 9.3 show. Furthermore, according to Dambach et al. [118], the mixing of the tip leakage flow with the main stream at the gap exit generates entropy, contributing up to a third of the efficiency loss in a turbine. This loss is proportional to the tip mass flow rate and the velocity components between the mainstream and tip leakage [114, 166, 177]. The behavior mentioned above discloses the cause of the lower efficiency at lower speed and how it drops further as the tip gap increases, in accordance with Figure 9.2(b).

9.4.2 Impact of the varying the tip gap on the main flow

Two streamlines in the relative reference frame of rotation and with an origin point at the rotor TE plane of the original geometry of +0pTG when the turbine operates at lower PR and lower and higher speeds are used to analyze the effects of the variation of the tip gap height on the flow through the blade channel, especially in the supersonic region at the TE plane as depicts Figure 9.15. At lower speed, the first streamline has the origin point at the subsonic region close to the shroud, and the second streamline at the supersonic region close to the hub. The exact coordinates of these points are used for the streamlines at higher speed. The streamlines go through the rotor channel without passing through the tip gap. Furthermore, the streamlines closer to the shroud and the hub show a negative and positive relative angle of attack, respectively, for the cases at lower speed, while at higher speed, the relative angle of attack is negative for both streamlines. This negative incidence reduces the acceleration on the SS, avoiding the choking at the inducer region of the spans that Figure 9.13 depicts and generates a swirl in the streamline close to the shroud downstream of the LE. The reduction in the tip gap does not affect significantly the path followed by the streamlines. However, when the tip gap increases to +50pTG at lower speed, the streamline at the shroud shifts closer to the PS at the rotor inlet due to the high incidence and separation bubble on the SS, then it is deflected to the middle of the channel by the high momentum of the tip leakage, while at higher speed, presents a reduction in the swirl.

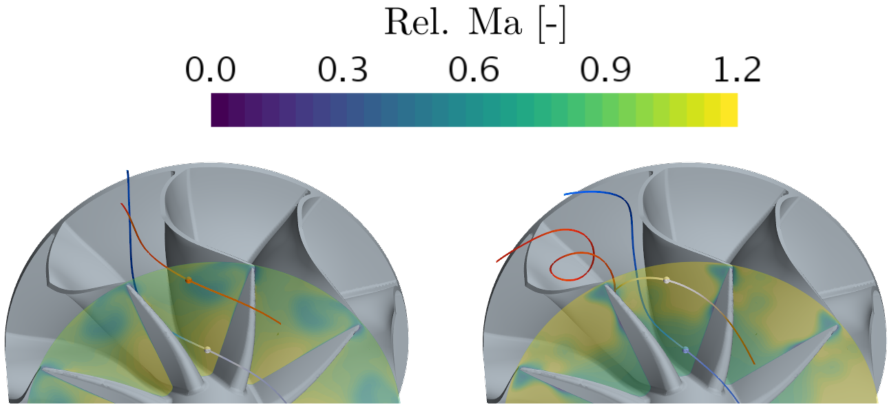

(a) Lower speed at lower PR -50pTG.

(b) Higher speed at lower PR -50pTG.

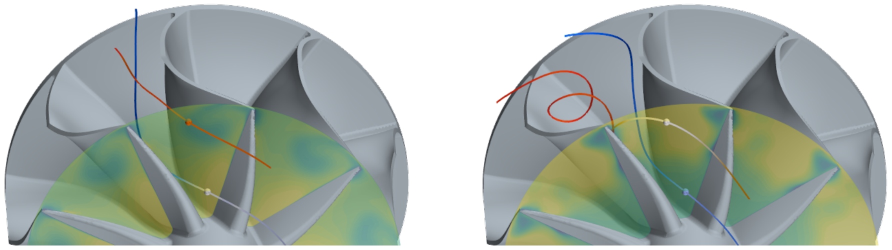

(c) Lower speed at lower PR -25pTG.

(d) Higher speed at lower PR -25pTG.

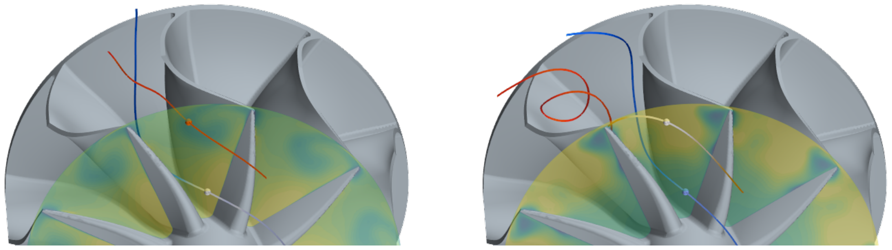

(e) Lower speed at lower PR +0pTG.

(f) Higher speed at lower PR +0pTG.

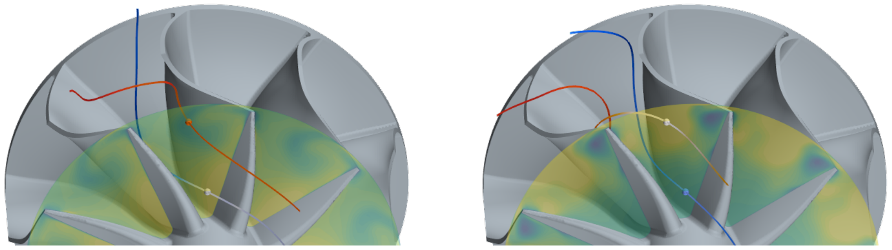

(g) Lower speed at lower PR +50pTG.

(h) Higher speed at lower PR +50pTG.

Figure 9.15: Relative velocity streamlines from the rotor TE going through two points: the first one closer to the shroud: blue streamline and the second one closer to the hub: orange streamline; RANS simulations

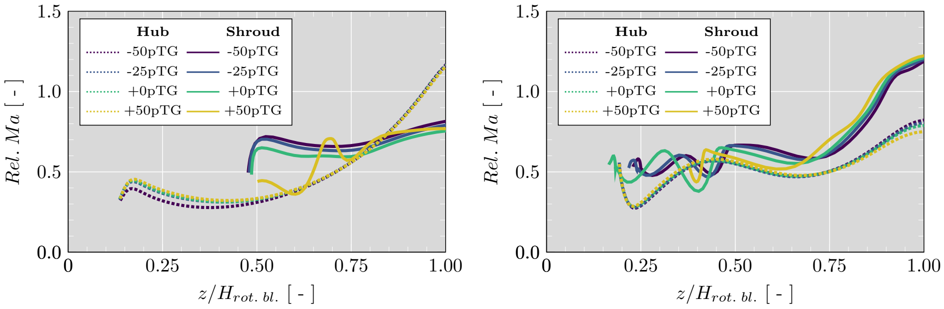

(a) Lower speed at lower PR.

(b) Higher speed at lower PR.

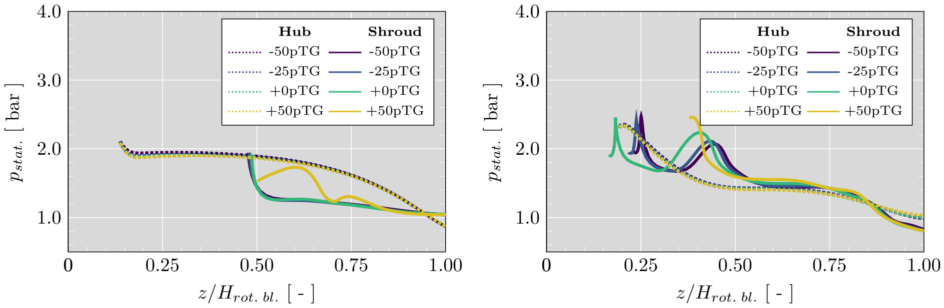

(c) Lower speed at lower PR.

(d) Higher speed at lower PR.

Figure 9.16: Relative Mach number and static pressure evolution along streamlines close to the shroud and hub (Figure 9.15); The value equal to 1.0 in the abscissa represents the position of the TE; RANS simulation

Different parameters along the streamlines are considered and depicted in Figure 9.16 to evaluate more in detail the characteristics of the flow. The flow at the shroud of the case of +50pTG presents a different variation in the analyzed parameters compared to the other geometries, whereas the flow close to the hub remains unchanged despite the variation in the tip gap, following the path of the channel and with a longer axial length. At lower speed, Figure 9.16(a), the vortex generated at the shroud close to the TE prevents the flow from reaching a relative Mach number above one. Furthermore, this induced large mixing loss generates a reduction in the static pressure. On the contrary, the flow close to the hub continues accelerating and reaches sonic conditions, with a corresponding drop in the static pressure, as presented in Figure 9.16(c). At higher speed, the strong relative motion of the shroud forces the vortex to stay closer to the tip gap SS rather than in the middle of the channel, as occurs at lower speed. Furthermore, the induced drag by the relative motion of the casing wall causes the flow close to the shroud to accelerates more than the flow close to the hub, so that the flow near to the shroud reaches supersonic conditions at the TE as depicts Figure 9.16(b), with a subsequent drop in the static pressure, Figure 9.16(d). To go deeper in the flow behavior and with the intention of analyzing the velocity profile Figure 9.17 shows the relative velocity in cylindrical components. The velocity components of the streamline at the hub for both rotational speeds further confirm how the flow remains without any variation despite of the increase in the tip gap height. On the one hand, at lower speed closer to the shroud, the velocity profiles present slight differences except for the case of +50pTG. On the other hand, at higher speed and closer to the shroud, the trends are similar but shift downstream as the tip gap decreases. The negative relative incidence angle at the shroud involves a negative tangential velocity (see Figure 9.17(a)) and is even greater at higher speed (Figure 9.17(b)). At higher speed, the swirl of the flow generates positive and negative fluctuations not only in the tangential velocity but also in the radial velocity. The radial velocity vector at the TE points to the rotor center, represented by the negative value in Figure 9.17(c) and Figure 9.17(d), due to the flow is being dragged to the SS by the relative motion of the shroud and then being redirected to the hub as faces the tip leakage flow. Furthermore, the magnitude of the radial component increases as the tip gap increases. The reduction in the static pressure along the axial direction depicted in Figure 9.16(c) and Figure 9.16(d) has a significant impact in the axial velocity at the hub and shroud rather than in the other components of the velocity as shown by Figure 9.17(e) and Figure 9.17(f). Besides, it is important to remark the higher and uniform flow acceleration at the hub at the lower speed. Regarding the effects produced by the tip gap height, the axial velocity presents higher values at the inducer and middle section as the tip gap decreases, but at the exducer, the axial velocity shows a decline.

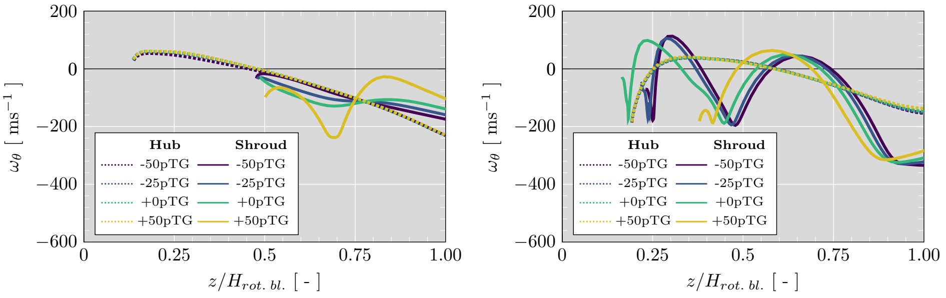

(a) Lower speed at lower PR.

(b) Higher speed at lower PR.

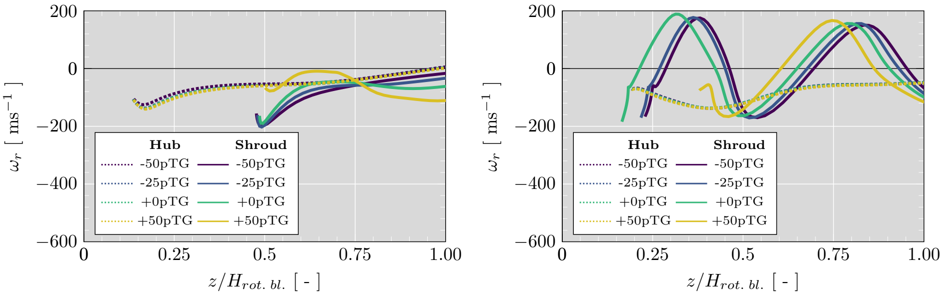

(c) Lower speed at lower PR.

(d) Higher speed at lower PR.

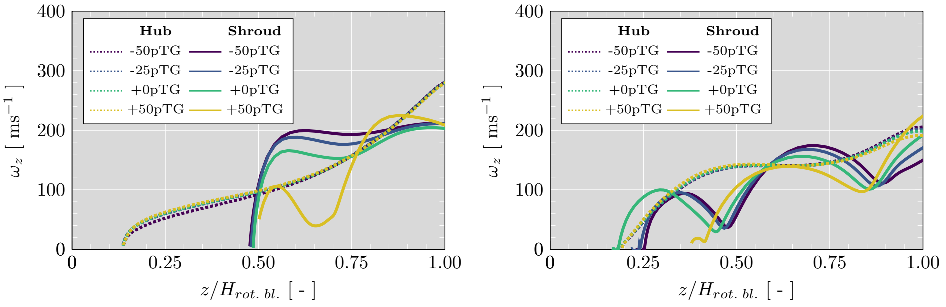

(e) Lower speed at lower PR.

(f) Higher speed at lower PR.

Figure 9.17: Tangential, radial and axial component of the relative velocity along streamlines close to the shroud and hub (Figure 9.15); The value equal to 1.0 in the abscissa represents the position of the TE; RANS simulation

9.4.3 Influence of tip gap on losses

To get a deeper insight into the influence of the changes in the tip gap height over the aerodynamic losses withing the rotor, the entropy generation rate per unit volume provides a good estimation of the location and magnitude of the aerodynamic losses. The entropy generation rate is evaluated using the expression of Ziaja et al. [127], which is based in the definition of Zhang et al. [128] and the work of Moore et al. [126], resulting in Equation 9.5. The first term of the equation accounts for losses due to molecular and turbulent viscous dissipation and the second term estimates irreversible heat flux.

$$\dot{s}_{gen} = \frac{1}{\bar{T}}\left(\bar{\tau}_{ij}\frac{\partial \bar{u}_i}{\partial x_j} + \frac{\mu_t}{\mu}\frac{\partial \bar{u}_i}{\partial x_j}\right) + \frac{\lambda}{\bar{T}^2}\left(\frac{\partial \bar{T}}{\partial x_i}\cdot\frac{\partial \bar{T}}{\partial x_i}\right) \tag{9.5}$$

The analysis is performed along two streamlines going through the tip gap at lower and higher speed, both at lower PR. The first streamline goes through the gap closer to the inducer region, while the second streamline passes the gap closer to the exducer as depicts Figure 9.18.

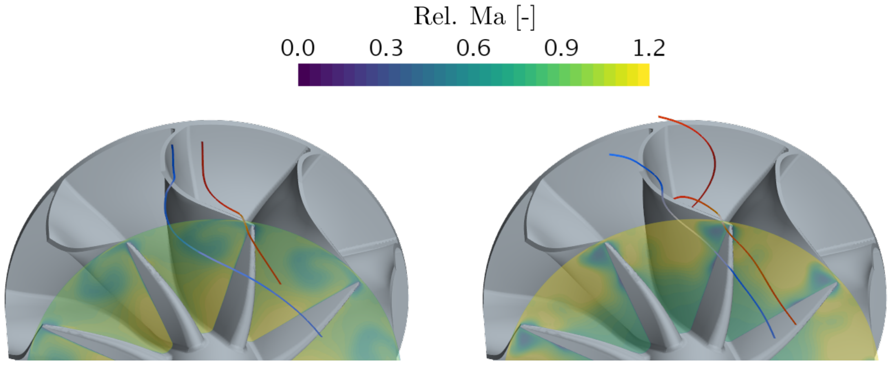

(a) Lower speed at lower PR +0pTG.

(b) Higher speed at lower PR +0pTG.

Figure 9.18: Relative velocity streamlines going through two points: the first one closer to the inducer: blue streamline and the second one closer to the exducer: orange streamline; RANS simulations

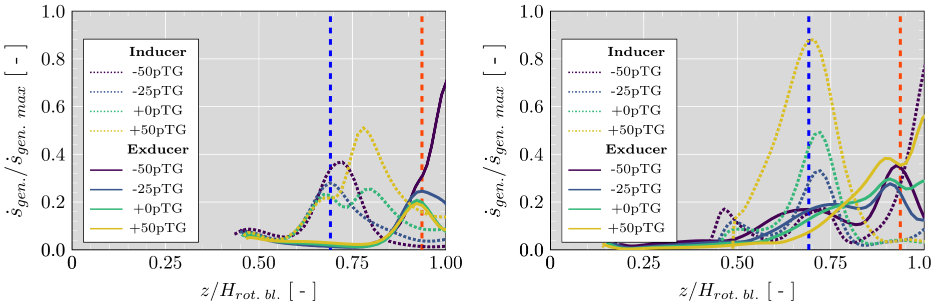

(a) Lower speed at lower PR.

(b) Higher speed at lower PR.

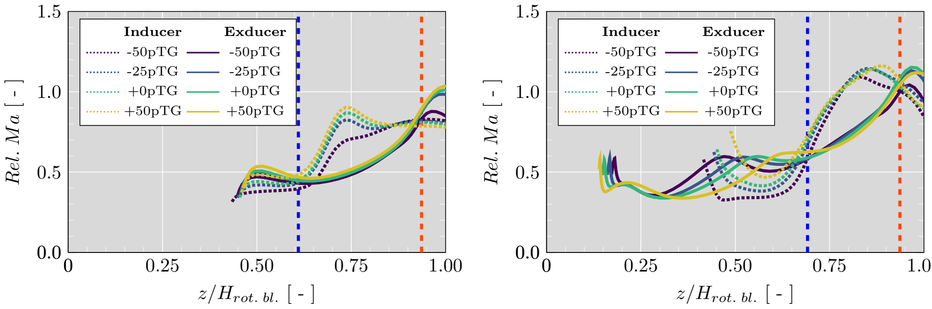

(c) Lower speed at lower PR.

(d) Higher speed at lower PR.

Figure 9.19: Entropy generation rate normalized along streamlines close to the inducer and exducer (Figure 9.18); the value equals 1.0 in the abscissa represents the position of the TE; blue vertical dashed line: the position where the streamline enters the PS tip gap at the inducer; orange vertical dashed line: the position where the streamline enters the tip gap PS at the exducer; RANS simulation.

Figure 9.19(a) and Figure 9.19(b) present the normalized entropy generation rate for the streamlines mentioned above. For the streamline passing through the tip gap closer to the inducer at lower speed, the most significant loss, based on the normalized entropy generation rate, appears when the flow goes through the gap, except for the case of +50pTG, where besides of the entropy peak on the tip gap, a greater peak occurs when the flow leaves the gap and mixes with the main flow. At the same rotational speed but for the flow passing the gap closer to the exducer, the highest losses occur just at the tip gap, except for the case of -50pTG, where the entropy generation rate keeps increasing after the flow passes the gap as a consequence of the reduction in the relative Mach number as depicts Figure 9.19(c) as the flow approaches to the TE passing a subsonic region close to the SS. Overall the streamlines follow a path close to the shroud and present the higher losses when passing through the gap and increasing as the tip gap height decreases. The entropy generation rate is similar for all the analyzed tip clearances before the streamlines enter the gap.

For the cases at higher speed, the losses reach the higher values when the flow goes through the gap closer to the inducer. The losses drop when the flow leaves the gap following a path close to the SS and accelerates, reaching supersonic conditions as Figure 9.19(d) shows between the vertical dashed lines. Furthermore, the streamlines following a path that passes the gap closer to the exducer present a considerable loss peak when the flow approaches the gap. Contrary to the case of lower speed in the streamline closer to the inducer, the losses increase as the tip gap height increases. It is also important to remark that the incidence losses are small as can be observed at the beginning of the entropy lines, being lower at higher speed due to the negative incidence angle [178].

The streamlines of Figure 9.15 are selected to analyze the losses in the main flow at lower and higher speed by means of the entropy generation rate, normalized using the maximum values of the streamlines depicted in Figure 9.19. Thus, Figure 9.20 shows that the losses in the main flow closer to the hub at lower and higher speed represent less than 8% of the loss generated with respect to the entropy generated by the flow going through the tip gap.

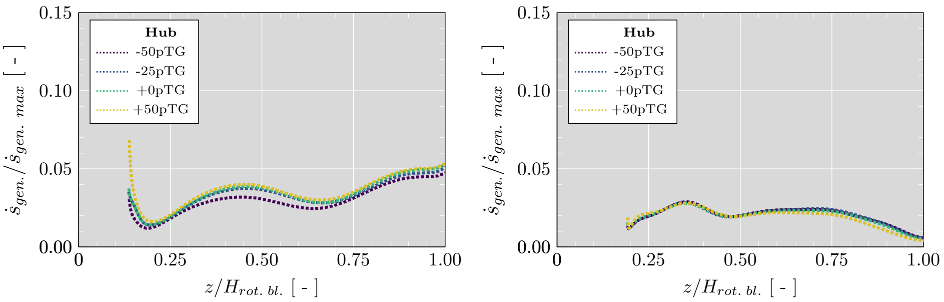

(a) Lower speed at lower PR.

(b) Higher speed at lower PR.

Figure 9.20: Entropy generation rate normalized along streamlines close to the hub (Figure 9.15); the value equals 1.0 in the abscissa represents the position of the TE; RANS simulation.

9.5 Summary

In this chapter, the turbine with the stator vanes at an opened position operating at two rotational speeds and two PR reaching choking conditions has been selected to characterize the flow through the tip gap and the effects on the main flow through the rotor channel by reducing and increasing the tip gap. Regarding the performance parameters, the isentropic efficiency decreases with enlarging the tip gap due to the generating entropy as the flow through the tip gap mixes with the main flow. Thus, an improvement of around 1.6% points can be achieved with a reduction in the tip gap height of 50% at lower speed and higher PR, while at higher speed and higher PR the increase in the efficiency is almost 3% points. On the contrary, a rise of 50% in the tip gap penalizes the efficiency by 1.3% at lower speed and 3% at higher speed.

The reduced mass flow also increases as the area of the plane at the rotor TE becomes bigger, affecting the sonic conditions at higher speeds. At higher speed the chocked area at rotor TE is reduced with the growth of the tip gap by the vortex generated close to the tip SS.

The ratio of the tip leakage mass flow rate and the mass flow at the turbine inlet raises with the tip gap height being higher at lower speed than at higher speed due to the reduction in the scrapping flow. For the analyzed operational points, the maximum ratio reached has a value of 1.05%, which means that 1.05% of the stage mass flow rate does not contribute to driving the rotor and corresponds to the case of lower speed, higher PR, and +50pTG.

Regarding the flow dynamics through the gap, the flow accelerates from the tip gap PS to the SS, reaching supersonic conditions in the exducer region for all the selected operational points. Furthermore, it is important to highlight that even at lower speed and lower PR, the flow entering through the tip gap PS close to the TE reaches Mach number greater than one. Furthermore, due to the relative motion of the shroud, the inducer SS drags some of the flow from the casing, causing one part of the flow to be deflected to the hub, and the remaining flow (negative tip leakage or scrapping flow) travels through the tip gap from the SS to the PS. Based on the mass flux through the gap, at lower speed the negative flow does not change significantly despite the growth in the tip gap, and its magnitude is due to the relative motion of the shroud wall. However, at higher speeds, the negative tip leakage is significant in the flow profile of the tip gap, filling almost more than the half of the inducer region and reducing the mass flux of positive tip leakage, which is reduced even more as the tip gap decreases. The negative tip leakage is reduced by increasing the PR and generating an increase in the positive tip leakage but without significantly affecting the extension of the supersonic pocket in the axial direction of the tip. The reduction in the negative tip leakage for the case of +0pTG is 23%.

The average difference between the static pressure on the PS and SS along the tip gap is slightly more significant at lower speed than at higher speed, representing a higher driven potential for the tip leakage. Furthermore, from around 0.75 relative axial length the difference in the static pressure decreases as the tip gap increases. However, close to the TE, the difference becomes smaller, confirming that the tip leakage flow pattern does not change significantly with varying the tip gap in the exducer region.

The effects on blade loading depends on the span location, as the thickness of blade decreases from the hub to the shroud, the load increases in the same direction at higher speed, while at lower speed the load decreases from 80% to 95% rotor span. A reduction in the tip gap height at lower speed does not affect significantly the pressure profile on the PS at 80% span, but generates a slight increase of the pressure on the SS from the 60% of the chord length. Thus, the pressure difference rises as the tip gap increases. For all the evaluated tip gaps geometries as the static pressure on the SS decreases, the relative velocity increase generating a small supersonic pocket. At higher speed, a reduction in the tip gap height leads to increased pressure on the PS and on the SS. As in the case of lower speed a supersonic region appears on the SS but with higher intensity and extends until the rotor passage outlet and reaches the PS of the neighboring blade at the TE. However, the flow remains subsonic close to the TE on the SS.

Analyzing the interaction between the the main flow and the tip leakage for both rotational speed it is observed that, at lower speed, the vortex created by the blend of the high velocity of the leakage flow and the main flow at the exducer region produces a subsonic region at the TE close to the shroud. However, with the increase in the tip gap height, and thus the relative mass flow, the chocked area at the TE is not significantly affected. For the cases at higher speed, a subsonic region appears on the SS at the TE and growths with the tip gap due to the increase of the secondary flow vortex generated by the interaction between tip leakage and the main flow. Thus, the choked area at TE close to the shroud decreases with the increase of the tip gap height. It is important to remark that the location of the supersonic region close to the shroud is due to the high relative inlet flow angle, swirling flow and the effects of the high relative motion of the wall at the shroud.

Two streamlines through the blade channel passing close to the shroud and hub were selected to evaluate the flow characteristics in more detail. The results show that significant change occurs with the increase of the tip gap compared with the original geometry rather than with the reduction of the gap for the streamline close to the shroud. In contrast, the conditions, such as the velocity profile, of the streamline close to the hub remain almost unaltered at lower and higher speed and reach choking conditions in the case of lower speed.

An analysis of the aerodynamic losses based on the entropy generation rate through different streamlines shows that at lower and higher speeds, the most significant losses occur when the flow goes through the tip gap close to the inducer and exducer. Furthermore, close to the inducer at lower speed, the losses increase with the reduction in the tip gap height. On the contrary, at higher speed, the losses increase with the tip gap height. Concerning the losses in the main flow closer to the hub at lower and higher speeds represent less than 8% of the loss generated with respect to the entropy generated by the flow going through the tip gap.

These results could be employed in the framework of small radial turbines to both improve tip leakage loss models and also to design tip clearance profiles that reduce such losses. However, researchers should be aware of the limitations of this study. First, the findings are obtained from a single turbine geometry with different tip gaps but the same tip clearance profile. Therefore, the quantitative results could be case-dependent, but the discussed qualitative trends are expected to be consistent for all small-size radial turbines, due to the similarities in their designs. Besides, despite the efforts to minimize the numerical errors (e.g., by achieving grid independence), the uncertainty of modeling turbulence and neglecting the effects of thermal and rotational deformation in the turbine impeller and shroud still exist.

9.6 References

[69] J. Galindo, A. Tiseira, R. Navarro, and M. A. López. "Influence of tip clearance on flow behavior and noise generation of centrifugal compressors in near-surge conditions". In: *International Journal of Heat and Fluid Flow* 52 (2015), pp. 129–139. ISSN: 0142-727X. DOI: https://doi.org/10.1016/j.ijheatfluidflow.2014.12.004. URL: https://www.sciencedirect.com/science/article/pii/S0142727X14001751 (cit. on pp. 13, 127).

[110] P. He, Z. Sun, H. Zhang, H. Chen, and C. Tan. "Investigation of clearance flows in deeply scalloped radial turbines". In: *Proceedings of the Institution of Mechanical Engineers, Part A: Journal of Power and Energy* 226.8 (2012), pp. 951–962. DOI: 10.1177/0957650912460361. URL: https://doi.org/10.1177/0957650912460361 (cit. on pp. 17, 144).

[112] J. R. Serrano, R. Navarro, L. M. García-Cuevas, and L. B. Inhestern. "Contribution to tip leakage loss modeling in radial turbines based on 3D flow analysis and 1D characterization". In: *International Journal of Heat and Fluid Flow* 78 (2019), pp. 1–7. ISSN: 0955-5986. DOI: 10.1016/j.ijheatfluidflow.2019.108423. URL: http://www.sciencedirect.com/science/article/pii/S095559861530042X (cit. on pp. 18, 39, 69, 111, 132, 136).

[114] A. P. S. Wheeler, T. Korakianitis, and S. Banneheke. "Tip-Leakage Losses in Subsonic and Transonic Blade Rows". In: *Journal of Turbomachinery* 135.1 (2012). ISSN: 0889-504X. DOI: 10.1115/1.4006424. URL: https://doi.org/10.1115/1.4006424 (cit. on pp. 18, 144).

[118] R. Dambach and H. P. Hodson. "Tip leakage flow: A comparison between small axial and radial turbines". In: *IMechE Symposium*. London, UK, 2000, pp. 1–9. URL: http://www-g.eng.cam.ac.uk/whittle/publications/hph/2000-IMechE-RadialTips.pdf (cit. on pp. 18, 144).

[119] *An Experimental Study of Tip Clearance Flow in a Radial Inflow Turbine*. Vol. Volume 1. Turbo Expo: Power for Land, Sea, and Air. Stockholm: ASME, 1998, p. 12. DOI: 10.1115/98-GT-467. URL: https://doi.org/10.1115/98-GT-467 (cit. on pp. 18, 128).

[120] J. R. Serrano, R. Navarro, L. M. García-Cuevas, and L. B. Inhestern. "Turbocharger turbine rotor tip leakage loss and mass flow model valid up to extreme off-design conditions with high blade to jet speed ratio". In: *Energy* 147 (2018), pp. 1299–1310. ISSN: 0360-5442. DOI: https://doi.org/10.1016/j.energy.2018.01.083. URL: https://www.sciencedirect.com/science/article/pii/S0360544218301014 (cit. on pp. 18, 39, 69, 104, 128, 131, 132).

[126] J. Moore and J. G. Moore. *Entropy Production Rates From Viscous Flow Calculations: Part I — A Turbulent Boundary Layer Flow*. Mar. 1983. DOI: 10.1115/83-GT-70. URL: https://doi.org/10.1115/83-GT-70 (cit. on pp. 19, 149).

[127] K. Ziaja, P. Post, A. Schramm, O. Willers, J. R. Seume, and F. di Mare. "Numerical Investigation of Loss Mechanisms in a Partially Loaded Supersonic ORC Axial Turbine Stage". In: Rotterdam, Netherlands, June 2022. DOI: 10.1115/GT2022-82852. URL: https://doi.org/10.1115/GT2022-82852 (cit. on pp. 19, 149).

[128] L. Zhang, W. Zhuge, Y. Zhang, and T. Chen. "Similarity Theory Based Radial Turbine Performance and Loss Mechanism Comparison between R245fa and Air for Heavy-Duty Diesel Engine Organic Rankine Cycles". In: *Entropy* 19.1 (2017), pp. 1–20. ISSN: 1099-4300. DOI: 10.3390/e19010025. URL: https://www.mdpi.com/1099-4300/19/1/25 (cit. on pp. 19, 149).

[166] J. D. Denton. "Loss mechanisms in turbomachines." In: *Journal of Turbomachinery* 115.(Cambridge, U.K.: Sep. 1-3, 1987), Bury St. Edmunds, U.K., Mech. Engng. Publications Ltd., 1987, Pap (1993), pp. 621–656. DOI: 10.1115/1.2929299. URL: https://doi.org/10.1115/1.2929299 (cit. on pp. 75, 144).

[172] Q. Deng, J. Niu, and Z. Feng. "Tip leakage flow in radial inflow rotor of a microturbine with varying blade-shroud clearance". In: *Proceedings of the ASME Turbo Expo* 6 PART B.1970 (2007), pp. 1081–1088. DOI: 10.1115/GT2007-27722. URL: https://asmedigitalcollection.asme.org/GT/proceedings-abstract/GT2007/47950/1081/363813 (cit. on p. 132).

[173] R. Dambach and H. P. Hodson. "Tip Leakage Flow in a Radial Inflow Turbine with Varying Gap Height". In: *Journal of Propulsion and Power* 17.3 (2001), pp. 644–650. DOI: 10.2514/2.5791. URL: https://doi.org/10.2514/2.5791 (cit. on p. 137).

[174] Q. Deng, J. Niu, and Z. Feng. "Study on leakage flow characteristics of radial inflow turbines at rotor tip clearance". In: *Science in China Series E: Technological Sciences* 51 (2008), pp. 1125–1136. DOI: 10.1007/s11431-008-0164-z (cit. on pp. 137, 143).

[175] Y. Xue, M. Yang, R. F. Martinez-Botas, A. Romagnoli, and K. Deng. "Loss analysis of a mix-flow turbine with nozzled twin-entry volute at different admissions". In: *Energy* 166 (Jan. 2019), pp. 775–788. ISSN: 0360-5442. DOI: 10.1016/J.ENERGY.2018.10.075 (cit. on p. 143).

[176] *A Numerical Investigation on a New Pulse-Optimized Flow Control Method for Turbocharger Turbine Performance Improvement Under Pulsating Conditions*. Vol. Volume 2C: Turbo Expo: Power for Land, Sea, and Air. Montréal, Canada: ASME, 2015, p. 12. DOI: `10.1115/GT2015-42059`. URL: `https://doi.org/10.1115/GT2015-42059` (cit. on p. 144).

[177] Z. Wei, G. Ren, X. Gan, M. Ni, and W. Chen. “Influence of Shock Wave on Loss and Breakdown of Tip-Leakage Vortex in Turbine Rotor with Varying Backpressure”. In: *Applied Sciences* 11.11 (2021). ISSN: 2076-3417. DOI: `10.3390/app11114991`. URL: `https://www.mdpi.com/2076-3417/11/11/4991` (cit. on p. 144).

[178] J. F. Kline, T. P. Moffitt, and R. G. Stabe. “Incidence loss for fan turbine rotor blade in two-dimensional cascade”. In: 1983, pp. 1–12. URL: `https://ntrs.nasa.gov/api/citations/19830022160/downloads/19830022160.pdf` (cit. on p. 151).

CHAPTER 10

Grooved Stator Vanes

Contents

10.1 Introduction 161
10.2 Geometry Description 161
10.3 Mesh analysis 162
10.4 Performance Characteristics 165
10.5 Analysis of the stator flow behavior 168
10.6 Summary 181
10.7 References 184

Figures

10.1 Stator geometry with different grooved surfaces. 161
10.2 View of mesh selected for the geometry with a grooved surface in the stator vanes. 162
10.3 Selected points to evaluate the Mach number. Point A (at the middle of the stator vaneless space) and Point B (at R6=26.08 mm, Figure 6.1).162
10.4 Mesh analysis Part A. The red dot corresponds to the mesh parameters used with the case without grooves. 163
10.5 Mesh analysis Part B. The red dot corresponds to the mesh parameters used with the case without grooves. 164
10.6 Turbine map based on steady results of the original stator geometry (0 grooves) and unsteady results with and without grooved surface; Steady: Dashed lines; Unsteady: Markers. 167

10.7 Mach number and stator vane pressure profile snapshots of URANS simulations at 50% span of the stator passage with closed VGT position at higher speed and higher PR; red line: $Ma = 1$. 170
10.8 Mach number and stator vane pressure profile snapshots of URANS simulations at 50% span of the stator passage with closed VGT position at lower speed and higher PR; red line: $Ma = 1$. 172
10.9 Transient numerical schlieren for closed VGT opening at 50% span of the stator passage with higher simulated PR and higher speed; left side: Original geometry; middle: Geometry with 5 grooves in the stator; right side: Geometry with 11 grooves in the stator. 175
10.10 Transient numerical schlieren for 10% VGT opening at 50% span of the stator passage with higher simulated PR and lower speed; left side: Original geometry; middle: Geometry with 5 grooves in the stator; right side: Geometry with 11 grooves in the stator. 176
10.11 Rotor blade loading at 50% span with closed VGT position. 177
10.12 Exergy analysis for the evaluated operational points; lower: 3882 rpm/$\sqrt{\text{K}}$; higher: 8421 rpm/$\sqrt{\text{K}}$. 180

Tables

10.1 Mesh independence study. 165
10.2 Differences in some parameters of the case at higher pressure ratio when using one degree and two degrees to define the time step. . . . 165
10.3 Pressure ratio and performance of the turbine and stator for the evaluated cases with and without grooved surface; URANS simulations. 168

10.1 Introduction

As was presented in Chapter 5 the flow passing over the channels guided by the stator vanes accelerates and under certain operational points can reach supersonic conditions and generates the presence of a shock wave on the stator vanes, which has a potential impact on the flow loss as well as on unsteady aerodynamic interaction. The shock wave generates a sudden increase in pressure and can lead to boundary separation and strong excitation force besides pressure fluctuation in the rotor blades. Thus, in this chapter, a simple parametric study with different grooved surfaces on the stator vanes is carried out to mitigate the shock wave intensity and improve efficiency. First, a description of the analyzed geometries is given. Then a mesh independence analysis is presented. Furthermore, the performance parameters of the original geometry and the grooved surface are compared. Finally, the flow field, the pressure profile, and a study of the exergy in each region of the computational domain are analyzed.

10.2 Geometry Description

The original geometry of the stator vanes was modified to generate two different groove configurations. The groove width, depth, and height are 0.7 mm, 0.15 mm, and 3.8 mm, respectively, which were kept constant for the two configurations changing only the number of grooves as depicts Figure 10.1. It is important to remark that the height of the grooves does not cover the hole vane height and are centered from the 50% stator span. Furthermore, the location of the grooves along the chord covers the region where the supersonic pocket and the shock wave is developed, as was presented in Chapter 5. Comparing both configurations, the vanes with 11 grooves contain the locations of the same grooves as the configuration with 5 grooves plus one groove downstream and five grooves upstream.

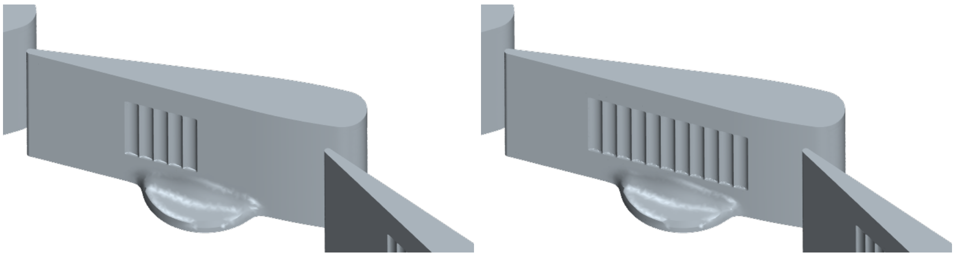

(a) Geometry with 5 grooves.

(b) Geometry with 11 grooves.

Figure 10.1: Stator geometry with different grooved surfaces.

10.3 Mesh analysis

The different configurations has been discretized by means of a unstructured polyhedral mesh [179] similar to the mesh presented in Chapter 3. Nevertheless, as the geometry has been changed and the intention is to analyze the flow profile on the stator vanes, a mesh independence study has been carried out to ensure valid results. The case of lower speed and higher PR with 11 grooves in the stator surface is selected for this mesh independece study. The inlet and outlet duct are meshed using an extruded mesh and kept for the different mesh densities, changing only the density of the regions of the stator and rotor, that will be denoted as core, and the number of prism layers for the boundary layer as it can be seen in Figure 10.2.

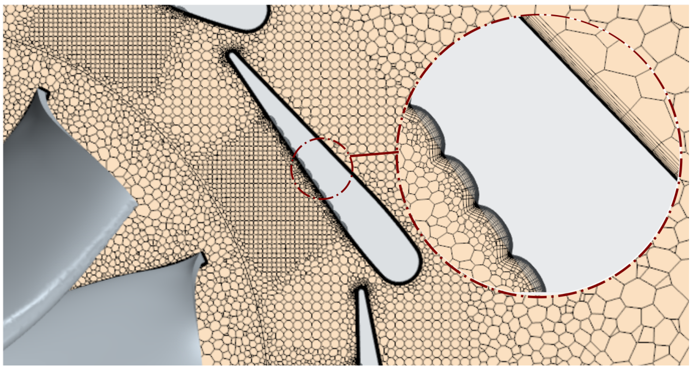

Figure 10.2: View of mesh selected for the geometry with a grooved surface in the stator vanes.

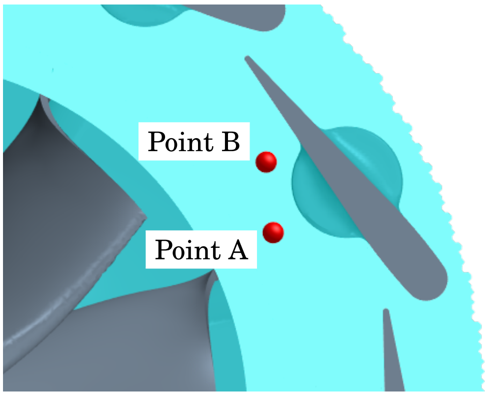

Figure 10.3: Selected points to evaluate the Mach number. Point A (at the middle of the stator vaneless space) and Point B (at R6=26.08 mm, Figure 6.1).

The Mach number at two points in the vaneless space, one at the middle of the vaneless space, Point A, and the other close to the shock wave at R=26.08 mm, Point B, as depicts Fig 10.3 are considered to compare the different mesh densities. The mass flow rate and the turbine power have been evaluated, as well as, the static pressure on the grooves and the density gradient, used to visualize the shock wave as show Fig 10.4 and Fig 10.5. The initial mesh parameters correspond to the mesh used for the case without grooves and will be referred to as the mesh with the coarser core and 15 layers in the boundary layer. Thus, the core is refined from this case, and the number of layers in the boundary layer is changed.

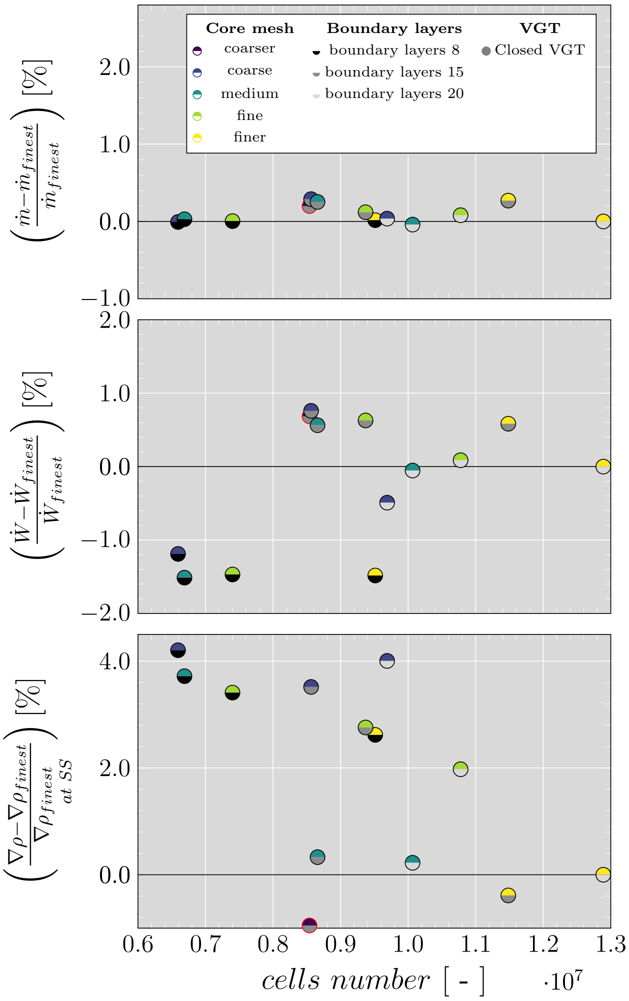

Figure 10.4: Mesh analysis Part A. The red dot corresponds to the mesh parameters used with the case without grooves.

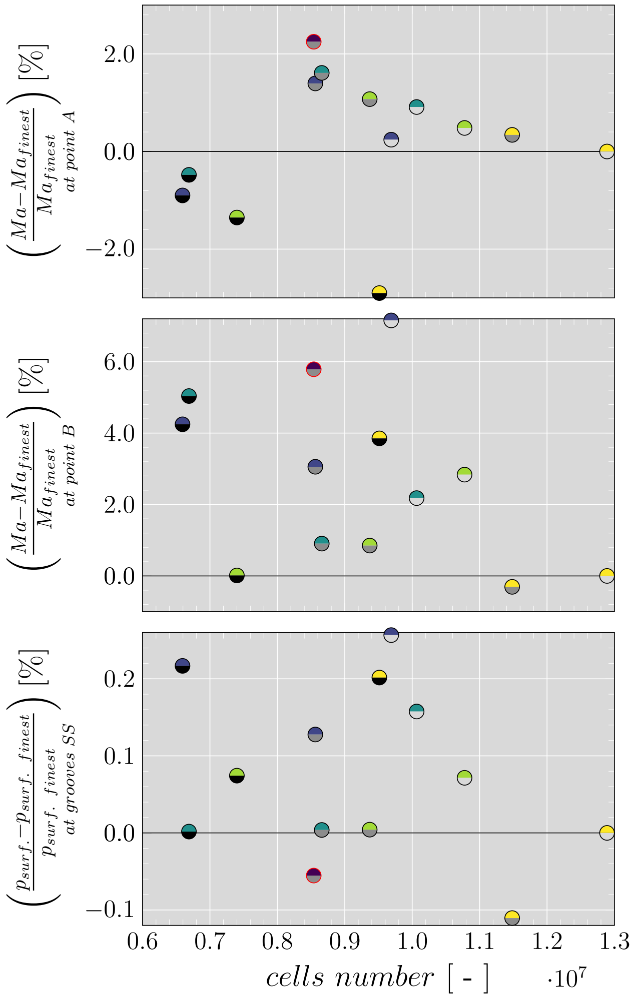

Figure 10.5: Mesh analysis Part B. The red dot corresponds to the mesh parameters used with the case without grooves.

In order to reach a compromise between results precision and computational cost and according to the results presented in Fig 10.4 and Fig 10.5, the best options are the medium core mesh with 15 or 20 cells in the boundary layer, since the results obtained are very close to the case with the finer mesh and are less computationally expensive. To select between the medium core mesh with 15 and 20 cells in the boundary layer, the grid convergence index (GCI) [153] is calculated with respect to the finer mesh as shows Table 10.1. The final chosen mesh corresponds to the medium mesh with 10 million cells and 20 cells in the boundary layer. It presents a lower GCI, implying a lower error in all variables, especially in the mass flow rate and turbine power. In order to capture adequately the behavior of the viscous sublayer, the selected mesh has a non-dimensional distance to the centroid of the first layer of cells close to the walls ($y+$) lower than 1.

Table 10.1: Mesh independence study.

Core mesh	Boundary layer	Cells number [$\cdot 10^6$]	$\dot{m}$ [kg/s]	$\dot{W}$ [kW]	Ma_{pointA} [-]	Ma_{pointB} [-]	$p_{surf.grooves}$ [bar]	$\nabla\rho_{at\,SS}$ [kg/m^3]
medium	15	8.65	0.17693	1.5001	1.0243	0.9952	2.41912	240.3590
medium	20	10.07	0.17641	1.4909	1.0173	1.0077	2.42284	240.1054
finer	20	12.89	0.17648	1.4917	1.0081	0.9862	2.41902	239.5689
GCI (for medium 15 boundary layer)[%]			0.62	1.39	3.97	2.23	0.01	0.81
GCI (for medium 20 boundary layer)[%]			0.10	0.13	2.25	5.38	0.39	0.55

10.4 Performance Characteristics

The variable geometry turbine with grooved surface in the stator vanes has been simulated with the vanes at a closed position (10% VGT), at two rotational speed, 3882 rpm/$\sqrt{\text{K}}$ (lower speed) and 8421 rpm/$\sqrt{\text{K}}$ (higher speed) and at two PR, lower and higher. The models and boundary conditions described in Chapter 3 have been implemented similarly and with a time step size selected as the time that the turbine wheel takes to rotate two degrees depending on the rotational speed instead of one degree as some authors recommend since it represents a lower computational cost with differences less than 1% as shown in Table 10.2.

Table 10.2: Differences in some parameters of the case at higher pressure ratio when using one degree and two degrees to define the time step.

Grooves [-]	$N_{red.}$ [$\frac{rpm}{\sqrt{K}}$]	Dev. $\dot{m}$ [%]	Dev. $\pi_{turb.}$ [%]
0	3882	-0.05	0.006
5		0.48	0.06
11		0.49	-0.13
0	8421	-0.56	0.35
5		0.66	0.61
11		-0.41	0.55

Figure 10.6 shows the reduced mass flow and the total-to-static efficiency of the different operational points for the three stator configurations. The results correspond to the unsteady and steady simulations. The steady simulations correspond only to the case of the stator without grooves and are shown only to mark the trend of the turbine map. Figure 10.6(a) shows that there is not a significant change in the reduced mass flow due to the presence of the grooved surface in the stator vanes and only a slight difference at higher speed and lower PR but less than 2%. Nevertheless, the grooved surface has an impact on the turbine efficiency at higher speed rather than at lower speed, as depicts Figure 10.6(b) and Figure 10.6(c). Table 10.3 is presented to see better the changes. An improvement in the efficiency can be achieved with the configuration of 11 grooves and an even better one with 5 grooves at higher speed and both PR. The major difference occurs at higher speed and lower PR with an increase of 3.0% points for the case of 11 grooves and 5.0% points for the case of 5 grooves. At the same speed but at higher PR the rise in the efficiency is 2.0% points and 3.0% points for 11 grooves and 5 grooves, respectively. Table 10.3 also reveals that the presence of the grooves has a slight impact on the total to total pressure ratio of the stator, as the velocity of the flow at the stator outlet decreases with the presence of the grooves and taking into account that the function of the vanes is to direct the flow toward the rotor, where the major expansion takes place to produce shaft work. Furthermore, the stator efficiency calculated using Equation 4.3, 4.4 slightly decrease with the increase of grooves. At higher speed and lower PR, the efficiency decreases by 6% points and 8% points with 5 grooves and 11 grooves, respectively. While at higher speed and higher PR the drop is just 1% points and 3% points with 5 grooves and 11 grooves, respectively. Nevertheless, this penalty in the stator efficiency is compensated with the improvement in the turbine total-to-static efficiency due to the effects of the grooves on the shock waves that will be analyzed in the following sections, together with other aspects of the stator flow profile. Furthermore, the regions where the efficiency is evaluated and that are depicted in Figure 4.1(b) present a flow conditions quite complex and even more downstream of stator affecting the report of the losses.

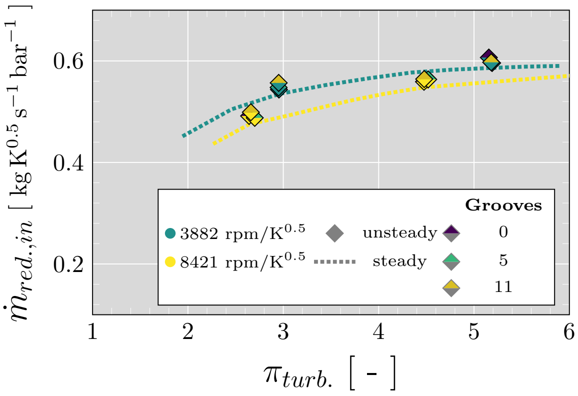

(a) Reduced mass flow map.

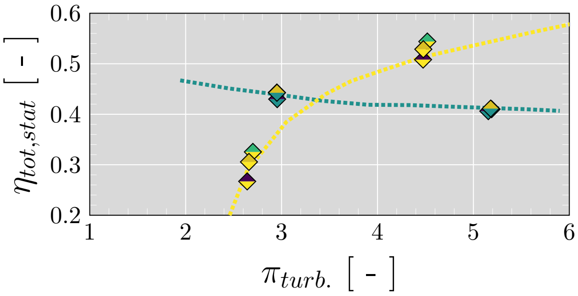

(b) Efficiency vs. expansion ratio map.

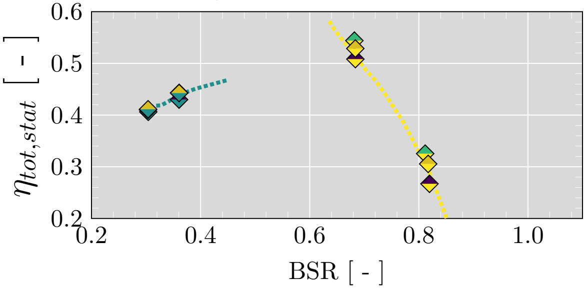

(c) Efficiency vs. blade-speed-ratio (BSR) map.

Figure 10.6: Turbine map based on steady results of the original stator geometry (0 grooves) and unsteady results with and without grooved surface; Steady: Dashed lines; Unsteady: Markers.

Table 10.3: Pressure ratio and performance of the turbine and stator for the evaluated cases with and without grooved surface; URANS simulations.

		Turbine			Stator		
Grooves	$N_{red.}$		$\pi_{turb.}$	$\eta_{tot,stat}$	$u_{stator\,out}$	$\pi_{stator\,tot,tot}$	η_{stator}
[-]	$\left[\frac{\text{rpm}}{\sqrt{\text{K}}}\right]$		[-]	[-]	$\left[\frac{\text{m}}{\text{s}}\right]$	[-]	[-]
0	3882	lower	2.95	0.43	278.82	1.21	0.69
		higher	5.16	0.41	307.88	1.34	0.83
	8421	lower	2.64	0.27	238.00	1.12	0.73
		higher	4.48	0.51	285.09	1.22	0.71
5	3882	lower	2.95	0.44	272.22	1.23	0.67
		higher	5.19	0.41	308.98	1.37	0.84
	8421	lower	2.70	0.32	231.37	1.16	0.67
		higher	4.52	0.54	282.57	1.26	0.70
11	3882	lower	2.95	0.44	269.90	1.25	0.65
		higher	5.18	0.41	306.83	1.39	0.83
	8421	lower	2.66	0.30	225.56	1.17	0.65
		higher	4.48	0.53	277.98	1.28	0.68

10.5 Analysis of the stator flow behavior

In the following part, the Mach number, pressure profile, and numerical Schlieren are evaluated to gain insight into the relationship between the shock wave structure and the groove surface geometry and the impact on the turbine performance.

10.5.1 Influence of grooved vanes on the flow profile

The Mach number profile has been evaluated at 50% stator span together with the stator vane pressure profile for the cases reaching choking conditions, corresponding to the points of higher PR at higher and lower speed. Figure 10.7 depicts how the supersonic region connecting the stator vane and the rotor entry shrink as the grooves number increase, resulting in the detachment of the supersonic pocket of the stator and the rotor for the case of 11 grooves. Nevertheless, the supersonic region closer to the vane SS extends more upstream and downstream than the original configuration for the cases at lower speed and remains without significant variation at higher speed. Furthermore, the wake at the vane TE increases as the number of grooves increases, generating a lower velocity region that contributes to the reduction or detachment of the aforementioned supersonic pocket connecting the stator and rotor of the neighboring vane. Thus, the unsteady behavior of the wake has a beneficial effect on the flow profile and with it on the efficiency [180, 181]. The pressure disturbances can be clearly seen in Figure 10.7 representing the static pressure distribution on the vane surface [125]. In Figure 10.7(a) the pressure drop on the SS of the vane starting at the LE is due to the acceleration of the flow, at 0.44 relative chord length flow reaches the sonic conditions ($Ma = 1$) and continues accelerating until 0.6 relative chord length, where the pressure suddenly rise due to the presence of the shock wave as will be show further and the flow decelerates, going back to $Ma = 1$ at 0.68 relative chord length and then to subsonic conditions. Due to the presence of grooves, Figure 10.7(b) depicts that the pressure on the SS with 5 grooves drops 4% compared with the original configuration at 0.07 relative chord length. From the LE, the pressure profile follows the same trend as the case without grooves until 0.48 relative chord length where the pressure sink. A pressure peak takes place at 0.52 relative chord length, followed by four other peaks that match the number of grooves and with the presence of small shock waves. At 0.6 relative chord length, where the case without grooves presents the lower pressure on the SS, the pressure increases by 15%. The pressure profile of the vanes with 11 grooves presents a signification variation, as shown in Figure 10.7(c), where the pressure disturbances extend from 0.3 to 0.78 relative chord length, while the supersonic pocket only cover the region between 0.4 and 0.66 relative chord length. At 0.07 relative chord length the pressure drops 4% compared with the original configuration. Then, from 0.07 until the first groove at 0.3 relative chord length, the flow starts to accelerate less than the original configuration, as depicted in the lower slope of the pressure profile. Furthermore, at 0.6 relative chord length, where the point of lower pressure is located in the original configuration and just before the shock wave, the pressure increases 26% and marked in the Mach number contour with less intensity for the case of 11 grooves. From another perspective, the vane load around 0.6 relative chord length decrease with a grooved surface. Furthermore, the pressure jump caused by the shock wave in the smooth vanes decreases and changes to several peaks with the grooved vanes, as was mentioned above. Comparing the pressure jump of the original geometry with the most significant jump in the 5 and 11 grooves configuration is possible to observe a decrease of 45% and 67%, respectively. Another aspect to highlight is that in the region before the shock wave, the Mach number in the case without grooves is higher than in the grooved vanes cases. Thus, the shock waves on the grooved vanes are less intense and generate less entropy, improving the turbine efficiency.

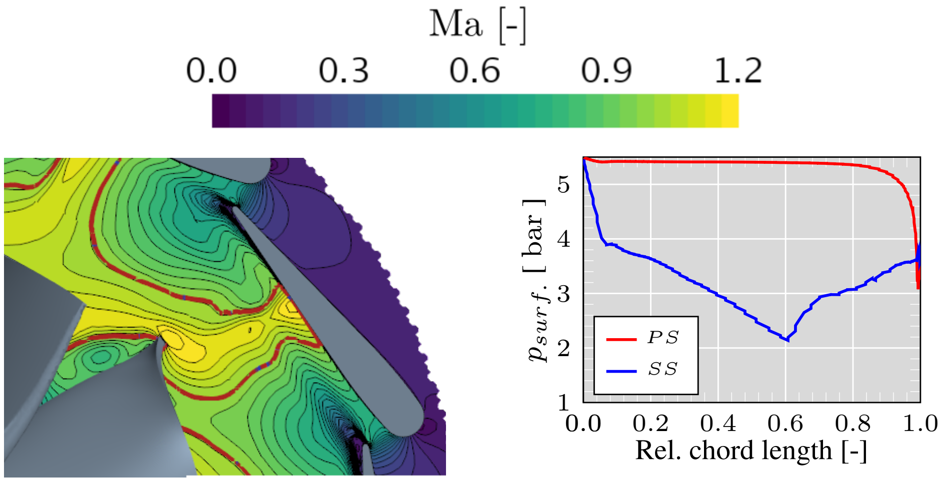

(a) Geometry with 0 grooves (original configuration).

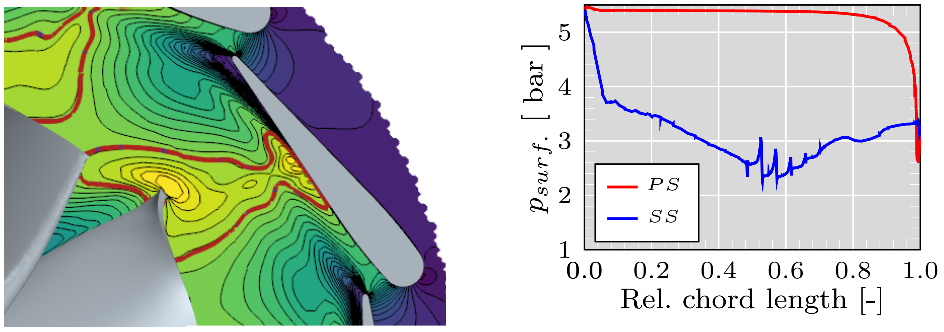

(b) Geometry with 5 grooves on the stator vanes.

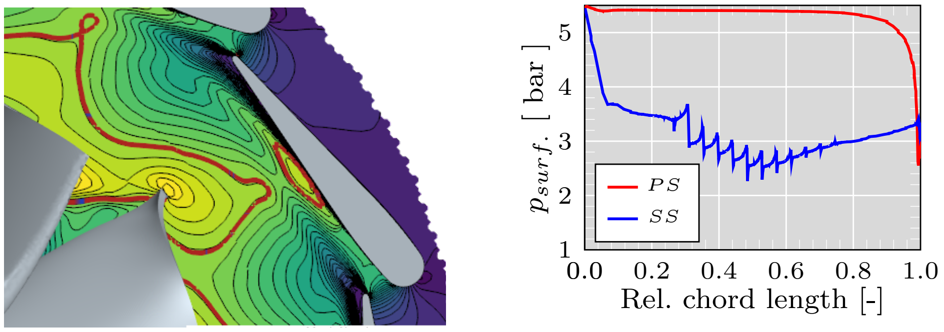

(c) Geometry with 11 grooves on the stator vanes.

Figure 10.7: Mach number and stator vane pressure profile snapshots of URANS simulations at 50% span of the stator passage with closed VGT position at higher speed and higher PR; red line: $Ma = 1$.

Analyzing the case of lower speed and higher PR as depicts Figure 10.8 is possible to observe how the presence of a grooved surface modified the Mach number contour, presenting a reduction around the middle of the supersonic region at the throat formed by the relative position of the rotor blade and the stator vane. Furthermore, this reduction is also caused by the effects of the wake of the adjacent stator vane TE [182, 82], as the flow reduce the velocity after passing by the grooves. Close to the SS, the supersonic region of the case without grooves extends from 0.3 to 0.73 relative chord length. In contrast, in the 5 and 11 grooves cases, the starting position does not change significantly but expands until 0.84 and 0.87 relative chord length, respectively, representing an increase of 30% for the 5 grooves and 32% for the case of 11 grooves. For the configuration of 5 and 11 grooves, before of the acceleration of the flow on the SS, the flow accelerates when passing close to the geometry throat formed by the convergent passage between the vanes [124] reaching $Ma = 1$, as depict Figure 10.8(b) and Figure 10.8(c). Nevertheless, this acceleration is particular for the time step depicted in these figures. Furthermore, in Figure 10.8(c) the whole passage presents an instantaneous choked flow. The presence of sonic conditions in this region is due to the wake at the TE that slows down and compresses the surrounding of the entering flow. Pressure profiles show the effect of the grooved surface compared with the original configuration, presenting a similar behavior as the case of higher speed and higher PR. Figure 10.8(a) depicts the pressure fall for the original configuration until 0.62 relative chord length followed by a sudden rise. Comparing the original geometry with the case of 5 and 11 grooves at 0.62 relative chord length, the static pressure increases 18% and 24%, respectively, as shown in the pressure profiles in Figure 10.8(b) and 10.8(c). Upstream at 0.15 relative chord length, the pressure on SS of the smooth vanes drops 8% when using grooved vanes. Furthermore, the highest pressure pick occurs after passing the first groove, followed by a sudden fall in the pressure. The pressure disturbances match the number of grooves affecting the velocity profile. Comparing the pressure jump of the original geometry with the most significant jump in the 5 and 11 grooves configuration is possible to observe a decrease of 39% and 56%, respectively.

As it was presented in Chapter 6, Figure 6.9, the low rotational speed can cause the development of a supersonic region close to the turbine wheel inlet, analyzing the system in the relative reference frame for rotation. Nevertheless, due to the presence of grooves the size of the region decrease for the case with 5 grooves and disappear for the case with 11 grooves, representing just a small increase in the efficiency of 0.4% and 0.5% points. At higher speed the flow remains subsonic in all cases.

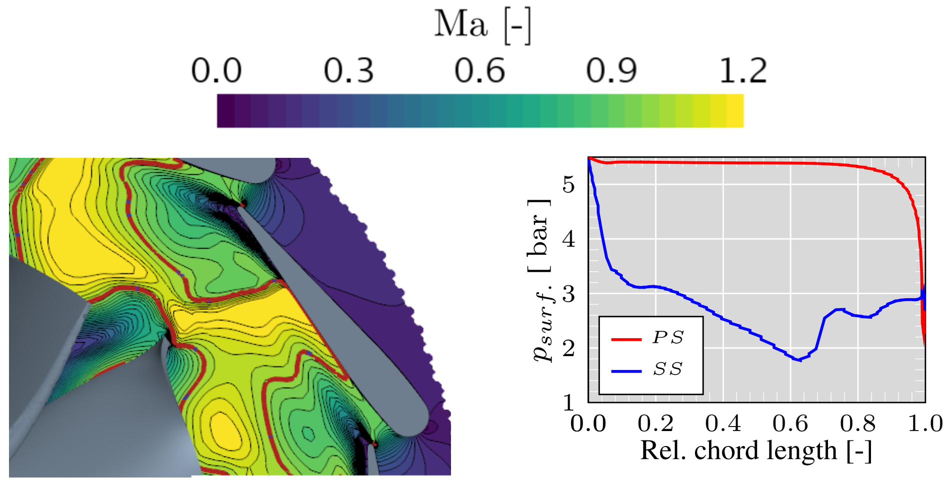

(a) Geometry with 0 grooves (original configuration).

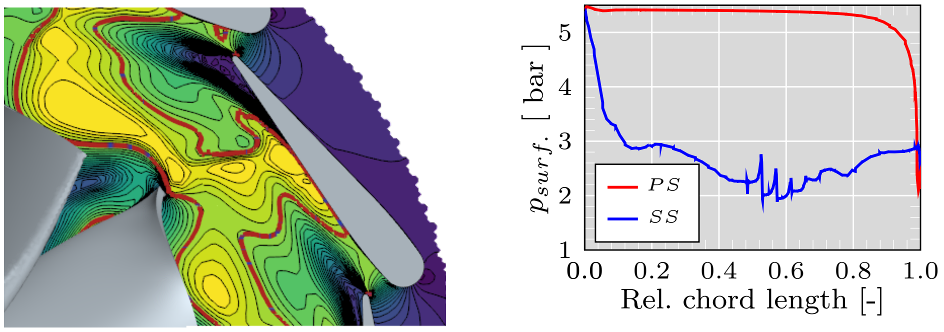

(b) Geometry with 5 grooves in the stator vanes.

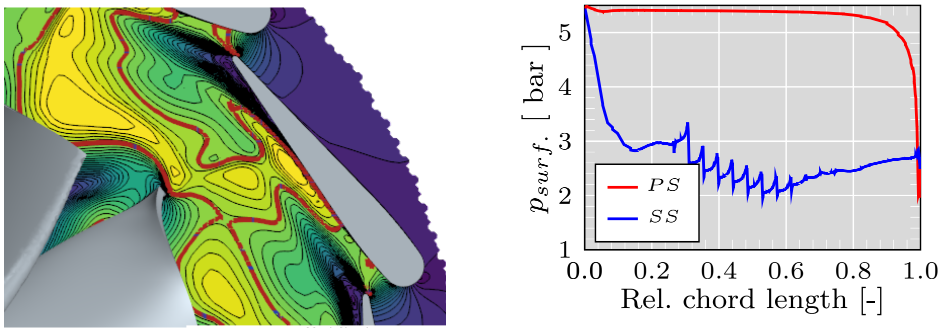

(c) Geometry with 11 grooves in the stator vanes.

Figure 10.8: Mach number and stator vane pressure profile snapshots of URANS simulations at 50% span of the stator passage with closed VGT position at lower speed and higher PR; red line: $Ma = 1$.

10.5.2 Shock wave structure in grooved surface vanes

For a deeper analysis of the effects of the grooved surface on the vaneless space flow profile, numerical Schlieren has been carried out for one blade passing for the two analyzed reduced speeds at higher PR. At higher speed and higher PR, the Schlieren images in Figure 10.9 show that normal shock wave pattern change to a less intense wave when increasing the number of grooves, and a multiple shock structure is generated. The main shock remains practically at the same position as in the original configuration near 0.6 relative chord length. For the case of 5 grooves, two front leg shock waves are developed before the main shock. A third and fourth small shock waves are combined, forming the base of the main shock; the last shock wave is not possible to distinguish in the Schlieren image due to its low intensity but is visible in the pressure profile depicted in Figure 10.7, thus the number of shock waves match with the number of grooves [123]. The configuration of 11 grooves also presents multiple shock waves. First, around the middle of the vane five shock waves of weak intensity stay close to the stator SS without extending to the rotor. Then an orthogonal shock wave where the main shock is expected in the original configuration is presented, followed by other five shock waves of low intensity. Furthermore, the rotor still contributes to the formation of a throat when goes by the stator vane shock, but with a weaker intensity for the case of 5 grooves and disappears for the case of 11 grooves due to the sudden disturbance generated by the the change of flow area.

At lower speed, the shock wave is leaned backward, slightly varying its angle depending on the rotor blade position and presents an increase in the intensity compared with the case at higher speed as was mentioned in Chapter 6. This shock wave appears at 0.62 relative chord length, and even with 5 or 11 grooves on the stator vanes, the shock wave has a longer extension toward the rotor compared with the cases of higher speed as depicted in Figure 10.10. The intensity of the shock wave is depressed when increasing the grooves number. Besides, a multiple shock structure consisting of a series of small waves are generated from each groove. The presence of these waves can be seen more clearly in the pressure profiles in Figure 10.8 than in the Schlieren image due to the intensity and the limitation of a highly detailed flow structure that can provide the URANS simulation, especially in the boundary layer [183, 182]. Furthermore the moving rotor blade encounters locally supersonic speed, resulting in the formation of shock waves in the relative frame.

The Schlieren images also support the results presented in Table 10.3 regarding the diminishing of the stator efficiency as the shock waves in cases of grooved surface are confined in the region delimiting the outlet of the stator. In contrast, the shock wave in the case without grooves interacts with the rotor, as was mentioned before, downstream of the limiting stator outlet plane.

The weakening of the intensity of the standing shock wave at both speeds can contribute to diminishing losses close to the rotor. Furthermore, at higher speed, the load fluctuation around the rotor LE, as was explained in Chapter 6, can be reduced and minimize the factors that compromise the integrity of the turbine [184, 185].

For the cases with a grooved surface at lower speed and higher PR, it is possible to observe the presence of a shock wave at the convergent section between the vanes, only between a time of 50% and 75% blade passing as shown in Figure 10.10 and in the Mach number contours of Figure 10.8.

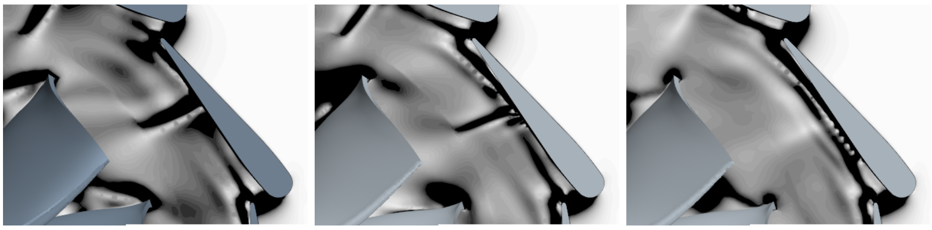

(a) $t = 25\%$ rotor blade passing.

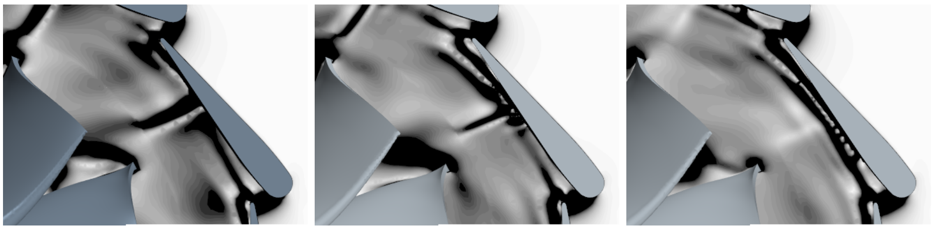

(b) $t = 50\%$ rotor blade passing.

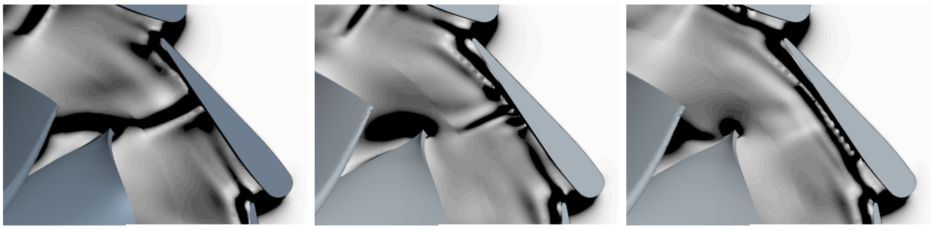

(c) $t = 75\%$ rotor blade passing.

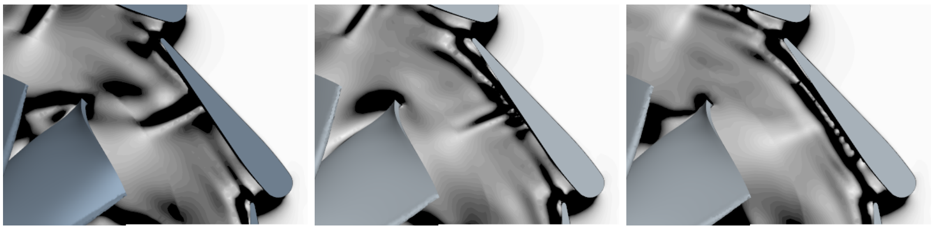

(d) $t = 100\%$ rotor blade passing.

Figure 10.9: Transient numerical schlieren for closed VGT opening at 50% span of the stator passage with higher simulated PR and higher speed; left side: Original geometry; middle: Geometry with 5 grooves in the stator; right side: Geometry with 11 grooves in the stator.

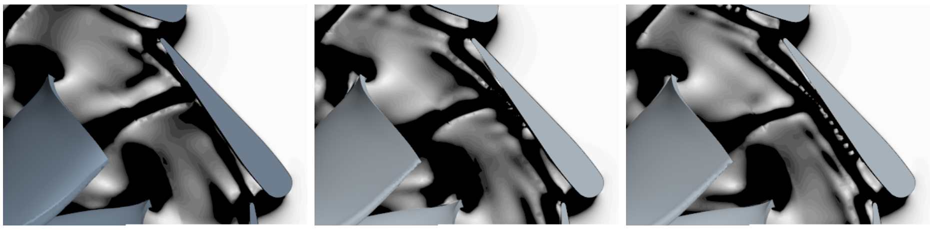

(a) $t = 25\%$ rotor blade passing.

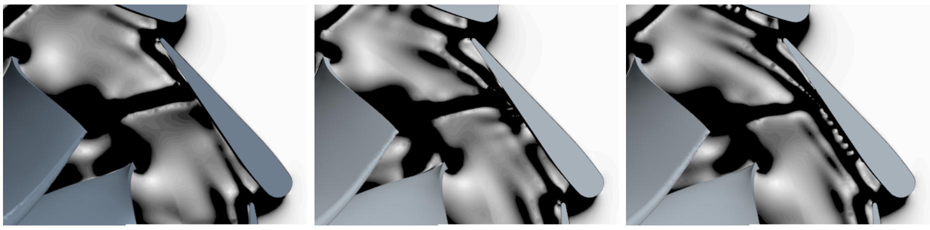

(b) $t = 50\%$ rotor blade passing.

(c) $t = 75\%$ rotor blade passing.

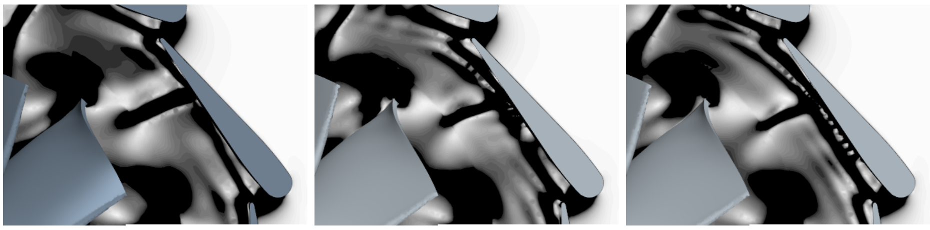

(d) $t = 100\%$ rotor blade passing.

Figure 10.10: Transient numerical schlieren for 10% VGT opening at 50% span of the stator passage with higher simulated PR and lower speed; left side: Original geometry; middle: Geometry with 5 grooves in the stator; right side: Geometry with 11 grooves in the stator.

10.5.3 Effects on the rotor blade

After analyzing the impact of the grooves on the stator and vaneless space reducing the supersonic pocket and the intensity of the shock waves, this section focus on the effects on the rotor evaluating the blade loading. The blade loading provides the work on the turbine shaft and is determined based on the pressure difference between the PS and SS. Thus, Figure 10.11 presents the blade loading at lower and higher speed, both at higher PR. At lower speed, the blade loading of the three stator vanes geometries presents the same trend in the first middle part of the vane as shown in Figure 10.11(a). Furthermore, the spike in the blade loading is due to the stator SS shock wave striking the blade LE [124, 86], besides the formation of shock waves in the relative frame. In the region between 0.7 and 0.9 relative chord length, the load improves more in the case of 5 grooves than in the case of 11 grooves. In contrast, the differences are insignificant at the rest of the chord length, explaining the slight variation in the turbine efficiency presented in Figure 10.6(b). At higher speed, Figure 10.11(b) depicts how the use of grooves on stator vanes increases the blade loading and can avoid the blade loading oscillates between negative and positive values every time a stator vane is passed as was analyzed in Chapter 6, especially in the case of 5 grooves, which presents a rise in the turbine efficiency of 3% points, followed by the case of 11 grooves with an increase of 2% compared with the original configuration.

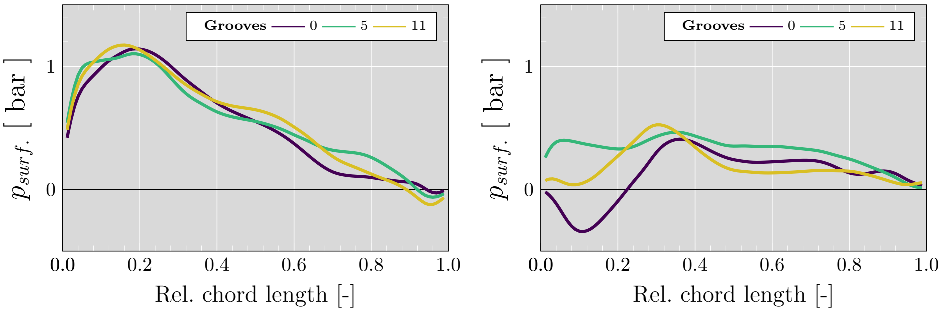

(a) Lower speed and higher PR.

(b) Higher speed and higher PR.

Figure 10.11: Rotor blade loading at 50% span with closed VGT position.

10.5.4 Exergy analysis

For the cases of lower and higher PR and both at lower and higher speed, with and without grooved surface, the exergy in each region of the computational domains has been evaluated following the same procedure as in Chapter 8. The normalized exergy change through the inlet duct and volute is negligible for all the cases as depicts Figure 10.12(a). Comparing the cases with grooved surfaces against those without grooves under the same operational conditions, one has the following results. At lower speed and lower PR, the normalized exergy change in the stator increases by 8.2% and 15.4% for the case of 5 grooves and 11 grooves, respectively. Nevertheless, the gain in the stator due to the presence of grooves is penalized in the vaneless space as the flow decelerates. Thus, the exergy decreases by 2.8% and 13.5% for the cases of 5 and 11 grooves, respectively. When the flow goes through the rotor, the changes in the exergy compared with the case without grooves are neglected. In the cases of higher speed and lower PR, where the flow does not reach sonic conditions in the stator vane, the exergy increase in the stator is lower than in the cases of lower speed and lower PR. Nevertheless, comparing the exergy variation of the original geometry with the grooved vanes, at higher speed is higher than at lower speed. The configurations of 5 and 11 grooves present a rise of 38.2% and 27.5%, respectively. Nevertheless, exergy variation in the vaneless space shows a drop of 38.6% and 53.4% for 5 and 11 grooves, respectively, while the fraction corresponding to the rotor can increase by 25.4% and 22.8%.

Focusing on the cases at higher PR and the two selected rotational speed, whose Mach number and density gradient profiles were analyzed in the previous section, the exergy fraction in each region of the computation domain with grooved surface on the stator vanes present the following variation concerning the original geometry. At lower speed, the energy usefulness in the stator increases 4.6% and 7.6% for the configuration of 5 and 11 grooves, respectively. In the vaneless space, the geometry with 5 grooves presents a particularity compared with the rest of the cases. The normalized exergy change increases by 8.7%, which is reflected in the stator efficiency shown in Table 10.3. While in the 11 grooves configuration drops by 2.2%. In the rotor, despite the reduction in the shock wave intensity on the stator vane that influences the rotor performance, the changes represent less than 0.5% compared with the original geometry. At higher speed and higher PR, the 5 and 11 grooves cases present in the stator an increase of the energy quality of 8.2% and 15.9%, respectively. Furthermore, the exergy variation in the vaneless space presents a degradation of 23.0% and 40.2% for 5 and 11 grooves, respectively, as a consequence of the flow distortion produced by the grooves and the wake increase at the TE. Then as a consequence of the reduction of the supersonic conditions in the vaneless space that affect the rotor, the normalized amount of work obtainable in this region can increase by 8.7% and 7.7%.

The fluid leaving the rotor contains a considerable portion of flow exergy, especially at higher speed. Increasing the PR at lower speed increases the exergy in the outlet region, while at higher speed decreases. Furthermore, the exergy budget grows with the grooves up to 16.7%; except for the case of higher speed and higher PR, where the exergy change decreases by 22.4% and 13.5% using 5 and 11 grooves, respectively.

Figure 10.12(b) presents the ratio of the turbine power over the exergy flow at the inlet probe section, which represents the effectiveness of available energy usage in the system. At lower speed the fraction of energy at the inlet destinated to produce power does not change significantly with a grooved surface on the stator vanes and is also reflected in the small change in the efficiency depicted in Figure 10.6(b) and Table 10.3. The maximum change relating to the original configuration occurs with the 5 grooves geometry at higher speed and lower PR, presenting an increase of 27.3%, followed by the case of 11 grooves with a rise of 13.3% at the same operational conditions. Furthermore, the most significant approach of the maximum energy corresponds to the configuration of 5 grooves at higher speed and higher PR.

The exergy analysis reveals that turbine efficiency does not reflect effective energy usage in the system. Furthermore, this analysis shows excellent potential to improve the available energy usage in the turbine system. From Figure 10.12(b), we observe that the effectiveness of available energy usage at higher speed and lower PR passed from 0.18 to 0.23 using 5 grooves on the stator vanes, which has a turbine efficiency of 32% against the 27% of the original configuration.

One can highlight that the use of grooves to take advantage of available energy at the turbine inlet, reducing the impact of the irreversibility generated by the shock waves, has a more significant effect at higher speed than at lower speed.

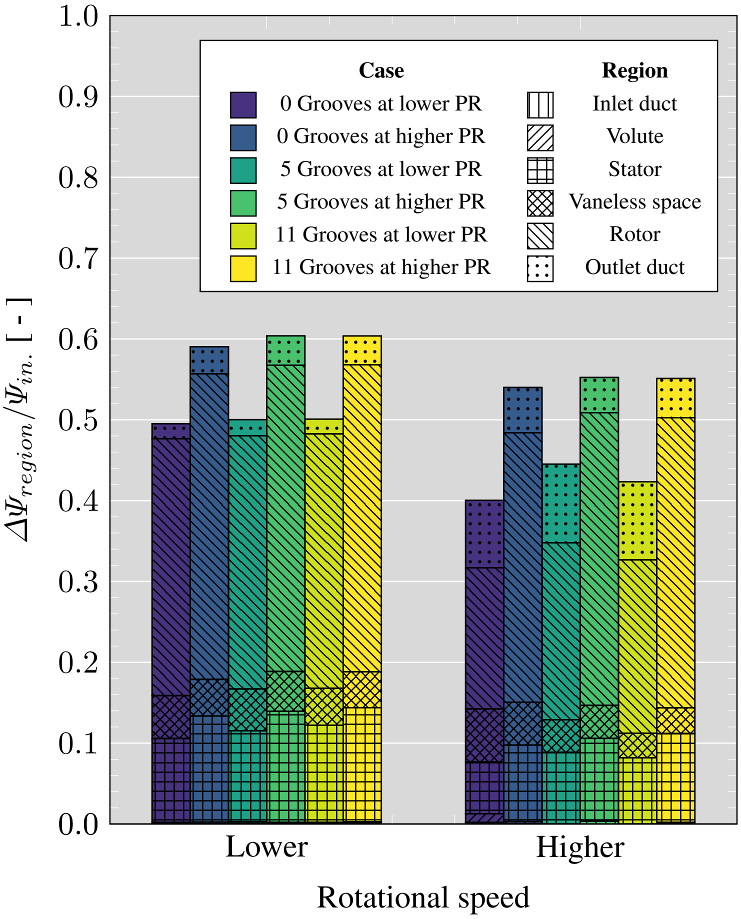

(a) Distribution of the normalized overall exergy in the turbine domain.

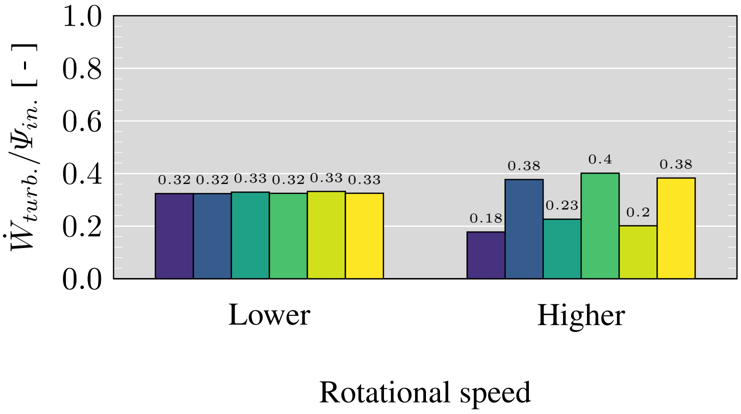

(b) Comparison of the turbine power with respect to the exergy at the inlet probe plane.

Figure 10.12: Exergy analysis for the evaluated operational points; lower: 3882 rpm/$\sqrt{\mathrm{K}}$; higher: 8421 rpm/$\sqrt{\mathrm{K}}$.

10.6 Summary

The stator vanes of the variable geometry turbine have been modified, changing the flat surface of the stator SS to a grooved surface. Two configurations have been analyzed and compared with the original geometry. The first configuration has 5 grooves on each stator vane, while the second has 11 grooves. A mesh independence study has been carried out with 11 grooves in stator vanes at a closed position (10% VGT) and operating at lower speed and higher PR. The selected unstructured polyhedral mesh has 10 million cells and 20 cells in the boundary layer. The turbine with the two type of grooves surface has been simulated at two rotational speed, 3882 rpm/$\sqrt{\mathrm{K}}$ (lower speed) 8421 rpm/$\sqrt{\mathrm{K}}$ (higher speed) and at two PR, lower and higher, using the mesh mentioned above. Regarding the turbine performance, the reduced mass flow is not significantly affected by the grooved surface. Nevertheless, the grooves' presence impacts the turbine efficiency, especially at higher speed. At higher speed and lower PR the rise in the turbine efficiency is 5.8% points and 3.8% points for the configuration with 5 and 11 grooves, respectively. While at higher PR the increase is 3.6% points and 2.0% points for the case of 5 and 11 grooves, respectively. On the one hand, the total to static efficiency of the turbine increases, but on the other hand, the stator efficiency slightly decreases with the rise of grooves.

The cases of lower and higher speed at higher PR have been selected to evaluate the Mach number profile at 50% stator span and the pressure profile. The results reveal that with increasing the number of the grooves, the supersonic region connecting the stator vane and the rotor entry becomes smaller. Furthermore, the wake at the vane TE increases, affecting the supersonic region of the neighboring vane along with the shock wave contributing to the rise in the efficiency. The presence of grooves generates pressure peaks on the vane SS, which are related to small shock waves. The number of pressure peaks matches the number of grooves. Comparing the pressure jump of the original geometry against the most significant jump in the 5 and 11 grooves configuration, the jump at higher speed decreases by 45% and 67%, respectively. While at lower speed, the reduction achieves 39% and 56%, respectively.

The numerical Schlieren images reveal that the shock wave pattern on the grooved vanes at higher speed is less intense, generating a multiple shock structure. The main shock normal to the SS remains practically at the same position as in the original configuration. At lower speeds, the shock wave is leaned backward with and without the grooved surfaces and extends longer toward the rotor than in the cases of higher speed. Small shock waves appear on each groove, weakening the main shock. Furthermore, the moving rotor blade encounters supersonic speed locally, resulting in the formation of shock waves in the relative frame. At higher and lower speeds, the intensity of the shock wave decreases with increasing the number of grooves. The weakening of the intensity of the standing shock wave at both speeds can contribute to diminishing losses close to the rotor. Furthermore, at higher speed, the load fluctuation around the rotor LE can be reduced and minimize the factors that compromise the integrity of the turbine.

For the cases with a grooved surface at lower speed and higher PR, it is possible to observe the presence of a shock wave at the convergent section between the vanes, only between a time of 50% and 75% blade passing.

The blade loading at higher PR has been evaluated to analyze the impact of the flow profile on the rotor blade when using a grooved surface in the stator and operating at higher PR. At lower speed, the blade loading of the three stator vanes geometries presents a similar trend in the first middle part of the vane but remains slightly higher in the case of 11 groves. Furthermore, between 0.7 and 0.9 relative chord length, the load improves more in the case of 5 grooves than 11 grooves. These results justifies the slight variation in the turbine efficiency. At higher speed, the blade loading rises, and the oscillation between negative and positive values is prevented due to the use of grooves justifying again the increase in the turbine efficiency of 3% points and 2% points for the configuration of 5 and 11 grooves, respectively.

An exergy analysis was carried out to quantify the potential for achieving the maximum possible work of the turbine. In order to do that, the cases with and without grooves operating at different conditions were selected to evaluate the exergy in each turbine region. The exergy changes through the inlet duct, and volute is negligible for all the cases. The exergy change at lower speed and lower PR does not suffer a significant difference with the grooved surface but is slightly greater when using 11 than 5 grooves. Under this operational conditions the increase in the stator is 15.4%, while in the vaneless space decreases by 13.5%, and no significant change occurs in the rotor. The exergy change in the regions mentioned above at higher speed and lower PR for the 5 grooves configuration, which presents the more significant changes, is a growth of 38.2%, a drop of 38.6%, and a rise of 25.4%, respectively. Furthermore, for this operational point, the flow does not reach sonic conditions as it does in the cases of higher PR. Considering the cases at higher PR, first at lower speed stand out the configuration with 11 grooves with an increase in the energy potential of 7.6%, a decrease of 2.2% and a slight rise of 0.5% in the stator, vaneless space, and rotor, respectively. While at higher speed, the 5 grooves geometry represents a better choice than the 11 grooves. Thus, the exergy change in the regions mentioned above increases by 8.2%, a reduction of 23.0%, and a rise of 8.7%.

Evaluating the effectiveness of the available energy usage in the turbine, at lower speed the fraction of energy at the inlet destinated to produce power does not change significantly with a grooved surface on the stator vanes and is reflected in an insignificant change in the efficiency. On the contrary, at higher speed and higher PR with 5 grooves occurs the most significant approach of the maximum energy. Thus, the use of grooves to take advantage of available energy at the turbine inlet, reducing the impact of the irreversibility generated by the shock waves, has a more significant effect at higher speed than at lower speed.

10.7 References

[82] B. Zhao, M. Qi, H. Zhang, and X. Shi. "Investigation on effects of shock wave on vortical wake flow in a turbine nozzle cascade". In: *Aerospace Science and Technology* 98 (2020), pp. 1–9. ISSN: 1270-9638. DOI: https://doi.org/10.1016/j.ast.2020.105690. URL: https://www.sciencedirect.com/science/article/pii/S1270963819327348 (cit. on pp. 15, 171).

[86] H. Chen. "Turbine wheel design for Garrett advanced variable geometry turbines for commercial vehicle applications". In: *8th International Conference on Turbochargers and Turbocharging*. Ed. by B. T. .-. 8. I. C. o. T. Institution of Mechanical Engineers Combustion Engines & Fuels Group and Turbocharging. Woodhead Publishing, 2006, pp. 317–327. ISBN: 1845691741. DOI: 10.1533/9781845697099.6.317. URL: http://www.sciencedirect.com/science/article/pii/B9781845691745500270 (cit. on pp. 15, 177).

[123] X. Lei, M. Qi, H. Sun, and L. Hu. "Investigation on the Shock Control Using Grooved Surface in a Linear Turbine Nozzle". In: *Journal of Turbomachinery* 139.12 (2017). ISSN: 0889-504X. DOI: 10.1115/1.4037860. URL: https://doi.org/10.1115/1.4037860 (cit. on pp. 18, 173).

[124] *Numerical Investigation of a Novel Approach for Mitigation of Forced Response of a Variable Geometry Turbine During Exhaust Braking Mode*. Vol. Volume 8: Turbo Expo: Power for Land, Sea, and Air. 2016. DOI: 10.1115/GT2016-56342. URL: https://doi.org/10.1115/GT2016-56342 (cit. on pp. 19, 171, 177).

[125] B. Zhao, M. Qi, H. Sun, X. Shi, and C. Ma. "Experimental and Numerical Investigation on the Shock Wave Structure Alterations and Available Energy Loss Variations With a Grooved Nozzle Vane". In: *Journal of Turbomachinery* 141.5 (2019). ISSN: 0889-504X. DOI: 10.1115/1.4041819. URL: https://doi.org/10.1115/1.4041819 (cit. on pp. 19, 169).

[153] P. J. Roache. "Perspective: A Method for Uniform Reporting of Grid Refinement Studies". In: *Journal of Fluids Engineering* 116.3 (1994), pp. 405–413. ISSN: 0098-2202. DOI: 10.1115/1.2910291. URL: https://doi.org/10.1115/1.2910291 (cit. on pp. 46, 164).

[179] F. Mendonça, J. Clement, D. Palfreyman, and A. Peck. "Validation of unstructured CFD modelling applied to the conjugate heat transfer in turbine blade cooling". In: *ETC_8-198, European Turbomachinery Conference*. Graz, 2008 (cit. on p. 162).

[180] M. A. Asghar, Y. Liu, J. Cui, and L. Lu. “Investigation of Unsteady Flow Interactions in a Transonic High Pressure Turbine Using Nonlinear Harmonic Method”. In: *Energies* 11.2 (2018). ISSN: 1996-1073. DOI: `10.3390/en11020342`. URL: `https://www.mdpi.com/1996-1073/11/2/342` (cit. on p. 169).

[181] L. Li, W. Tan, J. Zhang, G. Han, and Y. Zhang. “Unsteady Effects of Wake on Downstream Rotor at Low Reynolds Numbers”. In: *Energies* 15.18 (2022). ISSN: 1996-1073. DOI: `10.3390/en15186692`. URL: `https://www.mdpi.com/1996-1073/15/18/6692` (cit. on p. 169).

[182] X. BIAN, Q. WANG, X. SU, and X. YUAN. “Interaction mechanisms of shock waves with the boundary layer and wakes in a highly-loaded NGV using hybrid RANS/LES”. In: *Chinese Journal of Aeronautics* 33.1 (2020), pp. 149–160. ISSN: 1000-9361. DOI: `https://doi.org/10.1016/j.cja.2019.07.008`. URL: `https://www.sciencedirect.com/science/article/pii/S1000936119302754` (cit. on pp. 171, 173).

[183] T. Léonard, L. Y. M. Gicquel, N. Gourdain, and F. Duchaine. “Steady/Unsteady Reynolds-Averaged Navier–Stokes and Large Eddy Simulations of a Turbine Blade at High Subsonic Outlet Mach Number”. In: *Journal of Turbomachinery* 137.4 (2014). ISSN: 0889-504X. DOI: `10.1115/1.4028493`. URL: `https://doi.org/10.1115/1.4028493` (cit. on p. 173).

[184] B. J. Hancock and J. P. Clark. “Reducing Shock Interactions in Transonic Turbine via Three-Dimensional Aerodynamic Shaping”. In: *Journal of Propulsion and Power* 30.5 (2014), pp. 1248–1256. DOI: `10.2514/1.B35027`. URL: `https://doi.org/10.2514/1.B35027` (cit. on p. 174).

[185] B. Zhao, X. Shi, H. Sun, M. Qi, and P. Song. “Effects of grooved vanes on shock wave and forced response in a turbocharger turbine”. In: *International Journal of Engine Research* 22.3 (2021), pp. 805–814. DOI: `10.1177/1468087419879265`. URL: `https://doi.org/10.1177/1468087419879265` (cit. on p. 174).

CHAPTER 11

Conclusions and future works

Contents

11.1 Introduction 189
11.2 Stator flow features 189
11.3 Stator-Rotor interaction 189
11.4 Rotor flow features 190
11.5 Exergy analysis 191
11.6 Effects of the geometry change 192
11.7 Future works 194
11.8 References 203

Figures

11.1 Descriptions of the test bench. 194
11.2 Pressure taps for the measurement of the instant pressure. 196
11.3 Twin-entry turbine geometry [7]. 198
11.4 Twin-entry turbine computational domain [8]. 198
11.5 Relative Mach number snapshots of RANS simulations with opened VGT position; MFR=0.0; red line: $Ma_{rel.} = 1$. 199
11.6 Relative Mach number snapshots of RANS simulations with opened VGT position; MFR=0.53; red line: $Ma_{rel.} = 1$. 200
11.7 Relative Mach number snapshots of RANS simulations with opened VGT position; MFR=1.0; red line: $Ma_{rel.} = 1$. 201

Tables

11.1 Main characteristics of the engine. 195
11.2 Main characteristics of the screw compressor. 195

11.1 Introduction

THE current work has presented a computational analysis of the flow behavior within a variable geometry turbine reaching choking conditions, focusing on the regions of the stator, rotor, and the stator-rotor interaction in the vaneless space. Based on the analysis, the presence of supersonic areas depending on the stator vanes positions and the operational conditions at two PR and rotational speeds has been identified. The Mach number distribution, pressure profiles, and exergy analysis are useful to understand the characteristics of the flow and the impact on the turbine performance parameters when operating at off-design conditions. Hence, the results allow us to identify the regions where the main losses occur to develop other configurations with higher efficiency and adequate extrapolated models. This chapter presents the contributions of the flow through the stator, the rotor, the stator-rotor interaction, the summarized exergy analysis, and the impact of varying the turbine geometry.

11.2 Stator flow features

For the turbine geometry considered in this study at a closed position of the stator vanes, a shock develops first on the SS of the stator vanes and not in the perpendicular section that goes from the TE of one vane until the SS of the neighboring vane, which is considered as the geometrical throat of the stator in the literature, despite of the reduced area between the vanes. The effectively choked area spans from the stator SS towards the rotor inlet. At turbine PRs around 5, the full stator choking is achieved in the throat of the vaneless space just upstream of the rotor inlet.

11.3 Stator-Rotor interaction

The highly swirled flow in the vaneless space causes an increase of local mass flow leading to the generation of an effective throat in this region. This throat is formed by the SS of the stator vane and the moving rotor blades.

For 10% and 30% VGT openings and at lower and higher speeds, it was observed that the exact location of the shock wave on the SS varies more with rotational speed than with stator vane position. The shock wave's location slightly shifts to lower vane chord lengths as rotational speed rises and leans backward at the lower speed.

It is important to emphasize that the shock losses are related to the number of shocks a fluid particle experiences before entering the rotor. Losses increase as the flow approaches the stator vane and decrease as it approaches the center of the vaneless space. From there, shock losses increase again as the flow approaches closer to the rotor inlet.

Together with the stator vane, the rotor creates moving throats, and the number of shock waves equals the number of rotor blades. Weak shock waves are continuously produced in the absolute frame close to the LE. These shock waves become stronger when a rotor LE passes the circumferential positions of the local throats. The relative Mach number becomes locally supersonic close to the detected throat when the rotational speed is low, and additional strong shock waves are produced at the LE. These stronger shocks in the relative frame also turn the flow inwards, reducing the flow path. It can be assumed that this stronger shock is relevant for the pressure downstream of the shock front in the vaneless space and might influence the chordwise location towards the dependency on the rotational speed.

Rotor shock losses depend on how many times a fluid particle passes in front of a rotor blade. The shock waves can cause an alternating increase of static pressure on the PS and the SS close to the LE at higher speeds. The alternating pressure distribution results in oscillations of the blade loading, which might cause material failure according to the literature review.

At moderately closed positions (30% VGT), either the flow is choked in the rotor inlet or the stator, depending on the rotational speed.

11.4 Rotor flow features

With the stator vanes at a closed position and increasing turbine PR until high values, a partially choked rotor outlet has been identified at the already choked vaneless space throat. Nevertheless, a fully choking condition only happens in the rotor throat near the rotor outlet when stator vanes are opened. It has been observed that reduced mass flow stagnation in the rotor outlet appears at different values. In the mostly choked rotor outlet the flow reaches supersonic speeds above 1. Nevertheless, the subsonic regions in the rotor TE plane are due to the tip leakage when the turbine operates at lower speed. The flow going through the tip gap reaches supersonic speed and experiences a rough deceleration when it leaves the gap.

Expressing the reduced mass flow as a function of the Mach number and considering that the tip leakage flow decreases the Mach number in the rotor outlet, it is seen that the reduced mass flow increases. Furthermore, this effect can increase the spreading of the speed lines in the overall reduced mass flow map. Additionally, it has been shown that the total pressure ratio and the total temperature difference between turbine inlet and turbine outlet maintains constant at a similar turbine PR as the highest reduced mass flow has been identified. This confirms the aerodynamic choking of the overall passage flow except for the tip leakage flow.

Different trends were identified in the development of the choking conditions in the rotor passage depending on the rotational speed. The effectively choked area appears at the rotor hub and extends toward the shroud at lower speed. This behavior is due to the tip leakage vortex that provokes a choking delay close to the shroud. While at higher speed, the tip leakage is lower and thus the vortex in the main channel. Therefore, the choking at higher spans is not equally affected as at lower speed. In radial turbines, the naturally higher blade curvature at high spans supports the flow acceleration, resulting in reaching the sonic limit earlier. At the same time the flow enters with positive incidence at low spans. Thus, the relative inflow angle diminishes the acceleration along the SS at lower spans.

11.5 Exergy analysis

The exergy analysis was carry out in order to quantify the fraction of reversible work available in each region of the computational domain. The greater change of the exergy occurs in the rotor. The fractions in the stator and vaneless space are significant at closed VGT and increase as the PR increases which is also related with intensity of the choked flow. The biggest approach of the maximum amount of shaft work that can be extracted from the conditions of the fluid at the inlet until its equilibrium with the environment, corresponds to the operational point at opened VGT lower PR and middle speed. These result can be used in future work to quantify and identify the regions with the higher internal irrevesibilities in order to improve the performance of the turbine.

Besides the analysis for the original configuration given by the manufacturer, the study was also carried out for the configuration in the stator geometry with 5 and 11 grooves to compare them. The exergy changes through the inlet duct, and volute is negligible for all the cases. The exergy change at lower speed and lower PR does not suffer a significant difference with the grooved surface but is slightly greater when using 11 than 5 grooves. With 11 grooves, the stator presents an increase in the exergy, but then a reduction in the vaneless space occurs, while in the rotor, no significant change occurs. On the contrary at higher speed and lower PR, the 5 grooves present the major exergy change with gains in the rotor region. It is important to remember that at this operational point the flow does not reach sonic conditions as it does in the case of higher PR. At lower speed when the pressure increase the better results still correspond to the configuration of 11 grooves with the most significant change take place in the stator. While at higher speed and higher PR the 5 grooves geometry represents a better choice generating an improvement in the useful work potential in the rotor.

Evaluating the effectiveness of the available energy usage in the turbine, at lower speeds, the fraction of energy at the inlet destined to produce power does not change significantly with a grooved surface on the stator vanes and is reflected in the slight variation in the efficiency. Nonetheless, the most relevant use of available energy occurs at higher speeds and higher PR with 5 grooves. One can highlight that the use of grooves to take advantage of the work potential of the fluid entering the turbine, reducing the impact of the irreversibility generated by the shock waves, has a more significant effect at higher speed than at lower speed.

11.6 Effects of the geometry change

In this study were analyzed the effects of the geometry variation in the rotor and stator. Regarding the rotor the effects of the tip gap size on the choking conditions in rotor and the behavior of the flow through the tip gap was analyzed. Furthermore, different grooved surfaces in the stator vanes were evaluated in order to mitigate the intensity and impact of the shock wave developed on the stator SS.

11.6.1 Effects of the variation of the rotor tip gap

With the vanes at an opened position the turbine efficiency decreases with increasing the tip gap due to the entropy generation as the flow through the tip gap mixes with the main flow. On the contrary a reduction in the tip gap of 50% at lower speed generate a rise of 1.6% points in the efficiency while at higher speed can reach 3% points.

Concerning the behavior of the flow through the gap, the flow accelerates when passing from the PS of the tip gap to the SS, reaching supersonic conditions in the exducer region for all the evaluated operational points.

Due to the relative motion of the shroud wall, part of the flow is turned to the hub, and the remaining goes through the tip gap, which is denoted as negative tip leakages. At higher speed, the negative tip leakage is significant, filling almost more than half of the inducer region and diminishing the mass flux of positive tip leakages. The increase in the PR generates a reduction in the negative tip leakages and an increase in the positive tip leakage but without significantly affecting the extension of the supersonic region tip gap in the axial direction of the tip gap.

The difference between the static pressure on the PS and SS along the tip gap reveals that tip leakage does not change significantly when varying the tip gap in the exducer region.

The rotational speed and the span location affects the blade loading. At higher speed, the load increases from the hub to the shroud, where the thickness of the blade is lower. While at lower speed the load decreases from 80% to 95% rotor span. The increase in the tip gap generates the rise in pressure difference. Furthermore, all the different tip gap size at lower speed present a small supersonic pocket on the SS, while at higher speed the supersonic region on the SS has a higher intensity and extends until the rotor passage outlet reaching the PS of the neighboring blade at the TE.

The interaction of the tip leakage and the main flow results in subsonic regions at lower and higher speed. At lower speed, the vortex created by the blend of the tip leakages and the main flow is responsible for the subsonic region at the TE close to the shroud. Nevertheless, as the tip gap increases, the choked area at the TE varies slightly. At higher speed, the subsonic region is located on the SS at the TE and increases with the tip gap due to the secondary flow vortex. The swirling flow and high relative motion of the shroud wall contribute to the supersonic region near the shroud.

The increase in the tip gap produces a more significant change in the relative velocity and relative Mach number of the streamlines close to the shroud than the reduction in the gap. On the contrary, close to the hub, the flow remains unaltered at lower and higher speed. Furthermore, the flow losses close to the hub are less than when passing through the tip gap, according to the evaluated entropy generation in a streamline.

This research was carried out being aware of some limitations, such as the low numerical error that remains despite the grid independence study, the uncertainty of modeling turbulence, and neglecting the effects of thermal and rotational deformation in the turbine impeller and shroud.

11.6.2 Grooved Stator Vanes

The grooves on the stator vanes benefit turbine efficiency more at higher than lower speeds. The best improvement is obtained with the 5 grooves configuration at higher speed and at lower PR. Nonetheless, the stator efficiency decreases slightly as the flow velocity at the stator outlet decreases with the presence of grooves.

The supersonic region connecting the stator vane SS and the rotor entry becomes smaller with increasing the number of grooves. The grooves generate peaks on the vane pressure profile, which are related to small shock waves and match the number of grooves. Furthermore, a reduction in the pressure jump caused by the shock wave in the original configuration is achieved with the groove surface. Thus, the intensity of the main shock wave diminishes without changing its location, and a multiple shock wave structure, consisting of a small shock wave on each groove, is generated up and downstream of the main shock.

The weakening of the intensity of the standing shock wave at lower and higher speed can contribute to diminishing losses around the rotor entry. In particular, at higher speed and higher PR, the load fluctuation around the rotor LE can be reduced, minimizing the risk of mechanical failure and justifying the rise in the turbine efficiency.

11.7 Future works

11.7.1 Experimental validation

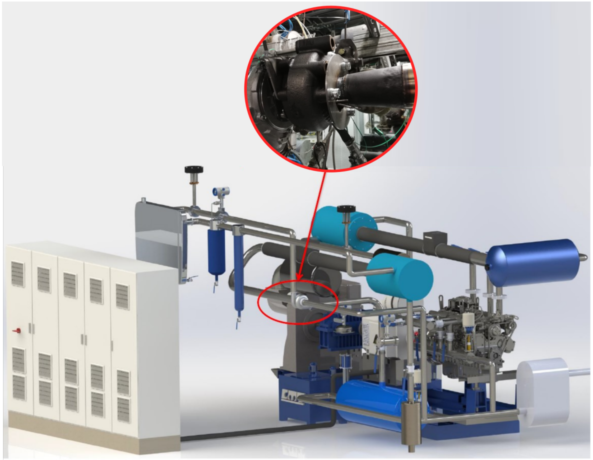

(a) Turbocharger test bench.

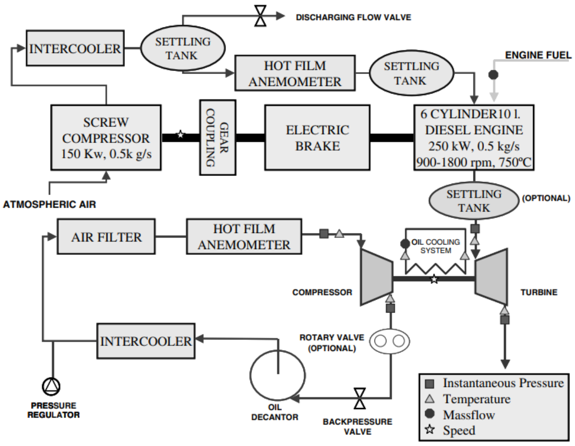

(b) Test bench scheme [186].

Figure 11.1: Descriptions of the test bench.

As was mentioned in Chapter 4 the experimental data shown in Figure 4.2 were obtained in the typical measurement range of automotive turbocharger turbines and low PR. Thus, to extend the turbine map to high PR as they were observed in this study, experimental measurements will be carried out in a test facility at CMT-Motores Térmicos that is depicted in Figure 11.1.

The test bench has two main systems: the power generation system and the turbocharger itself. The former drives the compressor and controls the turbine inlet conditions through the exhaust gases of a 6-cylinder diesel engine, mechanically coupled to a screw compressor to obtain additional energy. An electric brake is use to absorb the remaining power and regulate the rotating speed of the system, and a gearbox that adapts the speed of the engine and the compressor screw. The characteristics of the engine and the screw compressor are listed in Table 11.1 and Table 11.2, respectively.

Table 11.1: Main characteristics of the engine.

Engine: RVI MIDR 06-20-45	
Type of engine	Diesel
Number of cylinders	6
Swept volume [L]	9.84
Piston bore [mm]	120
Stroke [mm]	145
Compression ratio [-]	17.8:1
Maximum power [kW]	257
Speed range [rpm]	800-2000
Number of valves per cylinder	2
Fuel injection pump	In-line

Table 11.2: Main characteristics of the screw compressor.

Volumetric screw compressor Atlas Copco ZA 110-3.5	
Air mass flow rate [kg/s]	0.27-0.61
Compression ratio [bar]	1.5-4
Operation shaft speed [rpm]	1800-3600
Shaft power [kW]	30-130
Air outlet maximum temperature [$^{\circ}C$]	130

This installation has been used to obtains the turbine and compressor maps in conditions similar to reciprocanting internal combustion engine operational points [186]. The heavy duty diesel engine is used as a flow generator for driving the turbine allowing either continuous flow or pressure pulses similar to those existing in engine operation conditions. Thus, the use of electric heaters are not necessary, as the exhaust gases provides the necessary energy for the turbine. Other aspect of the system is that the engine has been devoid of its original turbocharger and is booted with the screw compressor and generate the desired turbine inlet conditions.

Besides obtaining the turbine map at a high PR, the experimental campaign also plans to get information regarding the pressure distribution in the vaneless space and close to the stator SS. The 30% VGT positions will be selected for such measurements when the turbine operates at lower and higher PR and lower and higher rotational speed. The pressure measurement is expected to reveal a sudden jump when the turbine operates at higher PR to try to capture the presence of a shock wave. Thus, several pressure taps are located along the vaneless space to install instantaneous pressure sensors with a range of 0-6 bar, 0-10 V, as depicts Figure 11.2. Nevertheless, using a scaled turbine [58] with an optical technique such as Schlieren images will be needed to obtain more reliable results.

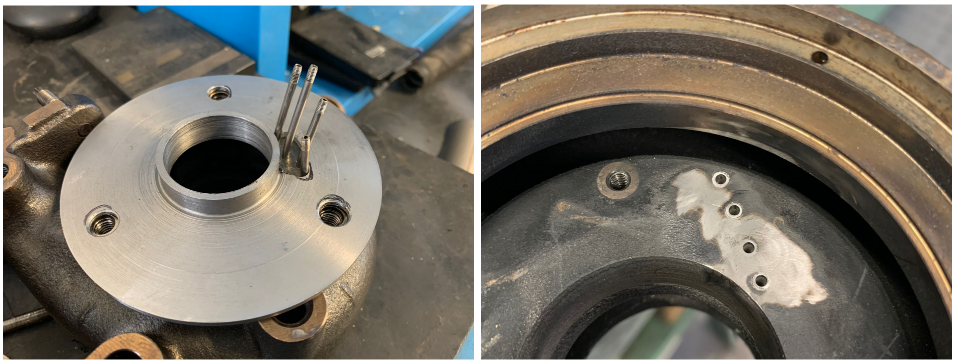
(a) External view of the pressure taps.

(b) Internal view of the pressure taps.

Figure 11.2: Pressure taps for the measurement of the instant pressure.

11.7.2 Study of the choking conditions in a different turbine

A twin-entry turbine will be selected to extend the research on the development of the choking conditions and validate that the distribution of the supersonic region in the rotor depends on the rotational speed and the tip-leakages. This turbine is depicted in Figure 11.3 and is used in a gasoline engine of 2 L and four cylinders. Some simulations have been carried out to study the sonic conditions in the rotor, with the following setup used by Galindo et al. [8] to analyze the losses in this turbine. The computational domain is shown in Figure 11.3 and was meshed using a non-structured polyhedral mesh with prism layers near the walls, resulting in a total of 5.5 million cells. The simulations are steady Reynolds averaged Navier Stokes (RANS) with a multiple reference frame for simulating the rotor movement. The turbulence model chosen is the k-ω SST model with compressibility correction and Durbin scale limiter for realizability. Furthermore, the y^+ obtained is lower than 2. The selected operational points for this turbine have the same inlet pressure and rotational speed as those considered for the variable geometry turbine presented in this thesis. These values correspond to a total pressure of 3.0 bar and 5.5 bar that produce the denoted lower and higher PR, while the rotational speed is 3882 rpm/$\sqrt{\mathrm{K}}$ and 8421 rpm/$\sqrt{\mathrm{K}}$ and denoted as lower and higher speed, respectively. As the twin-entry turbine has two branches at the inlet, denoted as hub branch and shroud branch, the Mass Flow Ratio (MFR) defined in Equation 11.1 is used to analyze the operating conditions when the flow enters only through the hub branch, through both branches and the shroud branch. Thus, for this study, the selected MFR is equal to 0.0, 0.53, and 1.0, respectively. Analyzing the Mach number distribution at the rotor TE plane (Figure 4.1(a)) is possible to observe for the case of MFR 0.0, depicted in Figure 11.5, the presence of supersonic regions. At lower speed and lower PR, Figure 11.5(a) the sonic conditions start to develop close to the hub. When the PR ratio increases to the higher evaluated value, as shown in Figure 11.5(b), the supersonic region extends toward the shroud, leaving a sonic zone close to the hub due to the tip leakage. For the case of higher speed at lower and higher PR, Figure 11.5(c) and Figure 11.5(c), respectively, the Mach number increases from the shroud to the hub. Thus, the distribution of the Mach number profile depending on the rotational speed is similar to the case of the variable geometry turbine. Figure 11.6 shows the results when the flow enters for the two inlet branches, presenting a similar behavior as the case mentioned above but with a section almost completely choked at higher speed and both PR, as the mass flow is higher. When the flow goes through the shroud branch having an MFR=1.0, Figure 11.7, the distribution is similar to the case of MFR=0.0. Nevertheless, as the flow enters by different branches, it is necessary to carry out a deeper analysis evaluating the incidence when the flow enters the rotor, the blade pressure profile, and the velocity distribution along different rotor spans to distinguish the impact on the Mach number distribution.

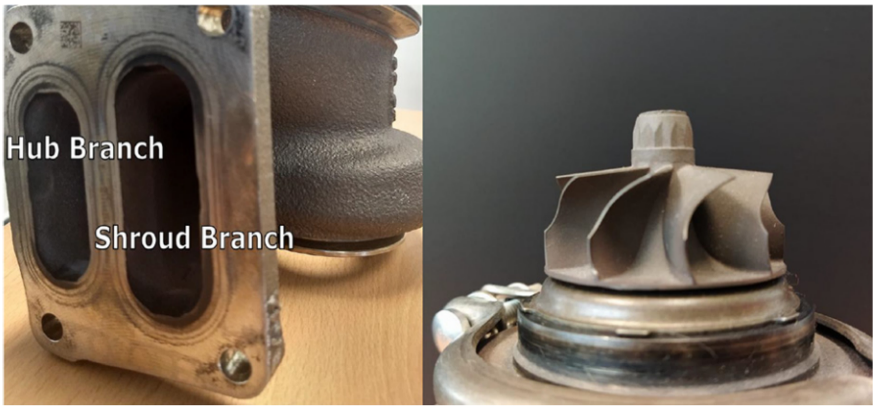

Figure 11.3: Twin-entry turbine geometry [7].

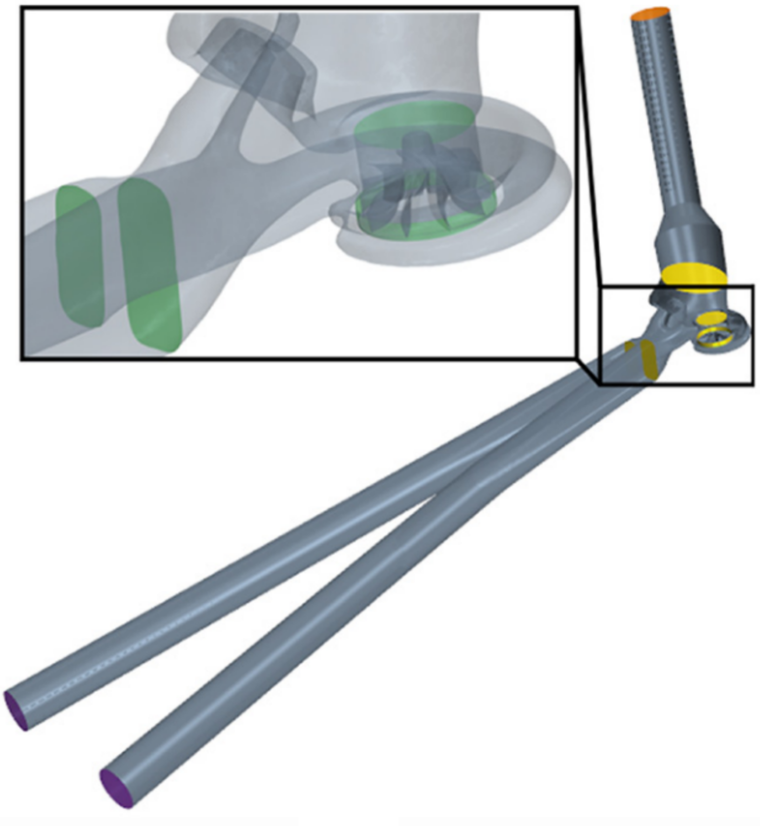

Figure 11.4: Twin-entry turbine computational domain [8].

$$MFR = \frac{\dot{m}_{shroud}}{\dot{m}_{shroud} + \dot{m}_{hub}} \tag{11.1}$$

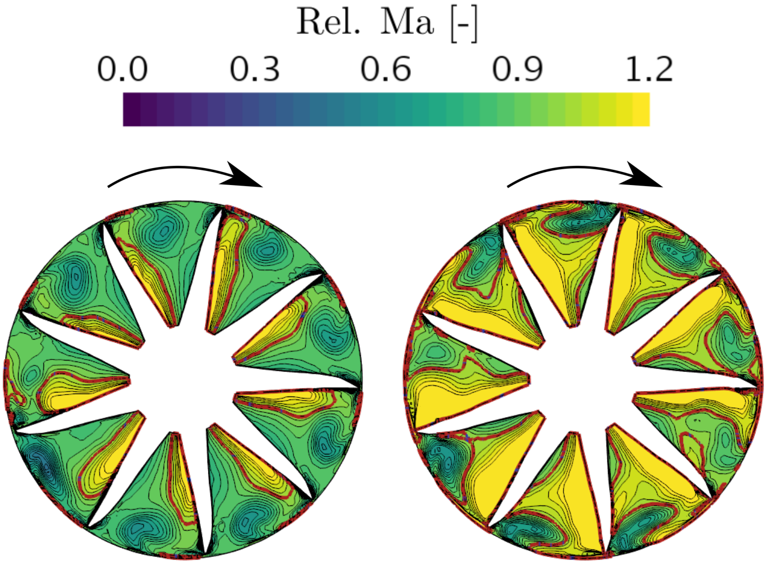

(a) Lower speed at lower PR.

(b) Lower speed at higher PR.

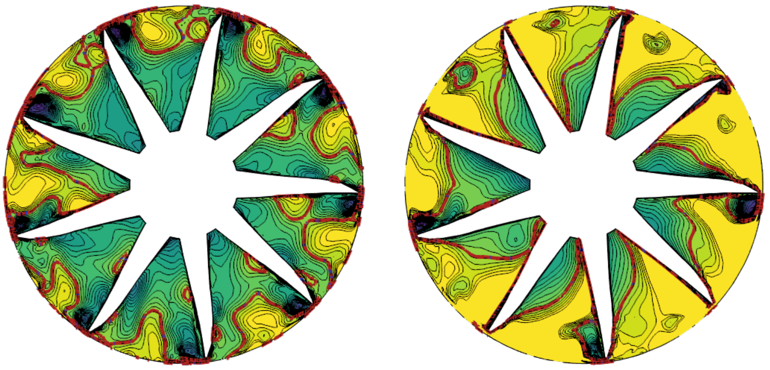

(c) Higher speed at lower PR.

(d) Higher speed at higher PR.

Figure 11.5: Relative Mach number snapshots of RANS simulations with opened VGT position; MFR=0.0; red line: $Ma_{rel.} = 1$.

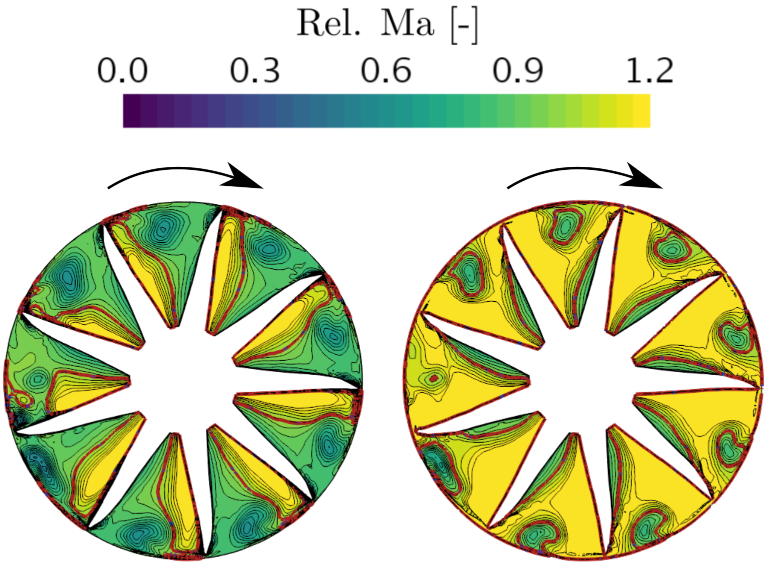

(a) Lower speed at lower PR.

(b) Lower speed at higher PR.

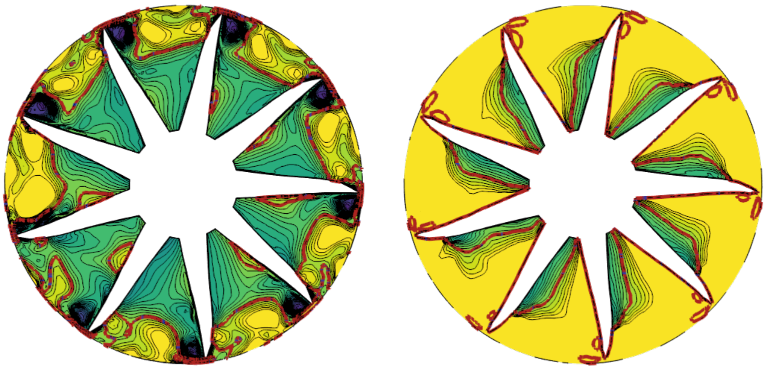

(c) Higher speed at lower PR.

(d) Higher speed at higher PR.

Figure 11.6: Relative Mach number snapshots of RANS simulations with opened VGT position; MFR=0.53; red line: $Ma_{rel.} = 1$.

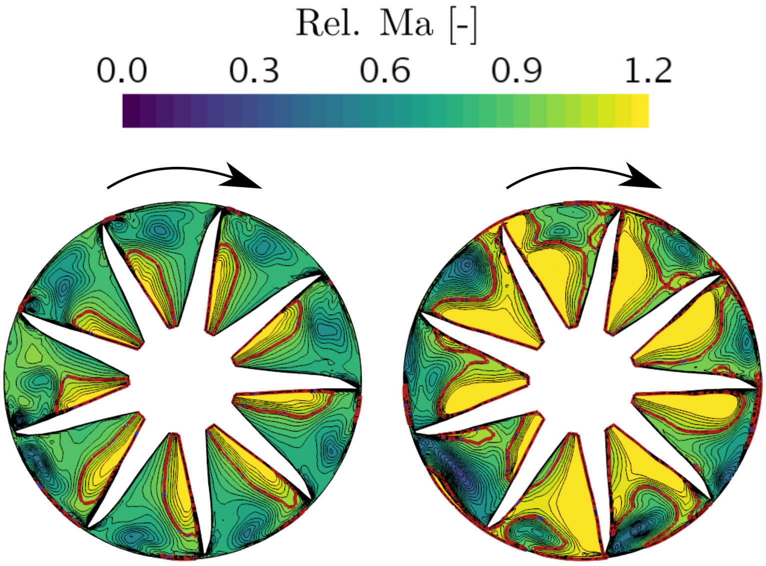

(a) Lower speed at lower PR.

(b) Lower speed at higher PR.

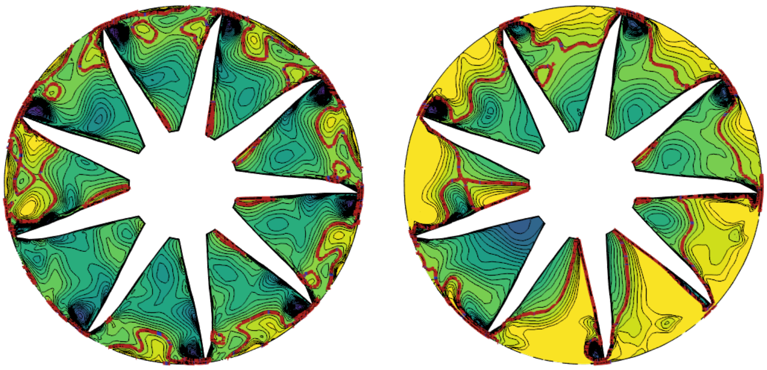

(c) Higher speed at lower PR.

(d) Higher speed at higher PR.

Figure 11.7: Relative Mach number snapshots of RANS simulations with opened VGT position; MFR=1.0; red line: $Ma_{rel.} = 1$.

11.7.3 1D modeling

The findings of this study are useful to develop physical one-dimensional models to extrapolate the turbine map toward high PRs. Here, the turbine will be considerate as an equivalent nozzle taking into account the VGT position, rotational speed, PR, inlet flow conditions as the mass flow as well as geometrical parameters. The model will evaluate the PR when the shocking appears first in the stator or in the rotor. Afterward, with all this data the model will use the definition of the critical mass flow through an isentropic nozzle to find an equivalent area, which will be recalculated following an iteration process and coefficients fitting. Once the equivalent area has been calculated the reduced mass flow can be interpolated or extrapolated in order to get the turbine map. Nevertheless, this is a previous idea of the model and certain modifications can occur during the development and implementation process. Furthermore, it is planned to enhance the one-dimensional modeling considering the influence of the tip leakage flows on the choking behavior in the rotor exit, which depends mainly on the rotational speed.

The importance of studying the flow characteristics at high PRs reaching choked flow for the development of a one-dimensional model is based on the literary review where authors such as Galindo et al. [74] concluded that the developed simplified physics model of a radial turbine in the interpolation flow capacity maps proved to have good results but extrapolations, which means high PRs, need to be improved. Serrano et al. [159] developed a one-dimensional adiabatic physically based efficiency model with loss correlations; the model used a tip leakage model contributing significantly to the extrapolation quality. Furthermore, the loss model of the vaneless space place plays an essential role in the VGT fitting. Thus, this model can be improved considering the flow behavior in the rotor tip gap and in the vaneless space under choked flow. Meroni et al. [63] proposed a loss model for a high-pressure ratio radial turbine for an Organic Rankine cycle, highlighting the importance of carefully estimating the blade throat to obtain correct mass flow rate values at high PR. Having an accurate one-dimensional model overcomes the problem of limited experimental maps available for the turbine to be used to characterize the turbine fully and during the matching and modeling with the engine [187, 188, 189].

11.8 References

[7] J. Galindo, A. O. Tiseira, L. M. García-Cuevas, and N. Medina. "Experimental assessment of the rotor outlet flow in a twin-entry radial turbine by means of Laser Doppler Anemometry". In: *International Journal of Engine Research* (2021), pp. 1–15. DOI: 10.1177/14680874211034411. URL: https://doi.org/10.1177/14680874211034411 (cit. on p. 198).

[8] J. Galindo, J. R. Serrano, L. M. García-Cuevas, and N. Medina. "Twin-entry turbine losses: An analysis using CFD data". In: *International Journal of Engine Research* (2021), pp. 1–21. DOI: 10.1177/14680874211007647. URL: https://doi.org/10.1177/14680874211007647 (cit. on pp. 61, 197, 198).

[58] J. Galindo, A. O. Tiseira Izaguirre, L. M. García-Cuevas, and N. Hervás Gómez. "Experimental approach for the analysis of the flow behaviour in the stator of a real centripetal turbine". In: *International Journal of Engine Research* 22.6 (2020), pp. 1–11. ISSN: 20413149. DOI: 10.1177/1468087420916281. URL: https://doi.org/10.1177/1468087420916281 (cit. on pp. 12, 15, 196).

[63] A. Meroni, M. Robertson, R. Martinez-Botas, and F. Haglind. "A methodology for the preliminary design and performance prediction of high-pressure ratio radial-inflow turbines". In: *Energy* 164 (2018), pp. 1062–1078. ISSN: 03605442. DOI: 10.1016/j.energy.2018.09.045. URL: https://doi.org/10.1016/j.energy.2018.09.045 (cit. on pp. 13, 202).

[74] J. Galindo, J. R. Serrano, L. M. García-Cuevas, and N. Medina. "Using a CFD analysis of the flow capacity in a twin-entry turbine to develop a simplified physics-based model". In: *Aerospace Science and Technology* 112 (2021), p. 106623. ISSN: 1270-9638. DOI: https://doi.org/10.1016/j.ast.2021.106623. URL: https://www.sciencedirect.com/science/article/pii/S1270963821001334 (cit. on pp. 14, 48, 202).

[159] J. R. Serrano, F. J. Arnau, L. M. García-Cuevas, and L. B. Inhestern. "An innovative losses model for efficiency map fitting of vaneless and variable vaned radial turbines extrapolating towards extreme off-design conditions". In: *Energy* 180 (2019), pp. 626–639. ISSN: 03605442. DOI: 10.1016/j.energy.2019.05.062. URL: http://www.sciencedirect.com/science/article/pii/S0360544219309314 (cit. on pp. 61, 202).

[186] J. Galindo, J. R. Serrano, C. Guardiola, and C. Cervelló. "Surge limit definition in a specific test bench for the characterization of automotive turbochargers". In: *Experimental Thermal and Fluid Science* 30.5 (2006), pp. 449–462. ISSN: 0894-1777. DOI: https://doi.org/10.1016/j.expt

hermflusci.2005.06.002. URL: https://www.sciencedirect.com/science/article/pii/S0894177705001275 (cit. on pp. 194, 196).

[187] N. F. Sakellaridis, S. I. Raptotasios, A. K. Antonopoulos, G. C. Mavropoulos, and D. T. Hountalas. “Development and validation of a new turbocharger simulation methodology for marine two stroke diesel engine modelling and diagnostic applications”. In: *Energy* 91 (2015), pp. 952–966. DOI: 10.1016/j.energy.2015.08.049 (cit. on p. 202).

[188] J. R. Serrano, F. J. Arnau, J. De la Morena, A. Gómez-vilanova, S. Guilain, and S. Batard. “A methodology to calibrate gas-dynamic models of turbocharged petrol engines with variable geometry turbines and with focus on dynamics prediction during tip-in load transient tests”. In: *ASME Turbo Expo 2020: Turbomachinery Technical Conference and Exposition*. Online: ASME, 2020, pp. 1–14. DOI: https://doi.org/10.1115/GT2020-15169. URL: https://doi.org/10.1115/GT2020-15169 (cit. on p. 202).

[189] J. R. Serrano, P. Piqueras, J. De la Morena, A. Gómez-Vilanova, and S. Guilain. “Methodological analysis of variable geometry turbine technology impact on the performance of highly downsized spark-ignition engines”. In: *Energy* 215 (2021), p. 119122. ISSN: 0360-5442. DOI: https://doi.org/10.1016/j.energy.2020.119122. URL: https://www.sciencedirect.com/science/article/pii/S0360544220322295 (cit. on p. 202).

References

[1] **Tiseira, A., Garcia-Cuevas, L. M., Inhestern, L. B., and Echavarría Olaya, J. D.**
"Numerical simulation of a radial turbine at off desing conditions in presence of choked flow"
in: *ASME Turbo Expo 2020: Turbomachinery Technical Conference and Exposition*. Virtual event: ASME 2020, pp. 1–14. URL: https://asmedigitalcollection.asme.org/GT/proceedings-abstract/GT2020/84102/V02ET39A018/1094614 (cit. on p. vii)

[2] **Tiseira, A., García-Cuevas, L. M., Inhestern, L. B., and Echavarría, J. D.**
"Development of Choked Flow in Variable Nozzle Radial Turbines"
in: *International Journal of Engine Research* (2021), pp. 1–18. DOI: 10.1177/14680874211018302. URL: https://doi.org/10.1177/14680874211018302 (cit. on p. vii)

[3] **Tiseira, A., Dolz, V., Inhestern, L. B., and Echavarría, J. D.**
"Choking dynamic of highly swirled flow in variable nozzle radial turbines"
in: *Aerospace Science and Technology* 122 (2022), p. 107396. ISSN: 1270-9638. DOI: https://doi.org/10.1016/j.ast.2022.107396. URL: https://www.sciencedirect.com/science/article/pii/S1270963822000700 (cit. on p. vii)

[4] **Galindo, J., Tiseira, A., Navarro, R., Inhestern, L. B., and Echavarría, J. D.**
"Numerical Analysis of the Effects of Different Rotor Tip Gaps in a Radial Turbine Operating at High Pressure Ratios Reaching Choked Flow"
in: *Energies* 15.24 (2022). ISSN: 1996-1073. DOI: 10.3390/en15249449. URL: https://www.mdpi.com/1996-1073/15/24/9449 (cit. on p. vii)

[5] **Galindo, J., Tiseira, A., Navarro, R., Inhestern, L. B., and Echavarría, J. D.**
"Numerical Analysis of the Effects of Grooved Stator Vanes in a Radial Turbine Operating at High Pressure Ratios Reaching Choked Flow"
in: *Aerospace* 10.4 (2023). ISSN: 2226-4310. DOI: 10.3390/aerospace10040359. URL: https://www.mdpi.com/2226-4310/10/4/359
(cit. on p. vii)

[6] **Mitsubishi Turbocharger and Engine Europe**
Turbo trends
2023. URL: https://www.turbocharger.mtee.eu/turbo-trends/
(cit. on p. 3)

[7] **Galindo, J., Tiseira, A. O., García-Cuevas, L. M., and Medina, N.**
"Experimental assessment of the rotor outlet flow in a twin-entry radial turbine by means of Laser Doppler Anemometry"
in: *International Journal of Engine Research* (2021), pp. 1–15. DOI: 10.1177/14680874211034411. URL: https://doi.org/10.1177/14680874211034411 (cit. on p. 198)

[8] **Galindo, J., Serrano, J. R., García-Cuevas, L. M., and Medina, N.**
"Twin-entry turbine losses: An analysis using CFD data"
in: *International Journal of Engine Research* (2021), pp. 1–21. DOI: 10.1177/14680874211007647. URL: https://doi.org/10.1177/14680874211007647 (cit. on pp. 61, 197, 198)

[9] **Mitsubishi Turbocharger and Engine Europe**
A history of turbocharging
2020. URL: https://www.turbocharger.mtee.eu/a-history-of-turbocharging/ (cit. on p. 2)

[10] **Garrett Motion**
VNT Turbochargers
2023. URL: https://www.garrettmotion.com/es/turbocharger-technology/how-a-turbo-works/broadest-turbo-range/vnt-turbochargers/ (cit. on p. 2)

[11] **BorgWarner**
BorgWarner Turbochargers with Variable Turbine Geometry (VTG)
2020. URL: https://www.borgwarner.com/newsroom/press-releases/2020/09/08/borgwarner-vtg-turbochargers-to-boost-large-number-of-global-oem-s-vehicles (cit. on p. 2)

[12] **Payri, F.**
"Predicción de las actuaciones de los grupos de sobrealimentación para motores diesel de automoción"
PhD thesis. Universidad Politécnica de Madrid 1973 (cit. on p. 4)

[13] **Serrano Cruz, J. R.**
"Análisis y modelado de transitorios de carga en MEC turboalimentados"
PhD thesis. Universitat Politècnica de València 1999 (cit. on p. 4)

[14] **Rodríguez, A.**
"Analisis comparativo y sintesis de la respuesta transitoria en motores diesel de inyeccion directa turboalimentados"
PhD thesis. Universitat Politècnica de València 2001 (cit. on p. 4)

[15] **Reyes-Belmonte, M. Á.**
"Contribution to the experimental characterization and 1-D modelling of turbochargers for IC engines"
PhD thesis. Universitat Politècnica de València 2013. DOI: 10.4995/Thesis/10251/34777 (cit. on p. 4)

[16] **López Hidalgo, M. A.**
"Estudio teórico-experimental de la dinámica rotacional de un turbocompresor de MCIA. Aplicación al diagnóstico de fallos"
PhD thesis. Universitat Politècnica de València 2014. DOI: 10.4995/Thesis/10251/37746 (cit. on p. 4)

[17] **Dombrovsky, A.**
"Synthesis of the 1{D} modelling of turbochargers and its effects on engine performance prediction"
PhD thesis. Universitat Politècnica de València 2017. DOI: 10.4995/Thesis/10251/82307 (cit. on p. 4)

[18] **Cervelló, C.**
"Contribución a la caracterización experimental y al modelado de turbinas de geometría variable en grupos de sobrealimentación"
PhD thesis. Universitat Politècnica de València 2005. DOI: 10.4995/Thesis/10251/1902 (cit. on p. 4)

[19] **Fajardo Peña, P.**
"Methodology for the numerical characterization of a radial turbine under steady and pulsating flow"
PhD thesis. Universitat Politècnica de València 2012. DOI: 10.4995/Thesis/10251/16878 (cit. on p. 4)

[20] **García-Cuevas González, L. M.**
"Experiments and modelling of automotive turbochargers under unsteady conditions"
PhD thesis. Universitat Politècnica de València 2014. DOI: 10.4995/Thesis/10251/48458 (cit. on p. 4)

[21] **Inhestern, L. B.**
"Measurement, simulation, and 1D-modeling of turbocharger radial turbines at design and extreme off-design conditions"
PhD thesis. Universitat Politècnica de València 2019. DOI: 10.4995/Thesis/10251/119989 (cit. on pp. 4, 47)

[22] **Soler Blanco, P.**
"Simulation and modelling of the performance of radial turbochargers under unsteady flow"
PhD thesis. Universitat Politècnica de València 2020. DOI: 10.4995/Thesis/10251/141609 (cit. on p. 4)

[23] **Samala, V.**
"Experimental characterization and mean line modelling of twin-entry and dual-volute turbines working under different admission conditions with steady flow"
PhD thesis. Universitat Politècnica de València 2020. DOI: 10.4995/Thesis/10251/153475 (cit. on p. 4)

[24] **Gómez Vilanova, A.**
"Modelling and analysis methodology of SI IC engines turbocharged by VGT"
PhD thesis. Universitat Politècnica de València 2021. DOI: 10.4995/Thesis/10251/181929 (cit. on p. 4)

[25] **Medina Tomás, N.**
"Flow capacity and efficiency modelling of twin-entry radial turbines under unequal admission conditoins through CFD analysis and experiments"
PhD thesis. Universitat Politècnica de València 2022. DOI: 10.4995/Thesis/10251/185820 (cit. on p. 4)

[26] **European Union**
UN Regulation No 49 – Uniform provisions concerning the measures to be taken against the emission of gaseous and particulate pollutants from compression-ignition engines and positive ignition engines for use in vehicles
Brussels 2023. URL: https://eur-lex.europa.eu/legal-content/EN/TXT/?uri=CELEX%7B%5C%%7D3A42023X0064%7B%5C&%7Dqid=1678886878531 (cit. on p. 12)

[27] **European Commission**
Commission proposes new Euro 7 standards to reduce pollutant emissions from vehicles and improve air quality
Brussels 2022. URL: https://ec.europa.eu/commission/presscorner/detail/en/ip%7B%5C_%7D22%7B%5C_%7D6495 (cit. on p. 12)

[28] **Cheng, L., Dimitriou, P., Wang, W., Peng, J., and Aitouche, A.**
"A novel fuzzy logic variable geometry turbocharger and exhaust gas recirculation control scheme for optimizing the performance and emissions of a diesel engine"
in: *International Journal of Engine Research* 21.8 (2020), pp. 1298–1313. DOI: 10.1177/1468087418809261. URL: https://doi.org/10.1177/1468087418809261 (cit. on p. 12)

[29] **Song, K., Upadhyay, D., and Xie, H.**
"An assessment of the impacts of low-pressure exhaust gas recirculation on the air path of a diesel engine equipped with electrically assisted turbochargers"
in: *International Journal of Engine Research* 22.1 (2021), pp. 3–21. DOI: 10.1177/1468087419854294. URL: https://doi.org/10.1177/1468087419854294 (cit. on p. 12)

[30] **Carey, C. et al.**
"Extreme engine downsizing"
in: *Innovations in Fuel Economy and Sustainable Road Transport*. Woodhead Publishing 2011, pp. 135–147. ISBN: 9780857092137. DOI: 10.1533/9780857095879. URL: http://www.sciencedirect.com/science/article/pii/B9780857092137500127 (cit. on p. 12)

[31] **Turner, J. W., Popplewell, A., Richardson, S., Lewis, A. G., Akehurst, S., Brace, C. J., and Bredda, S. W.**
"Ultra boost for economy: Realizing a 60% downsized engine concept"
in: *Internal Combustion Engines: Performance, Fuel Economy and Emissions*. London, UK: Woodhead Publishing 2013, pp. 3–17. ISBN: 9781782421849. DOI: 10.1533/9781782421849.1.3. URL: http://www.sciencedirect.com/science/article/pii/B9781782421832500019
(cit. on p. 12)

[32] **Feneley, A. J., Pesiridis, A., and Andwari, A. M.**
"Variable Geometry Turbocharger Technologies for Exhaust Energy Recovery and Boosting-A Review"
in: *Renewable and Sustainable Energy Reviews* 71 (2017), pp. 959–975. ISSN: 1364-0321. DOI: 10.1016/j.rser.2016.12.125. URL: http://www.sciencedirect.com/science/article/pii/S1364032116311807
(cit. on p. 12)

[33] **Dong, D., Moriyoshi, Y., and Zhu, J.**
"To improve the performance of a variable geometry turbocharged SI engine by porous material application"
in: *Applied Thermal Engineering* 197 (Oct. 2021), p. 117373. ISSN: 1359-4311. DOI: 10.1016/J.APPLTHERMALENG.2021.117373 (cit. on p. 12)

[34] **Kawakubo, T.**
"Unsteady Rotor-Stator Interaction of a Radial-Inflow Turbine With Variable Nozzle Vanes"
in: *Proceedings of ASME Turbo Expo 2010: Power for Land, Sea and Air*. Glasgow, UK 2010, pp. 2075–2084. DOI: 10.1115/GT2010-23677. URL: https://doi.org/10.1115/GT2010-23677 (cit. on pp. 12, 14, 103)

[35] **Hawley, J. G., Wallace, F. J., Cox, A. R. J., Horrocks, R. W., and Bird, G. L.**
"Reduction of Steady State NOx Levels from an Automotive Diesel Engine Using Optimised VGT/EGR Schedules"
in: *SAE Technical Paper* 108 (1999), pp. 1172–1184. DOI: 10.4271/1999-01-0835. URL: https://doi.org/10.4271/1999-01-0835 (cit. on pp. 12, 41, 83)

[36] **Romagnoli, A. et al.**
"Assessment of supercharging boosting component for heavily downsized gasoline engines"
in: *11th International Conference on Turbochargers and Turbocharging*. Oxford: Woodhead Publishing 2014, pp. 13–26. ISBN: 9780081000335. DOI: 10.1533/978081000342.13. URL: http://www.sciencedirect.com/science/article/pii/B9780081000335500020 (cit. on p. 12)

[37] **Hu, B., Brace, C., Akehurst, S., Copeland, C., and Turner, J. W.**
"The effect of divided exhaust period for improved performance in a highly downsized turbocharged gasoline engine"
in: *11th International Conference on Turbochargers and Turbocharging*. Ed. by Engineers, I. o. M. Oxford: Woodhead Publishing 2014, pp. 27–39. ISBN: 9780081000335. DOI: 10.1533/978081000342.27. URL: http://www.sciencedirect.com/science/article/pii/B9780081000335500032 (cit. on p. 12)

[38] **Bellis, V. de, Bozza, F., Marelli, S., and Capobianco, M.**
"Experimental Investigation and 1D Simulation of a Turbocharger Compressor Close to Surge Operation"
in: *SAE International Journal of Engines* 8.4 (2015). ISSN: 19463944. DOI: 10.4271/2015-01-1720. URL: https://doi.org/10.4271/2015-01-1720 (cit. on p. 12)

[39] **Mirza-Hekmati, D., Heath, W. P., Apsley, J. M., and Forbes, J. R.**
"Down-speeding diesel engines with two-stage turbochargers: Analysis and control considerations"
in: *International Journal of Engine Research* (2020), pp. 1–12. DOI: 10.1177/1468087420976482. URL: https://doi.org/10.1177/1468087420976482 (cit. on p. 12)

[40] **Bruensicke, W. and Cholvin, R.**
"The turbocharger function in the light aircraft field"
in: *General Aviation Aircraft Design and Operations Meeting*. Wichata, Kansas 1964, pp. 1–9. DOI: https://doi.org/10.2514/6.1964-191. URL: https://arc.aiaa.org/doi/abs/10.2514/6.1964-191
(cit. on p. 12)

[41] **Jiménez-Espadafor Aguilar, F. J. and Vélez Godiño, J. A.**
"Innovative power train configurations for aircraft auxiliary power units focused on reducing carbon footprint"
in: *Aerospace Science and Technology* 106.1270-9638 (2020), p. 106109. ISSN: 12709638. DOI: 10.1016/j.ast.2020.106109. URL: http://www.sciencedirect.com/science/article/pii/S1270963820307914
(cit. on p. 12)

[42] **Jennions, I., Ali, F., Miguez, M. E., and Escobar, I. C.**
"Simulation of an aircraft environmental control system"
in: *Applied Thermal Engineering* 172 (2020), p. 114925. ISSN: 1359-4311. DOI: 10.1016/j.applthermaleng.2020.114925. URL: https://doi.org/10.1016/j.applthermaleng.2020.114925 (cit. on p. 12)

[43] **Yang, H., Zhang, X., Wang, C., and Yang, C.**
"Design Analysis of Power Recovery Systems for Cabin Exhaust Air"
in: *Procedia Engineering* 121.1877-7058 (2015), pp. 248–255. DOI: 10.1016/j.proeng.2015.08.1065. URL: http://www.sciencedirect.com/science/article/pii/S1877705815027939 (cit. on p. 12)

[44] **Yang, H., Zhang, X., Wang, C., and Yang, C.**
"Experimental and theoretical study on a novel energy-saving ECS for commercial airliners"
in: *Applied Thermal Engineering* 127 (2017), pp. 1372–1381. ISSN: 1359-4311. DOI: https://doi.org/10.1016/j.applthermaleng.2017.08.043. URL: http://www.sciencedirect.com/science/article/pii/S1359431117324596 (cit. on pp. 12, 47)

[45] **Ribau, J., Silva, C., Brito, F. P., and Martins, J.**
"Analysis of four-stroke, Wankel, and microturbine based range extenders for electric vehicles"
in: *Energy Conversion and Management* 58 (2012), pp. 120–133. ISSN: 0196-8904. DOI: https://doi.org/10.1016/j.enconman.2012.01.011. URL: https://www.sciencedirect.com/science/article/pii/S0196890412000271 (cit. on p. 12)

[46] **García, A., Monsalve-Serrano, J., Martínez-Boggio, S., and Wittek, K.**
"Potential of hybrid powertrains in a variable compression ratio down-

sized turbocharged VVA Spark Ignition engine"
in: *Energy* 195 (2020), p. 117039. ISSN: 0360-5442. DOI: https://doi.org/10.1016/j.energy.2020.117039. URL: https://www.sciencedirect.com/science/article/pii/S0360544220301468 (cit. on p. 12)

[47] **Estrada, L., Moreno, E., Gonzalez-Quiroga, A., Bula, A., and Duarte-Forero, J.**
"Experimental assessment of performance and emissions for hydrogen-diesel dual fuel operation in a low displacement compression ignition engine"
in: *Heliyon* 8.4 (2022), e09285. ISSN: 2405-8440. DOI: https://doi.org/10.1016/j.heliyon.2022.e09285. URL: https://www.sciencedirect.com/science/article/pii/S2405844022005734 (cit. on p. 12)

[48] **Chiesa, S., Fioriti, M., and Fusaro, R.**
"Possible hybrid propulsion configuration for transport jet aircraft"
in: *Aviation* 20 (2016), pp. 145–154. DOI: 10.3846/16487788.2016.1200849. URL: https://doi.org/10.3846/16487788.2016.1200849 (cit. on p. 12)

[49] **Wittmann, T., Lück, S., Bode, C., and Friedrichs, J.**
"Modelling the Condensation Phenomena within the Radial Turbine of a Fuel Cell Turbocharger"
in: *International Journal of Turbomachinery, Propulsion and Power* 6.3 (2021). ISSN: 2504-186X. DOI: 10.3390/ijtpp6030023. URL: https://www.mdpi.com/2504-186X/6/3/23 (cit. on p. 12)

[50] **Altarazi, Y. S. M., Abu Talib, A. R., Yu, J., Gires, E., Abdul Ghafir, M. F., Lucas, J., and Yusaf, T.**
"Effects of biofuel on engines performance and emission characteristics: A review"
in: *Energy* 238 (2022), p. 121910. ISSN: 0360-5442. DOI: https://doi.org/10.1016/j.energy.2021.121910. URL: https://www.sciencedirect.com/science/article/pii/S0360544221021587 (cit. on p. 12)

[51] **Jeyaseelan, T., Chacko, N., N, P., O, S. M. K., Alexander, J., and Porpatham, E.**
"Partial hydrogenation and hydrogen induction: A comparative study with B20 operation in a turbocharged CRDI diesel engine"
in: *International Journal of Hydrogen Energy* 46.43 (2021), pp. 22659–22669. ISSN: 0360-3199. DOI: https://doi.org/10.1016/j.ijhydene.2021.04.068. URL: https://www.sciencedirect.com/science/article/pii/S0360319921013987 (cit. on p. 12)

[52] **Alshammari, F.**
"Radial Turbine Expander Design, Modelling and Testing for Automotive Organic Rankine Cycle Waste Heat Recovery"
Thesis. Brunel University London 2018, pp. 1–275. URL: http://bura.brunel.ac.uk/handle/2438/16007 (cit. on p. 12)

[53] **Permana, D. I., Rusirawan, D., and Farkas, I.**
"A bibliometric analysis of the application of solar energy to the organic Rankine cycle"
in: *Heliyon* 8.4 (2022), e09220. ISSN: 2405-8440. DOI: https://doi.org/10.1016/j.heliyon.2022.e09220. URL: https://www.sciencedirect.com/science/article/pii/S2405844022005084 (cit. on p. 12)

[54] **Polanco Piñerez, G., Valencia Ochoa, G., and Duarte-Forero, J.**
"Energy, exergy, and environmental assessment of a small-scale solar organic Rankine cycle using different organic fluids"
in: *Heliyon* 7.9 (2021), e07947. ISSN: 2405-8440. DOI: https://doi.org/10.1016/j.heliyon.2021.e07947. URL: https://www.sciencedirect.com/science/article/pii/S2405844021020508 (cit. on p. 12)

[55] *The Effect of Clearance Flow of Variable Area Nozzles on Radial Turbine Performance*
vol. 6. Turbo Expo: Power for Land, Sea, and Air. Berlin, Germany: ASME 2008, pp. 1519–1529. DOI: 10.1115/GT2008-50461. URL: https://doi.org/10.1115/GT2008-50461 (cit. on pp. 12, 17, 39)

[56] **Izaguirre, A. O. T., García, R. N., Inhestern, L. B., and Gómez, N. H.**
"Design and numerical analysis of flow characteristics in a scaled volute and vaned nozzle of radial turbocharger turbines"
in: *Energies* 13.11 (2020), p. 19. ISSN: 19961073. DOI: 10.3390/en13112930. URL: https://doi.org/10.3390/en13112930
(cit. on pp. 12, 15)

[57] **Dufour, G., Carbonneau, X., Cazalbou, J.-b., and Chassaing, P.**
"Practical Use of Similarity and Scaling Laws for Centrifugal Compressor Design"
in: *Turbo Expo: Power for Land, Sea, and Air*. Vol. 6. Barcelona, Spain: ASME 2006, pp. 1131–1140. DOI: 10.1115/GT2006-91227. URL: https://doi.org/10.1115/GT2006-91227 (cit. on pp. 12, 15)

[58] **Galindo, J., Tiseira Izaguirre, A. O., García-Cuevas, L. M., and Hervás Gómez, N.**
"Experimental approach for the analysis of the flow behaviour in the stator of a real centripetal turbine"
in: *International Journal of Engine Research* 22.6 (2020), pp. 1–11. ISSN:

20413149. DOI: 10.1177/1468087420916281. URL: https://doi.org/10.1177/1468087420916281 (cit. on pp. 12, 15, 196)

[59] **Binder, N., Le Guyader, S., and Carbonneau, X.**
"Analysis of the Variable Geometry Effect in Radial Turbines"
in: *Journal of Turbomachinery* 134.4 (July 2011). ISSN: 0889-504X. DOI: 10.1115/1.4003713. URL: https://doi.org/10.1115/1.4003713 (cit. on p. 13)

[60] **Marsan, A. and Moreau, S.**
"Analysis of the flow structure in a radial turbine"
in: *11th European Conference on Turbomachinery Fluid Dynamics and Thermodynamics, ETC 2015*. Madrid: EUROTURBO 2015, pp. 1–13. DOI: ETC2015-207. URL: euroturbo.eu/publications/proceedings-papers/etc2015-207/ (cit. on pp. 13, 39)

[61] **Serrano, J. R., Arnau, F. J., García-Cuevas, L. M., and Dombrovsky, A.**
"Development and validation of a radial turbine efficiency and mass flow model at design and off-design conditions"
in: *Energy Conversion and Management* 128 (2016), pp. 281–293. DOI: 10.1016/j.enconman.2016.09.032. URL: https://doi.org/10.1016/j.enconman.2016.09.032 (cit. on pp. 13, 61)

[62] **Romagnoli, A. and Martinez-Botas, R.**
"Performance prediction of a nozzled and nozzleless mixed-flow turbine in steady conditions"
in: *International Journal of Mechanical Sciences* 53.8 (2011), pp. 557–574. ISSN: 00207403. DOI: 10.1016/j.ijmecsci.2011.05.003. URL: http://www.sciencedirect.com/science/article/pii/S0020740311000920 (cit. on p. 13)

[63] **Meroni, A., Robertson, M., Martinez-Botas, R., and Haglind, F.**
"A methodology for the preliminary design and performance prediction of high-pressure ratio radial-inflow turbines"
in: *Energy* 164 (2018), pp. 1062–1078. ISSN: 03605442. DOI: 10.1016/j.energy.2018.09.045. URL: https://doi.org/10.1016/j.energy.2018.09.045 (cit. on pp. 13, 202)

[64] **Tancrez, M., Galindo, J., Guardiola, C., Fajardo, P., and Varnier, O.**
"Turbine adapted maps for turbocharger engine matching"
in: *Experimental Thermal and Fluid Science* 35.1 (2011), pp. 146–153. ISSN: 08941777. DOI: 10.1016/j.expthermflusci.2010.07.018. URL: http://dx.doi.org/10.1016/j.expthermflusci.2010.07.018 (cit. on pp. 13, 62)

[65] **Zamboni, G., Moggia, S., and Capobianco, M.**
"Effects of a dual-loop exhaust gas recirculation system and variable nozzle turbine control on the operating parameters of an automotive diesel engine"
in: *Energies* 10.1 (2017), p. 47. ISSN: 19961073. DOI: 10.3390/en10010047. URL: https://doi.org/10.3390/en10010047 (cit. on p. 13)

[66] **Petha Sethuraman, V. R. and Kim, H. D.**
"Characteristics of Shock Train Flow in Divergent Channels"
in: *Recent Asian Research on Thermal and Fluid Sciences*. Ed. by Suryan, A., Doh, D. H., Yaga, M., and Zhang, G. Singapore: Springer Singapore 2020, pp. 353–364. ISBN: 978-981-15-1892-8. DOI: DOIhttps://doi.org/10.1007/978-981-15-1892-8_28. URL: https://link.springer.com/chapter/10.1007%7B%5C%%7D2F978-981-15-1892-8%7B%5C_%7D28 (cit. on p. 13)

[67] **Siemens**
STAR-CCM + 2019.1 Release version 14.02.010-R8.
2019. URL: https://www.plm.automation.siemens.com/global/es/products/simcenter/STAR-CCM.html (cit. on pp. 13, 42)

[68] **Menter, F. R., Langtry, R., and Hansen, T.**
"CFD simulation of turbomachinery flows - Verfication, validation and modelling"
in: *ECCOMAS 2004 - European Congress on Computational Methods in Applied Sciences and Engineering*. July. Jyvaskyla 2004, pp. 1–14. URL: http://www.mit.jyu.fi/eccomas2004/proceedings/pdf/954.pdf (cit. on pp. 13, 42)

[69] **Galindo, J., Tiseira, A., Navarro, R., and López, M. A.**
"Influence of tip clearance on flow behavior and noise generation of centrifugal compressors in near-surge conditions"
in: *International Journal of Heat and Fluid Flow* 52 (2015), pp. 129–139. ISSN: 0142-727X. DOI: https://doi.org/10.1016/j.ijheatfluidflow.2014.12.004. URL: https://www.sciencedirect.com/science/article/pii/S0142727X14001751 (cit. on pp. 13, 127)

[70] **Bhide, K., Siddappaji, K., Abdallah, S., and Roberts, K.**
"Improved Supersonic Turbulent Flow Characteristics Using Non-Linear Eddy Viscosity Relation in RANS and HPC-Enabled LES"
in: *Aerospace* 8.11 (2021). ISSN: 2226-4310. DOI: 10.3390/aerospace8110352. URL: https://www.mdpi.com/2226-4310/8/11/352 (cit. on p. 13)

[71] **Bhide, K. and Abdallah, S.**
"Turbulence statistics of supersonic rectangular jets using Reynolds Stress Model in RANS and WALE LES"
in: *AIAA AVIATION 2022 Forum*. Chicago 2022. DOI: 10.2514/6.2022-3344. URL: https://arc.aiaa.org/doi/abs/10.2514/6.2022-3344
(cit. on p. 13)

[72] **Broatch, A., Galindo, J., Navarro, R., and García-Tíscar, J.**
"Numerical and experimental analysis of automotive turbocharger compressor aeroacoustics at different operating conditions"
in: *International Journal of Heat and Fluid Flow* 61 (2016), pp. 245–255. ISSN: 0142-727X. DOI: https://doi.org/10.1016/j.ijheatfluidflow.2016.04.003. URL: https://www.sciencedirect.com/science/article/pii/S0142727X16301163 (cit. on p. 14)

[73] **Serrano, J. R., Gil, A., Navarro, R., and Inhestern, L. B.**
"Extremely low mass flow at high blade to jet speed ratio in variable geometry radial turbines and its influence on the flow pattern a CFD analysis"
in: *ASME Turbo Expo 2017: Turbomachinery Technical Conference and Exposition*. Charlotte, NC, USA: ASME 2017, pp. 1–13. DOI: 10.1115/GT2017-63368. URL: https://asmedigitalcollection.asme.org/GT/proceedings-abstract/GT2017/50954/V008T26A005/243279
(cit. on pp. 14, 15, 39, 41, 44, 47, 48)

[74] **Galindo, J., Serrano, J. R., García-Cuevas, L. M., and Medina, N.**
"Using a CFD analysis of the flow capacity in a twin-entry turbine to develop a simplified physics-based model"
in: *Aerospace Science and Technology* 112 (2021), p. 106623. ISSN: 1270-9638. DOI: https://doi.org/10.1016/j.ast.2021.106623. URL: https://www.sciencedirect.com/science/article/pii/S1270963821001334 (cit. on pp. 14, 48, 202)

[75] **Huayin, T.**
"Application of Variable Geometry Turbine on Gasoline Engines and the Optimisation of Transient Behaviours"
PhD thesis. University of Bath 2016, p. 232. URL: https://purehost.bath.ac.uk/ws/portalfiles/portal/187959568/Huayin%7B%5C_%7DThesis.pdf (cit. on pp. 14, 15)

[76] **Tang, H., Akehurst, S., Brace, C. J., Garrett, S., and Smith, L.**
"Optimisation of transient response of a gasoline engine with variable geometry turbine turbocharger"
in: *11th International Conference on Turbochargers and Turbocharging*. Ed. by Engineers, I. o. M. Oxford: Woodhead Publishing 2014, pp. 163–

175. ISBN: 9780081000335. DOI: 10.1533/978081000342.163. URL: http://www.sciencedirect.com/science/article/pii/B9780081000335500147 (cit. on p. 14)

[77] **Zhao, B., Sun, H., Shi, X., Qi, M., and Guo, S.**
"Investigation of using multi-shockwave system instead of single normal shock for improving radial inflow turbine reliability"
in: *International Journal of Heat and Fluid Flow* 71.March (2018), pp. 170–178. ISSN: 0142727X. DOI: 10.1016/j.ijheatfluidflow.2018.03.018. URL: http://www.sciencedirect.com/science/article/pii/S0142727X17305507 (cit. on p. 14)

[78] **Sato, W., Yamagata, A., and Hattori, H.**
"A Study of Aerodynamic Excitation Forces on a Radial Turbine Blade Due to Rotor-Stator Interaction"
in: *Institution of Mechanical Engineers - 11th International Conference on Turbochargers and Turbocharging*. Ed. by Engineers, I. o. M. Oxford: Woodhead Publishing 2014, pp. 389–398. ISBN: 9780081000335. URL: http://www.sciencedirect.com/science/article/pii/B9780081000335500317 (cit. on pp. 14, 16)

[79] **Zhao, B., Yang, C., Hu, L., Sun, H., Yi, J., Eric, C., Shi, X., and Engeda, A.**
"Understanding of the Interaction between Clearance Leakage Flow and Main Passage Flow in a VGT Turbine"
in: *Advances in Mechanical Engineering* 7.2 (2015), p. 652769. DOI: 10.1155/2014/652769. URL: https://doi.org/10.1155/2014/652769 (cit. on p. 15)

[80] **Qiu, X., Anderson, M. R., and Baines, N. C.**
"Meanline Modeling of Radial Inflow Turbine With Variable Area Nozzle"
in: *ASME Turbo Expo 2009: Power for Land, Sea and Air*. Florida: ASME 2009, pp. 1–7. DOI: 10.1115/GT2009-59170. URL: https://doi.org/10.1115/GT2009-59170 (cit. on p. 15)

[81] **Yang, D., Cao, L., Yang, C., Lao, D., and Sun, H.**
"Investigations on the effect of guide vane thickness and solidity on shock and unsteady flow characteristic of VNT"
in: *Journal of Mechanical Science and Technology* 34.6 (2020), pp. 2423–2433. ISSN: 19763824. DOI: 10.1007/s12206-020-0518-4. URL: https://link.springer.com/article/10.1007/s12206-020-0518-4 (cit. on pp. 15, 16)

[82] **Zhao, B., Qi, M., Zhang, H., and Shi, X.**
"Investigation on effects of shock wave on vortical wake flow in a turbine nozzle cascade"

in: *Aerospace Science and Technology* 98 (2020), pp. 1–9. ISSN: 1270-9638. DOI: https://doi.org/10.1016/j.ast.2020.105690. URL: https://www.sciencedirect.com/science/article/pii/S1270963819327348 (cit. on pp. 15, 171)

[83] **Zhao, B., Qi, M., Sun, H., Shi, X., and Ma, C.**
"A comprehensive analysis on the structure of groove-induced shock waves in a linear turbine"
in: *Aerospace Science and Technology* 87.1270-9638 (2019), pp. 331–339. ISSN: 12709638. DOI: 10.1016/j.ast.2019.02.036. URL: http://www.sciencedirect.com/science/article/pii/S1270963818320388 (cit. on pp. 15, 42)

[84] **Mehrnia, S., Miyagawa, K., Kusaka, J., and Nakamura, Y.**
"Radial turbine optimization under unsteady flow using nature-inspired algorithms"
in: *Aerospace Science and Technology* 103.1270-9638 (2020), p. 105903. ISSN: 12709638. DOI: 10.1016/j.ast.2020.105903. URL: http://www.sciencedirect.com/science/article/pii/S127096382030585X (cit. on p. 15)

[85] **Liu, Y., Lao, D., Liu, Y., Yang, C., and Qi, M.**
"Investigation on the effects of nozzle openings for a radial turbine with variable nozzle"
in: *SAE 2014 World Congress & Exhibition*. Vol. 01. Detroit, United Staes: SAE International 2014, pp. 1–8. ISBN: 2014011648. DOI: 10.4271/2014-01-1648. URL: https://doi.org/10.4271/2014-01-1648 (cit. on p. 15)

[86] **Chen, H.**
"Turbine wheel design for Garrett advanced variable geometry turbines for commercial vehicle applications"
in: *8th International Conference on Turbochargers and Turbocharging*. Ed. by Institution of Mechanical Engineers Combustion Engines & Fuels Group, B. T. .-. 8. I. C. o. T. and Turbocharging. Woodhead Publishing 2006, pp. 317–327. ISBN: 1845691741. DOI: 10.1533/9781845697099.6.317. URL: http://www.sciencedirect.com/science/article/pii/B9781845691745500270 (cit. on pp. 15, 177)

[87] **Hu, L., Sun, H., Yi, J., Curtis, E., Morelli, A., Zhang, J., Zhao, B., Yang, C., Shi, X., and Liu, S.**
"Investigation of nozzle clearance effects on a radial turbine: Aerodynamic performance and forced response"
in: *SAE 2013 World Congress & Exhibition*. Vol. 1. Detroit, United States:

SAE International 2013, pp. 1–11. DOI: 10.4271/2013-01-0918. URL: https://doi.org/10.4271/2013-01-0918 (cit. on p. 15)

[88] **Heuer, T., Gugau, M., Klein, A., and Anschel, P.**
"An analytical approach to support high cycle fatigue validation for turbocharger turbine stages"
in: *Turbo Expo: Power for Land, Sea, and Air*. Vol. 1. Berlin, Germany: ASME 2008, pp. 723–732. ISBN: 9780791843116. DOI: 10.1115/GT2008-50764. URL: https://doi.org/10.1115/GT2008-50764 (cit. on p. 15)

[89] **Shi, X., Yang, C., Liu, Y., Liu, S. T., and Zhao, B.**
"Numerical investigation on the high-cycle pressure fluctuation mechanism of VNT rotor"
in: *11th International Conference on Turbochargers and Turbocharging*. Ed. by Engineers, I. o. M. Oxford: Woodhead Publishing 2014, pp. 411–418. DOI: 10.1533/978081000342.411. URL: https://doi.org/10.1533/978081000342.411 (cit. on p. 15)

[90] **Rubechini, F., Marconcini, M., Arnone, A., Del Greco, A. S., and Biagi, R.**
"Special Challenges in the CFD Modeling of Transonic Turbo-Expanders"
in: *ASME Turbo Expo 2013: Turbine Technical Conference and Exposition*. San Antonio, Texas, USA: ASME 2013, pp. 1–10. DOI: 10.1115/GT2013-95554. URL: https://doi.org/10.1115/GT2013-95554 (cit. on pp. 16, 103)

[91] **Allport, J. M., Jupp, M. L., Pezouvanis, A., Janicki, G. W., Pierończyk, A. I., Day, A. J., Olley, P., Mason, B., and Ebrahimi, M. K.**
"Turbocharger blade vibration: Measurement and validation through laser tip-timing"
in: *10th International Conference on Turbochargers and Turbocharging*. Ed. by IMechE. 2. Woodhead Publishing 2012, pp. 173–181. ISBN: 9780857092090. DOI: 10.1533/9780857096135.3b.173. URL: http://www.sciencedirect.com/science/article/pii/B978085709209090500145 (cit. on p. 16)

[92] **Bachschmid, N., Pesatori, E., Bistolfi, S., and Chatterton, S.**
"Blade Vibration Measurements and Excitation Force Evaluation"
in: *Proceedings of the 9th IFToMM International Conference on Rotor Dynamics*. Ed. by Pennacchi, P. Cham: Springer International Publishing 2015, pp. 65–78. ISBN: 978-3-319-06590-8. URL: https://link.springer.com/chapter/10.1007/978-3-319-06590-8%7B%5C_%7D6 (cit. on p. 16)

[93] **Sauret, E.**
"Open Design of High Pressure Ratio Radial-Inflow Turbine for Academic Validation"
in: *Proceedings of the ASME 2012 International Mechanical Engineering Congress and Exposition*. Ed. by ASME. Vol. 7. Houston, USA 2012, pp. 3183–3197. DOI: `10.1115/IMECE2012-88315`. URL: `https://doi.org/10.1115/IMECE2012-88315` (cit. on p. 16)

[94] **Yang, D., Lao, D., Yang, C., Hu, L., and Sun, H.**
"Investigations on the Generation and Weakening of Shock Wave in a Radial Turbine With Variable Guide Vanes"
in: *ASME Turbo Expo 2016: Turbomachinery Technical Conference and Exposition* 2D: Turbom (June 2016), pp. 1–9. DOI: `10.1115/GT2016-57047`. URL: `https://doi.org/10.1115/GT2016-57047` (cit. on p. 16)

[95] **Liu, J., Qiao, W. Y., and Duan, W. H.**
"Investigation of Unsteady Aerodynamic Excitation on Rotor Blade of Variable Geometry Turbine"
in: *International Journal of Rotating Machinery* 2019 (2019), pp. 1–13. ISSN: 15423034. DOI: `10.1155/2019/4396546`. URL: `https://www.hindawi.com/journals/ijrm/2019/4396546/` (cit. on p. 16)

[96] **Hayami, H., Senoo, Y., Hyun, Y. I., and Yamaguchi, M.**
"Effects of tip clearance of nozzle vanes on performance of radial turbine rotor"
in: *Journal of Turbomachinery* 112.1 (1990), pp. 58–63. DOI: `10.1115/1.2927421`. URL: `https://doi.org/10.1115/1.2927421` (cit. on p. 16)

[97] **Simpson, A. T., Spence, S. W., and Watterson, J. K.**
"Numerical and experimental study of the performance effects of varying vaneless space and vane solidity in radial turbine stators"
in: *Journal of Turbomachinery* 135.3 (2013), pp. 1–12. ISSN: 0889504X. DOI: `10.1115/1.4007525`. URL: `https://doi.org/10.1115/1.4007525` (cit. on p. 17)

[98] **Paniagua, G., Yasa, T., De La Loma, A., Castillon, L., and Coton, T.**
"Unsteady strong shock interactions in a transonic turbine: Experimental and numerical analysis"
in: *Journal of Propulsion and Power* 24.4 (2008), pp. 722–731. ISSN: 07484658. DOI: `10.2514/1.34774`. URL: `https://doi.org/10.2514/1.34774` (cit. on pp. 17, 42)

[99] **Kosuge, H., Yamanaka, N., Ariga, I., and Watanabe, I.**
"Performance of Radial Flow Turbines Under Pulsating Flow Conditions"
in: *Journal of Engineering for Power* 98.1 (1976), pp. 53–59. ISSN: 0022-

0825. DOI: 10.1115/1.3446110. URL: https://doi.org/10.1115/1.3446110 (cit. on p. 17)

[100] **Palfreyman, D. and Martinez-Botas, R. F.**
"The Pulsating Flow Field in a Mixed Flow Turbocharger Turbine: An Experimental and Computational Study"
in: *Journal of Turbomachinery* 127.1 (2005), pp. 144–155. ISSN: 0889-504X. DOI: 10.1115/1.1812322. URL: https://doi.org/10.1115/1.1812322 (cit. on p. 17)

[101] **Costall, A., Martinez-botas, R. F., and Palfreyman, D.**
"Detailed Study of Pulsating Flow Performance in a Mixed Flow Turbocharger Turbine"
in: *ASME Turbo Expo 2005: Power for Land, Sea, and Air*. Reno Hilton, Reno Tahoe, Nevada: ASME 2005, pp. 1415–1433. DOI: 10.1115/GT2005-68828. URL: https://doi.org/10.1115/GT2005-68828 (cit. on p. 17)

[102] **Qi, M., Lei, X., Wang, Z., and Ma, C.**
"Investigation on the flow characteristics of a VNT turbine under pulsating flow conditions"
in: *Proceedings of the Institution of Mechanical Engineers, Part D: Journal of Automobile Engineering* 233.2 (2019), pp. 396–412. DOI: 10.1177/0954407017744922. URL: https://doi.org/10.1177/0954407017744922 (cit. on p. 17)

[103] **Xue, Y., Yang, M., Martinez-Botas, R. F., Yang, B., and Deng, K.**
"Unsteady performance of a mixed-flow turbine with nozzled twin-entry volute confronted by pulsating incoming flow"
in: *Aerospace Science and Technology* 95.1270-9638 (2019), p. 105485. ISSN: 12709638. DOI: 10.1016/j.ast.2019.105485. URL: http://www.sciencedirect.com/science/article/pii/S1270963819323430 (cit. on p. 17)

[104] **Fontaneto, F., Arts, T., Simon, M., and Picot, P.**
"Aerodynamic Performance of an Ultra-Low Aspect Ratio Centripetal Turbine Stator"
in: *International Journal of Turbomachinery, Propulsion and Power* (2016), pp. 1–13. ISSN: 2504-186X. DOI: 10.3390/ijtpp1010003. URL: https://www.mdpi.com/2504-186X/1/1/3 (cit. on p. 17)

[105] **Jones, A. C.**
"Design and Test of a Small, High Pressure Ratio Radial Turbine"
in: *Journal of Turbomachinery* 118.2 (1996), pp. 362–370. ISSN: 0889-504X. DOI: 10.1115/1.2836651. URL: https://doi.org/10.1115/1.2836651 (cit. on p. 17)

[106] *Effects of Inlet Conditions on the Turbine Performance of a Radial Turbine*
vol. 6. Turbo Expo: Power for Land, Sea, and Air. Berlin, Germany: ASME 2008, pp. 1985–2001. DOI: 10.1115/GT2008-51088. URL: https://doi.org/10.1115/GT2008-51088 (cit. on p. 17)

[107] **Cerdoun, M. and Ghenaiet, A.**
"Unsteady behaviour of a twin entry radial turbine under engine like inlet flow conditions"
in: *Applied Thermal Engineering* 130 (2018), pp. 93–111. ISSN: 1359-4311. DOI: https://doi.org/10.1016/j.applthermaleng.2017.11.001. URL: https://www.sciencedirect.com/science/article/pii/S1359431117308712 (cit. on p. 17)

[108] *Validation and Development of Loss Models for Small Size Radial Turbines*
vol. 7. Turbo Expo: Power for Land, Sea, and Air. Glasgow, UK: ASME 2010, pp. 1937–1949. DOI: 10.1115/GT2010-22666. URL: https://doi.org/10.1115/GT2010-22666 (cit. on p. 17)

[109] **Tamaki, H., Ouchida, S., and Unno, M.**
"Experimental Fluid Dynamics Applications in Radial Turbomachines: Inlet Recirculation in Centrifugal Compressor, Rotating Stall and Flow in Vaneless Diffuser, and Improvement in Accuracy of CFD for Predicting Flow Fields in a Radial Turbine Rotor"
in: *Journal of Physics: Conference Series* 1909 (2021). DOI: 10.1088/1742-6596/1909/1/012089. URL: https://10.0.4.64/1742-6596/1909/1/012089 (cit. on p. 17)

[110] **He, P., Sun, Z., Zhang, H., Chen, H., and Tan, C.**
"Investigation of clearance flows in deeply scalloped radial turbines"
in: *Proceedings of the Institution of Mechanical Engineers, Part A: Journal of Power and Energy* 226.8 (2012), pp. 951–962. DOI: 10.1177/0957650912460361. URL: https://doi.org/10.1177/0957650912460361
(cit. on pp. 17, 144)

[111] **Kammeyer, J., Natkaniec, C., and Seume, J. R.**
"Tip leakage in small radial turbines: Optimum tip-gap and efficiency loss correlations"
in: *Turbo Expo: Power for Land, Sea, and Air*. Glasgow, UK: ASME 2010, pp. 1–11. DOI: 10.1115/GT2010-22680. URL: https://doi.org/10.1115/GT2010-22680 (cit. on p. 18)

[112] **Serrano, J. R., Navarro, R., García-Cuevas, L. M., and Inhestern, L. B.**
"Contribution to tip leakage loss modeling in radial turbines based on 3D

flow analysis and 1D characterization"
in: *International Journal of Heat and Fluid Flow* 78 (2019), pp. 1–7. ISSN: 0955-5986. DOI: 10.1016/j.ijheatfluidflow.2019.108423. URL: http://www.sciencedirect.com/science/article/pii/S095559861530042X (cit. on pp. 18, 39, 69, 111, 132, 136)

[113] **Zhang, Q. and He, L.**
"Over-tip choking and its implications on turbine blade-tip aerodynamic performance"
in: *Journal of Propulsion and Power* 27.5 (2011), pp. 1008–1014. ISSN: 07484658. DOI: 10.2514/1.B34112 (cit. on p. 18)

[114] **Wheeler, A. P. S., Korakianitis, T., and Banneheke, S.**
"Tip-Leakage Losses in Subsonic and Transonic Blade Rows"
in: *Journal of Turbomachinery* 135.1 (2012). ISSN: 0889-504X. DOI: 10.1115/1.4006424. URL: https://doi.org/10.1115/1.4006424
(cit. on pp. 18, 144)

[115] **Pashayev, A., Askerov, D., and Sadiqov, R.**
"Numerical modeling of gas turbine cooled blades"
in: *Aviation* 9 (2005), pp. 9–18. DOI: 10.3846/16487788.2005.9635905. URL: https://doi.org/10.3846/16487788.2005.9635905
(cit. on p. 18)

[116] **O'Dowd, D. O., Zhang, Q., He, L., Oldfield, M. L. G., Ligrani, P. M., Cheong, B. C. Y., and Tibbott, I.**
"Aero-Thermal Performance of a Winglet at Engine Representative Mach and Reynolds Numbers"
in: *ASME Turbo Expo 2010: Power for Land, Sea, and Air*. Glasgow, UK: ASME June 2010, pp. 357–367. ISBN: 978-0-7918-4399-4. DOI: 10.1115/GT2010-22794. URL: https://doi.org/10.1115/GT2010-22794 (cit. on p. 18)

[117] **Daabo, A. M., Mahmoud, S., Al-Dadah, R. K., Al Jubori, A. M., and Bhar Ennil, A.**
"Numerical analysis of small scale axial and radial turbines for solar powered Brayton cycle application"
in: *Applied Thermal Engineering* 120 (2017), pp. 672–693. ISSN: 1359-4311. DOI: https://doi.org/10.1016/j.applthermaleng.2017.03.125. URL: https://www.sciencedirect.com/science/article/pii/S1359431117320549 (cit. on p. 18)

[118] **Dambach, R. and Hodson, H. P.**
"Tip leakage flow: A comparison between small axial and radial turbines"
in: *IMechE Symposium*. London, UK 2000, pp. 1–9. URL: http://www-

g.eng.cam.ac.uk/whittle/publications/hph/2000-IMechE-RadialTips.pdf (cit. on pp. 18, 144)

[119] *An Experimental Study of Tip Clearance Flow in a Radial Inflow Turbine* vol. Volume 1. Turbo Expo: Power for Land, Sea, and Air. Stockholm: ASME 1998, p. 12. DOI: 10.1115/98-GT-467. URL: https://doi.org/10.1115/98-GT-467 (cit. on pp. 18, 128)

[120] **Serrano, J. R., Navarro, R., García-Cuevas, L. M., and Inhestern, L. B.**
"Turbocharger turbine rotor tip leakage loss and mass flow model valid up to extreme off-design conditions with high blade to jet speed ratio" in: *Energy* 147 (2018), pp. 1299–1310. ISSN: 0360-5442. DOI: https://doi.org/10.1016/j.energy.2018.01.083. URL: https://www.sciencedirect.com/science/article/pii/S0360544218301014 (cit. on pp. 18, 39, 69, 104, 128, 131, 132)

[121] *Variable Geometry Turbine Nozzle Design for High Expansion Ratios* vol. 2B. Turbo Expo: Power for Land, Sea, and Air. Oslo, Norway: ASME 2018, pp. 1–12. DOI: 10.1115/GT2018-75013. URL: https://doi.org/10.1115/GT2018-75013 (cit. on p. 18)

[122] **Sonoda, T., Arima, T., Olhofer, M., Sendhoff, B., Kost, F., and Giess, P.-A.**
"A Study of Advanced High-Loaded Transonic Turbine Airfoils" in: *Journal of Turbomachinery* 128.4 (2004), pp. 650–657. ISSN: 0889-504X. DOI: 10.1115/1.2221325. URL: https://doi.org/10.1115/1.2221325 (cit. on p. 18)

[123] **Lei, X., Qi, M., Sun, H., and Hu, L.**
"Investigation on the Shock Control Using Grooved Surface in a Linear Turbine Nozzle" in: *Journal of Turbomachinery* 139.12 (2017). ISSN: 0889-504X. DOI: 10.1115/1.4037860. URL: https://doi.org/10.1115/1.4037860 (cit. on pp. 18, 173)

[124] *Numerical Investigation of a Novel Approach for Mitigation of Forced Response of a Variable Geometry Turbine During Exhaust Braking Mode* vol. Volume 8: Turbo Expo: Power for Land, Sea, and Air 2016. DOI: 10.1115/GT2016-56342. URL: https://doi.org/10.1115/GT2016-56342 (cit. on pp. 19, 171, 177)

[125] **Zhao, B., Qi, M., Sun, H., Shi, X., and Ma, C.**
"Experimental and Numerical Investigation on the Shock Wave Structure Alterations and Available Energy Loss Variations With a Grooved Nozzle Vane"

in: *Journal of Turbomachinery* 141.5 (2019). ISSN: 0889-504X. DOI: 10.1115/1.4041819. URL: https://doi.org/10.1115/1.4041819 (cit. on pp. 19, 169)

[126] **Moore, J. and Moore, J. G.**
Entropy Production Rates From Viscous Flow Calculations: Part I — A Turbulent Boundary Layer Flow
Mar. 1983. DOI: 10.1115/83-GT-70. URL: https://doi.org/10.1115/83-GT-70 (cit. on pp. 19, 149)

[127] **Ziaja, K., Post, P., Schramm, A., Willers, O., Seume, J. R., and Mare, F. di**
"Numerical Investigation of Loss Mechanisms in a Partially Loaded Supersonic ORC Axial Turbine Stage"
in: Rotterdam, Netherlands June 2022. DOI: 10.1115/GT2022-82852. URL: https://doi.org/10.1115/GT2022-82852 (cit. on pp. 19, 149)

[128] **Zhang, L., Zhuge, W., Zhang, Y., and Chen, T.**
"Similarity Theory Based Radial Turbine Performance and Loss Mechanism Comparison between R245fa and Air for Heavy-Duty Diesel Engine Organic Rankine Cycles"
in: *Entropy* 19.1 (2017), pp. 1–20. ISSN: 1099-4300. DOI: 10.3390/e19010025. URL: https://www.mdpi.com/1099-4300/19/1/25 (cit. on pp. 19, 149)

[129] **Lim, S. M., Dahlkild, A., and Mihaescu, M.**
"Influence of Upstream Geometry on Pulsatile Turbocharger Turbine Performance"
in: *ASME Turbo Expo 2018: Turbomachinery Technical Conference and Exposition*. Oslo, Norway June 2018, pp. 1–10. DOI: 10.1115/GT2018-76706. URL: https://doi.org/10.1115/GT2018-76706 (cit. on p. 20)

[130] **Lim, S. M., Dahlkild, A., and Mihaescu, M.**
"Aerothermodynamics and Exergy Analysis in Radial Turbine With Heat Transfer"
in: *Journal of Turbomachinery* 140.9 (Aug. 2018), pp. 1–14. ISSN: 0889-504X. DOI: 10.1115/1.4040852. URL: https://doi.org/10.1115/1.4040852 (cit. on p. 20)

[131] **Lim, S. M., Kazemi Bakhshmand, S., Biet, C., and Mihaescu, M.**
"Experimental and Numerical Investigation of a Turbocharger Turbine Using Exergy Analysis at Non-Adiabatic Conditions"
in: *SAE Powertrains, Fuels & Lubricants Meeting*. SAE International 2020, pp. 1–9. DOI: 10.4271/2020-01-2225. URL: https://www.sae.o

rg/publications/technical-papers/content/2020-01-2225/ (cit. on p. 20)

[132] **Smirnov, E. M., Abramov, A. G., Ivanov, N. G., Smirnov, P. E., and Yakubov, S. A.**
"- DNS and RANS/LES-computations of complex geometry flows using a parallel multiblock finite-volume code"
in: *Parallel Computational Fluid Dynamics 2003*. Ed. by Ecer, A., Satofuka, N., Periaux, J., and Fox, P. Amsterdam: Elsevier 2004, pp. 219–226. ISBN: 978-0-444-51612-1. DOI: https://doi.org/10.1016/B978-044451612-1/50028-7. URL: https://www.sciencedirect.com/science/article/pii/B9780444516121500287 (cit. on p. 39)

[133] **SAE Engine Power Test Code Committee**
Turbocharger Gas Stand Test Code
1995. DOI: 10.4271/J1826_199503. URL: https://doi.org/10.4271/J1826%7B%5C_%7D199503 (cit. on p. 41)

[134] **Ammann, M., Fekete, N. P., Guzzella, L., and Glattfelder, A. H.**
"Model-based control of the VGT and EGR in a turbocharged common-rail diesel engine: Theory and passenger car implementation"
in: *SAE Technical Papers* 112 (2003), pp. 527–538. ISSN: 26883627. DOI: 10.4271/2003-01-0357. URL: https://doi.org/10.4271/2003-01-0357. (cit. on pp. 41, 83)

[135] **Chauvin, J., Albrecht, A., Corde, G., and Petit, N.**
"Modeling and control of a Diesel HCCI engine"
in: *Proceedings of the Fifth IFAC Symposium on Advances in Automotive Control* (2007), pp. 1–8. DOI: 10.3182/20070820-3-US-2918.00064 (cit. on pp. 41, 83)

[136] **Flärdh, O. and Mårtensson, J.**
"Exhaust pressure modeling and control on an si engine with vgt"
in: *Control Engineering Practice* 25 (2014), pp. 26–35. ISSN: 0967-0661. DOI: https://doi.org/10.1016/j.conengprac.2013.11.021. URL: https://www.sciencedirect.com/science/article/pii/S0967066113002359 (cit. on p. 41)

[137] **Dickinson, P., Glover, K., Collings, N., Yamashita, Y., Yashiro, Y., and Hoshi, T.**
"Real-time control of a two-stage serial VGT Diesel engine using MPC"
in: *IFAC-PapersOnLine* 48.15 (2015), pp. 117–123. ISSN: 2405-8963. DOI: https://doi.org/10.1016/j.ifacol.2015.10.017. URL: https://www.sciencedirect.com/science/article/pii/S2405896315018935 (cit. on p. 41)

[138] **Galindo, J., Dolz, V., Monsalve-Serrano, J., Bernal, M. A., and Odillard, L.**
"Impacts of the exhaust gas recirculation (EGR) combined with the regeneration mode in a compression ignition diesel engine operating at cold conditions"
in: *International Journal of Engine Research* 22.12 (2021), pp. 3548–3557. DOI: 10.1177/14680874211013986. URL: https://doi.org/10.1177/14680874211013986 (cit. on pp. 41, 83)

[139] **Serrano, J. R., Tiseira, A., García-Cuevas, L. M., Inhestern, L. B., and Tartoussi, H.**
"Radial turbine performance measurement under extreme off-design conditions"
in: *Energy* 125 (2017), pp. 72–84. ISSN: 03605442. DOI: 10.1016/j.energy.2017.02.118. URL: http://www.sciencedirect.com/science/article/pii/S0360544217303018 (cit. on pp. 42, 59, 61)

[140] **Menter, F. R.**
"Two-equation eddy-viscosity turbulence models for engineering applications"
in: *AIAA Journal* 32.8 (1994), pp. 1598–1605. ISSN: 00011452. DOI: 10.2514/3.12149. URL: https://doi.org/10.2514/3.12149
(cit. on p. 42)

[141] **Fajardo, P.**
"Methodology for the Numerical Characterization of a Radial Turbine under Steady and Pulsating Flow"
PhD thesis. Universitat Politècnica de València 2012, p. 222. URL: riunet.upv.es/bitstream/handle/10251/16878/tesisUPV3883.pdf
(cit. on p. 42)

[142] **Simpson, A. T., Spence, S. W. T., and Watterson, J. K.**
"A Comparison of the Flow Structures and Losses Within Vaned and Vaneless Stators for Radial Turbines"
in: *Journal of Turbomachinery* 131.3 (2009), pp. 1–15. ISSN: 0889-504X. DOI: 10.1115/1.2988493. URL: https://doi.org/10.1115/1.2988493
(cit. on p. 42)

[143] **Galindo, J., Fajardo, P., Navarro, R., and García-Cuevas, L. M.**
"Characterization of a radial turbocharger turbine in pulsating flow by means of CFD and its application to engine modeling"
in: *Applied Energy* 103 (2013), pp. 116–127. ISSN: 03062619. DOI: 10.1016/j.apenergy.2012.09.013. URL: http://dx.doi.org/10.1016/j.apenergy.2012.09.013 (cit. on p. 42)

[144] **Xue, Y., Yang, M., Pan, L., Deng, K., Wu, X., and Wang, C.**
"Gasdynamic behaviours of a radial turbine with pulsating incoming flow"
in: *Energy* 218 (2021), p. 119523. ISSN: 03605442. DOI: 10.1016/j.energy.2020.119523. URL: http://www.sciencedirect.com/science/article/pii/S036054422032630X (cit. on p. 42)

[145] **Ananthakrishnan, K. and Govardhan, M.**
"Influence of fillet shapes on secondary flow field in a transonic axial flow turbine stage"
in: *Aerospace Science and Technology* 82-83 (2018), pp. 425–437. ISSN: 1270-9638. DOI: https://doi.org/10.1016/j.ast.2018.08.040. URL: https://www.sciencedirect.com/science/article/pii/S1270963818307533 (cit. on p. 42)

[146] **Balasubramanian, R., Barrows, S., and Chen, J. P.**
Investigation of shear-stress transport turbulence model for turbomachinery applications
January. Reno, Nevada, United States: Amercian Institute of Aeronautics and Astronautics 2008, pp. 1–18. ISBN: 9781563479373. DOI: 10.2514/6.2008-566. URL: https://arc.aiaa.org/doi/abs/10.2514/6.2008-566 (cit. on p. 42)

[147] **Menter, F. R.**
"Review of the shear-stress transport turbulence model experience from an industrial perspective"
in: *International Journal of Computational Fluid Dynamics* 23.4 (2009), pp. 305–316. ISSN: 10618562. DOI: 10.1080/10618560902773387. URL: https://doi.org/10.1080/10618560902773387 (cit. on p. 42)

[148] **Ram, P., Kim, T., and Kim, H. D.**
"Numerical Study on Shock Train Characteristics in Divergent Channels"
in: *Journal of Applied Fluid Mechanics* 13 (2020), pp. 1081–1092. DOI: 10.36884/jafm.13.04.30837. URL: https://doi.org/10.36884/jafm.13.04.30837 (cit. on p. 42)

[149] **Zheltovodov, A.**
"Shock waves/turbulent boundary-layer interactions - Fundamental studies and applications"
in: *Fluid Dynamics Conference*. New Orleans, United States: AIAA 1996, pp. 1–28. DOI: 10.2514/6.1996-1977. URL: https://arc.aiaa.org/doi/abs/10.2514/6.1996-1977 (cit. on p. 42)

[150] **Bardina, J. E., Huang, P. G., and Coakley, T. J.**
Turbulence modeling validation
Snowmass Village, Colorado, United States: National Aeronautics and

Space Administration 1997, pp. 1–16. DOI: 10.2514/6.1997-2121. URL: https://arc.aiaa.org/doi/abs/10.2514/6.1997-2121
(cit. on p. 42)

[151] **Galindo, J., Hoyas, S., Fajardo, P., and Navarro, R.**
"Set-Up Analysis and Optimization of CFD Simulations for Radial Turbines"
in: *Engineering Applications of Computational Fluid Mechanics* 7.4 (2013), pp. 441–460. DOI: 10.1080/19942060.2013.11015484. URL: https://doi.org/10.1080/19942060.2013.11015484
(cit. on pp. 44, 48)

[152] **Hazizi, K., Ramezanpour, A., Costall, A., and Asadi, M.**
"Numerical analysis of a turbocharger compressor"
in: *XII International Conference on Computational Heat, Mass and Momentum Transfer (ICCHMT 2019)*. Vol. 128. E3S Web of Conferences 2019, pp. 1–8. DOI: 10.1051/e3sconf/201912806012. URL: https://doi.org/10.1051/e3sconf/201912806012 (cit. on p. 44)

[153] **Roache, P. J.**
"Perspective: A Method for Uniform Reporting of Grid Refinement Studies"
in: *Journal of Fluids Engineering* 116.3 (1994), pp. 405–413. ISSN: 0098-2202. DOI: 10.1115/1.2910291. URL: https://doi.org/10.1115/1.2910291 (cit. on pp. 46, 164)

[154] **Harinck, J., Turunen-Saaresti, T., Colonna, P., Rebay, S., and Buijtenen, J. van**
"Computational Study of a High-Expansion Ratio Radial Organic Rankine Cycle Turbine Stator"
in: *Journal of Engineering for Gas Turbines and Power* 132.5 (2010), pp. 1–6. ISSN: 0742-4795. DOI: 10.1115/1.3204505. URL: https://doi.org/10.1115/1.3204505 (cit. on p. 47)

[155] **Sauret, E. and Gu, Y.**
"Three-dimensional off-design numerical analysis of an organic Rankine cycle radial-inflow turbine"
in: *Applied Energy* 135 (2014), pp. 202–211. ISSN: 03062619. DOI: 10.1016/j.apenergy.2014.08.076. URL: https://www.sciencedirect.com/science/article/pii/S0306261914008873 (cit. on p. 47)

[156] **Li, S., Wang, S., Ma, Z., and Zhang, T.**
"An air cycle heat pump heating system using a turbocharger for full electric vehicle"
in: *Procedia Engineering* 205 (2017), pp. 1405–1411. ISSN: 1877-7058. DOI: https://doi.org/10.1016/j.proeng.2017.10.316. URL: https:

//www.sciencedirect.com/science/article/pii/S1877705817349810 (cit. on p. 47)

[157] **Li, S., Wang, S., Ma, Z., Jiang, S., and Zhang, T.**
"Using an air cycle heat pump system with a turbocharger to supply heating for full electric vehicles"
in: *International Journal of Refrigeration* 77 (2017), pp. 11–19. ISSN: 0140-7007. DOI: https://doi.org/10.1016/j.ijrefrig.2017.03.004. URL: https://www.sciencedirect.com/science/article/pii/S0140700717300993 (cit. on p. 47)

[158] **Pérez-Grande, I. and Leo, T. J.**
"Optimization of a commercial aircraft environmental control system"
in: *Applied Thermal Engineering* 22.17 (2002), pp. 1885–1904. ISSN: 1359-4311. DOI: https://doi.org/10.1016/S1359-4311(02)00130-8. URL: https://www.sciencedirect.com/science/article/pii/S1359431102001308 (cit. on p. 47)

[159] **Serrano, J. R., Arnau, F. J., García-Cuevas, L. M., and Inhestern, L. B.**
"An innovative losses model for efficiency map fitting of vaneless and variable vaned radial turbines extrapolating towards extreme off-design conditions"
in: *Energy* 180 (2019), pp. 626–639. ISSN: 03605442. DOI: 10.1016/j.energy.2019.05.062. URL: http://www.sciencedirect.com/science/article/pii/S0360544219309314 (cit. on pp. 61, 202)

[160] **Filipi, Z., Wang, Y., and Assanis, D.**
"Effect of variable geometry turbine (VGT) on diesel engine and vehicle system transient response"
in: *SAE 2001 World Congress*. 724. Detroit, Michigan, United States: SAE International 2001, pp. 1–21. DOI: 10.4271/2001-01-1247. URL: https://doi.org/10.4271/2001-01-1247 (cit. on p. 62)

[161] **Rogo, C., Hájek, T., and Chen, A. G.**
Variable stator radial turbine
Cleveland, Ohio, United States: NASA United States 1984, pp. 1–312. DOI: 9840014500. URL: https://ntrs.nasa.gov/search.jsp?R=19840014500 (cit. on p. 62)

[162] **Yaras, M. I. and Sjolander, S. A.**
"Prediction of Tip-Leakage Losses in Axial Turbines"
in: *Journal of Turbomachinery* 114.1 (1992), pp. 204–210. ISSN: 0889-504X. DOI: 10.1115/1.2927987. URL: https://doi.org/10.1115/1.2927987 (cit. on p. 69)

[163] **Pohl, D., Janssen, J., Jeschke, P., Halcoussis, A., and Wolf, H.**
"Variable Stator Vane Penny Gap Aerodynamic Measurements and Numerical Analysis in an Annular Cascade Wind Tunnel"
in: *International Journal of Gas Turbine, Propulsion and Power Systems* 11.2 (2020), pp. 44–55. DOI: https://doi.org/10.38036/jgpp.11.2_44. URL: http://www.gtsj.org/english/index.html (cit. on p. 74)

[164] **Stummann, S., Pohl, D., Jeschke, P., Wolf, H., Halcoussis, A., and Franke, M.**
"Secondary Flow in Variable Stator Vanes With Penny-Cavities"
in: *ASME Turbo Expo 2017: Turbomachinery Technical Conference and Exposition*. Vol. Volume 2A: Charlotte, North Carolina, USA: ASME 2017, pp. 1–12. ISBN: 978-0-7918-5078-7. DOI: 10.1115/GT201763771. URL: https://doi.org/10.1115/GT2017-63771 (cit. on p. 74)

[165] **Japikse, D. and Baines, N.**
Introduction to Turbomachinery
Concepts ETI, Inc 1994 (cit. on p. 74)

[166] **Denton, J. D.**
"Loss mechanisms in turbomachines."
in: *Journal of Turbomachinery* 115.(Cambridge, U.K.: Sep. 1-3, 1987), Bury St. Edmunds, U.K., Mech. Engng. Publications Ltd., 1987, Pap (1993), pp. 621–656. DOI: 10.1115/1.2929299. URL: https://doi.org/10.1115/1.2929299 (cit. on pp. 75, 144)

[167] **Alexin Putra, M. and Joos, F.**
"Investigation of Secondary Flow Behavior in a Radial Turbine Nozzle"
in: *Journal of Turbomachinery* 135.6 (2013). ISSN: 0889-504X. DOI: 10.1115/1.4024627. URL: https://doi.org/10.1115/1.4024627
(cit. on pp. 87, 90)

[168] **Yaras, M. I. and Sjolander, S. A.**
"Effects of simulated rotation on tip leakage in a planar cascade of turbine blades: Part I: Tip gap flow"
in: *Journal of Turbomachinery* 114.3 (1992), pp. 652–659. DOI: 10.1115/1.2929189. URL: https://doi.org/10.1115/1.2929189
(cit. on p. 106)

[169] **Yaras, M. I. and Sjolander, S. A.**
"Effects of Simulated Rotation on Tip Leakage in a Planar Cascade of Turbine Blades: Part II—Downstream Flow Field and Blade Loading"
in: *Journal of Turbomachinery* 114.3 (1992), pp. 660–667. DOI: 10.1115/1.2929190. URL: https://doi.org/10.1115/1.2929190
(cit. on p. 106)

[170] **Dincer, I. and Rosen, M. A.**
Exergy
ed. by Rosen, I. D. and A., M. Ontario, Canada: Elsevier Science 2013, p. 547. ISBN: 9780080970899. DOI: https://doi.org/10.1016/C2010-0-68369-6. URL: https://www.sciencedirect.com/book/9780080970899/exergy (cit. on p. 116)

[171] **Dincer, I.**
"Exergy"
in: *Comprehensive Energy Systems*. Vol. 1-5 2018. Chap. 1.6 Exergy, pp. 212–264. ISBN: 9780128095973. DOI: 10.1016/B978-0-12-809597-3.00106-1. URL: https://www.sciencedirect.com/referencework/9780128149256/comprehensive-energy-systems (cit. on p. 116)

[172] **Deng, Q., Niu, J., and Feng, Z.**
"Tip leakage flow in radial inflow rotor of a microturbine with varying blade-shroud clearance"
in: *Proceedings of the ASME Turbo Expo* 6 PART B.1970 (2007), pp. 1081–1088. DOI: 10.1115/GT2007-27722. URL: https://asmedigitalcollection.asme.org/GT/proceedings-abstract/GT2007/47950/1081/363813 (cit. on p. 132)

[173] **Dambach, R. and Hodson, H. P.**
"Tip Leakage Flow in a Radial Inflow Turbine with Varying Gap Height"
in: *Journal of Propulsion and Power* 17.3 (2001), pp. 644–650. DOI: 10.2514/2.5791. URL: https://doi.org/10.2514/2.5791
(cit. on p. 137)

[174] **Deng, Q., Niu, J., and Feng, Z.**
"Study on leakage flow characteristics of radial inflow turbines at rotor tip clearance"
in: *Science in China Series E: Technological Sciences* 51 (2008), pp. 1125–1136. DOI: 10.1007/s11431-008-0164-z (cit. on pp. 137, 143)

[175] **Xue, Y., Yang, M., Martinez-Botas, R. F., Romagnoli, A., and Deng, K.**
"Loss analysis of a mix-flow turbine with nozzled twin-entry volute at different admissions"
in: *Energy* 166 (Jan. 2019), pp. 775–788. ISSN: 0360-5442. DOI: 10.1016/J.ENERGY.2018.10.075 (cit. on p. 143)

[176] *A Numerical Investigation on a New Pulse-Optimized Flow Control Method for Turbocharger Turbine Performance Improvement Under Pulsating Conditions*
vol. Volume 2C: Turbo Expo: Power for Land, Sea, and Air. Montréal,

Canada: ASME 2015, p. 12. DOI: 10.1115/GT2015-42059. URL: https://doi.org/10.1115/GT2015-42059 (cit. on p. 144)

[177] **Wei, Z., Ren, G., Gan, X., Ni, M., and Chen, W.**
"Influence of Shock Wave on Loss and Breakdown of Tip-Leakage Vortex in Turbine Rotor with Varying Backpressure"
in: *Applied Sciences* 11.11 (2021). ISSN: 2076-3417. DOI: 10.3390/app11114991. URL: https://www.mdpi.com/2076-3417/11/11/4991 (cit. on p. 144)

[178] **Kline, J. F., Moffitt, T. P., and Stabe, R. G.**
"Incidence loss for fan turbine rotor blade in two-dimensional cascade"
in: 1983, pp. 1–12. URL: https://ntrs.nasa.gov/api/citations/19830022160/downloads/19830022160.pdf (cit. on p. 151)

[179] **Mendonça, F., Clement, J., Palfreyman, D., and Peck, A.**
"Validation of unstructured CFD modelling applied to the conjugate heat transfer in turbine blade cooling"
in: *ETC_8-198, European Turbomachinery Conference*. Graz 2008 (cit. on p. 162)

[180] **Asghar, M. A., Liu, Y., Cui, J., and Lu, L.**
"Investigation of Unsteady Flow Interactions in a Transonic High Pressure Turbine Using Nonlinear Harmonic Method"
in: *Energies* 11.2 (2018). ISSN: 1996-1073. DOI: 10.3390/en11020342. URL: https://www.mdpi.com/1996-1073/11/2/342 (cit. on p. 169)

[181] **Li, L., Tan, W., Zhang, J., Han, G., and Zhang, Y.**
"Unsteady Effects of Wake on Downstream Rotor at Low Reynolds Numbers"
in: *Energies* 15.18 (2022). ISSN: 1996-1073. DOI: 10.3390/en15186692. URL: https://www.mdpi.com/1996-1073/15/18/6692 (cit. on p. 169)

[182] **BIAN, X., WANG, Q., SU, X., and YUAN, X.**
"Interaction mechanisms of shock waves with the boundary layer and wakes in a highly-loaded NGV using hybrid RANS/LES"
in: *Chinese Journal of Aeronautics* 33.1 (2020), pp. 149–160. ISSN: 1000-9361. DOI: https://doi.org/10.1016/j.cja.2019.07.008. URL: https://www.sciencedirect.com/science/article/pii/S1000936119302754 (cit. on pp. 171, 173)

[183] **Léonard, T., Gicquel, L. Y. M., Gourdain, N., and Duchaine, F.**
"Steady/Unsteady Reynolds-Averaged Navier–Stokes and Large Eddy Simulations of a Turbine Blade at High Subsonic Outlet Mach Number"
in: *Journal of Turbomachinery* 137.4 (2014). ISSN: 0889-504X. DOI: 10.1

115/1.4028493. URL: https://doi.org/10.1115/1.4028493
(cit. on p. 173)

[184] **Hancock, B. J. and Clark, J. P.**
"Reducing Shock Interactions in Transonic Turbine via Three-Dimensional Aerodynamic Shaping"
in: *Journal of Propulsion and Power* 30.5 (2014), pp. 1248–1256. DOI: 10.2514/1.B35027. URL: https://doi.org/10.2514/1.B35027
(cit. on p. 174)

[185] **Zhao, B., Shi, X., Sun, H., Qi, M., and Song, P.**
"Effects of grooved vanes on shock wave and forced response in a turbocharger turbine"
in: *International Journal of Engine Research* 22.3 (2021), pp. 805–814. DOI: 10.1177/1468087419879265. URL: https://doi.org/10.1177/1468087419879265 (cit. on p. 174)

[186] **Galindo, J., Serrano, J. R., Guardiola, C., and Cervelló, C.**
"Surge limit definition in a specific test bench for the characterization of automotive turbochargers"
in: *Experimental Thermal and Fluid Science* 30.5 (2006), pp. 449–462. ISSN: 0894-1777. DOI: https://doi.org/10.1016/j.expthermflusci.2005.06.002. URL: https://www.sciencedirect.com/science/article/pii/S0894177705001275 (cit. on pp. 194, 196)

[187] **Sakellaridis, N. F., Raptotasios, S. I., Antonopoulos, A. K., Mavropoulos, G. C., and Hountalas, D. T.**
"Development and validation of a new turbocharger simulation methodology for marine two stroke diesel engine modelling and diagnostic applications"
in: *Energy* 91 (2015), pp. 952–966. DOI: 10.1016/j.energy.2015.08.049 (cit. on p. 202)

[188] **Serrano, J. R., Arnau, F. J., De la Morena, J., Gómez-vilanova, A., Guilain, S., and Batard, S.**
"A methodology to calibrate gas-dynamic models of turbocharged petrol engines with variable geometry turbines and with focus on dynamics prediction during tip-in load transient tests"
in: *ASME Turbo Expo 2020: Turbomachinery Technical Conference and Exposition*. Online: ASME 2020, pp. 1–14. DOI: https://doi.org/10.1115/GT2020-15169. URL: https://doi.org/10.1115/GT2020-15169
(cit. on p. 202)

[189] **Serrano, J. R., Piqueras, P., De la Morena, J., Gómez-Vilanova, A., and Guilain, S.**
"Methodological analysis of variable geometry turbine technology impact

on the performance of highly downsized spark-ignition engines” in: *Energy* 215 (2021), p. 119122. ISSN: 0360-5442. DOI: https://doi.org/10.1016/j.energy.2020.119122. URL: https://www.sciencedirect.com/science/article/pii/S0360544220322295 (cit. on p. 202)